MITIGATION OF MERCURY IN WATER USING COPPER SULFIDE

AU YOONG YOW LOO

THESIS SUBMITTED IN FULFILLMENT OF THE REQUIREMENTS FOR THE DEGREE OF DOCTOR OF PHILOSOPHY

DEPARTMENT OF CHEMISTRY
FACULTY OF SCIENCE
UNIVERSITY OF MALAYA
KUALA LUMPUR

2014

ABSTRACT

In response to the worldwide mercury contamination contributed by both natural and anthropogenic sources, two different domains of aqueous mercury (II), Hg(II) complexation have been carried out using homogeneous complexing agent, Rhodamine B and heterogeneous complexing agent, Covellite (CuS). The studies of Rhodamine B was conducted using UV-Vis spectroscopy (UV-Vis) where it revealed the instability of Rhodamine B-Hg(II)-Iodide complex in acidic media and it has been resolved either by extraction with benzene or stabilization in water using polyvinyalcohol (PVAl). The studies on Rhodamine B-Hg(II)-Iodide complex were further developed as a non-destructive spectrophotometric method for trace Hg(II) detection. The investigations of CuS in heterogeneous aqueous Hg(II) complexation were conducted using two analytical approach: (i) solution phase analysis *i.e.* atomic absorption spectrometry (AAS) and cold vapor atomic absorption spectrometry (CVAAS); (ii) solid characterization analysis *i.e.* powder X-ray diffraction (PXRD), field emission scanning electron microscopy (FESEM), high resolution transmission electron microscopy (HRTEM), energy dispersive X-ray spectroscopy (EDX) and X-ray photoelectron spectroscopy (XPS). From solution phase analysis, the trends of Hg(II) uptake observed were found to dependent on the sorption rate of Hg(II) onto CuS at acidic and alkaline pH. The relatively fast sorption rate of Hg(II) onto CuS at acidic pH can be viewed as the formation of both cubic phase mercury sulfide (Metacinnabar, β-HgS) and monoclinic phase mercuric sulfide chloride (m-$Hg_3S_2Cl_2$) from PXRD analysis. The relatively slow sorption rate of Hg(II) onto CuS at alkaline pH can be viewed by the sole formation of β-HgS from PXRD analysis. The formation of m-$Hg_3S_2Cl_2$ was associated with the growth of nanosize ranged needle like architecture namely nano-

needle crystallite on the edges of the initial CuS hexagonal plates from FESEM-EDX analysis. The formation of β-HgS was also observed at the edges of the CuS hexagonal plates but its formation was only preferred along the {101} and {100} plane of CuS hexagonal plates from HRTEM-EDX analysis. Furthermore, the uptake of Hg(II) onto CuS at different Hg(II) concentration has been modeled using sorption isotherm models. The equilibrium data suggested that the sorption behavior of Hg(II) onto CuS obeys well to the Langmuir isotherm with the maximum sorption capacity of CuS for Hg(II), Q_{max} reaching 434.78 mg Hg(II) / g of sorbent at 25°C. Apart from the Hg(II) uptake studies, a consecutive decrease of CuS dissolution and decrease on final solution pH were also detected when initial solution pH is raised. These results showed that an in-situ re-adsorption of Cu(II) and OH^- onto CuS has taken place at increasing pH in addition to the ion-exchange of Hg(II) onto CuS. The re-adsorption of Cu(II) and OH^- can be viewed as the formation of $Cu_4(SO_4)(OH)_6$ and its hydrate $Cu_4(SO_4)(OH)_6(H_2O)$ from PXRD analysis. Whilst, the re-adsorption of Cu(II) and OH^- can be also discussed in term of the formation of $Cu(OH)_2$ and CuO from XPS studies. Moreover, the precipitation of $Cu_4(SO_4)(OH)_6$ and $Cu_4(SO_4)(OH)_6(H_2O)$ has actually led to the growth of additional platelet crystallite in which it has been identified from FESEM-EDX analysis.

ABSTRAK

Memandangkan masalah pencemaran merkuri sedunia yang berpunca daripada kedua-dua sumber semula jadi dan antropogenik, dua kaedah pengkompleksan merkuri (II), Hg(II) yang berlainan telah dijalankan dengan menggunakan agen pengkompleksan homogen, Rhodamin B dan agen pengkompleksan heterogen, Covellite (CuS). Kajian mengenai Rhdomin B dalam pengkompleksan Hg(II) telah dilakukan dengan menggunakan Ultraviolet-Visible spekrophotometri (UV-Vis). Keputusan yang diperolehi mendedahkan pemendakan iodida-Hg(II)-Rhodamin B dalam media berasid. Namun begitu, masalah ini telah diselesaikan melalui pengekstrakan di dalam benzena ataupun penstabilan dalam air dengan menggunakan polivinilalkohol (PVAl). Kajian atas kompleks iodida-Hg(II)-Rhodamin B telah dibangunkan seterusnya sebagai kaedah spektrofometri penentuan Hg(II) yang tidak destruktif. Kajian mengenai CuS dalam pengkompleksan Hg(II) akues telah dijalankan dengan menggunakan kaedah analisasi: (i) analisasi cecair seperti spektometri serapan atom (AAS) dan spektometri serapan atom wap sejuk (CVAAS); (ii) analisasi pepejal seperti serbuk pembelauan sinar-X (PXRD), mikroskop elektron imbasan (FESEM), mikroskop elektron transmisi (TEM), taburan tenaga sinar-x (EDX) dan spektometri fotoelektron (XPS). Daripada kaedah analisasi cecair pengambilan Hg(II) pada lingkungan pH yang berlainan telah didapati berkait rapat dengan kadar penyerapan Hg(II) oleh CuS dalam larutan berasid atau beralkali. Kadar penyerapan Hg(II) yang lebih cepat oleh CuS dalam larutan berasid boleh dikenalpasti sebagai pembentukan kedua-dua fasa merkuri sulfida kubik (Metacinnabar, β-HgS) dan fasa merkuri sulfida klorida monoklinik (m-$Hg_3S_2Cl_2$). Kadar penyerapan Hg(II) yang lebih lambat oleh CuS dalam larutan beralkali boleh dikenalpasti sebagai pembentukan tunggal fasa β-HgS. Bagi pembentukan m-

Abstrak

$Hg_3S_2Cl_2$, penampilannya boleh dikaitkan dengan bentuk jarum yang dikenali sebagai kristal nano-jarum. Kristal nano-jarum yang diperhatikan telah berkembang pada sisi heksagonal plat CuS. Bagi pembentukan β-HgS, penampilannya didapati pada sisi heksagonal plat CuS di mana penyerapan Hg(II) oleh struktur CuS mengikut sisi kecenderungan {101} dan {100}. Pemuatan Hg(II) oleh CuS pada kepekatan Hg(II) telah dimodelkan dengan menggunakan model penyerapan isoterma yang berlainan. Data keseimbangan mencadangkan bahawa ciri penyerapan Hg(II) oleh CuS mematuhi isoterma Langmuir di mana penyerapan lapisan mono dijangkakan. Kapasiti penyerapan maksimum Hg(II) oleh CuS apabila mencapai ketepuan lengkap, Q_{max} adalah 434.78 mg Hg(II) / gram pengerap pada 25°C daripada isoterma Langmuir. Selain daripada kajian tentang pengambilan Hg(II), penurunan pelarutan kuprum dan pH akhir larutan telah dikesan apabila pH awal larutan ditingkatkan. Keputusan tersebut jelas mencadangkan penyerapan kuprum (II) dan OH^- oleh CuS semula secara in-situ telah berlaku pada pH yang meningkat di samping proses pertukaran ion penyerapan Hg(II) oleh CuS. Penyerapan semula kuprum (II) boleh dikatakan sebagai pembentukan $Cu_4(SO_4)(OH)_6$, $Cu_4(SO_4)(OH)_6(H_2O)$, $Cu(OH)_2$ dan CuO. Selain itu, pemendakan $Cu_4(SO_4)(OH)_6$ telah menjurus kepada pembentukan kristal platelet dalam serbuk CuS yang telah bertindak balas.

ACKNOWLEDGEMENTS

First and foremost, I would like to thank Prof. Dr. Sharifah Bee Abd Hamid, my supervisor for her advice and assistance as well as offering me the opportunity to work on this interesting research project. I truly wish that the studies done on this research topic would lead to a better understanding of the mercury mitigation methodology explored in which this can lead to the development of much greener, safer and cleaner technologies that can act as global mercury sink in the environment.

My sincere appreciation also goes to Prof. Robert Schlögl, director of Inorganic Chemistry Department, Fritz Haber Institute of the Max Planck Society for his willingness to support my research attachment (about 6 months) in Fritz Haber Institute (FHI). I am personally very much inspired by Prof. Robert Schlögl's dedication, and determination in pursuing his dreams in research. The research experience that I have gained in FHI is indeed enlightening in which this has undeniably broadened my research interest in this respective discipline.

I would like to express my sincere credit to my co-supervisors, Dr. Malte Behrens and Dr. Olaf Timpe for their valuable scientific discussion, contributions and useful comments in the project. Not forgotten, great appreciation also goes to Dr. Muralithran Kutty and Dr. Looi Ming Hong for their assistance in this project.

Besides that, I would like to extend my acknowledgement to my research partner, Yap Pei Lay for his everlasting support and constructive ideas periodically. I would also like to convey my sincere thanks to NanoC Sdn Bhd, NANOCAT science officers and the members of Inorganic Chemistry Department in FHI, particularly to those for helping me with sample characterizations as well as technical advice.

Furthermore, I would like to express my gratitude to my beloved family and my dear friends for their moral support throughout the years. They had encouraged me towards the success in achieving my goals in this project. I am grateful for their unconditional love and thoughtful consideration throughout the duration of my study.

My special thanks to the financial support from Fellowship Scheme of University of Malaya (SB) for covering my PhD studies, Research University Grant, (UMRG: RG022-09AET), and Postgraduate Research Grant (PPP: PS377-2010B) for research funds. Last but not least, this research journey would not have been smoothly sailed without the support from all the names mentioned above. Once again, thank you very much.

Au Yoong Yow Loo (John), 2013.

TABLE OF CONTENTS

Page

CHAPTER 2: LITERATURE REVIEW

CHAPTER 3: RESEARCH METHODOLOGY

LIST OF FIGURES

LIST OF TABLES

LIST OF SYMBOLS AND ABBREVIATIONS

AAS	Atomic absorption spectrometry
AC	Activated carbon
AES	Atomic Emission Spectroscopy
AES	Auger Electron Spectroscopy
AOAC	Association of Official Analytical Chemists
BDET	Benzenediamidoethanethiol
BDP	Dithiocarboxy piperazine
B.E.	Binding energy
BET	Brunauer-Emmett-Teller
BSEs	Backscattered electrons
C_0	Initial Concentration
C_e	Equilibrium concentration
N_2O-C_2H_2	Nitrous oxide-acetylene
CH_3Hg^+	Methylmercury
$(CH_3)_2Hg$	Dimethylmercury
CNF	Carbon nanofibers
CTAB	Cetyl trimethyl ammonium bromide
Cu_xS	Nonstoichiometric copper sulfide
CuS	Covellite
$Cu_4(SO_4)(OH)_6$	Copper (II) sulfate hydroxide
$Cu_4(SO_4)(OH)_6(H_2O)$	Copper (II) sulfate hydroxide hydrate
CVAAS	Cold vapor atomic absorption spectrometry

Cys	Cysteine
DMDTC	Dimethyldithiocarbamate
DTC	Dithiocarbamate
EDTA	Ethylenediaminetetraacetic acid
EDX / EDS	Energy Dispersive X-ray Spectroscopy
EXAFS	Extended X-ray absorption fine structure
$Fe_{1-x}S_x$	Pyrrhotite
FeS	Mackinawite
FeS_2	Pyrite
FESEM	Field Emission Scanning Electron Micrscopy
FFT	Fast fourier transform
FWHM	Full width at half maximum
GEb	Percentage calculated with reference to global emission
GL	Gaussian-Lorentz
H_2Dz	Diphenylthiocarbazone
Hg_2Cl_2	Mercury (I) chloride
$HgCl_2$	Mercury (II) chloride
$HgCl_2.3HgO$	Mercury (II) oxide chloride
HgClOH	Mercury (II) chlorine hydroxide
HgO	Mercury (II) oxide
$Hg(OH)_2$	Mercury (II) hydroxide
HgS	Mercury (II) sulfide, Cinnabar
β-HgS	Metacinnabar
$Hg_3S_2Cl_2$	Mercury (II) sulfide chloride
$Hg_3S_2Br_2$	Mercury (II) sulfide bromide

HMO	Hydrous manganese oxide
HRTEM	High Resolution Transmission Electron Microscopy
HSABT	Hard Soft Acid Base Theory
HTDC	Hexahydrotriazinedithiocarbamate
HTO	Hydrous tin oxide
ICP	Inductive Coupled Plasma
IMFP	Inelastic mean free path
k	Rate Constant
K	Kelvin
K_a	Equilibrium constant / Langmuir equilibrium constant
K_F	Freundlich constant
K_R	Separation factor
K_{sp}	Solubility product constant
K.E.	Kinetic Energy
Li_xES_2	Lithium-intercalated transition metal sulfide
L.O.D	Limit of detection
mg	Miligram
Mg	Megagram
MIOPS	Fe_3O_4 nano-particles modified with 2-mercaptobenzothiazole
MIP	Microwave Induced Plasma
MS	Mass spectroscopy
ng	Nanogram
nm	Nanometer
NPs	Nanoparticles
PIXE	Photon Induced X-ray Emission

PDF	Powder diffraction file
PbS	Galena
pg	Picogram
PGHyFeO-COOH	Carboxylate and polyacrylamide grafted iron oxide
ppb	Parts per billion
ppm	Parts per million
ppt	Parts per trillion
PVAl	Polyvinyl alcohol
PVC	Polyvinyl chloride
PXRD	Powder X-ray diffraction
Q_e	Equilibrium sorption capacity
Q_t	Sorption Capacity at time t
Q_{max}	Maximum sorption Capacity
R^2	Correlation coefficient
$R_{conversion}$	Conversion ratio
RGO	Reduced Graphene Oxide
SDS	Sodium dodecyl sulfate
SEs	Secondary electrons
SH	Mercapto / Thiol
SH-Fe_3O_4-NMPs	Mercapto-functionalized Fe_3O_4 polymers
$S_{specific}$	Specific surface area
SPR	Surface plasmon resonance
Tg	Teragram
TFZ	Thiol functionalized zeolite

TMR	Total mercury removal
TMT	Trimercaptotriazine
Triton X – 100	T-octylphenoxypolyethoxyethanol
UNEP	United Nations Environmental Programme
US ATSDR	The Agency for Toxic Substances and Disease Registry
US EIA	United States Energy Information Administration
US EPA	United States Environmental Protection Agency
US FDA	United States Food and Drug Administration
Rh B	Rhodamine B
UHV	Ultra high vacuum
UV-Vis	Ultraviolet-Visible
VCM	Vinyl chloride monomer
WHO	World Health Organization
XAS	X-ray absorption spectroscopy
XPS / ESCA	X-ray photoelectron spectroscopy / Electron microscopy for Chemical analysis
yr	year
λ_{max}	Absorbance maximum
$\Delta G°$	Gibb's free energy change of reaction
$\Delta H°$	Enthalpy change of reaction
$\Delta S°$	Entropy change of reaction
$\Delta E°$	Potential change of reaction

LIST OF APPENDICES

LIST OF PUBLICATIONS

1) Auyoong, Y. L., Yap, P. L., Huang, X., & Abd Hamid, S. B. (2013). Optimization of reaction parameters in hydrothermal synthesis: a strategy towards the formation of CuS hexagonal plates. ***Chemistry Central Journal***, *7*, 67.

2) Auyoong, Y. L., Yap, P. L., Kutty, M. G., Timpe, O., Behrens, M., & Abd Hamid, S. B. (2012). Spectrophotometric determination of mercury with iodide and Rhodamine B. ***Sains Malaysiana***, *41*(2), 213-218.

3) Auyoong, Y. L., Yap, P. L., Kutty, M. G., Timpe, O., Behrens, M., Hamid, S. B. A. & Schlögl R. (2012). Sorption profile of Hg(II) onto mixed phase of copper sulphide and copper sulphate. ***Advanced Materials Research***, *356-360*, 537-546.

4) Yap, P. L., Auyoong, Y. L., Kutty, M. G., Timpe, O., Behrens, M., & Hamid, S. B. A. (2012). Facile Remediation Method of Copper Sulfide by Nitrogen Pre-Treatment. ***Advanced Materials Research***, *361-363*, 1445-1450.

5) Auyoong, Y. L., Yap, P. L., Huang, X., Timpe, O., Behrens, M., Girgsdies, F., Hamid, S. B. A. & Schlögl R. Understanding the sorption profile of aqueous Hg(II) onto CuS: A comprehensive study from both solution and solid phase analysis. *Manuscript in preparation and to be submitted in* ***Environmental Science & Technology.***

CHAPTER 1

INTRODUCTION

This chapter consists of the brief introduction regarding the physical and chemical characteristic of mercury, applications, occurrence, contributions, impacts as well as the related technologies and materials employed in mercury mitigation. This chapter also gives the problem statement, motivations, objectives and outline of the entire research works.

1.1. Mercury

1.1.1. Physical and Chemical Properties

For decades, mercury is recognized as quicksilver or hydragyrum (from Greek "hydr-" water and "argyros" silver) with silvery white color appearance. Mercury is also known as the only heavy, d-block metal element with its existence as liquid state at room standard conditions for temperature and pressure (freezing point = −38.83 °C, melting point = 38.9 °C, boiling point = 356.73 °C) (Greenwood & Earnshaw, 1984; Lide, 2005). The only element that is present as liquid at room standard conditions for temperature and pressure is bromine, though metals such as cesium (Cs), gallium (Ga) and rubidium (Rb) melt just above room temperature (Greenwood & Earnshaw, 1984). Mercury is also the only element outside of noble gases that can exist as a monoatomic vapor with vapor pressure at room temperature = 1.9 x 10^{-3} torr (Hutchison & Atwood, 2003). Besides, it also possesses the property of dissolving some metals *i.e.* gold, silver, aluminum to form amalgams. Thus, these physical characteristic has made mercury an extraordinary metal compared to the others in the periodic table.

Mercury with chemical symbol of Hg, atomic number of 80 and electronic configuration of [Xe] $4f^{14}$ $5d^{10}$ $6s^2$ exists in the nature in three different forms: Hg^0 (zero

valent), Hg_2^{II} (monovalent) and Hg^{II} (divalent). Hg^0 which also known as the elemental mercury is appearing as the silver colored liquid found in thermometer and barometer. It has high volatility and relatively low water solubility compared to other form. Hg_2^{II} which is in the monovalent oxidation state *i.e.* [Xe] $4f^{14}$ $5d^{10}$ $6s^1$ is only found as the diatomic unit and never as the straight Hg^+ (Hutchison & Atwood, 2003). The chemistry of Hg(I) is very different from other element in the same group *i.e.* Zn and Cd. Due to the its instability, Hg(I) is constantly undergoing disproportionation to form Hg(II) (J. D. Lee, 1996). Hg^{II} which is in the divalent oxidation state *i.e.* [Xe] $4f^{14}$ $5d^{10}$ is the most universal form of mercury. Hg^{II} can be divided into inorganic and organic type where it consists of free Hg^{2+} ions and Hg^{2+}complexes. Inorganic Hg(II) comprises of oxide, chloride, hydroxide, sulfide and other complexes whereas organic Hg(II) is strictly bound to the attachment of carbon group to Hg(II). Organic mercury can be subsequently divided into 2 categories: (i) the covalently-bonded organomercurials (methylmercury and dimethylmercury) as well as (ii) mercuric complexes with organic matter (humid substances) (Q. Wang, Kim, Dionysiou, Sorial, & Timberlake, 2004). Finally, the common transformation of different form of mercury from one to another is shown in the following relationship (Okoronkwo, Igwe, & Okoronkwo, 2007):

$$Hg^0 \underset{\text{reduction}}{\overset{\text{oxidation}}{\rightleftharpoons}} Hg^+ \text{or } Hg^{2+} \underset{\text{demethylation}}{\overset{\text{methylation}}{\rightleftharpoons}} CH_3Hg^+ \text{ or } (CH_3)_2Hg \qquad (1.1)$$

1.1.2. Worldwide Applications

With regards to the physical and chemical characteristic of the various form of mercury, its application can be ranged into various industries. The use of mercury can be started with the extraction of precious metals, such as gold, silver, and other metals from ores as early as 2700 BC (Malm, 1998). Owning to the amalgamate properties, elemental mercury forms

alloy with the precious metal effortlessly during their contact. The precious metal can be easily recovered by evaporates off the volatile elemental mercury. Due to the uniform thermal expansion and contraction capacity of elemental mercury, it is commonly used as the liquid material in the conventional thermometer. Mercury is also widely used in barometers, manometers and sphygmomanometers mainly due to its relative low vapor pressure which is sensitive to the changes in the atmospheric pressure (Charlton, et al., 1994). Besides that, mercury is also an important component in electrolytic cells, widely used in the Chlor-alkali industry. In the Chlor-alkali plant, mercury serves as an anode in the electrolysis of brine which converts the sodium cations to sodium metal, amalgamates the sodium, and carries it into another reaction vessel, where it reacts with purified water to form sodium hydroxide (Swaddle, 1997). Another important application of mercury is the lighting industry where most fluorescent lamps use mercury vapor, along with an inert gas, convert electrical discharge to useful light (Finn & Ouellette, 1992; van Dijk, Hartgers, Jonkers, & van der Mullen, 2000).

Mercury cell batteries were once extensively flooded in the market. In a typical mercury cell battery, it consists of a mercury/ zinc amalgam as the anode and a mercuric oxide/ graphite cathode. Mercury can also be found in zinc-silver cell batteries (normally used in watches), where a mercury/zinc amalgam forms the anode (Jones, McGugan, & Lawrence, 1978). Recently, the production of vinyl chloride monomer (VCM) is also found to be one of the major components in contributing global mercury demand. VCM is an intermediate feedstock in manufacturing polyvinyl chloride (PVC). There are two processes employed to manufacture vinyl chloride, one of them is the acetylene process which uses mercuric chloride on carbon pellets as a catalyst, while the other does not involve the use of mercury (Pirrone, et al., 2010). Furthermore, mercury is also well known for its application in dental industry. It can easily form amalgam with silver, copper, or

other metals to build dental fillings. Moreover, mercury is also added to paints as fungicide (Sunderland & Chmura, 2000) and pharmaceuticals as an antimicrobial/ antibacterial agent (Márquez, Silva, & Perez-Bendito, 1988). In addition to the monovalent mercury, divalent mercury is also present as thimerosal (sodium ethylmercurythiosalicylate) in contact lens solutions and vaccines (Procopio, da Silva, del Carmen Asensio, Sevilla, & Hernandez, 1992). On top of that, organomercurials were also broadly used as pesticides or fungicide for the treatment of seeds due to their toxicity (Murphy & Aucott, 1999).

1.1.3. Global Sources

Another frequent question associated with mercury is actually where does mercury come from? In nature, mercury is found almost exclusively as its sulfide, the reddish mineral cinnabar (HgS). Large deposits of cinnabar have been located and mined in Spain, the former Soviet Union, Yugoslavia, Mexico, Italy, North Africa, and California, with by far the largest deposit being at Almaden, Spain. Elemental mercury can be easily isolated from cinnabar by roasting (Hutchison & Atwood, 2003). In a more specific classification, mercury can come from two different sources *i.e.* natural and anthropogenic sources (Pirrone, et al., 2010). The two sources of mercury contribution have resulted in its own environmental cycle as depicted in **Figure 1.1**. The key properties, transport and fate of different forms of mercury in the environment are also shown in **Table 1.1** (U.S. EPA, 1997a). Mercury vapor (Hg^0) is introduced into the atmosphere via several ways, including by volcanic geothermal activity, mineral deposit degassing in the Earth's crust, anthropegenic sources like mining by amalgams, fossil fuel combustion and by leaching from sediments as Hg^{II}, which can be reduced to Hg^0 and evaporate. The mercury is then oxidized in the atmosphere to Hg^{II} and deposited back in the environment primarily through precipitation. There it can be re-reduced, thereby perpetuating the cycle. In the

aquatic system, the dissolved mercury most probably will be methylated by sulfate reducing bacteria like *Desulfovibrio desulfricans* to become the deadly methyl mercury and carry forward to the food chain of living organisms (S.-C. Choi, Chase, & Bartha, 1994).

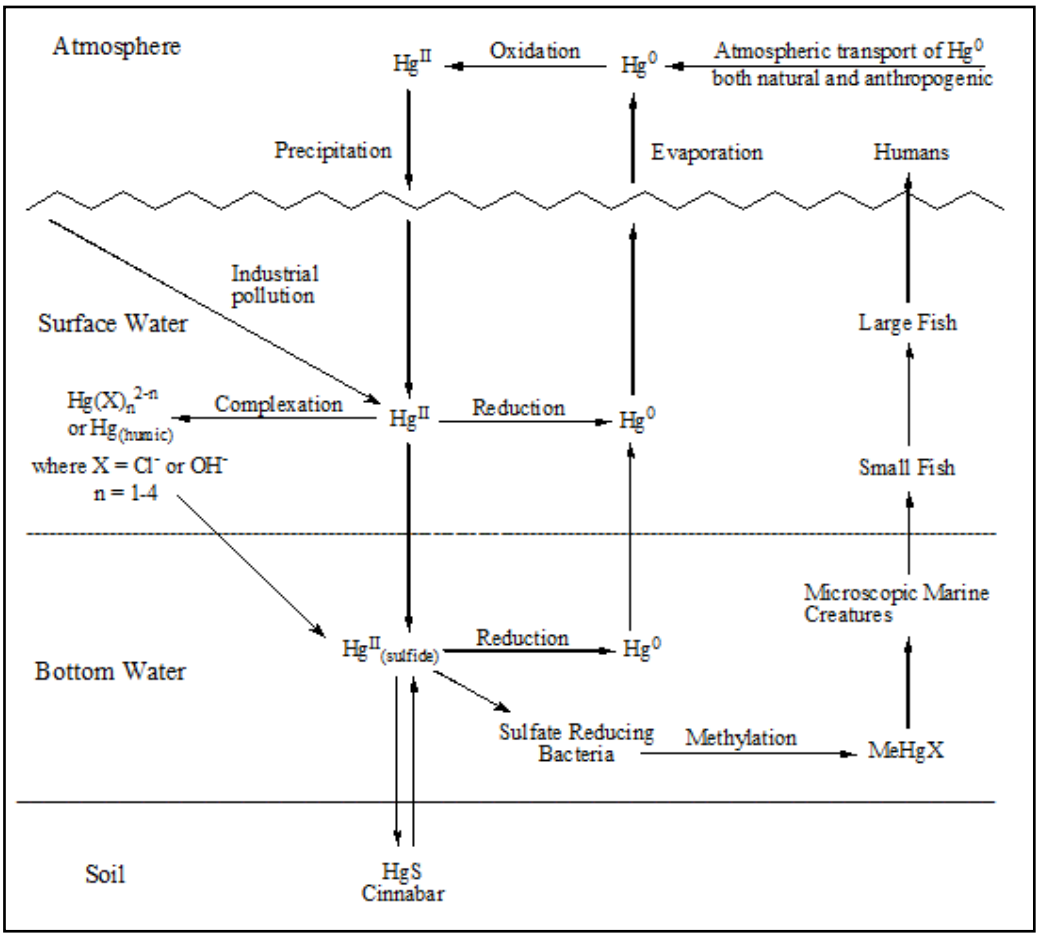

Figure 1.1. The mercury cycle (Hutchison & Atwood, 2003).

Table 1.1. Key properties, transport and fate of different forms of mercury (U.S. EPA, 1997a).

Forms	Elemental (Hg^0)	Inorganic divalent (Hg^{2+})	Organic divalent (Hg^{2+})
Key Properties	• 95 % of atmospheric mercury is Hg^0 vapor	• Bound to airborne particles and cover 5% atmospheric mercury. • Form mercuric salts and found in soil and water as a number of complex ions.	• Lipophylic ion produced by bacteria in the water column or sediment. • Nearly all mercury in fish is methylated.

Transport and fate	• Not easily deposited. • May travel long distances before conversion to other forms and deposition	• Deposited to Earth's surface in dry form or in precipitation. • Once in water, may volatilize or partition into particulates and mobile via sediment.	• Enters food chain through aquatic ecosystem. • Bioaccumulates and reaching highest concentrations in organisms at highest trophic level in food chain.

The global mercury emissions by natural sources are depicted in **Figure 1.2**. Among the natural sources, it is surprise that ocean is the main contributor for global mercury emission (Pirrone, et al., 2010). Mason reported estimates of total mercury evasion from ocean basins and lakes, which account for 2778 Mg yr^{-1} (37 % GEb) of net gaseous mercury evasion to the atmosphere (Mason, 2009). Biomass burning was reported as the second largest contributor after oceans in year 2008. The most recent estimate suggests that about 675 Mg of mercury is released to the atmosphere from biomass burning every year, (annual average for the period 1997-2006), accounts for 13 % of the total contribution from natural sources (Friedli, Arellano, Cinnirella, & Pirrone, 2009). In short, the global mercury emission by natural sources in 2008 is estimated at 5207 Mg yr^{-1}. The mercury from volcanoes, geothermal sources and topsoil enriched in mercury pertains to primary natural sources, whereas the re-emission of previously deposited mercury on vegetation, land or water surfaces is primarily related to land use changes, biomass burning, meteorological conditions and exchange mechanisms of gaseous mercury at air-water/top soil/snow-ice pack interfaces (Mason, 2009; Pirrone, et al., 2001).

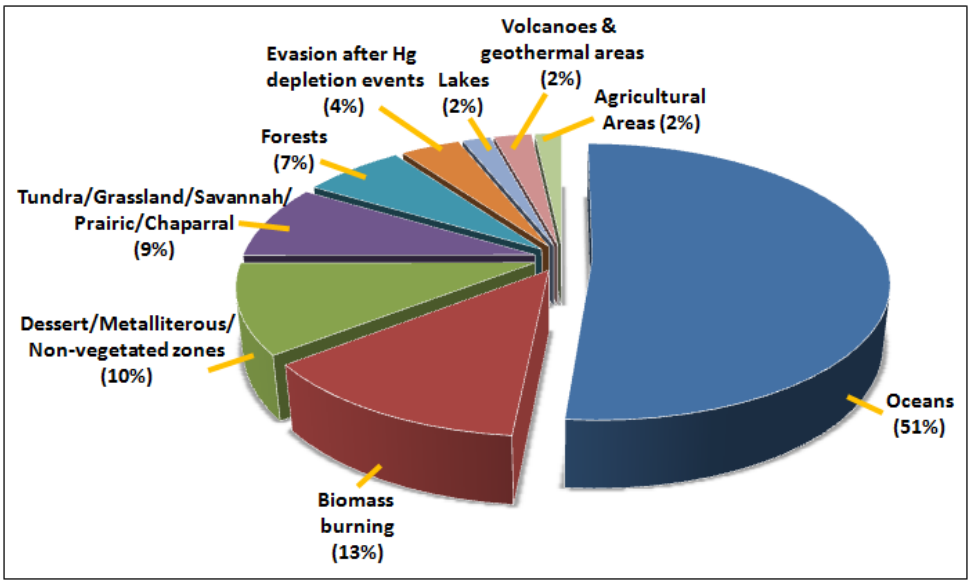

Figure 1.2. Mercury emissions by natural sources in 2008 (Pirrone, et al., 2010).

The global mercury emissions by anthropogenic sources are illustrated in **Figure 1.3**. Among the contributions, fossil fuel-fired power plants are the largest mercury contributor to the atmosphere. World coal consumption in 2006 was 6118 Tg, responsible for the primary fuel used in electrical power generation facilities (42 %) and attributed for about 27 % of world's energy consumption (U.S. EIA, 2009). Mercury from artisanal and gold mining activities is one of the notable issues as most of the activities are carried out in developing countries. The estimation mercury released from this industry is 17 % out of the total of 2320 Mg yr^{-1}. Smelting processes to produce non – ferrous metals such as copper, zinc, lead, nickel, as well as gold are believed to be one of the largest mercury contributors (Telmer & Veiga, 2009; UNEP, 2002). In cement production, the estimation of mercury emissions is based on an emission factor of 0.1 g per Mg of cement produced which leads to 236 Mg yr^{-1} of mercury emitted to the atmosphere (Pacyna, Pacyna, Steenhuisen, & Wilson, 2006). In combination to other man-made sources, nearly 2320 Mg yr^{-1} of mercury is released to the global atmosphere. Nonetheless, it is noteworthy that this value is still less than the total contribution from natural sources.

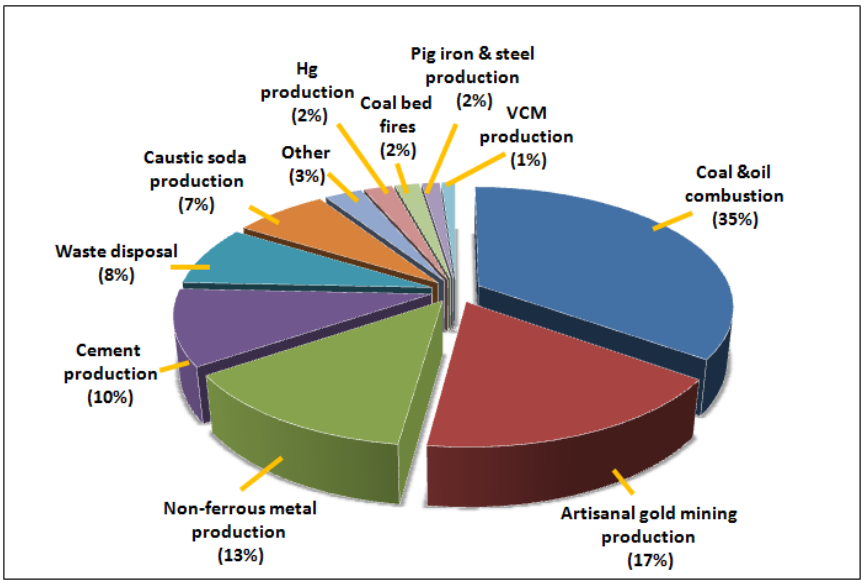

Figure 1.3. Mercury emissions by anthropogenic sources in 2008 (Pirrone, et al., 2010).

1.2. Impacts of Mercury

Despite of the advantages in utilizing mercury in various products and industries, mercury has undeniably led to some negative impacts towards the health, safety and environmental (HSE) issues. The first concern is related to the toxicity of mercury towards the ecosystems (humans, organisms and environment). The venomous of mercury depends on its chemical form *i.e.* elemental mercury, inorganic mercury or organic mercury. For elemental mercury, the symptoms on humans were always associated with renal toxicity (U.S. Centers for Disease Control (ATSDR), 1999a, 1999b; U.S. EPA, 1997b), high blood pressure (Beck, Krafchik, Traubici, & Jacobson, 2004; Koyun, Akman, & Güven, 2004) and pulmonary or lung toxicity (Moromisato, Anas, & Goodman, 1994; Solis, Yuen, Cortez, & Goebel, 2000). Other reported health effects following acute elemental mercury exposure include headache (Abbaslou & Zaman, 2006; Hryhorczuk, et al., 2006), tics (involuntary muscle movements) (A. M. Li, et al., 2000), weight loss (Beck, et al., 2004; Tunnessen, McMahon, & Baser, 1987), rashes (Chrysochoou, et al., 2003; Lerch & Bircher, 2004), and heart rate variability (Sørensen, Murata, Budtz-Jørgensen, Weihe, & Grandjean, 1999). Reports of death

following acute exposure to elemental mercury were also related to respiratory failure (Solis, et al., 2000; U.S. EPA, 1997b). In experimental animal studies, offspring of pregnant rats exposed to elemental mercury experienced decreased birth weight at doses that also resulted in maternal toxicity (Morgan, et al., 2002). Adverse behavioral effects (*e.g.* altered levels of spontaneous motor activity) were observed in adult rats whose mothers were exposed to mercury vapor during pregnancy into adulthood (Danielsson, et al., 1993; Fredriksson, Dencker, Archer, & Danielsson, 1996).

For inorganic mercury, reported effects of exposure in humans include kidney damage and digestive tract problems including diarrhea, nausea, ulcers (U.S. Centers for Disease Control (ATSDR), 1999b; U.S. EPA, 1997b), increased blood pressure and decreased heart rate variability (Grandjean, Murata, Budtz-Jørgensen, & Weihe, 2004; Torres, Rai, & Hardiek, 2000). Neurological effects including twitching, uncontrollable muscle movements and impaired gait have been reported in humans following exposure to mercuric chloride (Kang-Yum & Oransky, 1992; A. M. Li, et al., 2000). There are limited reports of death in following ingestion of mercuric chloride at doses of 10 – 42 mg mercury per kg body weight with cardiovascular failure, gastrointestinal damage, and acute renal failure (Otto, Ahlemeyer, Tasche, & von Muhlendahl, 1994). In experimental animal studies, mercuric acetate or mercuric chloride exposure during development led to embryotoxicity (increased fetal deaths, and increased occurrence of fetal abnormalities such as retarded growth and exencephaly, or exposed brain tissue) in hamsters and mice (Gale, 1981; Khan, et al., 2004). Following mercuric chloride exposure, neonatal rats exhibited altered rates of organ growth for several organs (*e.g.* liver, brain, heart), and altered levels of several neurotransmitters in the brain (Bartolome, Whitmore, & Slotkin, 1984); in adult rats exposure resulted in hair loss, weight loss, and immune-mediated kidney damage in adult rats (U.S. Centers for Disease Control (ATSDR), 1999b).

Following acute exposure to mercuric chloride (>0.46 mg/kg/day), adult rats experienced acute renal failure attributed to tubular and glomerular pathology (U.S. EPA, 1997b).

For organic mercury *i.e.* methyl mercury, it has been frequently reported as a neurotoxin and may affect many areas of the brain. Reported neurotoxic symptoms of chronic methylmercury exposure include poor performance on neurobehavioral tests, particularly on tests of attention, fine motor function, language, visual-spatial abilities (*e.g.* drawing), and verbal memory. Studies of neurological impairments in children who were prenatally exposed to methylmercury form the basis for the U.S. EPA Reference Dose (RfD) (National Research Council, 2000; U.S. Centers for Disease Control (ATSDR), 1999b; U.S. EPA, 1997b). Studies have reported an association between chronic adult exposure to methylmercury and increased blood pressure, increased risk of acute myocardial infarction (heart attack), heart palpitations, hand tremors, impaired hearing, dizziness, and staggering. More severe symptoms have been reported following maternal acute exposure to methylmercury from poisoning incidents during pregnancy, including mental retardation, cerebral palsy, deafness, blindness, and motor impairments in their children. More importantly, children and adults exposed to any form of mercury have also been reported to develop a disorder called acrodynia, or "pink disease". The symptoms of leg cramps; irritability; and redness and peeling of the skin of hands, nose, and soles of the feet, itching, fever, sweating, salivating, rashes, sleeplessness, and/or weakness were also associated with the disease (Tunnessen, et al., 1987; U.S. Centers for Disease Control (ATSDR), 1999b; U.S. EPA, 1997b, 2004; U.S. FDA, 2006).

Among all the form of mercury and related health issues discussed, methylmercury is the most vulnerable mercury form which can be easily absorbed and accumulated along the food chain in comparison to other forms of mercury. Inorganic mercury can also be absorbed, but in a much slower rate and lower efficiency than methylmercury (U.S. EPA,

1997b). The progressive build up of methylmercury has a significant impact on animals and humans. Fish and some of the seafood are found to bind methylmercury strongly and most of the methylmercury in fish tissue is covalently bound to protein sulfhydryl groups. Mercury concentrations in individuals of a given fish species tend to increase with age as a result of slow elimination of methylmercury and increased consumption, particularly with larger size fish. Older fish usually have higher mercury concentrations in the tissues than younger fish of the same species. At the top levels of the aquatic food web are fish-eating species, such as humans, seabirds, seals and others which is typically prone to the threat of methylmercury (U.S. EPA, 1997a).

The most famous incident that demonstrated bio-accumulation of methylmercury in the ecosystems is related to the catastrophic Minamata Bay accident in Japan, 1956. Prior to the detection of methylmercury poisonings on humans, birds were firstly showing signs of abnormal behaviors by experiencing difficulty in flying. In this event, the overall prevalence rate for the Minamata region of neurological and mental disorders was 59 %. Most of the affected adults were suffering from paresthesia, ataxia, sensory disturbances, tremors, hearing impairment and difficulty in walking. From the extensive studies of Minamata incident, severe disturbances of nervous function were mentioned and the affected offsprings were very late in reaching developmental milestones (Boca Raton, 1997; Harada, 1995; Tsubaki & Takahashi, 1986; WHO/IPCS, 1990). Serious effects were also found on few generation of new born baby as methylmercury can readily cross the placenta barrier and destroy the central nervous system of developing fetus (UNEP, 2002).

Although the unpleasant impacts of mercury towards the entire ecosystems are receiving the global concerns, the impacts of mercury towards the industry sector should also be paid attention. For instance, mercury compounds can present as many forms in some crude oils and natural gases, namely, elemental mercury, mercuric chloride, mercuric

sulfide, mercuric selenide, dimethylmercury, diethylmercury, and etc. In most of the oil and gas reservoirs, elemental mercury can cause corrosion/ embrittlement with the metal made reactors. The mechanisms involved are amalgamation, amalgam corrosion, liquid metal embrittlement, and galvanic corrosion. Several production plants experienced sudden heat exchanger failures resulting in plant shutdowns, repairs, fires, and even explosions (Markovs & Clark, 2005). Skikda explosion which occurred in Skikda, Algeria, is a concrete evidence of mercury corrosion in aluminium heat pipe exchangers at liquefaction plant and the specific plant had to shut down.

Moreover, mercury also tends to affect gas treatment catalyst such as molecular sieve in glycol dehydration, chloride as well as acid gas removal units. In petrochemical plants, mercury deactivated downstream catalyst systems in ethylene, aromatics and olefins manufacture (Visvanathan, 2003). Even though mercury present at very low concentrations, its accumulation in the feedstock can undeniably result in irreversible poisons on precious metals, such as palladium supported on alumina catalyst which is commonly used for selective hydrogenation of acetylenes. Catalyst poisoning has notably decreased the production yields in which the cost also increases as it requires regular replacement of deactivated catalyst systems. In short, the constant development of highly efficient and environmental friendly sorbent is still in need to solve mercury contamination issues. The continuous support from the scientific community is important in view of the mandate from UNEP to prepare a global legally binding instrument on mercury (UNEP, 2009, 2011).

1.3. Mercury Mitigation

1.3.1. Mercury Detection

Mercury mitigation is a big research and development area that aimed to overcome mercury pollution. Mercury mitigation covered not only the materials used for mercury

remediation; it also consisted of the development of analytical technique for mercury detection. The oldest method used for detection of mercury is micrometry. Although no analysis is performed by micrometric methods today, it is useful to refer to the technique as the methods are historically interesting. Mercury was first collected on copper dust from an acid solution, and was subsequently heated so that the distilled mercury was deposited on gold foil, which was then examined by eye with a hand lens (Elliott, 1917). Mercury has also been determined visually by reducing mercury compounds to the element in the form of a small sphere and measured by means of a microscope (Stock, 1931).

The most popular method for determining mercury in almost any type of sample has been based on cold vapor atomic absorption spectrometry (CVAAS). Mercury is unique among all other metals as it has a very high vapor pressure at relatively low temperatures and can be introduced quantitatively to the spectrometer as vapor without difficulty. Absorption at 253.7 nm in the ultra-violet (UV) region has been measured with the use of mercury vapor lamps as well as hollow cathode lamps as the light source. The way of liberating elemental mercury from aqueous or digested samples is reduction, followed by volatilization and introduction of the mercury by aid of a gas stream. In a typical procedure, Sn^{2+} ions are used as a reductant (Stanisz, Werner, & Matusiewicz, 2013; Yuan, Wang, & Jin, 2012). In addition, much works was also done with $NaBH_4$ as the reductant (Almeida & Coelho, 2012; Shah, et al., 2010; Z. Zhu, Liu, Zheng, & Hu, 2010). The use of chromium as a reductant has also been reported (Gil, et al., 2010; Yoshino, Tanaka, & Okamoto, 1995). Automatic apparatus utilizing CVAAS method has been constructed (Bergdahl, Schutz, & Hansson, 1995; Domínguez, Grünhut, Pistonesi, Di Nezio, & Centurión, 2012) and gold amalgamation were also applied to achieve elevated sensitivity (Ombaba, 1996; Puanngam, Dasgupta, & Unob, 2012) The limit of detection (L.O.D) of CVAAS technique can go down to 0.5 ppt of Hg (Falter & Schöler, 1995).

A number of articles have appeared on the development of atomic fluorescence spectrometry (AFS) and its application to the determination of mercury (Sanchez-Rodas, Corns, Chen, & Stockwell, 2010; Shafawi, Ebdon, Foulkes, Stockwell, & Corns, 2000; Yun, He, Wang, Wang, & Jiang, 2012). Most of the early work used flame atomization (Dagnall, Thompson, & West, 1967; Winefordner & Staab, 1964). The L.O.D for mercury in aqueous solution, as determined by flame atomic fluorescence spectrometry is 2 ppb Hg. Atomic fluorescence spectrometry was further developed by using an electrothermal atomization (Bratzel Jr, Dagnall, & Winefordner, 1969; Wen, Wu, Chen, & Hou, 2009) or cold vapor atomization (Hutton & Preston, 1980; Yun, et al., 2012) giving L.O.D up to pg (ppt level) of Hg. The use of an atomic fluorescence instrument that employs inductively coupled plasma (ICP) as an atomization cell and a Hg hollow cathode lamp produced a L.O.D of 0.5 ng dm^{-3} (ppt) (Lancione & Drew, 1985).

Historically, atomic emission spectrometry (AES) techniques have been very popular with geochemists. The method has sensitivity of about 1 pg Hg (Morita, Yoshinaga, & Edmonds, 1998). AES has been developed in the past two decades by replacing the flame or arc emission source with radio frequency plasma. Inductively coupled plasma, microwave induced plasma, and direct current plasma have also been used. Hg in water has been determined by atmospheric pressure He microwave-induced plasma coupled with a cold vapor technique (CV-MIP) (Červený, Horváth, & Broekaert, 2012; Tanabe, Chiba, Haraguchi, & Fuwa, 1981). The L.O.D was 4 pg cm^{-3}. The use of a hollow fibre membrane, by which hydrogen and water vapor were removed, for continuous introduction of Hg and other volatile metal hydrides to the plasma was also described (Tao & Miyazaki, 1991). The L.O.D of Hg is 500 pg dm^{-3}. Electrothermal vaporization was also used for ICP-AES determination of mercury in drinking water (Matusiewicz, Horvath, &

Barnes, 1985). Vaporization was enhanced by post-injection of $(NH_4)_2S$, and the peak height was linear from 10 – 1000 pg cm^{-3}.

Neutron activation and X-ray fluorescence analysis were another approach in determining mercury. The principal merits of the widely used neutron activation and X-ray fluorescence methods of analysis are the relatively short operator time, the ability to perform non-destructive analysis, and the good sensitivity and accuracy of the procedures. Neutron activation analysis measures the gamma radiation emitted by ^{197}Hg formed by irradiation with reactor neutrons while X-ray fluorescence analysis measures the fluorescence intensity by mercury. Both of the neutron activation and X-ray fluorescence analysis measure total mercury in solid samples without acid digestion. Several textbooks and articles have list numerous applications of these methods to various type of samples (Alfassi, 1990; Aranda, Colombo, Perino, De Vito, & Raba, 2013; Avino, Capannesi, Renzi, & Rosada, 2013; Ehmann & Vance, 1991; Rhea, Farag, Harper, McConnell, & Brumbaugh, 2013) and their application to atmospheric aerosols, particulates and sludge samples has been critically reviewed (Dams, 1992).

Mass spectrometry has been also applied to the determination of mercury. Early work used the method for the determination of mercury in apples (Tong, Gutenmann, & Lisk, 1969). It is important to note that by using a stable isotope as an internal standard, the method can be very accurate. Determination of total mercury in botanical and biological samples by isotope dilution spark source mass spectrometry has been reported (Moody & Paulsen, 1988). Inductively coupled plasma mass spectrometry, coupled with a continuous reduction system was applied to the micro determination of mercury in fish, natural waters and reference sediment (Kenduzler, Ates, Arslan, McHenry, & Tchounwou, 2012; Mladenova, Dakova, Tsalev, & Karadjova, 2012). The application combination of flow injection method to ICP-MS is reported (Stroh, Vollkopf, & Denoyer, 1992). The growing

popularity of ICP-MS is extending applications in various samples including human follicular fluid (Kruger, et al., 2012), petroleum (Kelly, Long, & Mann, 2003; Saint'Pierre, Chavez Rocha, & Duyck, 2012), urine (Kalamegham & Ash, 1992) and environmental samples (Pröfrock & Prange, 2012).

Polarographic techniques have been used to determine mercury species in dilute aqueous solutions. The redox potential of individual mercury species differs and thereby speciation is possible by polarography. Mercury was analyzed in a non complexing media by differential pulse anodic stripping voltammetry at Au film electrode, with a L.O.D of 2 x 10^{-8} mol dm^{-3} for 5 min plating time (Ireland-Ripert, Bermond, & Ducauze, 1982). It was also found that thin gold film shows a proportional increase in electric resistance in the presence of Hg vapor. This technique was utilized and commercialize as a gold film mercury analyzer with good linearity obtained between 5 – 40 μg Hg. The L.O.D is 500 pg/Hg or 10 μg dm^{-3} for a 50 cm^3 sample after borohydride reduction. However, it is important to note that the separation was needed for the procedure and it is not as simple and rapid compared to atomic absorption method when it was applied to real biological and environmental samples.

The final mercury detection method discussed is related to colorimetry. This method remained popular for mercury analysis in the 1960s, until the introduction of atomic absorption spectrometry (AAS) in the late 1960s (Morita, et al., 1998). Coloring reagent *i.e.* dithizone was widely used for mercury determination. The method is based on a spectrophotometric measurement of a colored complex extracted into an organic solvent after all the mercury in the sample has been converted to Hg(II) by acid-digestion and complexed with dithizone. The official method of analysis of the Association of Official Analytical Chemists (AOAC) employed a reversion procedure in which mercury dithionate in the chloroform layer was extracted into aqueous sodium thiosulfate solution and was

again extracted with dithizone in chloroform after decomposing the mercury thiosulfate complex (Horwitz, Chichilo, Clifford, & Reynolds, 1965). However, it seems necessary to review this method since relatively few laboratories are continuing this procedure. The use of colorimetry in mercury detection will be further reviewed in **Section 2.1** and **Section 2.2** under homogeneous and heterogeneous aqueous mercury complexation.

1.3.2. Mercury Remediation

In researching of good mercury remediation technologies, a diversity of materials has been examined in the literature to immobilize, decontaminate or remove aqueous mercury. Nonetheless, many studies reported that the removal of mercury by activated carbon (AC) is foremost economically favorable and technically easy (Dias, Alvim-Ferraz, Almeida, Rivera-Utrilla, & Sánchez-Polo, 2007; Khezami & Capart, 2005); thus, AC are extensively used in treating water contaminated with mercury. In actual fact, the main usefulness of AC for mercury removal is derived from its large micropore and mesopore volumes and the resulting high surface area (Fu & Wang, 2011). Furthermore, it can be also designed into different morphologies *i.e.* carbon nanofibers (CNFs) (Nabais, et al., 2006; Rinaldi, et al., 2009) and carbon nanotubes (CNTs) (Iijima, 1991) with better strength and thermal properties. Undoubtedly, this has led to a large number of research activities on AC towards heavy metal or aqueous mercury removal (Anoop Krishnan & Anirudhan, 2002; M. Choi & Jang, 2008; El-Shafey, 2010; Inbaraj & Sulochana, 2006; Jusoh, Su Shiung, Ali, & Noor, 2007; Kang, Kim, Choi, & Kwon, 2008; F.-S. Zhang, Nriagu, & Itoh, 2005). AC can be generally prepared from a variety of raw materials (Dabrowski, 2001), which should be abundant and cheap, with high carbon content and low inorganic content; raw materials should be easily activated and should have low degradation by aging (Moreno-Castilla & Rivera-Utrilla, 2001). Coal is the most commonly used, mainly due to its low cost and large

supply (Ahmadpour & Do, 1996). The raw materials can also the conventional agricultural wastes such as nuts, peanuts, olives, dates, almonds, apricots, cherries, rice, maize, sugar cane and coirpith; or non-conventional wastes such as fly ashes, pitch tires, sewage sludge and old newspaper (Dias, et al., 2007).

The factors that control the extent of adsorption on AC are: (i) the chemistry of the metal ion (speciation) or metal ion complex; (ii) the solution pH and the point of zero charge of the surface; (iii) the surface area and porosity (narrow and wider microporosity); (iv) the surface composition (oxygen functionality); and (v) the size of adsorbing species (hydrated ions in the range 1.0–1.8 nm), for carbons with significant volumes of narrow microporosity (Dias, et al., 2007). For metallic ions, they are renowned for its small size, being frequently charged in solution. Therefore, the predominant interactions in adsorption process on AC should be of electrostatic nature (López-Ramón, Moreno-Castilla, Rivera-Utrilla, & Radovic, 2002). For aqueous mercury, Sanchez-Polo and Rivera-Utrilla has studied the interactions of Cd(II) and Hg(II) onto ozonized AC. They concluded that electrostatic forces were dominant for the adsorption of Cd(II) while dispersive forces prevailed in the case of Hg(II) (Sanchez-Polo & Rivera-Utrilla, 2002), suggesting weak physisorption (physical adsorption) in governing the sorption of aqueous mercury onto AC. However, it is still important to note that foreign substances such as sulfur (Wajima & Sugawara, 2011), oxygen, nitrogen, (J. Zhu, Deng, Yang, & Gang, 2009), polypyrrole (M. Choi & Jang, 2008) and titanium oxide (Kwon, Fan, Cooper, & Yang, 2008) can be also incorporated onto AC. These foreign substances can significantly enhance the interaction of aqueous mercury species with AC and thus improving the adsorbing ability of AC for aqueous mercury removal.

The use of adsorbents containing natural polymers has received great attention, in particular polysaccharides such as chitosan and its derivative. Chitosan is a copolymer that

can be found naturally in some fungal cell walls and also chemically obtained by alkaline partial or total N-deacetylation of chitin (Miretzky & Cirelli, 2009). The polymer backbone consists of hydrophilic functional groups but is normally insoluble in water at near neutral pH and most common organic solvents (*e.g.* DMSO, DMF, NMP, organic alcohols, pyridine). The insolubility of chitosan in aqueous and organic solvents is a result of its crystalline structure, which is attributed to extensive intramolecular and intermolecular hydrogen bonding between the chains and sheets, respectively (Yui, et al., 1994). Nevertheless, it is still important to note that Chitosan is soluble at a degree of deacetylation above 40% (Sorlier, Denuzière, Viton, & Domard, 2001). The degree of deacetylation depends on the raw material from which chitin was obtained and the experimental procedure (Guibal, 2004). When the degree of deacetylation of chitin is larger than 40–50%, chitosan becomes soluble in acidic media. The solubilization occurs by protonation of the NH_2 groups on the C2 position of the d-glucosamine unit, although the distribution of acetyl groups along the chain may modify solubility (Kurita, Sannan, & Iwakura, 1979; Rinaudo, 2006).

Chitosan is well known as an excellent biosorbent for metal cation removal in near-neutral solutions because of (i) high hydrophilicity due to large number of hydroxyl groups of glucose units; (ii) presence of a large number of functional groups (acetamido, primary amino and/or hydroxyl groups); (iii) high chemical reactivity of these groups; and (iv) flexible structure of the polymer chain (Crini, 2005). The reactive amino group selectively binds to virtually all group III transition metal ions but does not bind to groups I and II (alkali and alkaline-earth metal ions) (Muzzarelli, 1973). In addition, due to its cationic behavior in acidic media, the protonation of amine groups leads to adsorption of metal anions by ion exchange (Guibal, 2004; Kunkoro, Roussy, & Guibal, 2005). Excellent reviews on metal complexation by chitosan have been written by Varma et al., Crini and

Kurita (Crini, 2005; Kurita, 2006; Varma, Deshpande, & Kennedy, 2004). For aqueous mercury remediation, Kunkoro et al. showed that the presence of chloride ions strongly influenced the retention, due to the possibility of protonated chitosan (in acidic solutions) attracting anionic chloride-complexes (Kunkoro, et al., 2005). Shafaei et al. studied the effect of pH and chitosan particle size on the Hg(II) adsorption capacity (Shafaei, Ashtiani, & Kaghazchi, 2007). They concluded that Langmuir isotherm was the best fit for experimental data with adsorption capacity obtained was 1127 mg g^{-1} at pH 6.0 and chitosan particle size 0.177mm. Although chitosan shows outstanding sorption capacity for Hg(II) ions ranging from 430 to 1127 mg g^{-1} specially in pH close to neutral, some disadvantages are the fact that chitosan is soluble in acidic media and cannot be used as adsorbent under these conditions (Miretzky & Cirelli, 2009). Nevertheless, several methods have been used to modify chitosan either physically by solvent evaporation (Krajewska, 2004), freeze drying (Gupta & Kumar, 1999), and cryogenic phase separation (Merrifield, 2002); or chemically by substitution of N/O groups (Cardenas, Orlando, & Edelio, 2001), grafting (LM Zhou, Liu, & Huang, 2007), polymerization (Tabakci & Yilmaz, 2008), and crosslinking (Ngah & Fatinathan, 2008). This has successfully improved the mechanical, chemical properties or even the adsorption capacity of chitosan and its derivatives (Baba, Matsumura, Shiomori, & Kawano, 1998; Jeon & Höll, 2003).

In addition to the natural polymers *i.e.* chitosan, synthetic polymer such as ion exchange resins, usually utilizing sulfur based groups were also used to bind aqueous mercury. A good candidate is TMR (name from Total Mercury Removal) from Rohm and Haas (Dujardin, Cazé, & Vroman, 2000). It is a styrene based divinylbenzene copolymer with pendant aryl thiol groups. It has the capability to adsorb nearly 0.7 g of mercury per gram of resin, an important value, since this limits shows how often it will have to be replaced. The resin can be also regenerated using concentrated hydrochloric acid. Another

artificial polymer is related to polymer supported crown thioethers. Somewhat surprisingly, these appear to be a very active area of research, even though there is literature evidence that macrocyles are not as effective for binding mercury as open chain compounds (Bach & Vardhan, 1986). One amazing example is 2-aminomethylthiacrowns immobilized on a polystyrene–divinylbenzene matrix through amine linkage (Baumann, Reynolds, & Fox, 2000). This polymer showed excellent extraction properties, with mercury removal rates of 97 – 99% after 30-min exposed to solutions of as high as 34 ppm mercury. An impressive of 91% mercury removal rate was achieved in an extremely concentrated solution of 170 ppm mercury. The authors attributed the success of their compound to its increased hydrophilicity in acidic water due to the amine linker. More importantly, this polymer can be also regenerated by treatment with dithizone.

Another technology for mercury remediation is mesoporous silica. This material contains inorganic Si-O backbones and having advantage of established pores and shapes which resulting in high surface area. They are often functionalized via reactions between ligands and surface and surface hydroxyl (-OH) groups. Such ligand-grafted materials mainly utilize the inner pores and surface of performed silica gels. In an effort to enhance the adsorption capacity and selectivity of the bulk of SiO_2-based materials to bind Hg^{2+} ions, the grafting of S-H containing *i.e.* mercapto ligands have been have been introduced (J. Aguado, Arsuaga, & Arencibia, 2008; Arencibia, Aguado, & Arsuaga, 2010; Feng, et al., 1997; Pérez-Quintanilla, Del Hierro, Fajardo, & Sierra, 2006). At neutral or high pH, the mercapto-grafted silica could lower mercury concentrations by as much as four orders of magnitude in ppm concentration solutions. Furthermore, it was also reported that sorption capacity of 1343.95 mg of Hg(II) / g of sorbent can be achieved when silica is modified with benzoylthiourea (Olkhovyk, Antochshuk, & Jaroniec, 2004). This marked a remarkably high sorption capacity which can be hardly reached by other sorbent materials.

Nonetheless, there are also problems dealing to thiol functionalized mesoporous silica. The first is related to the slight decrease in efficiency at lower pH mainly due to protonation of the thiol, but this was not large enough to represent a serious concern. The second issue is associated to the synthesis of thiol functionalized mesoporous silica in which the resulting functionalized material is typically comprised of micron-sized particles. These particles are quite difficult to handle in which it had to be immobilize on a second substance such as kaolin clay before used. However, a later synthesis succeeded in creating similar silica particles of macroscopic size which performed as well as their micron sized counterparts (Nooney, Kalyanaraman, Kennedy, & Maginn, 2001). Moreover, a silane condensation similar to that used for synthesis of functionalized silica has also been used to attach thiol groups to montmorillonite, a smectite clay (Mercier & Detellier, 1995). However, the resulting clay called thiomont was not as effective a mercury filter as the silica derivative, but still far superior to activated carbon.

Apart from mercapto functionalized mesoporous silica, a different idea for aqueous mercury remediation is to add homogeneous complexing surfactants, which will combine with mercury and other toxic metals and change their solubility so that they can be extracted into an organic solvent (Schwuger, Subklew, & Woller, 2001). The popular and important ligands for this application are sodium or potassium sodiumthiocarbonate (DTC), sodium or potassium dimethyldithiocarbamate (DMDTC) and trimercaptotriazine (TMT) (Matlock, Henke, & Atwood, 2002; Tassel, Rubio, Misra, & Jena, 1997). These ligands are effective at removing mercury from mixed gold/mercury cyanide waste streams. However, the long-term stability of these precipitates is very questionable. Studies showed that the leaching of mercury can be resulted if the precipitates are not removed from the water (Matlock, Henke, et al., 2002). Furthermore, if the precipitates are immediately filtered, dried and transferred to clean and mercury free water, that solution will soon show a high

concentration of dissolved mercury in which a further treatment or disposal is required (Rabenstein, 1978). Moreover, the resulting complexes also appear to go through multiple changes in form, releasing mercury or toxic compound such as thiram which can be hazardous to the aquatic systems (Matlock, Henke, et al., 2002).

In response to the toxicity of aforementioned homogeneous complexing surfactants, Matlock et al. has eventually designed and synthesized a new thiol based compound, 1,3-benzenediamidoethanethiol dianion (BDET) dianion (Matlock, Howerton, & Atwood, 2002, 2003). This compound can effectively precipitate mercury in the leachate solution and heavy metals from acid mine drainage. In addition, supramolecular dithiocarbamate heavy metal precipitants dithiocarboxy piperazine (BDP) and hexahydrotriazinedithiocarbamate (HTDC) were also employed in treating complex heavy metal wastewater (Fu, Chen, & Xiong, 2006; Fu, et al., 2007). The results indicated that both BDP and HTDC could effectively reduce heavy metal ions in wastewater to much lower than 0.5mg/L. As mentioned earlier, the conventional chemical precipitation has many limitations. Thus, it is difficult to meet the increasingly stringent environmental regulations by applying these processes to treat the heavy metal wastewaters. Although improvement has been done on the existing ligands, there are still too many environmental risks needed to be considered before it can be safely utilized. Hence, there is a definite need for new and more effective precipitants to be synthesized in order to meet the discharged and safety requirements.

From the discussion above, most of the materials used for mercury remediation have its own advantage and some of it could even be regenerated by washing with acid. However, the regeneration of the sorbent has indirectly presented a slight problem. If one treats the sorbent with HCl to remove the mercury, a new batch of mercury contaminated water has just been created. Disposal of this secondary waste could prove costly and more importantly, the mercury pollution can be keep recycling. On the other hand, the leach-

ability of the mercury complex or compound from the sorbent to the environment is also another important issue needed to be addressed. In the attempt to overcome these problems, the adsorbents can be designed in such a way that stable mercury complexes are formed in the sorbent. The formation of these stable mercury complexes can ensure the easy and safe disposal of the reacted sorbent in the environment. This can undeniably reduce the need in disposing secondary mercury waste. More importantly, this terminates the real mercury pollution issues. A vital route which leads to the formation of strong mercury complexes in the sorbent is associated to the metal sulfide systems. The current research progress on the metal and metal chalcogenide systems (metal oxide and sulfide) will be further reviewed in **Section 2.2** under heterogeneous aqueous mercury complexation.

1.4. Motivations

The toxicity of mercury, impacts and pollutions have long been recognized from various reports described earlier. Hereby, a few problem statements have been addressed: what type of material is suitable to detect, remove and immobilize aqueous mercury; why it is being selected; and what is the interaction between the material and mercury that can prevent the mercury pollution issues from perpetuating. In this work, two type of complexing agent (homogeneous and heterogeneous) were studied for aqueous mercury mitigation. In homogeneous aqueous Hg(II) complexation, it is well recognized that the d^{10} electronic configuration of Hg(II) has forbidden the d-d transition for any electronic excitation. This has resulted in colorless Hg(II) complexes formed and no absorption of Hg(II) can occur in the visible region (380 – 780 nm).

In our study, fluorescence xanthene basic dye, Rhodamine B was identified as the potential candidate for homogeneous Hg(II) complexation. It is because Rhodamine B dissolves in water to give a red color solution which also acts as a coloring and wavelength

shifting agent for Hg(II). In fact, Hernandez-Cordoba et al. has demonstrated that Rhodamine B is a good spectrophotometric reagent for mercury detection (Hernandez-Córdoba, López-Garcia, & Sánchez-Pedreño, 1984). Nonetheless, muck research works can be still done to further improve the method's sensitivity. One way of achieving it is introducing iodide anion in the Rhodamine B-mercury complex. It has been shown earlier that iodide anion is functioning well in the mercury detection method of Rhodamine 6G (Ramakrishna, Aravamudan, & Vijayakumar, 1976). In addition, halogen or specifically iodide anion is also a good candidate for complexing mercury when mercury determination studies were conducted with other basic dye such as Crystal violet, Malachite green, Methyl violet, Pyronine G, and Bindschedler's Green (De & Pal, 1979; Kothny, 1969; Mathew, Sukumar, Rao, & Damodaran, 1992; Tsubouchi, 1970). Thus, in a similar manner, it is expected that the addition of iodide anion in the Rhodamine B-mercury complex is possible in providing a more promising and sensitive method for the mercury detection. Moreover, the extraction of Rhodamine B-mercury complex into stable organic solvent should be also considered. This is because extraction is working as the pre-concentration of Hg(II) species and it can notably decrease the method's L.O.D. Thus, this provides a great opportunity of developing mercury detection method based on Rhodamine B and iodide via the use of non-desctructive UV-Vis spectrophotometry.

In heterogeneous aqueous mercury complexation, the approach of employing pure metal, metal oxide and metal sulfide for aqueous mercury complexation has been actively investigated by researchers for the past three decades. Nevertheless, the existing problem is still revolving on finding a good sorbent system that can eventually acts as a permanent mercury sink in the environment. In view of this particular problem, copper sulfide (Covellite, CuS) has been investigated to capture aqueous Hg(II). The key reason for choosing CuS is associated to the stability and solubility of CuS in water as well as affinity

of mercury towards sulfur compound. According to Hard-soft acid base theory (HSABT), mercury compound is a soft Lewis acid whereas sulfur compounds is actually a soft lewis base (Pearson, 1963). Therefore, the reaction between Hg(II) and CuS is thermodynamically and kinetically preferred. Strong bond *i.e.* chemical sorption (chemisorption) processes and faster reaction *i.e.* faster rate would be expected from the chemical interaction. Since chemisorption is expected from the reaction, it is predicted that the formation of cinnabar (HgS) is also one of the product at the end of the reaction. In general, cinnabar (HgS) is the most stable form of mercury in the environment with $K_{sp} = 2 \times 10^{-53}$. Cinnabar (HgS) is mostly found in the volcanic region where it is also one of the main product emitted from the geothermal processes. It is the most ideal compound for storing mercury compounds because it is relatively insoluble and less volatile than other forms of mercury. Therefore, the idea of utilizing the formation of cinnabar (HgS) as the environmental sink can definitely become the main solution in terminating the mercury pollution issues.

Apart from that, metal sulfide is also identified as a naturally occurring compound which can be easily synthesized or obtained in the environment. There were supporting facts from the literature suggested that metal sulfides are good candidates towards heavy metal sorption. Among the metal sulfides systems, only Fe_xS *i.e.* Pyrite (FeS_2) (Bower, et al., 2008), Pyrrhotite ($Fe_{1-x}S_x$) (Hyland, Jean, & Bancroft, 1990), Mackinawite (FeS) (J. Liu, Valsaraj, Devai, & DeLaune, 2008), and Mo_xS (Gash, et al., 1998) were deeply investigated for aqueous Hg(II) trapping. Studies showed that these sulfide system is promising in scavenging aqueous Hg(II) in water. However, Fe_xS and Mo_xS system are still not selective enough in mercury sequestration. The sorption site of Fe_xS and Mo_xS can be fully occupied by other metal ions before it reached the vicinity of our main target i.e. Hg(II).

In particular for the sorption of aqueous Hg(II) onto copper sulfide, the reaction has been generally described as an ion-exchange sorption purely based on the solution phase analysis. The sorption mechanism was also correlated to mercury sulfide, HgS and double salt, $2Hg_2X \cdot HgX_2$ (X = Cl, Br, NO_3 and etc) formation barely based on the deduction without concrete proof from solid phase characterization (Harold O. Phillips & Kraus, 1965). Furthermore, there are still many questions regarding the structural, physical and chemical properties of copper sulfide used to adsorb Hg(II) in water aqueous system. This is because most of the researchers failed to confirm the properties of copper sulfide used in prior to the Hg(II) removal studies. In comparison to other metal sulfide or metal oxide, the in depth understanding on the sorption kinetic (rate of reaction), sorption equilibrium (sorption isotherms), maximum Hg(II) retention capacity and sorption mechanism of Hg(II) onto CuS is still left uncovered. However, these questions can be answered accordingly by referring to the related strategies employed (experimental design and characterization technique) in the studies of other metal sulfide and metal oxide for aqueous Hg(II) removal. Thus, this has indirectly broadened up the research opportunity in this discipline.

1.5. Objectives of Research

The aims of this research work are listed as the following:

- To develop mercury detection procedures based on the use of homogeneous aqueous mercury complexing agent, Rhodamine B and UV-Vis spectrophotometry.
- To evaluate the performance of pure and mixed phase Covellite (CuS) *i.e.* surface oxidized CuS in heterogeneous aqueous mercury complexation.
- To investigate the effect of solution pH on Hg(II) uptake, Cu(II) leached and final pH changes as well as the related reactions during the sorption of Hg(II) onto pure phase Covellite (CuS).

1.6. Outline of Research Work

Mercury management research program was initiated in Nanotechnology and Catalysis Research Centre (NANOCAT), University of Malaya (UM) since 2009. This is a research program in collaboration with Fritz Haber Institute of the Max Planck Society (FHI der MPG), Germany. Overall, there are three research projects under this mercury management program that this research work was involved: (i) Mercury detection method development by using homogeneous complexation agent and UV-Vis spectrophotometry, (ii) Synthesis and characterization of unsupported copper sulfide and (iii) Performance assessment and understanding of the reaction profile of copper sulfide in aqueous mercury immobilization. Nonetheless, the main focus of this thesis is centered on (i) Mercury detection method development and (iii) Performance assessment and understanding of the reaction profile of copper sulfide in aqueous mercury immobilization. The research project on (ii) Synthesis and characterization of copper sulfide has been primarily covered by Emily Yap Pei Lay in her Master of Science dissertation titled "Synthesis and Characterization of Unsupported Copper Sulfide for Mercury Trapping in Aqueous System" (Pei Lay Yap, 2012).

With the aim to achieve the objectives mentioned in **Section 1.5**, the research work in this thesis is well organized in three sections. The first section is presented in Chapter 4 in which it is dealing with the development of mercury detection procedures using Rhodamine B (Rh B). In the procedures, mercury (II) chloride solution was firstly mixed with potassium iodide in acidic medium. The anionic mercury iodide complexes were then complexed with Rh B to form Rh B-Hg-Iodide complexes. Two different approaches *i.e.* extraction into organic solvent and stabilized in water system by polymer were employed to study the resulting Rh B-Hg-Iodide complexes via UV-Vis spectrohotometry. The mercury detection method developed was also tested in assessing the preliminary performance of CuS in removing Hg(II).

The second section i.e. Chapter 5 in this thesis is associated with the performance evaluation of mixed phase CuS in heterogeneous Hg(II) immobilization. Mixed phase CuS (surface oxidized CuS) was examined for their performance in terms of sorption kinetic (how fast aqueous mercury can be totally removed) and sorption equilibrium (what is the maximum limit of aqueous mercury that can be loaded onto CuS). In this part, well established cold vapor atomic absorption spectrometry (CVAAS) has been used to analyze the remaining amount of Hg (II) present in the solution. In addition, a preliminary analysis on the sorption profile of Hg(II) onto CuS was also established using powder XRD, FESEM-EDX and synchrotron XPS.

The third section i.e. Chapter 6 in this thesis presented the performance evaluation of pure phase CuS in heterogeneous Hg(II) immobilization. Pure phase CuS (surface oxidized CuS) was examined for their performance in terms of sorption kinetic (how fast aqueous mercury can be totally removed) and sorption equilibrium (what is the maximum limit of aqueous mercury that can be loaded onto CuS) under detail reaction parameter i.e. solution pH, reaction temperature and Hg(II) concentration variation. Again, well established CVAAS technique has been utilized to analyze the remaining amount of Hg (II) present in the solution. Meanwhile, AAS and pH probe were used to analyze the amount of Cu(II) present in the solution and final solution pH changes respectively. Moreover, the unreacted and reacted solid CuS samples were also characterized using various solid analytical tools *i.e.* PXRD, FESEM-EDX, Synchrotron XPS and HRTEM-EDX. Finally, this has led to an in depth understanding and establishment on the sorption mechanism of aqueous Hg(II) onto CuS.

CHAPTER 2

LITERATURE REVIEW

This chapter is divided into three sections. The first section gives the review on the methods used for mercury detection. The second section provides the review on the interaction of mercury with metal, metal oxide and metal sulfide sorbents. Lastly, this chapter is concluded by the executive summary and theoretical details on the model used in the analysis of heterogeneous aqueous mercury complexation.

2.1. Homogeneous Aqueous Mercury Complexation

Homogeneous complexation is defined as a complexation process in which the substance to be complexed or trapped (target) and the complexing agent are brought together in one phase, most often the liquid phase. The entire process involves no phase separation throughout the reaction in which the liquid phase reagents of the target and complexing agent are completely miscible in a particular solvent system. The interactions exist between the target and complexing agents are generally based on covalent, dative and hydrogen bonding. Often, it can be also relied on the electrostatic charges formed between the metal-ligand complex and complementary complexing agent. In the whole process of homogeneous complexation, ligand effects are extremely important by metal complexes (Van Leeuwen & Leeuwen, 2004). One metal can give a variety of product from one single substrate simply by changing the ligands around the metal centre. This give rise to different stability of metal complexes in which it can interact dissimilarly with the complementary complexing agent. Homogeneous complexation is always related to the reaction between solution phase metal-ligand complex as well as solution phase complexing agent. Therefore, analyses of the resulted homogeneous product/complexes are regularly carried out via the

solution technique i.e. nuclear magnetic resonance spectroscopy (NMR), Infra-red spectroscopy (IR) and UV-Vis spectroscopy (UV-Vis).

2.1.1. Dithizone

Dithizone also recognized as diphenylthiocarbazone or 3-mercapto-1,5-diphenylformzane (H_2Dz) is one of the most powerful organic spectrophotometric reagents which provide the basis of sensitive determination of Hg(II). Dithizone is insoluble in aqueous solution at pH < 7. It dissolves in alkaline media, forming an orange colored solution and dissolves in CCl_4, $CHCl_3$, hydrocarbon, and alcohols giving green colored solution. The two tautomeric forms of dithizone: keto (I) and enol (**Figure 2.1**) coexists in organic solvents (Wagler & Koch, 1984). Study of the structures of primary nickel dithizonate has shown that the metal to be bonded to the sulfur atoms by replacement of the hydrogen in the thiol group, also coordinately bonded to a nitrogen atom (**Figure 2.2**) (Laing & Alsop, 1970).

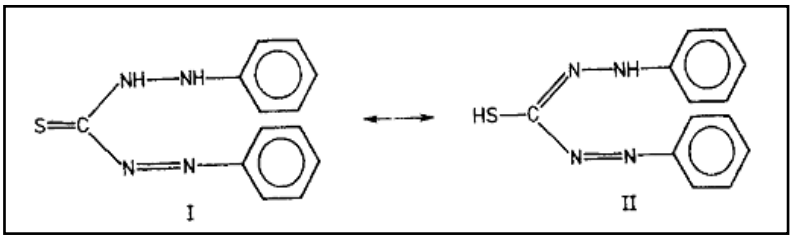

Figure 2.1. The structure and Keto – Enol tautomerism of dithizone.

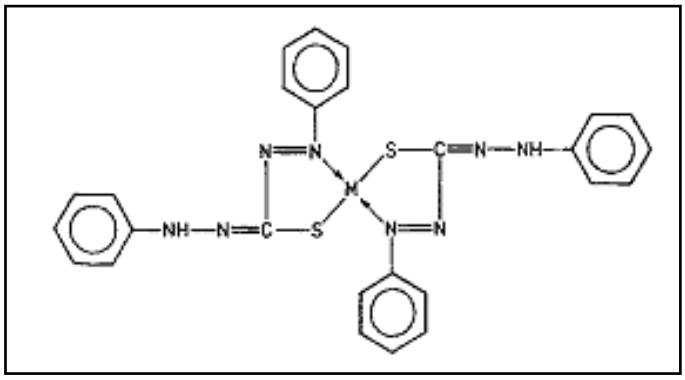

Figure 2.2. Metal complexation by dithizone.

Dithizone has often been used in the extractive separation and determination of traces metals such as lead, zinc, cadmium, silver, palladium, copper and bismuth (Irving, 1977; Irving & Iwantscheff, 1980; Iwantscheff, 1958; Marczenko & Balcerzak, 2000). For mercury detection, orange-yellow Hg(II) dithizonate, $Hg(HDz)_2$ is readily formed when dithizone in is shaken with acidic media containing mercury (Litman, Williams, & Finston, 1977). The most frequently applied method for determining Hg(II) with dithizone consists of: (i) extracting the Hg(II) from aqueous solutions with an excess of dithizone solution in organic solvent, (ii) removing the free dithizone from non-aqueous phase by shaking with an alkaline aqueous solution, and (iii) measuring the absorbance of the colored metal dithizonate solution. CCl_4 and $CHCl_3$ are the normal solvents for dithizone. Its solubility is greater in $CHCl_3$ (1 g/100 ml) than in CCl_4 (0.08 g/100 ml). CCl_4 is preferable as a solvent because of its lower volatility and greater specific gravity, which results in a more rapid phase-separation on shaking with the aqueous solution. CCl_4 is less soluble in water (0.08%) than is $CHCl_3$ (0.8%) and is also less toxic. Free dithizone is stripped from the extract with either dilute NH_3 or NaOH. The absorbance of the orange-yellow $Hg(HDz)_2$ solution is measured at λ_{max} = 485 nm with molar absorptivity = 485 nm is 7.1×10^4 l $mole^{-1}cm^{-1}$. The L.O.D was of the order of l pg mercury.

The mercury dithizonate in CCl_4 or $CHCl_3$ change color under the action of sunlight (Marczenko & Balcerzak, 2000). With that, mercury has been determined with dithizone in aqueous media in the presence of the surfactants Triton X – 100 (Paradkar & Williams, 1994; Singh, Kumar, Sharma, & Katyal, 1989; Ueno, et al., 1979). In the assistance of surfactants, it is possible to determine metals with dithizone directly in the aqueous phase without the hassle of performing extraction (Paradkar & Williams, 1994). However, it still important to note that atmospheric oxygen oxidizes dithizone to diphenylthiocarbodiazone. Unlike dithizone, diphenylthiocarbodiazone is insoluble in aqueous alkaline solutions. It

dissolves in CCl_4 and $CHCl_3$ giving a brown colored solution which is chemically inactive. Commercial dithizone preparations are always contaminated with the oxidation products. The active dithizone content of a reagent preparation also diminishes with time giving the issue to prepare fresh dithizone regularly for Hg(II) determination.

2.1.2. Rhodamine B

Rhodamine B is a xanthene basic dye which occurs in the form of amphoteric salt in aqueous solution. The existence of different protonated species in aqueous solution has been shown in the literature (Hasanin, Tsukahara, & Fujiwara, 2010; Moreno-Villoslada, et al., 2006; Ramette & Sandell, 1956) where the equilibrium between these species is highly pH dependent. In addition, the type of Rhodamine B species can also be altered with different type of solvent used (Elderfield, 1950; Gahlmann, Kester, & Mayer, 2005; Golkowska & Pszonicki, 1973). **Figure 2.3** depicts the chemical equilibrium of Rhodamine B species in different solvent systems. At first, the colorless lactone form of Rhodamine B can be retained in any non-polar solvent. Further dissolution in polar solvent break up the lactone ring which leading to the amphoteric salt of Rhodamine. The protonation of Rhodamine B occurs in 3 stages. The first stage involves the protonation on the carboxyl group. Second stage involves the protonation on the amino nitrogen atom. Further protonation mostly occur on the oxygen atom, and this can only be done using concentrated sulphuric acid or perchloric acid medium (Golkowska & Pszonicki, 1973). However, among the different forms of Rhodamine B in aqueous solution, only the singly protonated species is active and responsible in forming the ion association compound with metal anionic complexes (Biyum & Pavlova, 1963; Hosseini & Naseri, 2003).

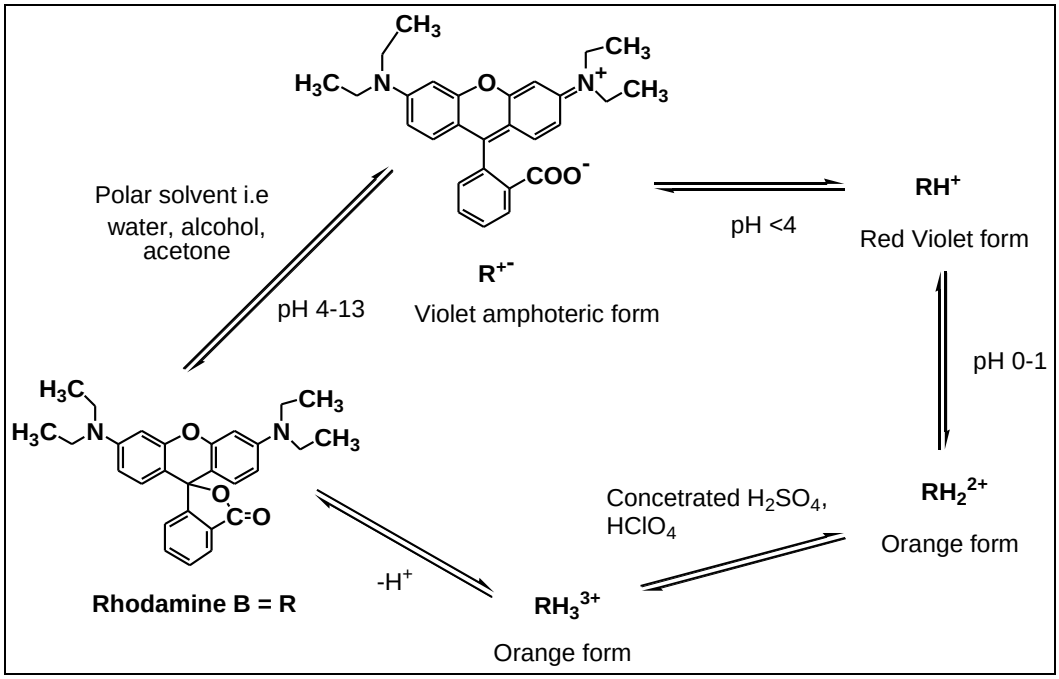

Figure 2.3. Chemical Equilibrium of Rhodamine B species in different solvent systems.

In the past, Rhodamine B has been tried in determining metal ions such as gallium, uranium, thallium, palladium and gold (Hasegawa, Inagake, Karasawa, & Fujita, 1983; Hosseini & Naseri, 2003; Lopez-Garcia, Martinez-Aviles, & Hernandez-Cordoba, 1986; Macnulty & Woollard, 1955; Moeken & Van-Neste, 1967). For mercury detection, the early work involved the use of analogous compound of Rhodamine B *i.e.* Rhodamine 6G (Ramakrishna, et al., 1976). The procedure has been carried out in the presence of iodide and gelatin in which this has led to the formation of pink colored Rhodamine 6G-Hg(II)-Iodide complexes during the reaction. This method provided a linear calibration graph in the range of 5 – 25 μg mercury per 25 ml at 575 nm with molar absorptivity = 7.0 x 10^4 l $mole^{-1}cm^{-1}$. Another report is related to the use of Rhodamine B thiocyanate and polyvinylalcohol (PVAl) to form violet colored Rhodamine B-Hg(II)-Thiocyanate complexes (Hernandez-Córdoba, et al., 1984). They have reported a linear calibration graph in the range of 1 – 15 μg mercury per 25 ml at 610 nm with molar absorptivity = 1.1

x 10^5 l $mole^{-1}cm^{-1}$. This method was also tested in determination of gaseous mercury in their laboratory with satisfactory result.

2.2. Heterogeneous Aqueous Mercury Complexation

Heterogeneous complexation is well known as a complexation process in which the substance to be complexed or trapped (target) and the complexing agent are distinguished by two different phases. It is often recognized as the sorption process which involves a surface phenomenon, consists of a solid material, which providing sites to interact with the particles in a matrix. The solid material, which provide the sites for interaction is called the sorbent whereas the interacting particle (gas, solid) toward the sorbent are called the adsorbate. Sorption can be categorised as two main types i.e physical sorption (physisorption) and chemical sorption (chemisorption). In physisorption, there is a van der Waals interaction between adsorbate and the substrate (adsorbent) with the enthalpy change in the region of $20kJmol^{-1}$. This small enthalpy change is insufficient to lead to bond breaking, so a physisorbed molecule retains its identity. In chemisorption, the molecules stick to the surface of adsorbent by forming chemical bond with a very much greater enthalpy change, in the region of $200kJmol^{-1}$. The chemisorbed molecule therefore may be torn apart results in a newly forming species which explains why solid surfaces catalyse reactions (Atkins & De Paula, 2010). Besides, the sorption process can also be enhanced by some other substances, namely promoter which can further reduce the interaction potential energy barrier between the adsorbents and adsorbates.

Specifically for liquid particle sorption reactions, it can be further discussed in term of adsorption and ion-exchange process. Adsorption involves the direct contact of adsorbates selectively transferred from the liquid phases to the surface of rigid solid particles. The interaction of the liquid particles with the adsorbent can be the type of

physical or chemical that described earlier. The bonding involves can be: ionic bonding, covalent bonding, coordination-complexation bonding, or even the weakest van der waals forces. For ion-exchange process, the reaction scheme is almost similar to adsorption. However, as for the compensation for the sorption of adsorbates, the pre-existing species on the ion-exchanger will be leached out during the sorption of reacting liquid particles. This makes the significant difference between the two sorption processes and will be deeply investigated in our research studies.

2.2.1. Pure Metal

The first type of heterogeneous aqueous mercury complexing agent which utilized pure metal is associated to tin (Sn). This is not exactly a mineral based filter but a somewhat related idea involves using mossy tin as a mercury filter (Biester, Schuhmacher, & Müller, 2000). In this approach, reduction of divalent mercury Hg(II) by mossy tin combined with Hg(0) air stripping has been proposed as a method to remove Hg from groundwater. The effectiveness of mossy tin to remove Hg(II) from aqueous solution at different flow rates and the retention of Hg through the formation of HgSn amalgams have been investigated. The results show that mossy tin layers of only 2 cm thickness can reduce 100% of 800 μg Hg(II)/liter at a flow rate of about 1 volume of drainable porosity min^{-1} (Vol min^{-1}), and even 100% of 5000 μg/liter at 0.125 Vol min^{-1}, 89% and 97% of the Hg(0) were retained through amalgamation. Although mossy tin shows high capacity to remove Hg from aqueous solution, it was much less effective at trapping the reduced metal. It also leached tin into the environment. Therefore, this idea appears obviously unpromising.

Another pure metal used for heterogeneous aqueous mercury complexation is related to zinc (Zn). This method is aimed to alter the solubility of the mercury components so that they will either precipitate or can be extracted from the waste stream. At its simplest,

this means the treatment of wastewater containing mercury ions in aqueous solution by cementation with sacrificing metal, Zn. This process is similar to the use of Sn in which the resulting spontaneous redox reaction will reduce all the divalent mercury in solution but does not involve the amalgamation with Zn. In the studies, the removal of mercury ions from aqueous solutions by cementation of Zn powder was found to be a function of solution pH and temperature, amount of zinc, concentration of mercury ion, contact time and the addition of several organic surfactants. Cementation of mercury was shown to be a feasible process to achieve a very high degree of mercury removal fairly reasonable contact time. The reaction rate is approximately first order with respect to the concentration of mercury ion in aqueous solution. Among the surfactants used in this study, only the presence of SDS, an anionic surfactant, slightly enhanced the cementation rate of mercury. The presence of CTAB and Triton X – 100 will retard the cementation of mercury by zinc. The disadvantage of this technique is dealing to the companion of highly contaminated Zn water at the end of the process. Moreover, this technique also possesses the need of recover the metallic mercury and further treatment on the secondary waste stream.

In comparison to Sn and Zn, the application of gold (Au) in heterogeneous aqueous mercury complexation has unexpectedly received an enormous attention from the scientific society. Despite of the expensive cost of gold, the research activities on gold as mercury complexing agent has never been halted. Conversely, gold and different gold-polymer systems have been extensively studied in the literature which showed a capable technology for mercury mitigation. The gold film electrode has been one of the electrodes of choice in electrochemical stripping analysis techniques for the detection of aqueous mercury (Watson, Dwyer, Andle, Bruce, & Bruce, 1999). In the electrochemical stripping analysis, a three step cycle is commonly employed for mercury detection: pre-concentration (electrodeposition), measurement (stripping) and regeneration (cleaning). One reason for

the use of gold is its high affinity for mercury which enhances the pre-concentration effect (Zen & Chung, 1995). This has in return demonstrated the L.O.D below 1 ppb with high sensitivity (Pinilla Gil & Ostapczuk, 1994; Rievaj, Mesároš, & Bustin, 1993; Q. Wu, Apte, Batley, & Bowles, 1997). Nevertheless, XPS studies showed that the nature of gold surface is fundamentally altered by irreversible adsorption of mercury; that is, mercury is strongly adsorbed during deposition and some of the mercury is retained even after stripping and cleaning (Watson, et al., 1999). This has undeniably resulted in some loss of expensive and active gold surface for further adsorption of aqueous mercury.

Instead of using gold electrode coupled electrochemical stripping analysis for mercury detection, the utilization of gold nanoparticles (Au NPs) as important colorimetric sensor seems to be an emerging methodology. The fundamental concept is based on the aggregation of spherical Au NPs which can induce a rapid visible color change from red to blue due to the coupling of interparticle surface plasmon resonance (SPR) (Nam, Won, Jin, Chung, & Kim, 2009; Polavarapu & Xu, 2008; Srivastava, Frankamp, & Rotello, 2005). The SPR band is sensitive to sizes, shape and interparticle distance. Different sized and shaped Au NPs displayed different color solution systems. For instance, 13-nm and 56-nm diameter Au NPs exhibit large surface plasmon extinction bands centered at 520 and 530 nm, producing rose red and purple red colored solution respectively (C.-C. Huang & Chang, 2007; C.-I. Wang, Huang, Lin, Chen, & Chang, 2012). The color change provides a useful platform for the colorimetric detection of Hg(II). In addition, the extinction coefficients of Au NPs are 1000 times larger than those of organic dyes (Chen, Yu, Cheng, & Tseng, 2008; Saha, Agasti, Kim, Li, & Rotello, 2012). This has made AuNPs very suitable for applications in colorimetric sensing systems.

In the way of employing Au NPs as mercury sensor, the important step is always connected to the introduction of stabilizer or capping agent to disperse Au NPs. The further

aggregation of AuNPs upon interact with mercury would result in color changes (Y.-R. Kim, Mahajan, Kim, & Kim, 2009). In this discipline, different type of AuNPs-polymer systems have been studied with the aim to improve the sensitivity, and selectivity for Hg(II) detection. For example, Liu et al. provided a highly sensitive and selective assay to detect Hg^{2+} in aqueous solutions using quaternary ammonium group-terminated thiols modified Au NPs (D. Liu, et al., 2010). Lee et al. developed a highly sensitive and selective colorimetric Cys based detection method upon oligonucleotide-functionalized Au NPs probes that contain strategically placed thymidine−thymidine (T-T) mismatches coordination with Hg^{2+} (J.-S. Lee, Ulmann, Han, & Mirkin, 2008). In most cases, Au NPs are surface modified with DNA, DNAzymes, conjugated polymers, oligonucleotide- or thiol-containing organic molecules to indicate color or light intensity change (C.-C. Huang & Chang, 2007; Y.-R. Kim, et al., 2009; L. Li, Li, Qi, & Jin, 2009; T. Li, Dong, & Wang, 2009; X. Liu, et al., 2007; Y. Zhu, et al., 2012). These assays own some advantages but are still cost- or pollution-consuming (T. Li, et al., 2009). Hence, vigorous research activities are still ongoing to develop a facile, low cost, rapid, and eco-friendly method for on-site Hg^{2+} detection (You, et al., 2013).

2.2.2. Metal Oxide

For decades, metal oxide has been one of the main mercury de-contamination materials that have been studied comprehensively in the literature. Metal oxide can be further divided into the main group and transition metal oxide in which their chemical reactivity towards aqueous Hg(II) are different. For main group oxide, Bhakta et al. has reported the use of volcanic ash soil-ceramic (A-ceramic) and magnesium oxide (MgO) impregnated volcanic ash soil-ceramic (MA-ceramic) for aqueous Hg(II) removal (Bhakta & Munekage, 2011). The results showed that the sorption of Hg(II) onto MA-ceramic follows the Freundlich

isotherm with adsorption capacity reaching 265 ± 8.5 μg Hg(II) /g sorbent. In addition, the sorption capacity of MA-ceramic was shown to be 12 times higher than A-ceramic. This observation clearly suggested the additional interaction between Hg(II) and oxide surfaces which increased the sorption capacity of MA-ceramic during the removal process.

The second main group oxide that has been studied intensely for heterogeneous aqueous Hg(II) complexation is dealing with aluminum oxide (Al_2O_3). Kim et al. has reported a detail extended X-ray absorption fine structure (EXAFS) studies on the sorption of Hg(II) onto γ-alumina (γ-Al_2O_3) and bayerite (β-$Al(OH)_3$) (C. S. Kim, Rytuba, & Brown, 2004). For β-$Al(OH)_3$, the authors identified that Hg(II) forms inner-sphere sorption complexes over pH ranges 4–8. The Hg(II) complexes sorb dominantly in bidentate corner sharing, bidentate edge-sharing, and monodentate modes to the $Al(O,OH)_6$ octahedra. For γ–alumina, outer-sphere complexation may be an important component of Hg uptake. Furthermore, Hg(I) species is also found to be bonded to the $Al(O,OH)_6$ octahedra of the hydrated γ-alumina surface as both monodentate and bidentate corner-sharing complexes. Unquestionably, this molecular-scale EXAFS studies have provided solid proves for the interaction between aqueous Hg(II) with oxide surfaces.

On top of aluminum oxide, aluminosilicate minerals *i.e.* zeolite is also progressively receiving numerous focus for its ability in sequestrating aqueous mercury. Blanchard et al. have studied the applicability of natural zeolite, Clinoptilolite with chemical formula of $(Na,K,Ca)_{2\text{-}3}Al_3(Al,Si)_2Si_{13}O_{36}\cdot 12H_2O$ for trace heavy metal removal (Blanchard, Maunaye, & Martin, 1984). In their studies, the selectivity of Na-exchanged Clinoptilolite has been achieved by plotting the exchange isotherms relative to various cations in the presence of ammonium ions. Nonetheless, the result indicated that the affinity of Clinoptilolite towards Hg^{2+} is the worst among the metal ions studied ($Pb^{2+} > NH_4^{2+} > Cu^{2+}$, $Cd^{2+} > Zn^{2+}$, $Co^{2+} > Ni^{2+} > Hg^{2+}$). In another report, Gebremedhin-Haile et al. have once again examined the

sorption of aqueous Hg(II) using unmodified zeolite and modified zeolite with cysteamine hydrochloride and dihydrochloride. It was also found that the zeolites used in these studies showed more selectivity for mercury than Cu, Ni and Zn when a mixed metal ion solutions were employed in their studies (Gebremedhin-Haile, Olguín, & Solache-Ríos, 2003). For all the materials studied, the sorption of Hg(II) onto zeolite obeyed well with Langmuir isotherm. The low uptake of Hg(II) onto unmodified zeolite was also confirmed. However, modified zeolite showed elevated mercury retention with maximum adsorption capacity achieving 0.25 μg Hg / g sorbent. Apparently, the surface modification with S functionality has successfully increased the amount of Hg(II) that can be loaded onto zeolite.

Further research on zeolite for aqueous mercury complexation was continued by the studies from Chojnacki et al. (Chojnacki, Chojnacka, Hoffmann, & Gorecki, 2004). In their studies, the sorption of Hg(II) onto zeolite was rapid, reversible first order and followed Langmuir-Freundlich (Sips) isotherm with maximum sorption capacity reaching 6.03 μg Hg / g sorbent. The dominating mechanism in governing the uptake of Hg(II) was found to be ion-exchange with three functional cation-exchange groups identified at pK_a of 2.1, 7.3 and 10.7. Besides, thiol functionalized zeolite (TFZ) was also developed by Zhang et al. in stabilizing mercury containing solid waste (X.-Y. Zhang, Wang, Zhang, Sun, & Zhang, 2009). The result showed that the sorption of Hg(II) by TFZ conform Freundlich isotherm with maximum sorption capacity reaching 2.22 μg Hg / g sorbent. A new idea by encapsulating magnetic iron oxide and colored Rhodamine B into zeolite was also proposed by Yin et al. In their studies, the fluorescence intensities of Magnetic Functionalized-Rhodamine Hydrazine (MMZ-RH) exhibited high selectivity towards Hg^{2+} in the presence of various biologically and environmentally relevant metal ions such as Zn^{2+}, Cu^{2+}, Ca^{2+}, Mn^{2+}, Mg^{2+}, Cr^{2+}, Na^{+}, Ni^{2+}, Pb^{2+}, Cd^{2+}, and Fe^{3+}. No significant change was observed when this material was added into the mixed metal solution together with Hg^{2+} which

strongly suggests the high ion-selectivity of this material towards the detection of Hg^{2+} (Yin, Li, Liu, Yang, & Ren, 2011). The incorporation of these materials into zeolite seem to facilitate the detection and further removal of aqueous Hg(II).

Owing to the variable oxidation state and catalytic properties of transition metals (Greenwood & Earnshaw, 1997; J. D. Lee, 1996), transition metal oxides were also widely employed in aqueous Hg(II) immobilization. Early studies involved the use of radiotracer technique in studying the removal of aqueous Hg(II) using hydrous zirconium oxide (ZrO_2) (Mishra, Singh, & Tiwari, 1996). The kinetic of the sorption process follows the first order rate law and obeys the Freundlich isotherm model. The uptake of Hg(II) was identified to increase with temperature elevation from 303 to 333K. In addition, the pre-irradiation of adsorbent with neutrons and γ-radiation has practically no effect on the extent of Hg(II) sorption. Sorption kinetic and sorption isotherm studies of aqueous Hg(II) onto zinc oxide (ZnO) nanoparticles at different temperature was also conducted by Sheela and her co-workers applying different kinetic and isotherm models (Sheela, Nayaka, Viswanatha, Basavanna, & Venkatesha, 2012). The sorption kinetic data were well fitted by the pseudo-second order rate model while the adsorption isotherms were well described by Langmuir isotherm model with high correlation coefficient (R^2). The adsorption capacity was also found to decrease with temperature elevation and the thermodynamic calculation suggested that the adsorption of Hg(II) onto ZnO is an exothermic process.

Batch radiotracer studies were again carried out by Misha et al. in removal of aqueous Hg(II) using well synthesized and characterized hydrous manganese oxide (HMO) and hydrous tin oxide (HTO) (Mishra, Dubey, & Tiwari, 2004). The results revealed that an increased in Hg(II) concentration, temperature as well as solution pH enhance the removal efficiency of both oxide materials. The sorption kinetic data collected were well fitted by the first order rate model while the adsorption isotherms were well described by Freundlich

isotherm model. Thermodynamic calculations indicated endothermic process has taken place. Furthermore, these materials are stable with the irradiation of neutrons and γ-radiation for up to 96 hours which ensure a greater applicability of these solids in waste management. In addition to pure manganese oxide, manganese oxide (MnO_2) supported on reduced graphene oxide (RGO), MnO_2-RGO composite was also developed for aqueous Hg(II) removal (Sreeprasad, Maliyekkal, Lisha, & Pradeep, 2011). The kinetic data was found to obey the Lagergren's pseudo-first order rate equation while the calculated distribution coefficient, K_d is greater than 10 L / g, suggesting they are excellent aqueous removal agent for Hg(II). On the other hand, the reacted MnO_2-RGO-Hg(II) samples were characterized using EDX, TEM and XPS. The results showed that the adsorbed mercury is more concentrated on MnO_2 rather than RGO, indicating the significant role of MnO_2 in improving the Hg(II) uptake capacity of RGO. Moreover, the adsorption of Hg(II) onto MnO_2-RGO also does not results in any change of oxidation state of manganese during the sorption process.

The removal of Hg(II) using iron oxide impregnated activated carbon (FeAC) and virgin activated carbon (AC) was studied by Reed et al. at different solution pH (Reed, Vaughan, & Jiang, 2000). From the studies, the removal of Hg(II) using FeAC increases with solution pH elevation. In addition, FeAC also demonstrates a slightly higher activity compared to AC. An improvement on iron oxide based sorbent for aqueous Hg(II) removal was achieved by Manju et al. by introducing carboxylate and polyacrylamide into hydrous iron(III) oxide system (PGHyFeO-COOH) (Manju, Anoop Krishnan, Vinod, & Anirudhan, 2002). From the studies, the sorption of Hg(II) onto the sorbent increased with solution pH elevation up to a certain limit but decreased again with further increase in solution pH. The sorption kinetic data collected were well fitted with first-order reversible and intraparticle diffusion rate equation while the adsorption isotherms were well described by Langmuir

sorption isotherm model with maximum sorption capacity at 30 °C reaching 155.01 mg Hg /g sorbent. The maximum sorption capacity was also found to increase with temperature elevation and the thermodynamic calculation suggested that the adsorption of Hg(II) onto PGHyFeO-COOH is an endothermic process. Experiments of competition among cations were also conducted by using PGHyFeO-COOH and the result showed that PGHyFeO-COOH has the highest affinity towards Pb(II), followed by Hg(II) and finally Cd(II).

Further understanding on the sorption of Hg(II) onto iron oxide sorbent system was carried out by Kim et al. using sophisticated studies of extended X-ray absorption fine structure (EXAFS) (C. S. Kim, et al., 2004). Hg(II) was found to adsorb onto Geothite (α-FeOOH) primarily as a bidentate sorption complex in a corner sharing arrangement to the $Fe(O,OH)_6$ octahedra. Undeniably, this studies have again proved the existence of interaction between aqueous Hg(II) and oxide surfaces. With respect to the affinity of sulfur towards mercury, Parham et al. have reported the use of Fe_3O_4 nano-particles modified with 2-mercaptobenzothiazole (MIOPs) in aqueous Hg(II) immobilization (Parham, Zargar, & Shiralipour, 2012). In the studies, MIOPS achieved better removal efficiency result compared to unmodified Fe_3O_4. MIOPS was also identified to follow Langmuir sorption isotherm with maximum sorption capacity achieving 590 μg Hg /g sorbent. It was also found that most of the investigated ions (SO_4^{2-}, NO_3^-, Cl^-, Ca^{2+}, Mg^{2+}, Ba^{2+}, and etc) do not interfere with the removal of Hg^{2+} from the water solutions, except for As^{3+} and Cu^{2+}, which strongly interfered during the removal process.

In another report, an intensive study was also conducted by Pan et al. to investigate the sorption mechanism of aqueous Hg(II) removal onto mercapto-functionalized Fe_3O_4 polymers (SH-Fe_3O_4-NMPs) (Pan, Zhang, Shen, & Hu, 2012). From the results, the adsorption process of Hg(II) onto SH-Fe_3O_4-NMPs was highly related to the content of Fe_3O_4 core in the sorbent in which the optimized amount is 5.88%. Kinetic studies showed

that SH-Fe_3O_4-NMPs followed pseudo-second order model, suggesting chemisorptions process. Meanwhile, the adsorption processes also fitted well with the Langmuir isotherms with the maximum sorption capacities reaching 256.4 mg Hg / g sorbent. Thermodynamic evaluation indicated that the adsorption of Hg(II) onto SH-Fe_3O_4-NMPs is an endothermic process. Furthermore, the reacted SH-Fe_3O_4-NMPs-Hg(II) samples were also characterized using PXRD and XPS. The outcomes showed that Hg(II) ions have successfully incorporated onto SH-Fe_3O_4-NMPs via coordination interactions. Moreover, Hg(II) might be also partially reduced to Hg_2Cl_2 through solid state reaction via charge transport on the surface of SH-Fe_3O_4-NMPs. The studies also showed that the effect of coexisting cations (Ca^{2+}, Mg^{2+}, Na^{+}, and Cu^{2+}) on the adsorption of Hg(II) was insignificant onto SH-Fe_3O_4-NMPs since these ions have less affinity towards –SH group based on Hard-Soft Acid-Base (HSAB) theory as compared to Hg(II).

The final transition metal oxide discussed for aqueous Hg(II) sequestration is related to titanium dioxide, TiO_2. In comparison to other transition metal oxide studied in the literature, TiO_2 is well known for its photocatalytic ability in the presence of sunlight, resulting in that reduction of Hg(II) to metallic Hg(0) and subsequently plating out onto TiO_2 particles. Early study of TiO_2 in aqueous Hg(II) removal is reported by Aguado et al. (M. A. Aguado, Cervera-March, & Giménez, 1995). The studies were conducted in a continuous system to investigate the kinetic and catalytic activity of TiO_2 in reducing aqueous Hg(II). The results showed that the conversion reaction is first order with respect to Hg(II) concentration and the deposited metallic mercury on TiO_2 can affect the rate of Hg(II) reduction. Lau and his co workers further carried out the experiments in high pH solutions (Lau, Rodriguez, Henery, Manuel, & Schwendiman, 1998). The results showed that more than 97 % of aqueous Hg(II) was deposited as mercury metal on the surface of TiO_2 at pH 9. Furthermore, Botta et al. studied the removal of different type of Hg(II) salt

i.e. $Hg(NO_3)_2$, $Hg(ClO_4)_2$ and $HgCl_2$ under the photocatalysis of TiO_2 in the presence and absence of oxygen (Botta, Rodríguez, Leyva, & Litter, 2002). The studies indicated that the $HgCl_2$ was best converted and reaction inhibition by oxygen was observed in acidic and neutral media but not at basic pH. Bussi et al. investigated the removal of Hg(II) by TiO_2 in chlor-alkali plant (Bussi, Ohanian, Vázquez, & Dalchiele, 2002). They revealed the process is effective but it can be inhibited by the presence of Ca(II) or Mg(II) ions.

In the studies performed by Dou et al., several research questions dealing with the synthesis and properties of different crystallographic form of TiO_2 (rutile, anatase and brookite) have been reviewed (Dou & Chen, 2011). The advantages of nanosized TiO_2 in Hg(II) removal over commercially available TiO_2, Degussa has been discussed. In addition, they have investigated TiO_2 nanoparticles with characteristic of average diameter of about 10 nm, a specific surface area of higher than 200 m^2 / g, and high purity of anatase crystal in aqueous Hg(II) removal. In the studies, the photocatalytic removal percentages of Hg(II) increased greatly with increasing solution pH values, and the removal percentage of Hg(II) by TiO_2 nanoparticles was more than 65% after 30 min. The kinetic data collected was well described using pseudo-first order rate equation. In another report, Lopez-Munoz et. al. have conducted an intensive Hg(II) removal study using TiO_2 under the influence of pH, addition of methanol, formic acid and oxalic acid as sacrificial additives (López-Muñoz, Aguado, Arencibia, & Pascual, 2011). The result showed that the overall process was strongly pH dependent which being enhanced as the pH was increased. At pH 10, an efficient removal of Hg(II) was achieved even in the absence of organic additives. In acidic conditions, the addition of sacrificial organic molecules notably increased the rate and extent of aqueous Hg(II) removal. More importantly, the nature and distribution of mercury products deposited on TiO_2 were also analyzed using PXRD and SEM. The resulted showed that Hg_2Cl_2 and Hg^0 were identified in both acidic and alkaline media in the

absence of additives. Nonetheless, the addition of organic additives enhanced the photocatalytic reduction to Hg^0 in which their role are not only as hole traps but also as source of strong reducing radicals.

2.2.3. Metal Sulfide

In the approach of using metal sulfide as aqueous mercury complexing agent, Phillips et al. have studied the reaction of cadmium sulfide (CdS) with Hg(II) using continuous operation technique (H. O. Phillips & Kraus, 1963). In the studies, the authors found that the sorption of Hg(II) onto CdS is primarily occurred through the displacement reaction where Cd^{2+} will be leached out concurrently. In addition, they observed a progressive color changed on the CdS powder in which a red colored HgS often formed first, slowly converted to the black sulfide to white colored powder at room temperature. In order to explain the observation, white colored double salt of $(HgS)_nHg(NO_3)_2$ is deduced to form at the end of the reaction. The formation of the double salt is mainly due to the reaction between HgS and $Hg(NO_3)_2$. In another studies, Park et al. investigated the chemical reaction between hydrous CdS with Cu(II) and Hg(II) by electrophoretic mobility and adsorption experiments (Park & Huang, 1989). The results showed that cation exchange, followed by re-adsorption of the released Cd(II) ions onto the freshly-formed CuS occurred during the reaction. Moreover, it was also found that EDTA ligand can greatly enhance the ion-exchange reaction.

In the studies by Hasany et al., the retention of Hg(II) by mercury sulfide (HgS) has been investigated in detail using batch operation mode at acidic condition (Hasany, Saeed, & Ahmed, 1999). Four different types of acid *i.e.* HNO_3, HCl, $HClO_4$ and H_2SO_4 were used but only HNO_3 shows slightly lower Hg(II) removal performance. The sorption behavior of Hg(II) onto HgS was also analyzed using different isotherm models. The result showed that the sorption data followed Langmuir isotherm over the entire Hg(II) concentration used

with maximum sorption capacity approaching 0.0017 μg Hg / g sorbent. Meanwhile, Freundlich and Dubinin-Radushkevich isotherms were only obeyed up to low and moderate Hg(II) concentrations. Thermodynamic calculation suggested that the adsorption of Hg(II) onto HgS is an endothermic process. More importantly, Cu(II), Ba(II), Zn(II), Ni(II) and Cr(III) were identified as potential competitive cations that can affect the performance of HgS in aqueous Hg(II) immobilization.

The adsorption of Hg(II) complexes onto lead, zinc and iron sulfide (PbS, ZnS, FeS_2 and $Fe_{1-x}S$) was studied by Jean et al. as a function of pH and nature of the ligands in solution using XPS (Jean & Bancroft, 1986). The adsorption of Hg(II) onto the sulfides are strongly pH dependent *i.e.* there is a critical pH at which the adsorption increases dramatically. The pH dependency is related to the hydrolysis of Hg(II) in which the hydrolyzed species adsorbed directly on sulfide group, probably as a monolayer. The results also suggest the presence of $HgCl_n^{2-n}$ species physisorbed on the adsorbed monolayer. In another studies, Hyland et al. has again examined the sorption of Hg(II) onto PbS, FeS_2 and $Fe_{1-x}S$ and its desorption using XPS as well as Auger electron spectroscopy (AES) (Hyland, et al., 1990). In the studies, detail investigation indicated that there are at least three different Hg(II) species present on the reacted sulfides surface. The most weakly bound species is related to $Hg_3S_2Cl_2$ and $HgCl_x$ which can be removed by $S_2O_3^{2-}$ containing solution. The most stable mercury species is associated to HgS which can only be removed by CN^- containing solution. Both of these reports are acting as the important prove of the existence of different Hg(II) species on sulfide surface.

Among the metal sulfide studied for aqueous Hg(II) removal, iron sulfide is the most investigated in the literature. Beside the two reports mentioned above, Bowel et al. have investigated the immobilization of Hg(II) by pyrite (FeS_2) using X-ray absorption Spectroscopy (XAS) (Bower, et al., 2008). In the studies, they revealed that the batch

sorption of Hg(II) onto FeS_2 increases with both pH and time. XAS analysis showed that a transformation in the coordination environment at low pH occurred during aging over 2 weeks, to form an order monolayer of mono-dentate HgCl complexes on FeS_2. Moreover, the transport of Hg(II) was also tested on a thin FeS_2 column packed with pure quartz sand. The result showed that dissolved oxygen can inhibit Hg(II) sorption onto FeS_2 but it is only in a very minute manner. Jeong at al. have examined the sorption of Hg(II) onto synthetic nanocrystalline disordered mackinawite (FeS) as a function of initial Hg(II) concentration, initial FeS concentration, chloride concentration and pH (Jeong, Klaue, Blum, & Hayes, 2007). In the studies, the authors found that adsorption is mainly responsible for Hg(II) removal when molar ratio of Hg(II)/FeS is as low as 0.05. As the molar ratio increases, the adsorption capacity becomes saturated, resulting in ion-exchange product, metacinnabar, β-HgS (identified from PXRD) being precipitated from the solution. Concurrent with HgS precipitation, the released Fe(II) from FeS was readsorbed by adsorption at acidic pH and either adsorption or precipitation as Fe (hydr)-oxides at neutral to basic pH. In another studies, Liu at al. also studied the sorption of Hg(II) onto FeS (J. Liu, et al., 2008). In the studies, they found that aeration of reacted FeS did not cause significant release of Hg(II) into the water. Furthermore, PXRD analysis showed that the major products formed are metacinnabar, cinnabar and mercury iron sulfides.

In addition to the pure single metal sulfide systems, mixed sulfides system *i.e.* zinc and tin sulfide chalcogel was also prepared by Oh et al. for aqueous Hg(II) removal (Oh, Bag, Malliakas, & Kanatzidis, 2011). Owing to the high surface area of the synthesized material (363 – 520 m^2 /g), the maximum sorption capacity of zinc and tin sulfide chalcogel in removing Hg(II) was found to as high as 280.83 – 339.00 mg Hg / g of sorbent. This showed a remarkably high sorption capacity that can be hardly achieved by other sorbent systems. Furthermore, lithium-intercalated transition metal sulfide, Li_xES_2 ($0.25 \leq x \leq 1.9$;

E = Mo, W, Ti, Ta) as redox-recycable ion-exchange materials was successfully developed by Gash et al. for aqueous Hg(II) sequestration (Gash, et al., 1998). For Li_xTiS_2 and Li_xTaS_2, hydrolysis of these materials produced S^{2-} ions that can precipitate HgS from solution. In contrast, the materials of Li_xMoS_2 and Li_xWS_2 did not undergo hydrolysis to form S^{2-} ions. Instead, ion-exchanged material such as $Hg_{0.50}MoS_2$ was isolated from the Hg(II) removal reaction. When Hg_yMoS_2 was heated under vacuum at 425 °C, an entropy-driven internal redox reaction resulted in deactivation of the extractant, producing essentially mercury-free MoS_2 and a near-quantitative amount of mercury vapor (collected in a cold trap). Moreover, the decontaminated MoS_2 could be reactivated back to Li_xMoS_2 with n-butyl lithium and reused further in aqueous Hg(II) extraction.

2.2.4. Copper Sulfide

In the studies by Martellaro et al., Cu_2S has been used in removing Hg(II) in water aqueous system (Martellaro, Moore, Peterson, Abbott, & Gorenbain, 2001). The results showed that the quantity of Hg^{2+} removed from solution corresponds directly with the quantity of Cu_2S dissolved. This suggests that the Hg(II) are removed through precipitation with dissolved sulfide ion from metal sulfide. This also indicates that in acidic solutions there is no physical or chemical adsorption of Hg^{2+} onto Cu_2S. In another studies of Moore et al., CuS was also tried to remove Hg(II) in aqueous water system under batch equilibration mode (Moore, Martellaro, & Peterson, 2000). The results showed that cinnabar, HgS does not appear to be forming and mercuric ion is not removed by precipitation. No reaction mechanism is deduced for CuS to remove Hg(II) from aqueous water solution.

Hg(II) adsorption onto CuS has been deeply described by Phillips et al. (Harold O. Phillips & Kraus, 1965). Continuous column chromatographic technique has been applied to investigate the sorption of Hg^{2+} and Ag^{+} onto CuS in 0.0002M nitric acid medium. Their

studies showed that both Hg(II) and Ag(I) adsorb onto CuS via ion-exchange displace reaction and their selectivity is related primarily to the solubility of sulfides formed and being displaced (K_{sp}). In the studies of adsorption of Hg(II) onto CuS, formation of white colored double salt, $2Hg_2S \cdot Hg(NO_3)_2$ is expected in addition to the mercury sulfide formed. The formation of the double salt is mainly due to the adsorption of $Hg(NO_3)_2$ onto the HgS or Hg_2S formed during the reactions. Besides, crystallite size of the reacted CuS powder also decreased after the adsorption experiment. This provides the proof of surface adsorption phenomenon of Hg(II) onto CuS instead of bulk diffusion reaction.

Competitive adsorption of Hg(II) and other radioactive tracer metal ions such as Cu(II) onto CuS have been studied in strongly acidic media (HCl, $HClO_4$, and H_2SO_4) under both batch and continuous operation mode (C.-C. Wu & Yang, 1976). For Hg(II), the adsorption capacity of CuS decreases in strongly acidic HCl media regardless of the experiments. For Cu(II), 100% removal efficiency was achieved in column chromatography experiments while it decreases in batch experiments. Nonetheless, the authors have tried to explain these observations by increased solubility of different sulfide formed. A stronger interaction of copper sulfides with chloride ions is also expected in disturbing the Hg(II) adsorption. In any case, Cu(II) seems not to be interfering on the Hg(II) adsorption where removal of Hg(II) performs well even in the presence of large amount of Cu(II). Lastly, industrial applications of CuS/C and CuS/Al_2O_3 to remove Hg(II) in wastewater has been found in US patent: 5080799 (Yan, 1992). Dynamic flow system has been employed in the process and HgS is claimed to be formed during the reaction. Nevertheless, an interesting finding is that the reacted adsorbent can be successfully regenerated by heating the reacted powder in a stream of hot gases (flue gas, steam, and …etc) preferably at 300^0F or higher or by oxidative regeneration.

2.3. Considerations in Heterogeneous Aqueous Mercury Complexation

2.3.1. Batch Sorption Processes

From the literature review above, it can be summarized that in most batch sorption processes, the sorbent is contacted with the solution in a reactor for a period of time at fixed operation conditions. The duration required to approach a specific time or equilibrium depends on the physical properties of sorbent, the nature of sorbent applied, concentration of sorbate, the dose of sorbent, the degree of agitation, solution temperature and pH. For batch operations, the physical properties of sorbent *i.e.* smaller particle size can offer a higher surface area and result in faster reaction. The nature of the sorbent such as containing very active material towards targeted sorbate can led to better interaction and stable sorbate-sorbent formation. In most cases, the sorbent is usually applied in powdered form to increase the surface area and reduce the diffusion resistance inside the pores. Agitation of the suspension improves contact of sorbent with solution and decreases the mass transfer resistance at the surface. Solution pH plays a very important role in governing the chemical state of metal ions in the solution as well as the surface functional group present on the sorbent. Higher pH values of the solution improve ion-exchange in the system provided that adsorption is largely by ion-exchange reactions rather than complexing (Ho, 1995). Exothermic reaction can be enhanced by decreasing the reaction temperature while endothermic reaction can be improved at higher temperature of reaction. Upon the reaction, the sorbent is separated from the mixture solution by settling, filtration or centrifugation. The solution samples can be analyzed for remaining sorbate concentration for sorption kinetic and sorption isotherm establishment. Meanwhile, the solid samples can be characterized using solid analytical techniques for reaction mechanism investigation.

2.3.2. Sorption Kinetic

The overall process for adsorbing metal ions onto the active sites of the sorbent can be divided into 3 stages: (1) Mass transfer of metal ion from bulk solution through an artificial film to the external surface of adsorbent; (2) Diffusion of metal ion from the pore mouth to the immediate vicinity of active site of internal pore surface; (3) Adsorption of metal ion onto the active sites of the internal pore surface (Fogler, 1999). The overall rate of the adsorption is equal to the slowest step (rate-determining step) where it can be any single step or the combination of any 3 steps. Adsorption at a site on the surface (internal or external) will involve energy and the energy will depend on the binding process (physical or chemical). In this study, three different kinetic models have been selected to investigate the kinetics of adsorption of Hg(II) onto CuS surface.

Elovich Kinetic Model

Elovich's kinetic model or the Elovich equation is the rate equation, proposed by Roginsky and Zeldovich in 1934 to describe the adsorption of carbon monoxide onto manganese dioxide (Roginsky & Zeldovich, 1934). This model is one of the most useful models for describing activated chemical adsorption where it takes into account of the chemical adsorption of adsorbate onto solid surface. The Elovich equation can be described as below:

$$\frac{dQ_t}{dt} = a\exp(-bQ_t) \qquad (2.1)$$

by applying the boundary conditions $Q_t = 0$ at $t = 0$ and $Q_t = Q_t$ at $t = t$, the equation becomes:

$$Q_t = \frac{1}{b}\ln(t + t_0) - \frac{1}{b}\ln(t_0) \qquad (2.2)$$

Due to its complexity, Chien et al. (Chien & Clayton, 1980) have simplied the equation by assuming $t_0 = 1/ab$, when $t >>> t_0$, $abt >> 1$, the equation becomes (Sparks, 1986):

$$Q_t = \frac{1}{b}\ln(ab) + \frac{1}{b}\ln(t + t_0) \quad (2.3)$$

with a is the initial sorption rate (mg/gmin), b is the desorption constant (g/mg) and t is the time (min) during any one experiment.

Pseudo First-order Kinetic Model

The pseudo first-order kinetic model was first presented by Lagergren in describing the adsorption of oxalic acid and malonic acids onto charcoal (Lagergren, 1898). This model considers the rate of sites occupation is proportional to the number of unoccupied sites. The pseudo-first order model of Lagergren is generally expressed as follows:

$$\frac{dQ_t}{dt} = k(Q_e - Q_t) \quad (2.4)$$

which after integration and applying boundary conditions t = 0 to t = t and $Q_t = 0$ and $Q_t = Q_t$, the equation becomes:

$$\ln(Q_e - Q_t) = \ln Q_e - kt \quad (2.5)$$

where k is the rate constant of pseudo-first order sorption (l/min) and Q_e is the amount of metal sorbed at equilibrium (mg of metal ion sorbed/g sorbent).

Pseudo Second-order Kinetic Model

The pseudo second-order kinetic model was first proposed by Blanchard et al. in describing the ion exchange reaction of heavy metal by natural zeolite (Blanchard, et al., 1984). The assumption behind this model is that the kinetic order of this reaction is two with respect to the number of adsorption site available for the exchange processes. The pseudo-second order model can be illustrated as:

$$\frac{dQ_t}{dt} = k(Q_e - Q_t)^2 \qquad (2.6)$$

After integrating the above equation with boundary conditions t = 0 to t = t and Q_t = 0 to Q_t = Q_t, the equation becomes (Ho, 1995):

$$Q_t = \frac{Q_e{}^2 kt}{1 + Q_e kt} \qquad (2.7)$$

which can be rearranged in the linear form as below:

$$\frac{t}{Q_t} = \frac{1}{k(Q_e)^2} + \frac{t}{Q_e} \qquad (2.8)$$

where k is the rate constant of pseudo-second order sorption (g/mgmin) and Q_e is the amount of metal sorbed at equilibrium (mg of metal ion sorbed/g sorbent).

2.3.3. Sorption Isotherm

Two important aspects for evaluation of sorption process as a unit of operation are the sorption equilibrium and sorption kinetic. Equilibrium studies in sorption processes (sorption equilibrium) access the performance or capability of the sorption systems *i.e.* capacity of the sorbent toward saturation by theoretical approach. The sorption equilibrium

usually described by an isotherm whose parameters express the surface properties and affinity of the sorbent at a fixed temperature at equilibrium. Sorption isotherm for a particular sorbent system can be obtained by batch reaction at various pH values, temperature and other parameters of the sorption processes. In order to investigate the sorption isotherms, two equilibrium isotherm models frequently applied to the sorption of metals from aqueous solution were fitted to the experimental results. These included the two-parameter isotherms the Langmuir and Freundlich sorption isotherm.

Langmuir Sorption Isotherm

Irving Langmuir, an American chemist, was born in Brooklyn, New York. In 1932, he was awarded the Nobel Prize in chemistry for "his discoveries and researches in the realm of surface chemistry". In the beginning of 1916, Langmuir developed a relationship between the amount of gas adsorbed on a surface and the pressure of that gas; such equations are now referred to as Langmuir adsorption isotherms; a theoretical adsorption isotherm in the ideal case. This model is adopted later for the solid-liquid sorption systems. The Langmuir adsorption isotherm is based on the assumptions that: (i) adsorption proceeds only until a single adsorption layer is formed (a monolayer); (ii) adsorbed molecule are not free to move on the surface; (iii) the enthalpy of adsorption for each molecule is the same (Langmuir, 1916, 1917, 1918). By combining the rate of adsorption and desorption of solutes from the sorbent surface, the Langmuir rate equation becomes:

$$\frac{d\theta}{dt} = k_a C(1-\theta) - k_d \theta \qquad (2.9)$$

where k_a and k_d are adsorption and desorption rate constant respectively. C is concentration in solution and θ is the fractional coverage on surface adsorption sites. At equilibrium, the net rate will approach zero, and

$$K_a = \frac{k_a}{k_d} \tag{2.10}$$

Since Q_t is proportional to θ:

$$\theta = \frac{Q_t}{Q_e} \tag{2.11}$$

The saturated monolayer Langmuir isotherm can be represented:

$$Q_e = \frac{Q_{max} K_a C_e}{1 + K_a C_e} \tag{2.12}$$

The above equation can be rearranged to the following linear form:

$$\frac{C_e}{Q_e} = \frac{1}{K_a Q_{max}} + \frac{1}{Q_{max}}(C_e) \tag{2.13}$$

where C_e is the equilibrium concentration (mg/l); Q_e is the amount of metal ion sorbed at equilibrium or equilibrium sorption capacity (mg of metal ion sorbed/g sorbent); Q_{max} is the maximum complete monolayer sorption capacity (mg of metal ion sorbed/g sorbent); K_a is the equilibrium sorption constant (l/mg). A plot of C_e/Q_e vs C_e should give a straight line plot with slope of $1/Q_{max}$ and intercept of $1/K_aQ_{max}$.

Freundlich Sorption Isotherm

Herbert Max Finlay Freundlich, who was a German physical chemist, in 1906, presented an empirical adsorption isotherm that can be used for non ideal systems. The Freundlich isotherm is the earliest known relationship describing the adsorption and it was developed when Freundlich studied the sorption of a type of sorbate onto animal charcoal in 1906 (Freundlich, 1906). This fairly satisfactory empirical isotherm can be used for non ideal multilayer adsorption and is expressed by the following equation:

$$Q_e = K_F C_e^{1/n} \tag{2.14}$$

This equation is easily linearized to the form:

$$\ln Q_e = \ln K_F + \frac{1}{n} \ln C_e \tag{2.15}$$

where C_e is the equilibrium concentration (mg/l); Q_e is the equilibrium sorption capacity (mg of metal ion sorbed/g sorbent); K_F and n are Freundlich constants. The constant (n) gives an indication of the favourability and k the capacity of the sorbent. The Freundlich equation is most useful for dilute solutions over small concentration ranges.

CHAPTER 3

RESEARCH METHODOLOGY

This chapter is divided into four sections. The first section gives the details on the raw materials and chemicals employed in the studies. The second and third section provides the investigations and experimental procedure involved in homogeneneous and heterogeneous aqueous mercury complexation respectively. Finally, the last section is concluded by the brief description on the characterization techniques used in the analysis.

3.1. Raw Materials and Chemicals Selection

The raw materials and chemicals used in homogenenous aqueous mercury complexation are Rhodamine B chloride, potassium iodide, sulfuric acid, dichloromethane, benzene, and polyvinylalcohol. The raw materials and chemicals used in the synthesis of Covellite (CuS) and heterogeneous aqueous mercury complexation are copper nitrate pentasemihydrate, sodium tiosulfate pentahydrate, silica gel, nitric acid, sodium hydroxide, mercuric chloride, stannous chloride and purified nitrogen gas. For illustration purpose, the list of raw materials, chemicals, gas used as well as its related information are displayed in **Table 3.1**.

Table 3.1. List of raw materials, chemicals and gas used in the studies of homgoenenous and heterogeneous aqueous mercury complexation.

Materials/ Chemicals/ Gas	Brand	Specifications
Rhodamine B	Merck	Chemical Formula: $C_{28}H_{31}ClN_2O_3$ Molar Mass = 479.02 g/mol Purity = For microscopy
Potassium Iodide	Merck	Chemical Formula: KI Molar Mass = 166.00 g/mol Purity = EMSURE® grade

Sulfuric Acid	Merck	Chemical Formula: H_2SO_4 Molar Mass = 98.08 g/mol Purity = EMSURE® grade
Dichloromethane	Merck	Chemical Formula: CH_2Cl_2 Molar Mass = 84.93 g/mol Purity = EMSURE® grade
Benzene	Merck	Chemical Formula: C_6H_6 Molar Mass = 78.11 g/mol Purity = EMSURE® grade
Polyvinylalchohol	Merck	Chemical Formula: $(C_2H_4O)_n$ Molecular Weight ≈ 15000 Purity = For synthesis
Copper nitrate pentasemihydrate	Riedel de Häen	Chemical Formula: $Cu(NO_3)_2.2.5H_2O$ Molar Mass = 232.59 g/mol Purity = 98.00 %
Sodium thiosulfate pentahydrate	Merck	Chemical Formula: $Na_2S_2O_3.5H_2O$ Molar Mass = 242.81 g/mol Purity = 99.50 %
Silica gel	Bendosen	Commercial Grade
Nitric acid	Merck	Chemical Formula: HNO_3 Molar Mass = 63.01 g/mol Purity ≥ 65.00 %
Sodium hydroxide	Merck	Chemical Formula: $Na_2S_2O_3.5H_2O$ Molar Mass = 40.00 g/mol Purity ≥ 99.00 %
Mercuric chloride	Merck	Chemical Formula: $HgCl_2$ Molar Mass = 271.50 g/mol Purity ≥ 99.50 %
Stannous chloride dihydrate	Merck	Chemical Formula: $SnCl_2.2H_2O$ Molar Mass = 225.63 g/mol Purity = Max. 0.000001% Hg
Purified nitrogen gas	MOX	Chemical Formula: N_2 Molar Mass = 28.02 g/mol Purity = 99.99 %

3.2. Homogeneous Aqueous Mercury Complexation

3.2.1. Mercury-Rhodamine B complex in Organic Solvent

20 mL of $HgCl_2$ solution containing not more than 25 μg of Hg(II) was pipette into a separating funnel. 1 mL of 10.8 M H_2SO_4, followed by 1 mL of 0.15 M KI was added into the solution and shaken vigorously for 1 min. After that, 1 ml of 5×10^{-3} M of Rhodamine B was added and again shaken vigorously for 1 min. The resulting red-violet solution was then extracted with 10 mL of benzene or dichoromethane for 3 mins. Allowing the phases to separate, the absorbance of the benzene / dichloromethane extracted layer was measured with UV-Visible spectrophotometer against the solvent at 565 nm and 556 nm respectively.

3.2.2. Mercury-Rhodamine B complex in Water

An aliquot of solution (10 mL) containing not more than 120 μg of Hg(II) was transferred to a 25 mL volumetric flask. 1 ml of 10.8 M H_2SO_4, followed by 1 mL of 0.15 M KI was added into the solution. After shaken for 1 min, the mixture was added with 1 ml of 5×10^{-4} M of Rhodamine B. Finally, the mixture solution was added with 5 mL of 1% PVAl solution, diluting to calibration mark and left it to stabilize for 10 mins. The absorbance of this solution was measured with UV-Vis spectrophotometer against water at 590 nm. For the pH dependency study, the pH of the final stabilized Hg(II) containing solution was then adjusted using pH probe (Rondolino DL 50, DG-114, Mettler Toledo) by employing H_2SO_4 and NaOH solutions. The absorbance of the solution was again measured with UV-Visible spectrophotometer against water at 590 nm.

3.2.3. Assessment of Rhodamine B in Mercury Determination

For this study, 0.1 g of Covellite powder was added into 100 mL of 100 ppm $HgCl_2$ solution under constant stirring of magnetic stirrer. Sampling was performed each hour for

the duration of 4 hours. After that, each sample collected was analyzed with UV-Visible spectrophotometer using the benzene extracted mercury-Rhodamine B complex method (**Section 3.2.1**) and mercury analyzer *i.e.* cold vapor atomic absorption spectrometry.

3.3. Heterogeneous Aqueous Mercury Complexation

3.3.1. Preparation of Pure and Mixed Phase Covellite

In this study, phase pure Covellite (CuS) powder was prepared via hydrothermal route by using the rotating furnace (custom made by ITQ, Spain). All reagents used in this study are of analytical grade, obtained from commercial market and were used without further purification. In the procedure, CuS was synthesized by reacting 0.025 mol of copper nitrate with 0.05 mol of sodium thiosulphate (Cu^{2+}: $S_2O_3^{2-}$ mole ratio = 1: 2.0) in 40.00 ml deionized water. The solutions were mixed thoroughly under constant stirring for 15 minutes; homogeneous slurry was formed, which was then transferred into a sealed 100 ml Teflon-lined stainless steel tube and put into a custom-made rotating furnace. The rotating furnace was maintained at 155.0°C for 12 hours. To measure the synthesis temperature during the reaction, a thermocouple was placed inside the furnace every hour through an injection port without opening the furnace. After 12 hours, the Teflon-lined stainless steel tube was allowed to cool down naturally at ambient temperature. The obtained product was washed with batches of deionized water until the final filtrate showed conductivity of less than 10 μS/cm. The collected product was then dried overnight at ambient temperature in a vacuum desiccator which consists of silica gels as drying agent. After that, the dried phase pure Covellite (CuS) powder was purged with purified nitrogen gas for 3 minutes prior storage to prevent the oxidation of the sample. On the other hand, the heavily oxidized, mixed phase Covellite, was prepared by storing the dried phase pure Covellite (CuS) powder in ambient environment for 12 weeks without any protective shield to allow the

transformation of single phase CuS to mixed phase of CuS and $CuSO_4$. The resulting products from the procedures above were subjected to different solid characterization tools *i.e.* PXRD, FESEM-EDX, XPS as well as HRTEM techniques to determine their physical and chemical properties.

3.3.2. Mercury Uptake Studies

5000 ppm of $HgCl_2$ stock solution was prepared with 5.000 g of $HgCl_2$ in 1 ml of concentrated HNO_3 and deionized water using a 1.00 L volumetric flask. The working solutions were prepared by diluting the stock solution with deionized water. After that, 100 mL of predetermined concentration of $HgCl_2$ was added into different conical flasks using pipette. The pH of the solution was adjusted using pH probe (Rondolino DL 50, DG-114, Mettler Toledo) by employing HNO_3 and NaOH solutions. Next, the well-adjusted solutions were purged with purified nitrogen gas for 3 minutes to drive off any dissolved O_2 or CO_2. Then, 0.100 g of the synthesized phase pure CuS powder was weighted and added into the conical flasks. The conical flasks were sealed with parafilm and put into a temperature controlled orbital shaker (OLS200, Grant) under constant stirring at 155 rpm for 15 hours. After 15 hours, the conical flasks were removed from the shaker and the solution in the conical flasks was filtered with filter paper (125 mm, Advantec). The filtrate was kept in a dark bottle for further concentration determination. For the mercury oxide precipitation studies, the experiments were performed based on the procedure described above. Nonetheless, the experiments were conducted without the addition of Covellite powder into Hg(II) solution. The concentration of Hg^{2+} was measured with mercury analyzer *i.e.* cold vapor atomic absorption spectrometry. The mercury uptake or recovery (%) was calculated based on the equation:

$$\text{Mercury Removal or Recovery}(\%) = \frac{C_0 - C_e}{C_0} \times 100 \qquad (3.1)$$

where C_0 and C_e are the initial and final Hg(II) concentrations (ppm or mg/L) respectively. The reaction parameters varied in the studies of mercury oxide precipitation, heterogeneous aqueous mercury complexation with mixed phase and pure phase Covellite are shown in **Table 3.2 – 3.4** respectively. The resulting reacted solid samples from the procedures above were subjected to different solid characterization tools *i.e.* PXRD, FESEM-EDX, XPS as well as HRTEM techniques to determine their physical and chemical changes.

Table 3.2. The reaction parameters varied in the studies of mercury oxide precipitation.

Solution pH	Solution Temperature (°C)	Mercury Concentration (ppm)
1, 4, 7 & 9	25.0	300
		400
		800
	45.0	300
		400
		800

Table 3.3. The reaction parameters varied in the studies of heterogeneous aqueous mercury complexation with mixed phase Covellite.

Solution pH	Solution Temperature (°C)	Mercury Concentration (ppm)
1 – 9	25.0	100
		250

Table 3.4. The reaction parameters varied in the studies of heterogeneous aqueous mercury complexation with pure phase Covellite.

Solution pH	Solution Temperature (°C)	Mercury Concentration (ppm)
1 – 9	25.0	50
		150
		250
		600
	35.0	250
	45.0	250

3.3.3. Copper Leached Studies

Studies were conducted according to the experimental procedure shown **Section 3.3.2**. For the studies of dissolution of Covellite, experiments were performed in the absence of Hg(II) in which only pH adjusted deionized water was used. The concentration of Cu^{2+} was measured with atomic absorption spectrometry. The copper leached (%) was then calculated according to the equation:

$$\text{Copper Leached (\%)} = \frac{C_{0,Cu} - C_{e,Cu}}{C_{0,Cu}} \text{ x } 100 \qquad (3.2)$$

where $C_{0,Cu}$ and $C_{e,Cu}$ are the initial and final Cu(II) concentrations (ppm or mg/L) respectively. The $C_{0,Cu}$ is calculated based on the total dissolution of CuS. The reaction parameters varied in the studies of dissolution of Covellite (CuS) and heterogeneous aqueous mercury complexation with pure phase Covellite are shown in **Table 3.5** and **Table 3.6** respectively.

Table 3.5. The reaction parameters varied in the studies of dissolution of Covellite.

Solution pH	Amount of Covellite used (g)	Solution Temperature (°C)
1 – 9	0.1	25.0
		35.0
		45.0

Table 3.6. The reaction parameters varied in the studies of heterogeneous aqueous mercury complexation with pure phase Covellite.

Solution pH	Solution Temperature (°C)	Mercury Concentration (ppm)
1 – 9	25.0	50
		150
		250
		600
	35.0	250
	45.0	250

3.3.4. Solution pH Changes Studies

Studies were conducted according to the experimental procedure shown **Section 3.3.2**. For the controlled studies *i.e.* the examination on the ability of Covellite in alternating the final solution pH, experiments were performed in the absence of Hg(II) in which only pH adjusted deionized water was used. The final solution pH resulted was measured using pH probe (Rondolino DL 50, DG-114, Mettler Toledo). The reaction parameters varied in the controlled studies and heterogeneous aqueous mercury complexation with pure phase Covellite are shown in **Table 3.7** and **Table 3.8** respectively.

Table 3.7. The reaction parameters varied in the controlled studies *i.e.* the examination on the ability of Covellite in alternating the final solution pH.

Solution pH	Amount of Covellite used (g)	Solution Temperature (°C)
1 – 9	0.1	25.0
		35.0
		45.0

Table 3.8. The reaction parameters varied in the studies of heterogeneous aqueous mercury complexation with pure phase Covellite.

Solution pH	Solution Temperature (°C)	Mercury Concentration (ppm)
1 – 9	25.0	50
		150
		250
		600
	35.0	250
	45.0	250

3.3.5. Effect of Contact Time and Sorption Kinetic Studies

Studies were performed according to the experimental procedure shown in **Section 3.3.2**. However, instead of allowing the reaction to achieve the equilibration, 3 ml of the Hg(II) solution was collected and filtered with filter membrane (Whatman, 0.2μm) at selected time interval. Then, the concentration of Hg^{2+} in the sample was again measured with mercury analyzer *i.e.* cold vapor atomic absorption spectrometry. The amount of Hg(II) adsorbed (sorption capacity) at time t, Q_t (mg/g) was calculated from the mass balance equation below:

$$Q_t = \frac{(C_0 - C_t)V}{m} \quad (3.3)$$

where C_0 and Ct are the initial and Hg(II) concentrations at time t (ppm or mg/L) respectively. The reaction parameters varied in the heterogeneous aqueous mercury complexation with mixed and pure phase Covellite are shown in **Table 3.9** and **Table** 3.10 respectively. The results collected were analyzed with Elovich's kinetic model, Lagergren's pseudo first order and Ho's pseudo second order kinetic model.

Table 3.9. The reaction parameters varied in the studies of heterogeneous aqueous mercury complexation with mixed phase Covellite.

Solution pH	Solution Temperature (°C)	Mercury Concentration (ppm)
4	25.0	100
		250
		400
		800

Table 3.10. The reaction parameters varied in the studies of heterogeneous aqueous mercury complexation with pure phase Covellite.

Solution pH	Solution Temperature (°C)	Mercury Concentration (ppm)
1	25	50
		150
		250
	35	250
	45	250

9	25	50
		150
		250
	35	250
	45	250

3.3.6. Sorption Isotherm Studies

Studies were again performed according to the experimental procedure shown in **Section 3.3.2**. The concentration of Hg^{2+} in the sample was again measured with mercury analyzer *i.e.* cold vapor atomic absorption spectrometry. The amount of Hg(II) adsorbed (sorption capacity) at equilibrium, Q_e (mg/g) was calculated from the mass balance equation below:

$$Q_e = \frac{(C_0 - C_e)V}{m} \qquad (3.4)$$

where C_0 and C_e are the initial and final Hg(II) concentrations (ppm or mg/L) respectively, V is the volume of solution used (L) and m is the mass of sorbent (g) used. The reaction parameters varied in the heterogeneous aqueous mercury complexation with mixed and pure phase Covellite are shown in **Table 3.11** and **Table 3.12** respectively. The results obtained were analyzed with Freundlich and Langmuir isotherm.

Table 3.11. The reaction parameters varied in the studies of heterogeneous aqueous mercury complexation with mixed phase Covellite.

Solution pH	Solution Temperature (°C)	Mercury Concentration (ppm)
4	25.0	100 – 1200

Table 3.12. The reaction parameters varied in the studies of heterogeneous aqueous mercury complexation with pure phase Covellite.

Solution pH	Solution Temperature (°C)	Mercury Concentration (ppm)
1	25.0	100 – 500
	35.0	
	45.0	

3.4. Analytical and Characterization Techniques

3.4.1. Ultraviolet-Visible Spectroscopy (UV-Vis)

UV-Visible spectroscopy or UV-Visible spectrophotometry is commonly regarded as an absorption technique which measures the absorption of UV and visible radiation as it passes through a sample substance. Both of the UV and visible light are part of the electromagnetic radiation as illustrated in **Figure 3.1** where the UV and visible light source is ranged in the wavelength of 200 – 380 nm and 380 – 780 nm respectively. The absorption of UV and visible radiation by the analyzed sample substance generates a UV-Vis spectrum which also called an electronic spectrum. The spectrum is the result from changes in the energy states of electron (σ, π, free electron pairs, orbital splitting) in a molecule or metal. The changes depend on the probability of electronic transitions between the individual energy states of the molecule or metal. The spectral parameters in the UV-Vis spectra like number of absorption bands, their wavelength of absorption and shapes provides the important information for qualitative possible compound identification. Meanwhile, the maximum intensities of absorption bands at different wavelength of absorption will form the basis for compound concentration quantification (Marczenko & Balcerzak, 2000; Sommer, 1989).

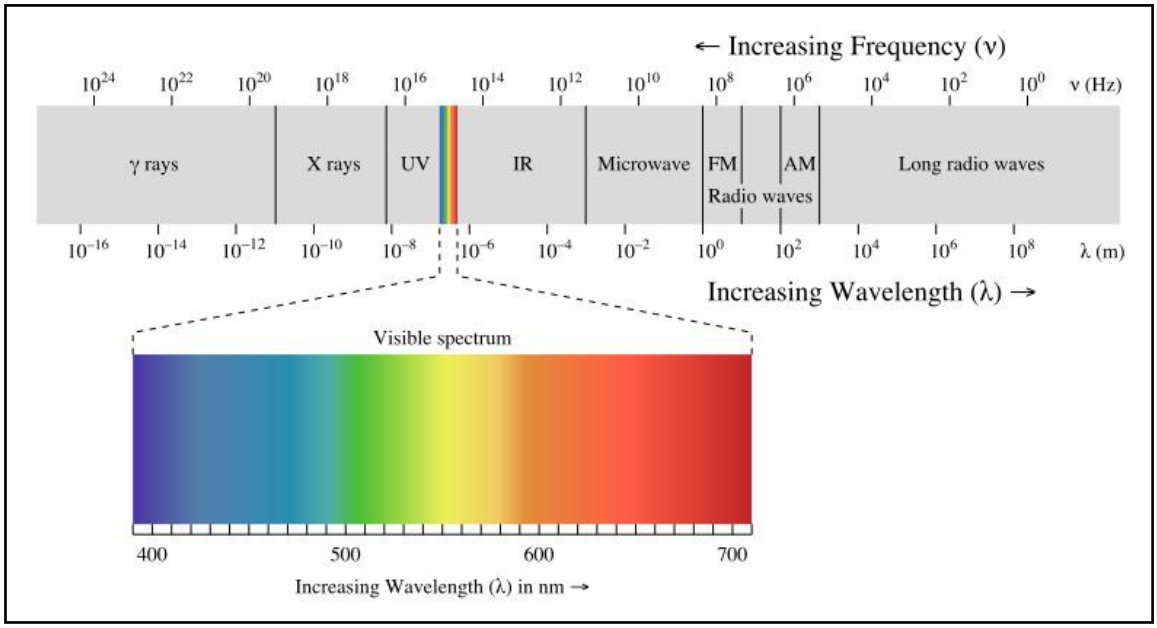

Figure 3.1. Spectrum of electromagnetic radiation (Wikipedia, 2014).

In general, the spectrophotometric measurement are mostly conducted in the form of solutions, either in water or organic solvents, contained in a measuring cell, cuvette which is placed in the path of a beam of monochromatic radiation of chosen wavelength. The incident beam intensity, I_0 from the light source is actually a form of relationship which can be described by the following equation:

$$\log \frac{I_0}{I_t} = A \qquad (3.5)$$

where I_t, and A are the intensity that transmitted and absorbed by the sample substance in the cuvette respectively. On the other hand, the amount of radiation also depends on the thickness of the absorbing layer, *l* and on the concentration of the solution, c (Buijs & Maurice, 1969; Lothian, 1963). If the concentration of the absorbing substance is doubled and the absorbing layer thickness is reduced by a factor of two, then the total number of absorbing species remains the same, hence the absorbance, A will also remain the same.

Therefore, the absorbance is a function of the number of absorbing centre in the light-beam, *i.e.* of the product of c*l*, and the above equation can be given the form:

$$\log \frac{I_0}{I_t} = A = \varepsilon c l \qquad (3.6)$$

where ε is a new unitless constant called the molar absorptivity or absorption coefficient, c is the concentration of absorbing species (mol/L) and *l* is the layer thickness or cuvette path length (cm). The expression described above is the fundamental law of spectrophotometry, the Beer Lambert law (Beer, 1852). In spectrophotometrc measurement, the thickness or cuvette path length of the sample and reference solution is usually identical. Thus, it is apparent that Beer's law relates the absorbance of the absorbing species with its respective concentration. If a sample substance obeys Beer's law, the graph of A = *f*(c) will give a straight line plot which provide significant information of the absorbing species concentration.

UV-Visible spectroscopy was employed in the studies of homogeneous aqueous mercury complexation using iodide and Rhodamine B. The absorbance measurement of Rhodamine B, Rhodamine B-Hg(II)-Iodide complex in dichloromethane, benzene and polyvinylalcohol-water system were performed using a double beam spectrophotometer (Lambda 35, Perkin-Elmer) as depicted in **Figure 3.2**. The broad scan of the UV-Vis spectrum was measured in the region of 400 – 700 nm with slit width = 1 nm and scan rate = 240 nm/min. In addition, the analysis was also performed using a single wavelength mode at 565 nm and 590 nm under the same condition as stated above in order to measure the absorbance of different amount of Rhodamine B-Hg(II)-Iodide complex in benzene and polyvinylalcohol stabilized water system.

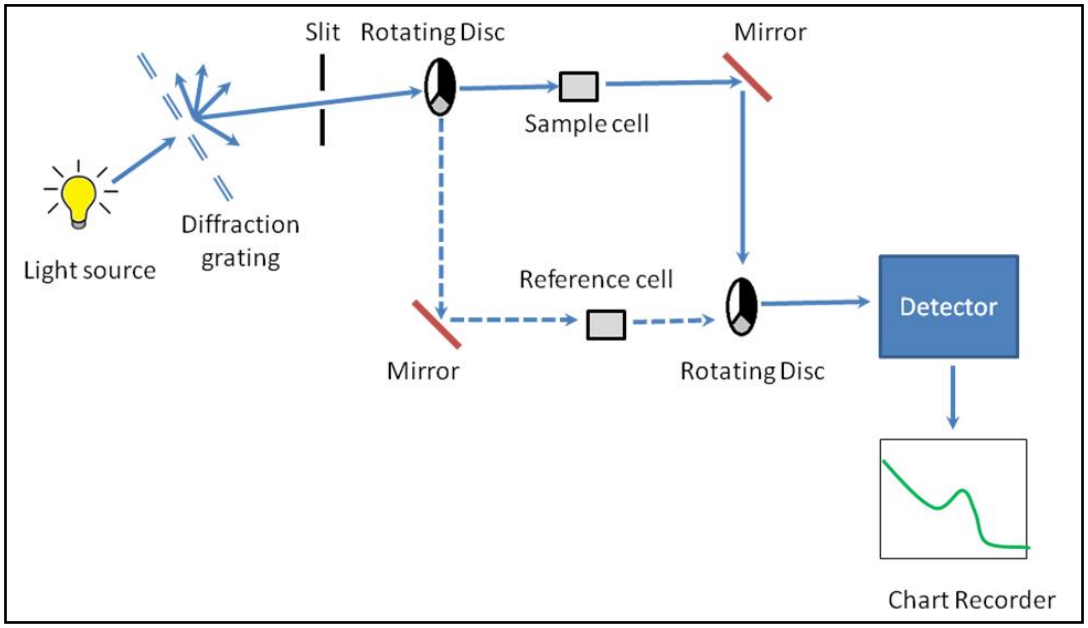

Figure 3.2. Schematic of double beam UV-Vis spectrophotometer (Gullapalli & Barron, 2010).

3.4.2. Atomic Absorption Spectrometry (AAS)

Atomic absorption spectrometry is an analytical technique for qualitative and quantitative assessment of chemical elements. The ultimate principle of atomic absorption spectrometry is in actual fact similar to the UV-Vis spectrophotometry in which it also makes use of the absorption of light by the sample analyte. Nevertheless, the absorbance measurement of the chemical element is carried out in its gaseous elemental state and normally only one single wavelength analysis can be performed for a specific element during the measurement. AAS have been widely employed in determining the concentration of a particular metal element within a sample. Up to date, AAS can be used to analyze the concentration of over 62 different metals in a solution. In a typical procedure, AAS utilized a flame to atomize the liquid sample into its gaseous elemental state prior to the absorbance measurement by wavelength specific spectrophotometer (**Figure 3.3**). Two different types of fuel mixture can be used in the atomization *i.e.* the air-acetylene (air-C_2H_2) which gives temperature of 2300 °C and nitrous oxide-acetylene (N_2O-C_2H_2) which provide temperature of 2700 °C.

The latter fuel mixture system offers a more reducing environment and it is ideally suited for analytes with high affinity to oxygen.

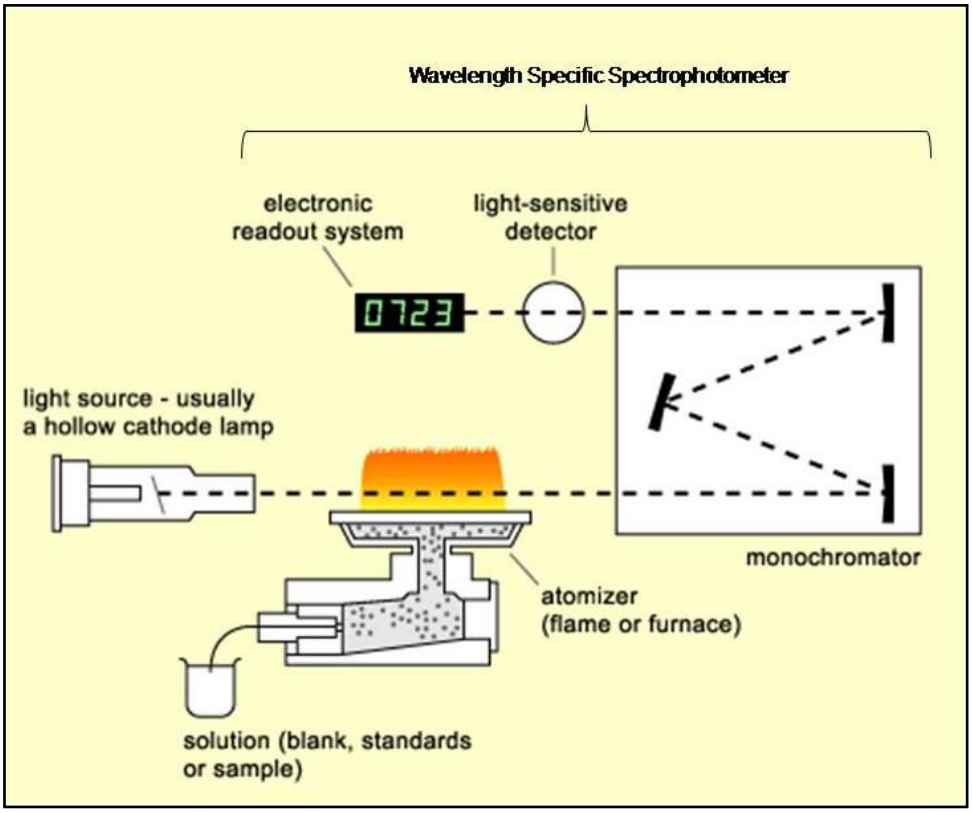

Figure 3.3. Schematic of flame atomic absorption spectrophotometer ("Study Notes: AAS Detector,").

In the atomization chamber, three stages are generally involved in turning the liquid sample into an atomic gas: Desolvation which evaporates the liquid solvent and remained the dry sample; Vaporization which vaporize the dry solid sample to its gaseous state; Atomization which converting the gaseous sample into its free elemental state. The sample in its gaseous elemental state will subjected to the absorbance measurement via the internal wavelength specific spectrophotometer which described earlier. The light that is focused into the flame is produced by a hollow cathode lamp in which a cylindrical metal cathode containing the specific metal for excitation and an anode is built inside the lamp. When a high voltage is applied across the anode and cathode, the metal atoms in the cathode are

excited into producing light with a certain emission spectra. The type of hollow cathode tube depends on the metal being analyzed *i.e.* for copper analysis; a copper cathode tube would be used. In analyzing the analyte concentration, Beer Lambert Law is strictly applied in analysis. A calibration curve (**Figure 3.4**) is produced by several solutions of known concentration and it is used to determine the unknown analyte concentration.

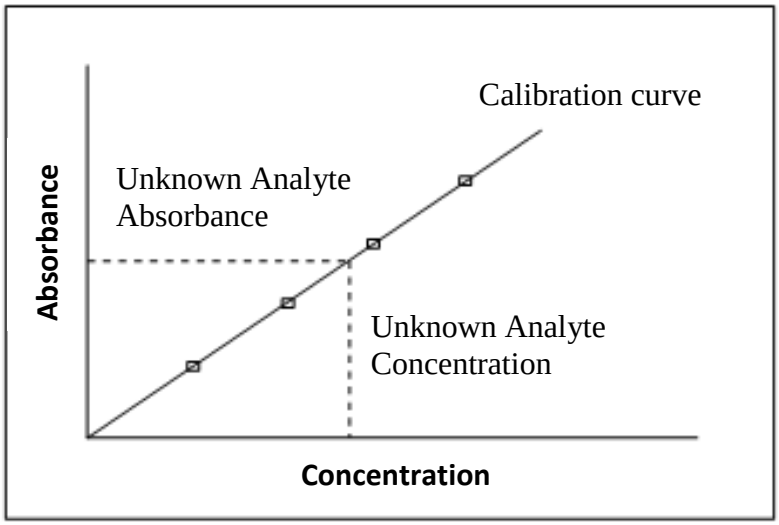

Figure 3.4. Calibration curve and unknown analyte concentration determination.

Atomic absorption spectrometry was applied in the copper leached studies of heterogeneous aqueous mercury complexation using Covellite. The amount of copper leached into the solutions was performed using an air-acetylene (air-C_2H_2) flame atomic absorption spectrophotometer (AA-6200, Shimadzu). Copper hollow cathode lamp was used as the light source. The wavelength for measurement was set at 324.8 nm and slit width at 0.7 nm. A five point calibration curve was constructed using the Cu(II) solution with concentration ranging from 0, 1, 2, 5, 10 ppm. The Cu(II) solution was prepared from consecutive dilution from 1000pm standard stock solution (Fisher Scientific). The Cu(II) concentration in the sample was measured up to 3 times to ensure the reproducibility and reported as average value.

3.4.3. Cold Vapor Atomic Absorption Spectrometry (CVAAS)

Cold vapor atomic absorption spectrometry is a type of atomic absorption spectrometry which utilized the chemical reduction instead of flame in the atomization process. The cold vapor atomization technique is widely employed in mercury analysis because mercury exerts high vapor pressure at relatively low temperatures. The use of flame atomization technique will result in mercury loss to the environment in which this has undeniably affects the sensitivity and accuracy of results acquired using flame AAS. In CVAAS, the experimental workflow is initiated firstly by oxidizing any form of mercury into Hg^{2+} (**Figure 3.5**). This can be done by adding concentrated sulfuric or nitric acid into the sample. It is then followed by chemical reduction of Hg^{2+} into Hg vapor using tin (II) chloride, $SnCl_2$. After that, the mercury vapor is swept into a long-pass absorption tube by bubbling a stream of inert gas through the reaction mixture. The mercury concentration is determined by measuring the absorbance of mercury vapor at 253.7 nm using the light source coming from mercury vapor lamp. The L.O.D of CVAAS are in the parts-per-billion (ppb) range and it makes the cold vapor technique an excellent mercury detection method.

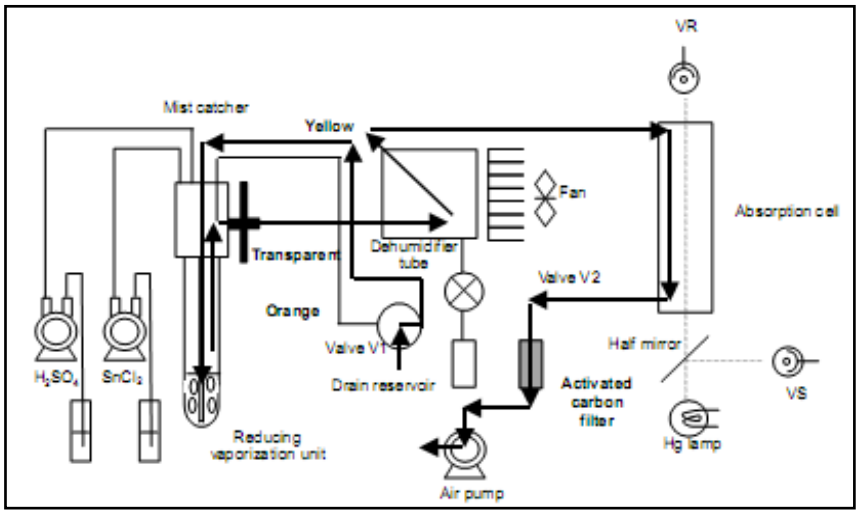

Figure 3.5. Schematic of cold vapor atomic absorption spectrophotometer (Nippon Instrument Corporation, 2005).

Cold vapor atomic absorption spectrometry was applied in the mercury uptake studies of heterogeneous aqueous mercury complexation using Covellite. The amount of mercury left in the solution was measured using mercury analyzer (RA-3, NIC) with freshly prepared 10% (w/v) tin (II) chloride, $SnCl_2$ as reducing agent. Mercury vapor lamp was used as the light source with wavelength for absorbance measurement was set at 253.7 nm. A five point calibration curve was constructed using Hg(II) solution with concentration ranging from 0, 1, 2, 5, 10 ppb. The Hg(II) solution was prepared by consecutive dilution from 1000pm standard stock solution (Wako, Japan). The Hg(II) concentration in the sample was measured up to 3 times to ensure the reproducibility and reported as average value.

3.4.4. Powder X-Ray Diffraction (PXRD)

Powder X-ray diffraction is the most widely used technique for general crystalline material characterization. In PXRD technique, a collimated beam of X-rays, with wavelength λ = 0.5 – 2Å, is incident on a specimen (**Figure 3.6**). When there is constructive interference from X-rays scattered by the atomic planes in a crystal, a diffraction peak is observed. The condition for constructive interference from planes with spacing d_{hkl} is given by Bragg's Law:

$$\lambda = 2d_{hkl} \sin\theta_{hkl} \qquad (3.7)$$

where θ_{hkl} is the angle between the atomic planes and the incident (and diffracted) X-ray beam, λ is the wavelength of the X-ray photons, d is the distance between lattice planes (hkl). For diffraction to be observed, the detector must be positioned in such a way that the diffraction angle is $2\theta_{hkl}$. The crystal must be oriented so that the normal to the diffracting

plane is coplanar with the incident and diffracted X-rays. Therefore, the angle between the diffracting plane and the incident X-rays is equal to the Bragg angle θ_{hkl} (Brundle, Evans, & Wilson, 1992).

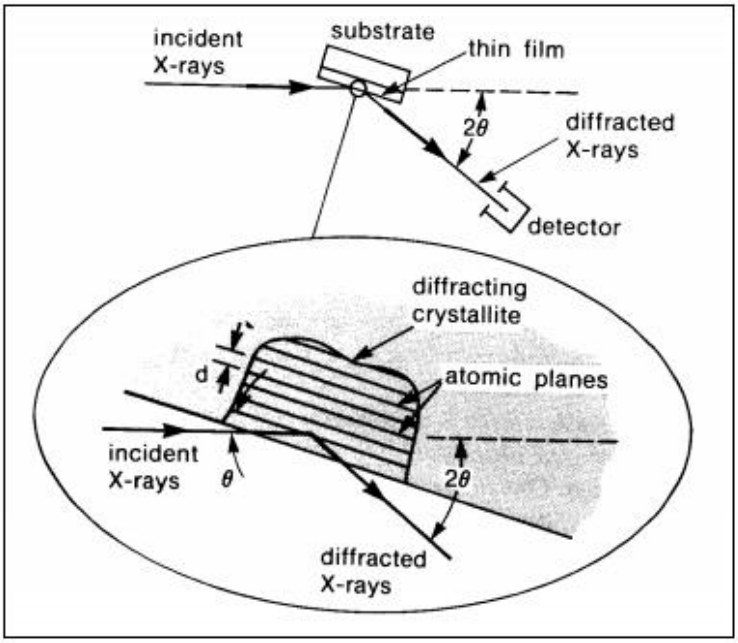

Figure 3.6. Schematic of a typical PXRD experiment (Brundle, et al., 1992).

From the PXRD patterns generated, different important information on the structural properties of a solid material can be obtained. **Table 3.13** shows the information that can be collected from the parameters found on a PXRD pattern. For qualitative phase identification, the analysis is carried out by comparing the line positions and intensity distributions of a set of reflections of the sample material with a database. The Powder Diffraction File (PDF), distributed by the International Centre for Diffraction Data (ICDD) (formerly ASTM, then JCPDS), is the most commonly used and is often distributed together with or included in the most common X-ray powder diffraction software for data analysis. For full width at half maximum (FWHM) determination, the analysis is conducted using the single peak parameter in which the procedure is shown in **Figure 3.7**.

Table 3.13. Information that can be extracted from an idealized PXRD pattern (Girgsdies, 2009).

Parameters	Information extracted
Overall peak position	Phase identification.
Single peak position	Approximation of FWHM, d-spacing, lattice parameter (metrics of the unit cell).
Peak height (maximum intensity)	Approximation of peak intensity and relative quantification in a mixture.
Peak area (integral intensity)	Crystal structure (contents of the unit cell) and relative quantification in a mixture.
Peak width	Crystallite size, defects (strain, disorder).
Peak shape	Crystallite size, defects (strain, disorder).

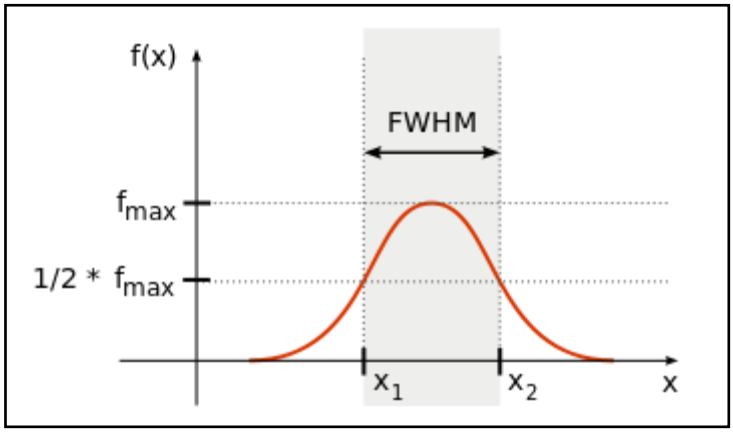

Figure 3.7. Determination of FWHM (Wikipedia, 2013).

For lattice cell parameters determination, a Rietveld refinement maybe needed to solve entire crystal structure. The relative phase quantification can be either carried out using peak area ratio analysis or a more accurate Rietveld refinement. Lastly, for crystallite sizes and micro-strain determination, the analyses are performed using the respective Scherrer equation (equation 3.8) and the Wilson equation (equation 3.9):

$$\text{FWHM} = \frac{K\lambda \text{ x } 57.3}{D\cos\theta} \quad (3.8)$$

$$\text{FWHM} = 4\varepsilon\tan\theta \quad (3.9)$$

where FWHM is in °θ, K is the crystallite shape form factor (for spherical crystallites K = 0.94), λ is the X-ray wavelength, D is the crystallite size, θ is the Bragg angle corresponding to the maximum of the diffraction peak (in θ) and ε is the micro-strain. Therefore, PXRD is apparently a powerful tool which can provide qualitative and quantitative assessment in a crystalline material as well as quantification of crystalline content in a crystalline – amorphous mixture.

Rietveld refinement which also known as full PXRD pattern analysis (Rietveld, 1967, 1969) is a significant improvement in the analysis of powder diffraction data. In this analytical technique, it allows not only the quantitative analysis of multiphase samples, it also provide an alternative platform in recognizing unknown crystal phases without the need of conducting single crystal experiment. The Rietveld refinement analysis requires a starting model in the form of single crystal data which can be obtained from phase identification analysis. The procedure is then followed by refining the crystal cell parameters of the crystalline material until a good R *i.e.* R_{wp} (Single phase < 10, Mixed phases < 15 for good fit) and GOF values (Goodness of fit, Best is 1.0) are obtained. The goodness of the fit is not only depends on the data quality (signal/ noise ratio) and detection limits, but also from the appropriateness of the structure models used. The level of accuracy is usually unknown, unless the procedure is checked with known mixtures. "100 %" corresponds to the total of all phases accounted for in the fit, which is not necessarily identical to 100 % of the sample (PXRD amorphous material, unknown phases, known

phases without crystal structure model are neglected). The results may be re-scaled using a known amount of an internal diffraction standard. However, it is important to note that PXRD is unlike the case in spectroscopy, the diffraction peaks area or intensities of the components in a phase mixture are not directly proportional to the concentration of the compounds present (Girgsdies, 2009).

PXRD was employed to characterize the selected samples of unreacted and reacted pure and mixed phase Covellite powder collected in the mercury uptake studies of heterogeneous aqueous mercury complexation. The PXRD measurement has been performed either using STOE Stadi-P equipped with autosampler or Bruker X-ray Diffraction model D-8 which supplied with EVA Diffract software for data acquisition. The PXRD measurements were done by using a CuK_{α} monochromatized radiation source (λ = 1.5406 Å) operated at 40 kV and 40 mA at ambient temperature. The measured samples were grinded into fine powder and placed in the sample holder. The surface of the sample was flattened and smoothened before putting it into the sample chamber of the diffractometer. A continuous 2θ scan mode from 4 – 80 °, with step time of 1 s and step size of 0.02 ° was set for the PXRD measurement. The diffraction patterns generated were matched with Powder Diffraction File (PDF) database for phase identification. For Rietveld refinement, the analysis was carried out using Topas software with crystal structure model loaded from Inorganic Crystal Structure Database (ICSD). The refinement procedure was performed repeatedly using Prof. Ray Young's strategy until a good R and GOF value was obtained (Young, 1993).

3.4.5. Field Emission Scanning Electron Microscopy (FESEM)

Scanning Electron Microscope is often the first analytical instrument used when a "quick look" at a material is required. The SEM provides the investigator with a highly magnified

image of the surface of a material that is very similar to what one would expect if one could actually "see" the surface visually. In SEM, a source of electron beam which produced from the electron gun is focused into a fine probe and raster over the surface of the specimen (**Figure 3.8**). As the electron beam penetrates the surface, it creates various signals *i.e.* secondary electrons (SE), backscattered electrons (BSE) and X-ray (**Figure 3.9**) which can be collected by appropriate detectors. The most commonly used imaging mode makes use of secondary electrons (SEs) that are emitted when the sample is excited by the electron beam. These are low energy electrons (0-100 eV), making their collection very easy by means of an appropriately biased scintillator. Due to the low energy, the electron have a small mean free path ensuring that the signal comes from the surface region of the specimen. Another imaging mode within an SEM makes use of backscattered electrons (BSEs). These electrons have energies comparable to those in the incident beam (1-30 keV) and hence have larger mean free paths. Therefore, the signal is less sensitive to the surface topography, and instead the image intensity depends on the composition of the specimen. The higher energies of the BSEs make them more difficult to collect than the low energy SEs, which can be collected efficiently by applying a bias voltage to a grid in front of the detector. These signals are highly localized to the area directly under the beam. By using these signals to modulate the brightness of a cathode ray tube, which is raster scanned in synchronism with the electron beam, an image is formed on the screen. This image is highly magnified and usually has the "look" of a traditional microscopic image but with a much greater depth of field. Resolution in the SEM is determined by the size of the incident electron beam and the beam-specimen interactions (Ertl, Knözinger, Schüth, & Weitkamp, 2008). The resolution of SEM can approach a few nm and it can operate at magnifications that are easily adjusted from about 10x – 300000x (Brundle, et al., 1992).

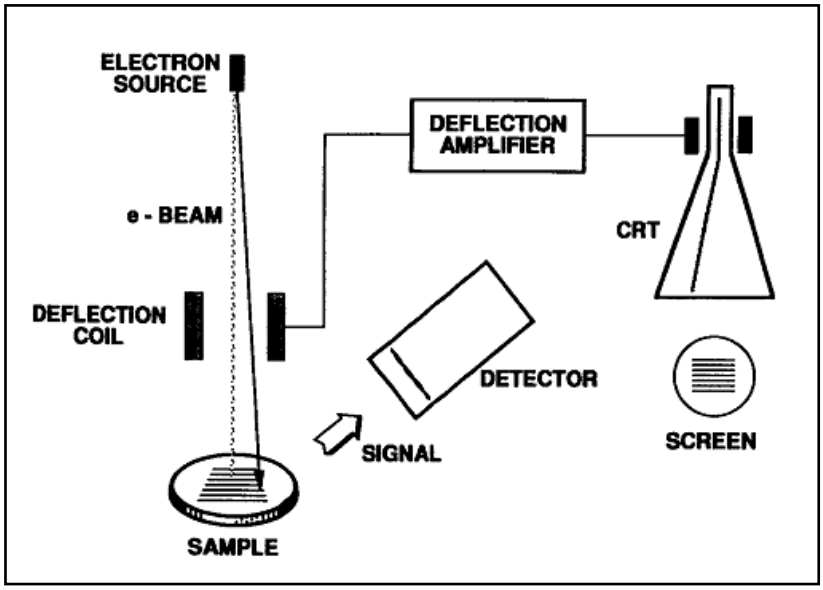

Figure 3.8. Schematic of a typical scanning electron microscope (Brundle, et al., 1992).

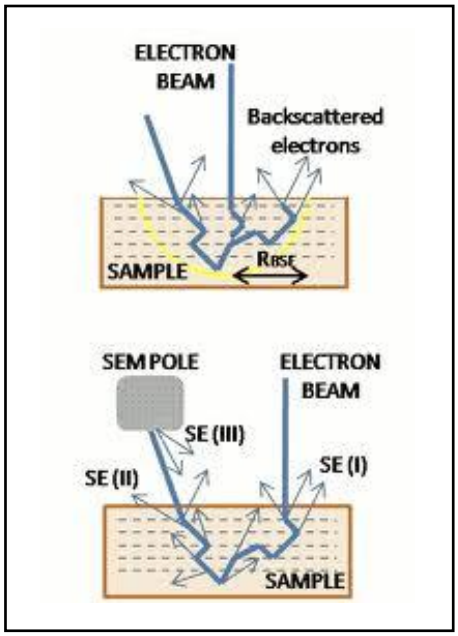

Figure 3.9. Generation of SE and BSE during the bombardment of electron beam onto sample surface (Bijoor, 2008).

In scanning electron microscopy, various modifications have been performed by the researchers to improve the resolution of the microscope. An obvious effort is in fact observed in the introduction of field emission technique in SEM *i.e.* FESEM technique. This technique improvises a better electron gun for the production of stable electron beam

prior to the bombardment on sample specimen. In conventional SEM, thermionic emitters is utilized as the electron gun in which it use electrical current to heat up a filament; the two most common materials used for filaments are Tungsten (W) and Lanthanun Hexaboride (LaB_6). When the heat is enough to overcome the work function of the filament material, the electrons can escape from the material. Nevertheless, thermionic sources have relative low brightness, evaporation of cathode material and thermal drift during operation. Thus, the introduction of field emitter as the electron gun is one way of generating electrons that avoids these problems. A field emission source (FES); also called a cold cathode field emitter, does not heat the filament. The emission is reached by placing the filament in a huge electrical potential gradient. The FES is usually a wire of Tungsten (W) fashioned into a sharp point. The significance of the small tip radius (~ 100 nm) is that an electric field can be concentrated to an extreme level, becoming so big that the work function of the material is lowered and electrons can leave the cathode. Therefore, FESEM can produce a cleaner image, less electrostatic distortions and spatial resolution less than 2 nm in which it is 3 or 6 times better compared to conventional SEM.

FESEM was utilized to characterize the selected samples of unreacted and reacted pure and mixed phase Covellite powder collected in the mercury uptake studies of heterogeneous aqueous mercury complexation. The surface morphology of the unreacted and reacted Covellite samples was studied by using a Quanta 200 FEI FESEM instrument. The powder samples were adhered to the aluminium made stub using a small piece of carbon conductive tape before loaded to the sample chamber of the instrument. High vacuum condition *i.e.* below 10^{-3} Pa under the ESEM mode was set during the measurement. In addition, two detectors i.e. secondary electron – large field detector (SE – LFD) and backscattered electron – solid state detector (BSE – SSD) detectors were also used in the measurement.

3.4.6. High Resolution Transmission Electron Microscopy (HRTEM)

For decades, transmission electron microscopy (TEM) and high resolution transmission electron microscopy (HRTEM) has becomes a mainstay in repertoire of characterization techniques. TEM and HRTEM's advantage is dealing to its high lateral spatial resolution in which it provides both image and diffraction information due to scattering mechanisms associated with interactions between electrons and the atomic constituents of the sample (**Figure 3.10**). Analysis of transmitted electron images yields information about atomic structure and defects present in the material (Brundle, et al., 1992).

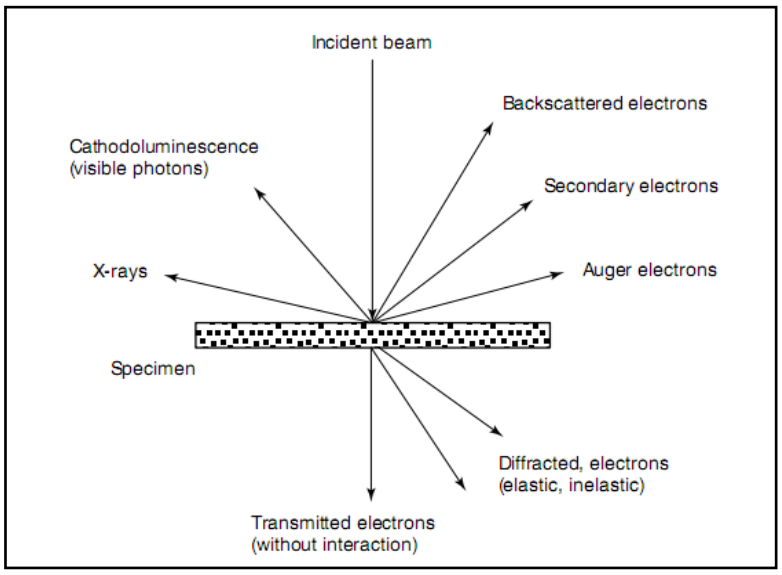

Figure 3.10. Interaction of an electron beam with a thin foil (Drake, 2012).

In TEM, a focused electron beam which is generated by electron gun is incident on a thin (less than 200 nm) sample specimen under vacuum condition (**Figure 3.11**). The signal in TEM is obtained from both un-deflected and deflected electrons that penetrate the sample thickness. A series of electromagnetic lenses will then transmit the electron signal into a detector *i.e.* a fluorescent screen, a film plate or a CCD video camera. The lens produce a 2D diffraction pattern of the sample in its focal plane and these diffracted beams

recombine to form the image. A magnified image or the diffraction pattern on detector is observed by varying the excitation of a series of projection lenses. The most commonly used TEM instruments operate in the 100 – 400 KV range; the higher the energy, the better the resolution (Ertl, et al., 2008).

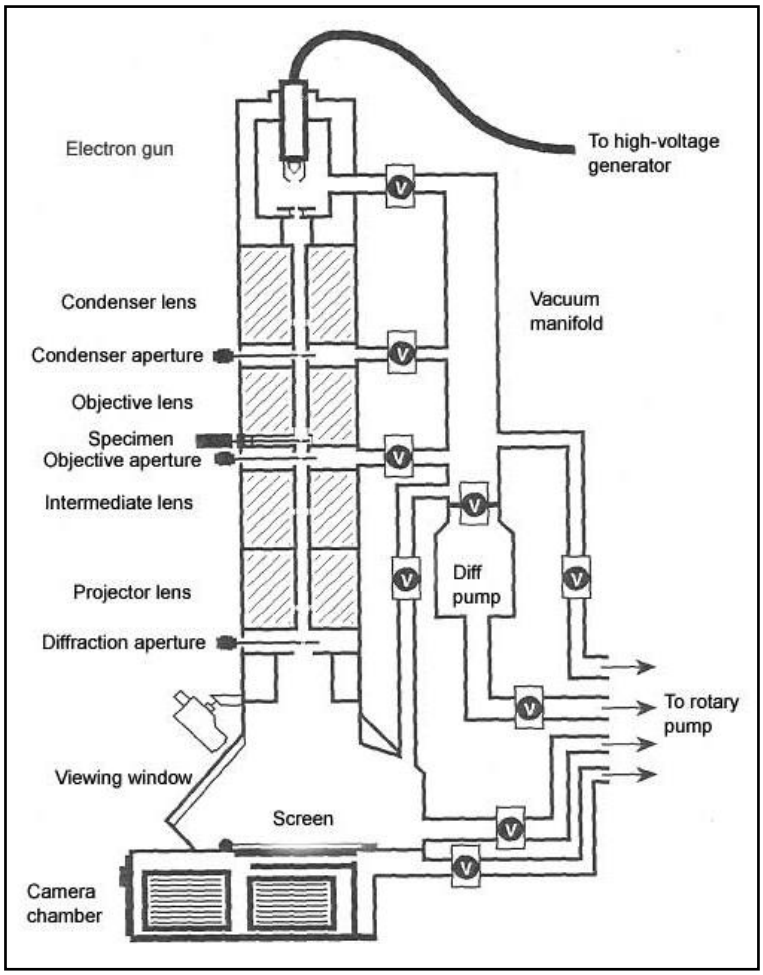

Figure 3.11. Schematic of typical transmission electron microscope (Shiue, Hung, Chen, & Chang, 2011).

TEM offers two operating modes: conventional TEM (CTEM) and high resolution TEM (HRTEM). In CTEM, two imaging modes are possible: bright field and dark field. In bright field imaging, all diffracted electrons are excluded by the aperture in forming the image. In order to detect the presence of metallic particles, this image mode is preferred. If

the image is formed from diffracted electrons alone and the central beam is excluded by the objective aperture, a dark field image is obtained. Two beam imaging refers to the condition where the crystal is oriented to yield transmitted and diffracted beams of equal intensity. The bright field, dark field, and two beam imaging modes are broadly applied in studying defects and morphology of thin crystals (Hirsch, Howie, Nicholson, Pashley, & Whelan, 1965; Smith, 2005). Meanwhile, HRTEM technique is performed using an objective aperture which allows diffracted beams to interfere with the axial transmitted beam to form the image. Phase contrast imaging is the preferred imaging mode for resolving the atomic lattice of the specimen (Ertl, et al., 2008).

TEM and HRTEM was used to characterize the selected samples of unreacted and reacted pure and mixed phase Covellite powder collected in the mercury uptake studies of heterogeneous aqueous mercury complexation. The TEM specimens were prepared without using any liquids on Cu grids covered with amorphous carbon film. TEM and HRTEM images were recorded from either a FEI Cs-corrected Titan 80-300 microscope or a Philips CM200FEG microscope equipped with Gatan imaging filter. Several images of representative areas of the sample were taken at different magnifications with a CCD camera, and selected image areas were processed to obtain the power spectra (Fast Fourier Transform, FFT, of image). The power spectra (PS) were used for measuring interplanar distances (+/- 0.5 %) and angles (+/- 0.5 °) for phase identification.

3.4.7. Energy Dispersive X-ray Spectroscopy (EDX)

Energy dispersive X-ray spectroscopy also known as energy dispersive spectroscopy (EDS), is the most commonly used analytical technique in a microscope *i.e.* FESEM and HRTEM. With modern detectors and electronics, most EDX systems can detect X-rays generated from all the elements in the periodic table above beryllium, Z = 4, if present in sufficient

amount. The L.O.D for elements with atomic numbers greater than Z = 11 is as low as 0.02 wt%, if the peaks are isolated and the spectrum has a total of at least 2.5 x 10^5 counts (Brundle, et al., 1992). Thus, EDX technique is a powerful non-destructive tool for elemental analysis.

In EDX, the atoms in a material are bombarded with high energy electron beam in which secondary electron (SE), backscattered electron (BSE), cathodoluminescence as well as X-rays are produced simultaneously (**Figure 3.12**). X-rays are produced as a result of the ionization of an atom by high energy radiation where an inner shell electron is removed. To return the ionized atom to its ground state, an electron from a higher energy outer shell fills the vacant inner shell and, in the process, releases an amount of energy equal to the potential energy difference between the two shells. Thus, in an atom with many shells, many emissions can result from a single primary ionization that leads to X-rays production. A solid state detector, usually made from lithium-drifted silicon, Si (Li); and signal processing electronics is used for X-rays detection. X-ray spectrum can be obtained from almost any sample, as long as it can be put on the specimen stage of microscope.

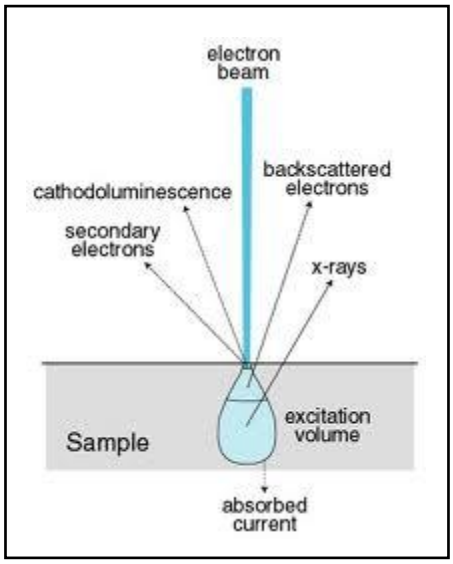

Figure 3.12. Generation of various signals during bombardment of electron beam onto sample surface (Wittke, 2008).

The choice of accelerating voltage which generated the amount of electron beam should be determined by the type of sample one is studying, since the X-ray generation volume depends on the electron range in the material. The ultimate goal in using an EDS analytical system is to be able to measure the concentrations of all the elements in the sample. To this end, a series of measurement are made in which the peak intensity from each element in X-ray spectrum is compared to the peak intensity obtained from a reference standard using the same operation conditions. The number of counts in each peak may be further converted into elemental weight concentration either by comparison with standards or by standardless calculations. EDS is an extremely powerful analytical technique of special value in conjunction with electron column instruments. In a few seconds a qualitative survey of the elements present in almost any sample can be made, and in only a few minutes' sufficient data can be collected for quantification (Brundle, et al., 1992).

EDX was used in conjunction with SEM, TEM and HRTEM to characterize the selected samples of unreacted and reacted pure and mixed phase Covellite powder collected in the mercury uptake studies of heterogeneous aqueous mercury complexation. The surface elemental composition and elemental mapping of the samples were determined by using INCA Energy 400 software with the images captured by Quanta 200 FEI microscope instrument. The powder samples were adhered to the aluminium made stub using a small piece of carbon conductive tape before loaded to the sample chamber of the instrument. High vacuum condition *i.e.* below 10^{-3} Pa under the ESEM mode was set during the measurement. The surface elemental composition and elemental mapping of the samples were carried out under the accelerating voltage of 20kV using SATW (silicon) detector.

3.4.8. X-ray Photoelectron Spectroscopy (XPS)

X-ray photoelectron spectroscopy also recognized as electron spectroscopy for chemical analysis (ESCA) is a surface sensitive technique which has a probing depth from top 2 atomic layers to 15 – 20 layers (< 50Å). The area examined can be as large as 1 cm x 1cm or small as 70 μm x 70 μm (10 μm diameter spots may be achieved with very specialized equipment). It is applicable to biological, organic and polymeric materials through metals, ceramics, and semiconductors. XPS identified all elements except hydrogen and helium with a sensitivity variation across the periodic table of only about 30. Samples can be gaseous, liquid or solid, but the vast majority of electron spectrometers are designed to deal with solids. The surface sensitivity, combined with quantitative and chemical state analysis capabilities have made XPS the most broadly applicable general surface analysis today (Brundle, et al., 1992).

XPS involves a photon with sufficiently short wavelength *i.e.* soft X-rays ionizes atom producing ejected free electrons, photoelectrons from the sample (**Figure 3.13**). The kinetic energy (K.E.) of the photoelectron depends on the energy of the photon, hv expressed by the Einstein photoelectric law:

$$\mathrm{K.E.} = \mathrm{hv} - \mathrm{B.E.} \qquad (3.10)$$

where B.E. is the binding energy of this particular electron to the atom concerned. All of photoelectron spectroscopy is based on equation 3.10. Since hv is known, a measurement of K.E. determines B.E. The classical photon sources are the quasimonochromatic line spectra of either rare gas discharge lamp (Nefedov, Sergushin, Band, & Trzhaskovskaya, 1973) or X-ray anodes (Siegbahn, et al., 1967) *i.e.* an Al anode which gives 1486eV. Nevertheless, the utilization of synchrotron radiation seems to be in great favor due to its remarkable characteristic *e.g.* linear or circular polarization of this radiation (Ley &

Cardona, 1979). More importantly, it also provides a tunable light source covering all energies of interest when coupled with a suitable monochromator. Two classes of electron energy analyzer are used to measure the K.E. of photoelectron ejected. The first type is dealing to an integral analyzer where a voltage between two grids set up a potential barrier that the photoelectrons have to overcome before they reach the detector. The second type is actually a differential analyzer where electrons are deflected by either a magnetic or an electric field. Both of the technique ensures a simultaneous recording of energy during the K.E. measurement (Cardona & Ley, 1978).

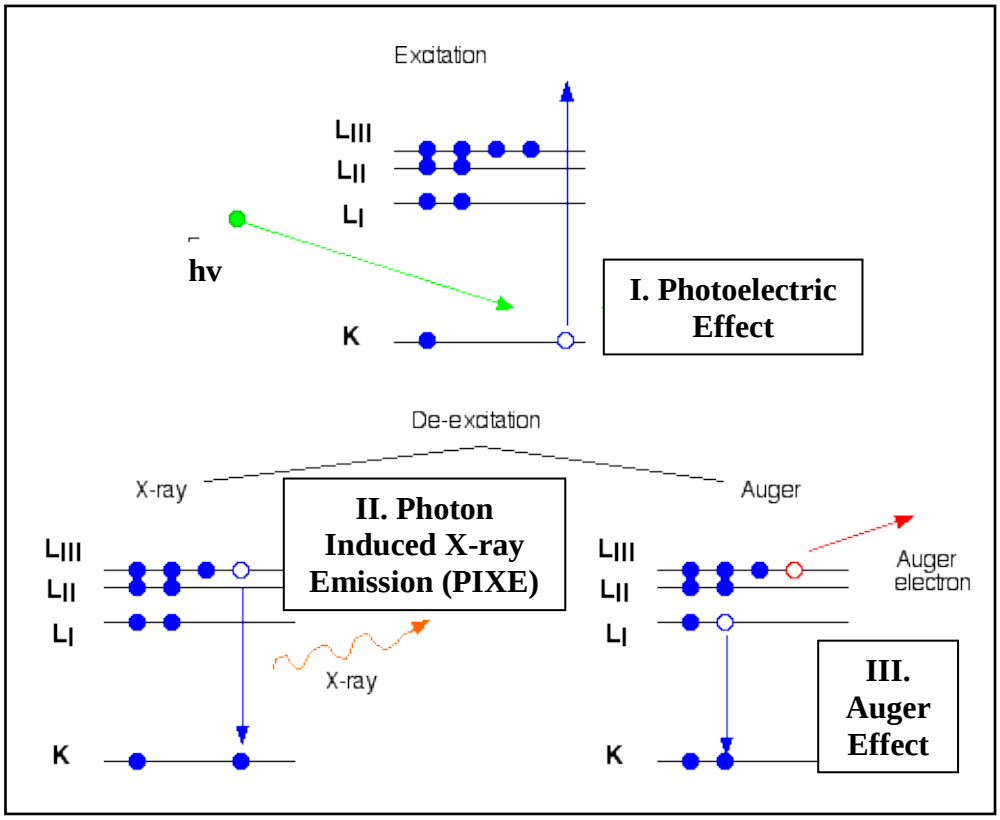

Figure 3.13. Emission process during the excitation and de-excitation of hv (ACEPT Group, 2005; Meta, 2009).

The electron energy levels of an atom can be divided into two types; valence levels, which are only weakly bound and core levels, which are tightly bound to the nucleus. The valence levels of an atom are the ones that interact with the valence levels of other atoms to

form chemical bonds in molecules and compounds. Their characteristic and energy changed remarkably by this process, becoming characteristic of the new species formed. The study of valence levels is the basis of ultraviolet photoelectron spectroscopy (UPS). The identification of core-level B.E.s provides unique signature of the elements in which this is the main aim in XPS. All the elements in the periodic table can be identified in this manner, except H and He, which have no core levels. Quantitative analysis, yielding relative atomic concentrations, requires the measurement of relative peak intensities of the core level electrons combined with knowledge of cross section values plus any experimental artifacts that affect the intensities (Brundle, et al., 1992). On the other hand, qualitative chemical state analysis is performed by identifying the small "chemical shifts" in the B.Es and compares it with reported standard chemical shift values.

The inelastic mean free path (IMFP) is an index of how far an electron can travel through a solid before it loses the energy. On other words, the IMFP is a measure of the average distance travelled by an electron through a solid before it is in-elastically scattered. The IMFP is dependent upon the initial kinetic energy of the electron as well as the nature of the sample present in the analysis. The IMFP is actually defined by the following equation which gives the probability of the electron travelling a distance, d, *i.e.* P(d) through the solid without undergoing scattering:

$$P(d) = \exp (- d / \lambda) \qquad (3.11)$$

where λ is the IMFP for the electrons of energy E. It is important to note that $\lambda = f(E)$, and this inelastic mean free path, which relates to the movement of electrons in the solid, is completely unrelated to the mean free path in the gas phase once they escape from the solid. The "universal curve" for the variation of IMFP with initial photon source (eV) is depicted

in **Figure 3.14**. From the figure, the IMFP exhibits a minimum for electrons with a kinetic energy of around 50 - 100 eV; at lower energies the probability of inelastic scattering decreases since the electron has insufficient energy to cause plasmon excitation, and consequently the distance between inelastic collisions and the IMFP increases. This universal curve provides important information in calculating the thickness of the surface analyzed. Thus, a depth profiling using synchrotron XPS can be carried out by varying the X-ray radiation applied *i.e.* the photon energy is adjusted, so that the desired kinetic energy for the photoelectrons can be achieved (Brundle, et al., 1992).

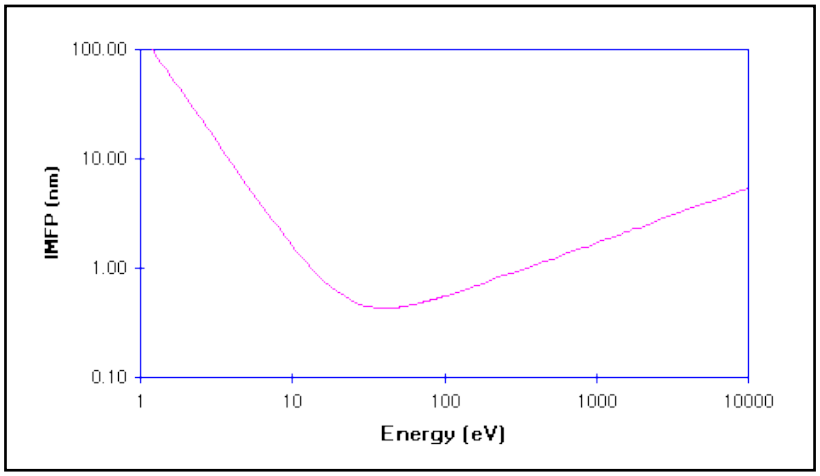

Figure 3.14. Universal curve of IMFP vs thickness of the sample measured (University of London, 2005).

XPS was used to characterize the selected samples of unreacted and reacted pure and mixed phase Covellite powder collected in the mercury uptake studies of heterogeneous aqueous mercury complexation. The XPS measurements were carried out using Soft X-ray Spectroscopy beamline at Helmholtz-Zentrum Berlin (HZB). The sample was pressed into pellet and ultra high vacuum (UHV) was set before and during the measurement. The analysis has been conducted under two photon energy sources in order to achieve K.E. of 200eV and 600eV during the measurement.

CHAPTER 4

HOMOGENEOUS AQUEOUS MERCURY COMPLEXATION – RHODAMINE B

The use of liquid phase complexing agent provides a simple way in trapping and detecting mercury. The studies on homogeneous complexation was conducted with the use of cationic dye namely Rhodamine B in different solvent systems. With the assistant of iodide anion, Rhodamine B has shown to be effective in forming Rhodamine B-Hg-Iodide complexes. These Rhodamine B-Hg-Iodide complexes are intensely colored and are easily measured by UV-Visible spectrophotometer. Under a careful and systematic investigations, facile, non-destructive as well as reasonably cost effective Hg(II) detection method is readily developed via the spectrophotometric technique.

4.1. Formation of Mercury-Rhodamine B Complex

In the following studies, fluorescence xanthene basic dye, Rhodamine B has been selected as the coloring and wavelength shifting agent for Hg(II) complexation. Rhodamine B dissolves in water to give a red color solution, with absorbance maximum (λ_{max}) occurred at 552 nm (**Figure 4.1**). In comparison to other basic dyes (Crystal violet, Rhodamine 6G, Rhodamine S, Malachite Green, Brilliant Green, Pyronine G and Fuchsin), Rhodamine B was also determined as the best coloring agent for metal ion detection (Hernandez-Córdoba, et al., 1984).

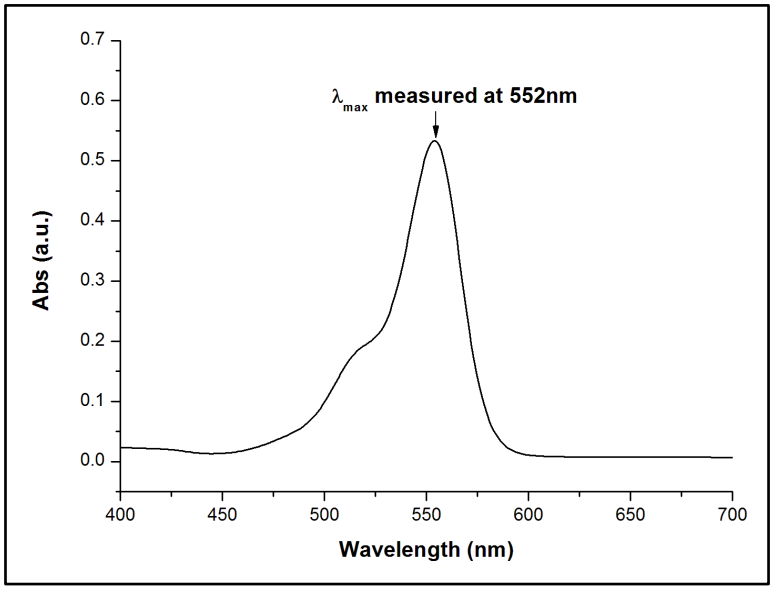

Figure 4.1. Absorbance spectra of 5 x 10^{-6} M Rhodamine B aqueous solution.

The homogeneous complexation of Hg(II) was carried out using iodide and Rhodamine B. The reaction between Hg(II), iodide and Rhodamine B involve a two step process. The complexation of Hg(II) was at first established using a large excess of iodide in which the Hg(II)-iodide complexes formed stepwisely through the complex ion equilibria below (Birk, 2001):

$Hg^{2+}(aq) + I^{-}(aq) \leftrightarrows HgI^{+}(aq)$ $\quad K_{F1} = 7.9 \times 10^{12}$ (4.1)

$HgI^{+}(aq) + I^{-}(aq) \leftrightarrows HgI_2(aq)$ $\quad K_{F2} = 1.0 \times 10^{11}$ (4.2)

$HgI_2(aq) + I^{-}(aq) \leftrightarrows HgI_3^{-}(aq)$ $\quad K_{F3} = 5.0 \times 10^{3}$ (4.3)

$HgI_3^{-}(aq) + I^{-}(aq) \leftrightarrows HgI_4^{2-}(aq)$ $\quad K_{F4} = 2.5 \times 10^{2}$ (4.4)

Arrange and combine all four equations above, it yield:

$Hg^{2+}(aq) + 4I^{-}(aq) \leftrightarrows HgI_4^{2-}(aq)$ $\quad K_F = K_{F1} \times K_{F2} \times K_{F3} \times K_{F4} = 9.9 \times 10^{29}$ (4.5)

or Log $K_f = 29.68$

Upon the formation of Hg(II)-Iodide complexes, Rhodamine B which is in its protonated form is then introduced into the solution mixture. The protonated form of Rhodamine B react with Hg-Iodide complexes and results in the formation of Rhodamine B-Hg(II)-Iodide complexes as below:

$$HgI_3^-\ (aq) + \text{Rhodamine B}^+ \leftrightarrows [(HgI_3)^-][(\text{Rhodamine B})^+] \quad (4.6)$$

$$HgI_4^{2-}\ (aq) + \text{Rhodamine B}^+ \leftrightarrows [(HgI_4)^{2-}][(\text{Rhodamine B})^+]_2 \quad (4.7)$$

Among the two Rhodamine B-Hg(II)-Iodide complexes formed, the complexation of Hg(II) with iodide mainly proceed through the formation of $[(HgI_4)^{2-}][(\text{Rhodamine B})^+]_2$ under the highly stable tetraiodomercurate(II) (log K = 29.68) and singly charged Rhodamine B. The successful interaction between Hg-Iodide complexes and Rhodamine B are mostly due to the strong electrostatic forces between the Hg-iodide anion and protonated Rhodamine B cation. In the entire reaction, a major problem of gradual precipitation of the violet ternary $[(HgI_4)^{2-}][(\text{Rhodamine B})^+]_2$ complex (**Figure 4.2**) was observed in which this has made the spectrophotometric analysis becomes difficult. Thus, to overcome the precipitation issue, this complex is either extracted into a stable solvent system or stabilized in the solution by protective water soluble polymer before any spectrophotometric measurement.

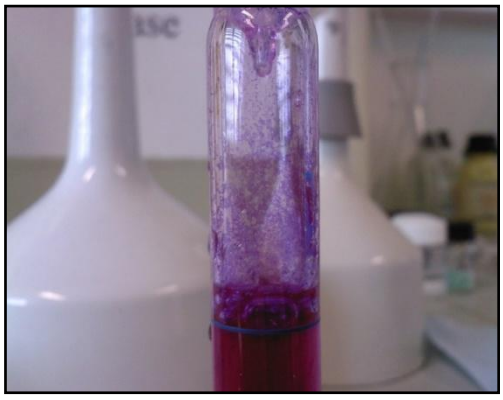

Figure 4.2. Precipitation of violet violet ternary $[(HgI_4)^{2-}][(\text{Rhodamine B})^+]_2$ complex.

4.2. Mercury-Rhodamine B Complex in Organic Solvent

The $[(HgI_4)^{2-}][(\text{Rhodamine B})^{+}]_2$ complex was extracted into dichloromethane and benzene. **Figure 4.3** and **Figure 4.4** show the absorbance spectra of the dichloromethane and benzene extracted Hg(II) sample and its respective reagent blank. For Hg(II) sample extracted with dicholoromethane, the absorbance maximum (λ_{max}) is found to occur at 556 nm. Whilst, for Hg(II) sample extracted with benzene, the λ_{max} is identified to occur at 565 nm. The general shape of the absorption spectrums of dichloromethane and benzene extracted Rhodamine B-Hg(II)-Iodide complexes as well as its respective extracted blank is identical to the spectrum of an aqueous solution of Rhodamine B (**Figure 4.1**). This suggests the absorption of the Rhodamine B-Hg(II)-Iodide complexes follows well to the absorption nature of Rhodamine B. On the other hand, it is observed that both of the absorption spectrums of dichloromethane and benzene extracted Hg(II) sample show a slight red shift to the right of the absorbance maximum (λ_{max}) of Rhodamine B solution (552 nm). These confirms that Rhodamine B has successfully combined with Hg(II) and it shifted the wavelength of Hg(II) towards the visible region for spectrophotometric measurement. In comparing the absorbance of reagent blank and extracted Hg(II) sample at its respective wavelength, the contribution of absorbance by reagent blank in dichoromethane seem to be higher than the case in benzene. The relatively low absorbance of reagent blank measured in benzene is most probably due to the low contribution of Rhodamine B-sulfate (sulfate comes from the sulfuric acid used, See **Section 3.2.1**), Rhodamine B-Iodide, and Rhodamine B-chloride in the benzene solvent. From this observation, it is indicative that the use of more polar solvents can eventually lead to higher values of reagent blank while the use of less polar solvent can result in lower values of reagent blank being measured. In fact, the effect of different solvent system towards the value of reagent blank measured was also reported by Hermandez et al. (Hernandez-

Córdoba, et al., 1984). They described the contribution of colorless form of Rhodamine B will predominate in the less polar solvent and results in a relatively low reagent blank being measured. Therefore, it is apparent that the less polar solvent i.e. benzene is a better solvent for extraction when compared to dichloromethane. The use of benzene rather than dichloromethane to extract Rhodamine B-Hg(II)-Iodide can actually provide a more sensitive Hg(II) determination method which assure a lower L.O.D.

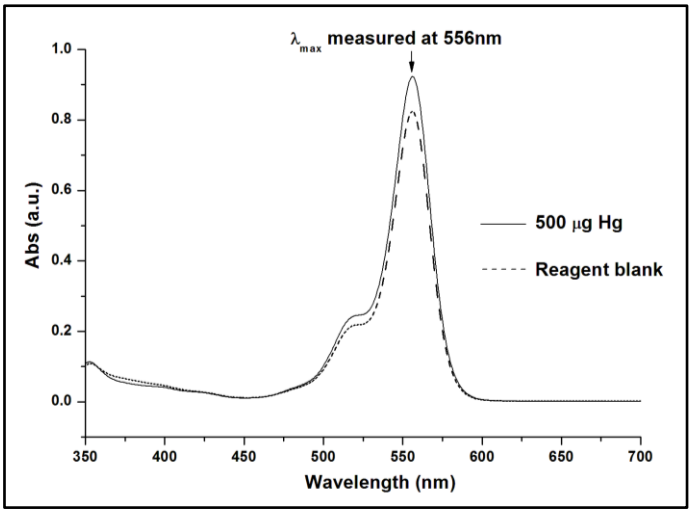

Figure 4.3. Absorbance spectra of dichloromethane extracted Hg(II) sample and reagent blank.

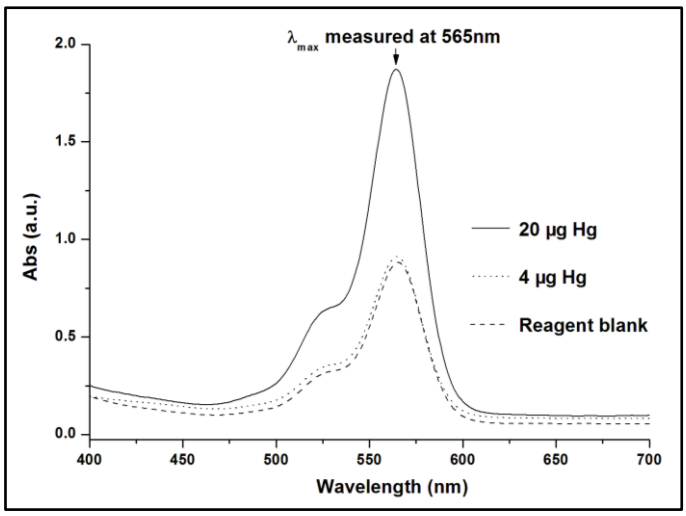

Figure 4.4. Absorbance spectra of benzene extracted Hg(II) sample and reagent blank.

The analysis of Rhodamine B-Hg(II)-Iodide complex was further carried using benzene as extraction solvent. The absorbance spectra of benzene extracted Rhodamine B-Hg(II)-Iodide complex at different Hg(II) concentration are shown in **Figure 4.5**. A graph of the absorbance against amount of Hg(II) at 565 nm is re-plotted as indicated in **Figure 4.6**. From the analysis, the Beer's law validity is identified to be ranged from ≈ 5 µg to 27 µg Hg(II). Above the validity limit, Beer's law started to deviate due to high analyte concentration and fluorescence interferences. Further increasing the concentration can also lead to the instrument limitation where a plateau of absorbance is observed. For a given method, it is regarded as sensitive when the molar absorptivity (absorption coefficient), Є is greater than 1 x 10^3 l $mole^{-1}cm^{-1}$ (Marczenko & Balcerzak, 2000). Thus, this method is seemed to be sensitive with the molar absorptivity determined at 565 nm = 17.68 x 10^4 l $mole^{-1}cm^{-1}$ and L.O.D to be approximately 5 µg @ 5 µg / 20 ml = 0.25ppm of Hg(II).

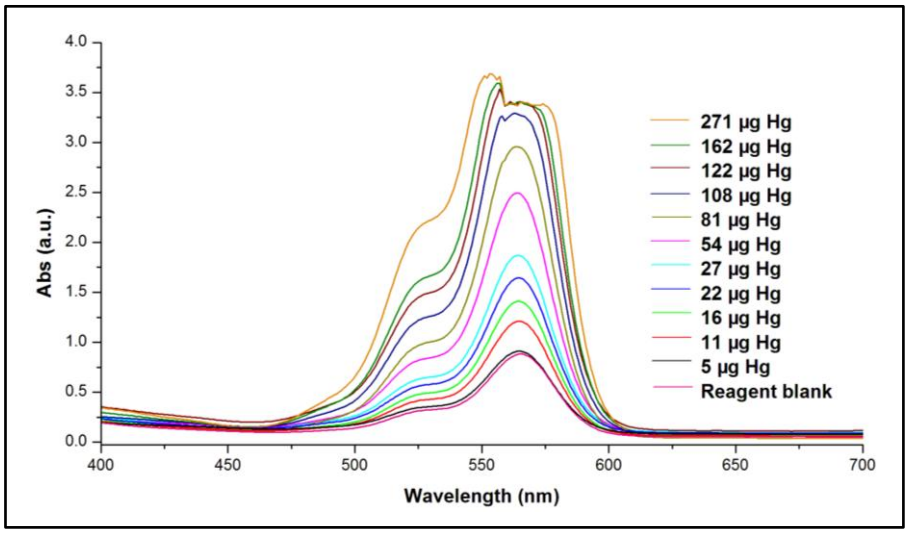

Figure 4.5. Absorbance spectra of benzene extracted Rhodamine B-Hg(II)-Iodide complex at different amount of Hg(II).

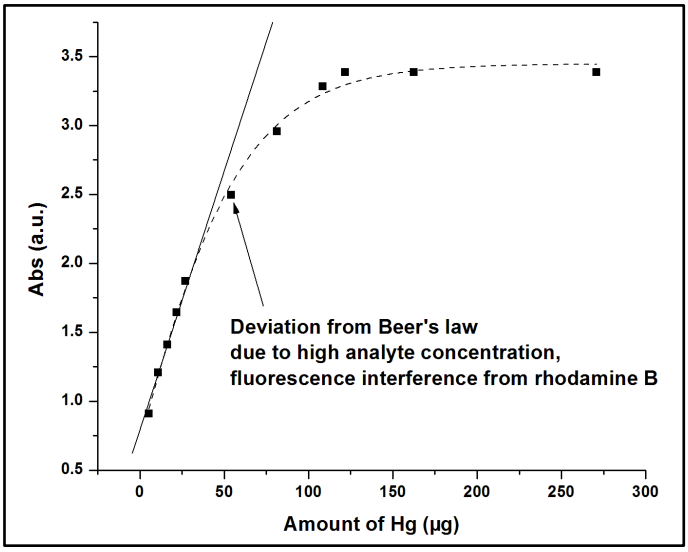

Figure 4.6. Single wavelength analysis (565 nm) of benzene extracted Rhodamine B-Hg(II)-Iodide complex at different amount of Hg(II).

4.3. Mercury-Rhodamine B Complex in Water

Beside the extraction approach in preventing the precipitation of HgI_4(Rhodamine B)$_2$, the use of PVAl to stabilize the ion associate in the water was also explored. Preliminary studies showed that the concentration of Rhodamine B needed to be decreased from 5 x 10^{-3} to 5 x 10^{-4} M to get a satisfactory result. This is because the former gives a very high reagent blank contribution in the absorbance measured and this has imposed difficulty for further spectrophotometric measurement. **Figure 4.7** shows the absorption spectra of reagent blank and stabilized HgI_4(Rhodamine B)$_2$ complex at different amount of Hg(II) in water using 5 x 10^{-4} M Rhodamine B solution.

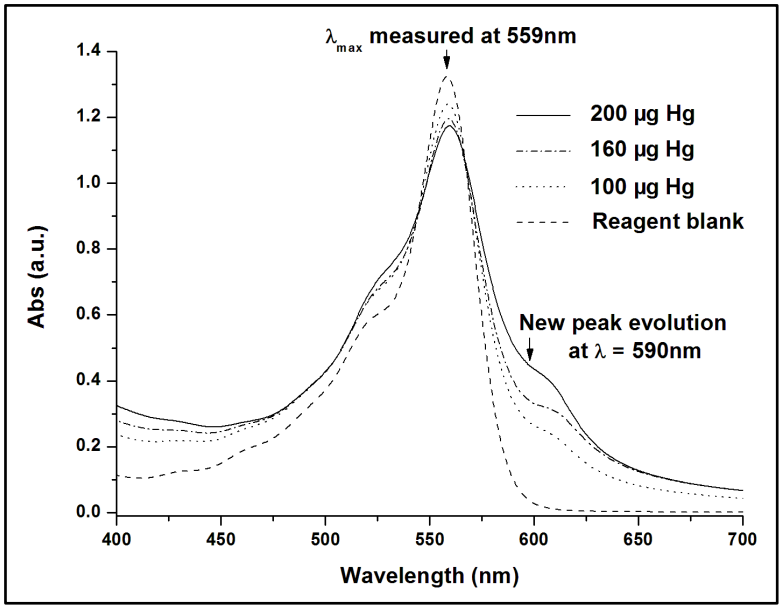

Figure 4.7. Absorption spectra of reagent blank and stabilized HgI_4(Rhodamine B)$_2$ complex at different amount of Hg(II) in water using 5 x 10^{-4} M Rhodamine B solution.

From the spectra, the stabilization of PVAl does not alter the shape of the spectrum as compared to the extraction approach. However, the absorbance maximum (λ_{max}) occurs at 560 nm does not give any indication on the concentration measured. Detailed analysis shows that there is an extra peak evolution occurs at approximately 590 nm when comparing the absorption spectra of reagent blank and stabilized HgI_4(Rhodamine B)$_2$ complex at different amount of Hg(II). The peak evolution that occurs is apparently due to the HgI_4(Rhodamine B)$_2$ formation of in polyvinyalcohol stabilized system. The specific wavelength of this additional peak evolution shows the most significant distinction between different Hg(II) concentration samples for UV-Visible spectrophotometric measurement. Therefore, further studies were carried out at this particular wavelength via the single wavelength measurement mode in UV-Visible spectrophotometer.

In PVAl stabilized system, solution pH is identified to play an important role in controlling the final absorbance of HgI_4(Rhodamine B)$_2$ measured. The absorbance measured at 590 nm for PVAl stabilized HgI_4(Rhodamine B)$_2$ complex at different pH is

depicted in **Figure 4.8**. From the analysis, it is observed that this method gives the highest absorbance from pH 0 to 1.5. Further increase in pH would result in the declination of absorbance measured. This phenomena can be explained using the pH dependency diagram that shown earlier (See **Section 2.1.2**) in which Rhodamine B can only function well in the protonated ionized form that only exists at low pH. As pH increases to 2, some of the proton (H^+) which attached on unreacted protonated Rhodamine B has dissociated back into the solution. This has resulted in a decrease on the absorbance measured. This situation is becoming worse when pH decreases beyond pH 4. Beyond this level, the singly charged Rhodamine B that binded to the HgI_4^{2-} species also re-dissociates back into the solution and exists as its amphoteric form. This amphoteric form of Rhodamine B is useless in binding any anionic metal complexes in which this has led to the minimum absorbance of final solution mixture being detected.

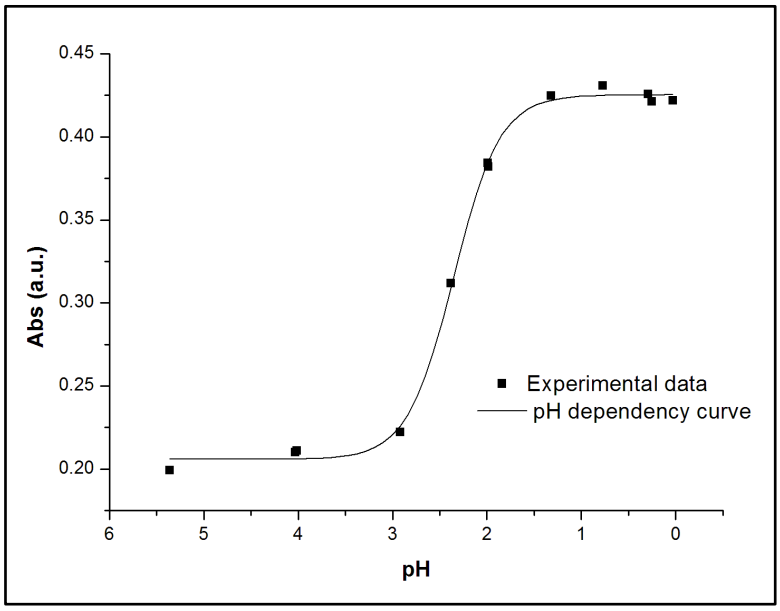

Figure 4.8. Absorbance measured at 590 nm for PVAl stabilized $HgI_4(Rhodamine\ B)_2$ complex at different pH.

Efforts has been tried to prove the pH-dependency trend against the absorbance of solution mixture measured at 590 nm (**Figure 4.8**). During the complexation process, the fate of $HgI_4(Rhodamine\ B)_2$ in PVAl stabilized system is described by the following equations:

$$Hg\left(RH^+\right)_2 \quad \overset{K^*}{\longleftrightarrow} \quad Hg + 2\,RH^+ \quad \overset{K^\xi}{\longleftrightarrow} \quad 2\,R + 2\,H^+ + Hg \tag{4.8}$$

where Hg = Tetra-iodo-mercury complex, $[HgI_4]^{2-}$

RH^+ = Singly protonated Rhodamine B

R = Rhodamine B

The equilibrium constant of Rhodamine B species in the PVAl stabilized solution mixture is calculated based on the equation below:

$$K^\xi = \frac{[R]^2\left[H^+\right]^2}{\left[RH^+\right]^2} \Rightarrow \sqrt{K^\xi} = \frac{[R]\left[H^+\right]}{\left[RH^+\right]} \equiv K \tag{4.9}$$

$$K^* = \frac{\left[Hg\left(RH^+\right)_2\right]}{[Hg]\left[RH^+\right]^2} \Rightarrow K^* = \frac{\left[Hg\left(RH^+\right)_2\right]K^\xi}{[Hg][R]^2\left[H^+\right]^2} = \frac{\left[Hg\left(RH^+\right)_2\right]K^2}{\left[RH^+\right]} \tag{4.10}$$

Arranging equations (4.9) and (4.10), the final concentration of Hg(II)-Rhodamine B complex that being measured by using UV-Vis spectrophotometry is described as:

$$\left[Hg\left(RH^{+}\right)_2\right] = \frac{K^*}{K^2}[Hg][R]^2\left[H^{+}\right]^2 \tag{4.11}$$

Furthermore, the mass balance of Rhodamine B species in the solution can be described as the following:

$$[R]+\left[RH^{+}\right]+2\left[Hg\left(RH^{+}\right)_2\right] = [R_{total}] \tag{4.12}$$

By replacing [R] from equation (4.12) into equation (4.11), the resulting equation becomes:

$$\left[Hg\left(RH^{+}\right)_2\right] = \frac{K^*}{K^2}[Hg]\left[H^{+}\right]^2\left\{\frac{[R_{total}]-2\left[Hg\left(RH^{+}\right)_2\right]}{1+\frac{\left[H^{+}\right]}{K}}\right\}^2 \tag{4.13}$$

By simple transformation, the equation for $[Hg(RH^+)_2]$ is resolved where in this case only the subtraction results is a meaningful solution:

$$\left[Hg\left(RH^{+}\right)_2\right]=[R_{total}]\frac{1+\frac{\left[H^{+}\right]^2}{K^2}+2\frac{\left[H^{+}\right]}{K}}{8\frac{K^*}{K^2}[Hg]\left[H^{+}\right]^2}-\sqrt{\left([R_{total}]\frac{1+\frac{\left[H^{+}\right]^2}{K^2}+2\frac{\left[H^{+}\right]}{K}}{8\frac{K^*}{K^2}[Hg]\left[H^{+}\right]^2}\right)^2-\frac{[R_{total}]^2}{4}} \tag{4.14}$$

From equation 4.14, the amount on $[Hg(RH^+)_2]$ is directly proportional to the absorbance value measured by UV-Vis spectrophotometer. This implies that an increase in the amount of $[Hg(RH^+)_2]$ in the solution will also lead to an increase on the absorbance value measured. By substituting the constant K with 7.9433exp(-4) and all other values are set to unity, the amount of $[Hg(RH^+)_2]$ at different solution pH can be estimated. **Figure 4.9**

shows the pH dependency diagram against absorbance at different solution pH. From the analysis, an inflection point at around pH = 3.1 is observed. This value agrees well with the pKa value of Rhodamine B reported by Arbeloa et. al. (Arbeloa & Ojeda, 1981).

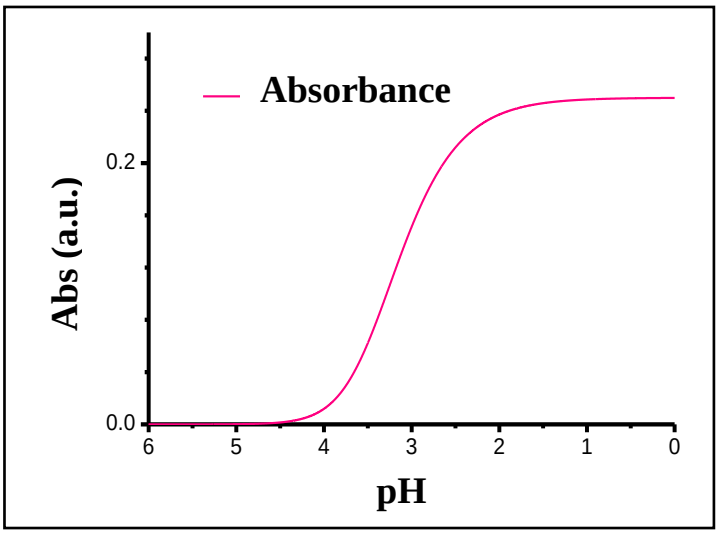

Figure 4.9. Calculated pH dependency curve for Rhodamine B in PVAl stabilized system (The curve shows an inflection point at pH 3.1 indicating pKa of 3.1).

In order to confirm the trueness of the experimental data (**Figure 4.8**), the constant K^* is further lowered to exp (-4) in which the calculated pH dependency curve is illustrated in **Figure 4.10**. This can be noticed that the inflection point has been shifted to lower pH. Apparently, the evaluated result calculated is comparable to the pH dependency curve determined in **Figure 4.8**. This analysis verify that the singly protonated Rhodamine B species is highly important in complexing mercury in which it give rises to the absorbance of $[Hg(RH^+)_2]$ measured. To ensure the dominance of active singly protonated Rhodamine B species in the solution, the solution mixture has been added with 1 ml of ≈ 11 M sulfuric acid (see **Section 3.2.2**). It is important to note that the addition of 1 ml of ≈ 11 M sulfuric acid is sufficient in maintaining the solution pH in the range of 0 – 1. This has undeniably provides significant amount of active singly charged protonated Rhodamine B present in

the solution in which a successful homogeneous complexation of Hg(II) is finally established using the PVAl stabilized system.

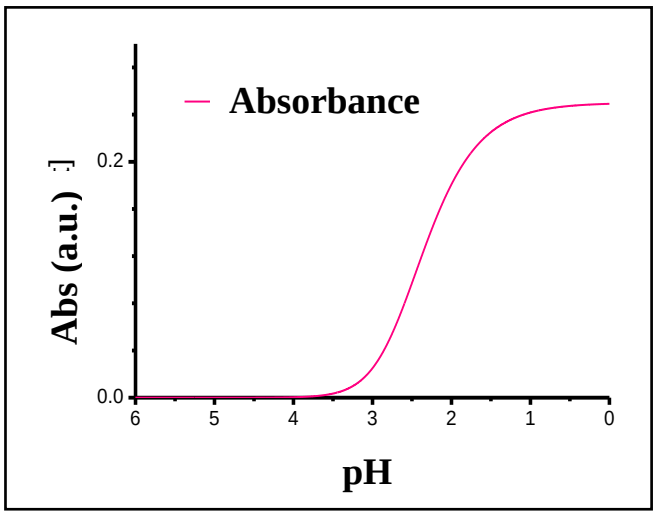

Figure 4.10. Calculated pH dependency curve for Rhodamine B in PVAl stabilized system (This curve shows an inflection point at pH 2.3 indicating pKa of 2.3).

The single mode measurement of $HgI_4(Rhodamine\ B)_2$ in PVAl-water based system at 590 nm is shown in **Figure 4.11**. The Beer's law validity is ranged from 10µg to 120µg of Hg(II). Above the validity limit, Beer's law started to deviate due to high analyte concentration and fluorescence interference. Further increasing the concentration can also lead to the instrument limitation where a plateau of absorbance is observed. For a given method, it is regarded as sensitive when the molar absorptivity (absorption coefficient), Є is greater than 1×10^3 l $mole^{-1}cm^{-1}$ (Marczenko & Balcerzak, 2000). Therefore, this method is classified to be sensitive with the molar absorptivity determined at 590 nm = 16.84×10^3 l $mole^{-1}cm^{-1}$ and L.O.D to be approximately 10 µg @ 10 µg / 10 ml = 1ppm of Hg(II). As compared to the benzene extraction method, this method seems to be less sensitive due to the lower Є and higher L.O.D value detected. However, this method does not require an extra step of extraction in which this can directly decrease the analysis time as well as lowering the error imposed during the measurement.

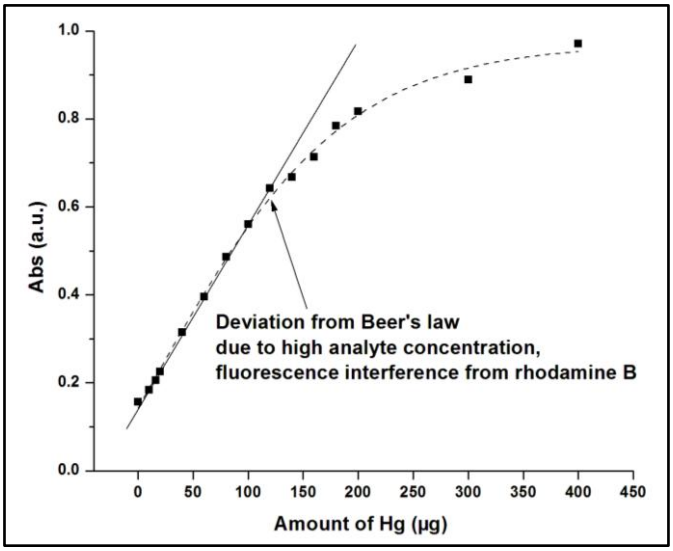

Figure 4.11. Single wavelength analysis (590 nm) of PVAl stabilized Rhodamine B-Hg(II)-Iodide complex at different amount of Hg(II).

4.4. Assessment of Rhodamine B in Mercury Determination

Due to higher sensitivity and lower L.O.D. of benzene extraction method, the applicability of benzene extraction method was tested in studying the sorption of Hg(II) onto CuS. **Table 4.1** shows the analytical results measured using benzene extraction method and cold vapor atomic absorption spectrometry (CVAAS). The % concentration difference measured by benzene extraction method and CVAAS are estimated to be 9.5 to 12.4%. These results signify that the Hg(II) concentration measured by benzene extraction method is comparable to the case of CVAAS. Thus, this method is highly applicable for trace Hg(II) analysis.

Table 4.1. Comparison of the results obtained from benzene extraction method using UV-Visible spectrophotometry and CVAAS method.

Time (Hour)	Benzene extraction method (ppm)	CVAAS (ppm)	% Concentration difference
1	34.02 ± 6.80	37.61 ± 3.76	9.54
2	34.08 ± 6.82	36.67 ± 3.67	7.06
3	33.25 ± 6.65	36.36 ± 3.64	8.56
4	31.04 ± 6.21	35.61 ± 3.56	12.83

4.5. Summary

Homogeneous Hg(II) complexation by Rhodamine B and iodide revealed the precipitation of Rhodamine B-Hg(II)-Iodide in acidic media. The precipitation of Rhodamine B-Hg(II)-Iodide seems to be a promising way in separating mercury from aqueous solution. However, its usage is still restricted due to the labile characteristic of Rhodamine B-Hg(II)-Iodide complex in the water stream. Thus, mercury and its species cannot be immobilized in water system and they can be re-dispersed back into the environment upon the complexation process. The problem on the utilization of Rhodamine B for aqueous complexation can be also associated to the stability of Rhodamine B-Hg(II)-Iodide complex at alkaline solution pH. It has been shown in our studies that Rhodamine B can only function well in protonated ionized form at low pH. Apparently, an increase in solution pH can degrade the Rhodamine B-Hg(II)-Iodide complex. This has indirectly resulted in a secondary pollution by introducing Rhodamine B as well as regenerating mercury and its related species back into the water system.

Despite the labile and pH dependent properties of Rhodamine B in complexing mercury, the reaction between Rhodamine B and tetraiodomercurate(II) does provide a non-destructive approach for mercury detection in comparison to the well established destructive technique, cold vapor atomic absorption (CVAAS). The extraction of Rhodamine B-Hg(II)-Iodide complex in organic solvent *i.e.* benzene or stabilization using protective colloid polymer i.e PVAl in water shows that this complex can be measured easily using spectrophotometric method. Both of the proposed methods are regarded as sensitive with molar absorptivity, ϵ, 17.68×10^4 L $mole^{-1}cm^{-1}$ for benzene extraction and 16.84×10^3 $Lmole^{-1}cm^{-1}$ for PVAl stabilization. The benzene extraction method was also tested in assessing the performance of Covellite in Hg(II) removal. The results obtained using the benzene extraction is comparable to the well established CVAAS method.

Therefore, this suggested the applicability of the benzene extraction method for trace Hg(II) analysis.

In comparison of the two methods, the applicable ranges for benzene extraction seem to be narrower than PVAl stabilization in which the range is evaluated to be 5 – 27 μg @ (0.25 – 1.25) ppm of Hg(II) and 10 – 120 μg @ (1 – 12) ppm of Hg(II) respectively. However, the L.O.D for benzene extraction seem to be better than PVAl stabilization with the values estimated to be 5μg @ 5 μg / 20 ml = 0.25 ppm of Hg(II) and 10μg @ 10 μg / 10 ml = 1 ppm of Hg(II) respectively. The L.O.D for the benzene extraction technique is similar to the method developed by Ramakrishna et al. who employed Rhodamine 6G and iodide in the presence of gelatin. The method gave L.O.D of 5 μg mercury per 25 ml at 575 nm with molar absorptivity = 7.0×10^4 l $mole^{-1}cm^{-1}$ (Ramakrishna, et al., 1976). Nevertheless, the L.O.D for the benzene extraction technique seems to be higher when compared to the method demonstrated by Hermandez et al. The method showed 1 μg mercury per 25 ml at 610 nm with molar absorptivity = 1.1×10^5 l $mole^{-1}cm^{-1}$ (Hernandez-Córdoba, et al., 1984).

CHAPTER 5

HETEROGENEOUS AQUEOUS MERCURY COMPLEXATION – MIXED PHASE COVELLITE

With restricted mobility of solid phase complexing agent, solid phase sorbent can be more effective towards the immobilization of mercury species from re-disperse back into the environment. In the following sections, the examination is focusing on the use of solid phase sorbent *i.e.* Covellite (CuS) for Hg(II) removal. The assessment of CuS in removing aqueous Hg(II) was examined preliminary using heavily oxidized CuS namely, mixed phase Covellite which consists of about 67% CuS and 33% $CuSO_4$. Effect of solution pH on mercury uptake, sorption kinetic and sorption isotherm of Hg(II) onto mixed phase CuS has been studied. The reacted samples were also characterized using PXRD, FESEM-EDX and XPS to obtain the initial understanding on the sorption profile. The investigation of mixed phase Covellite in removing Hg(II) is of importance because mineral sulfides are prone to oxidation in the oxidic condition. The passivation of $CuSO_4$ on CuS towards the activity of Hg(II) sorption is a critical issue that needed to be explored before the studies is extended to the use of well preserved phase pure Covellite (CuS).

5.1. Effect of Initial Solution pH on Mercury Uptake

The solution pH plays an important role in the sorption processes. An alternation of the solution pH condition can undeniably result in a huge change on the ionization species that present in the solution and affect the activity of the solid sorbent (Al Rmalli, Dahmani, Abuein, & Gleza, 2008). Therefore, the information on optimum pH for maximum Hg(II) sorption must be obtained before proceeding into further physicochemical analysis. **Figure 5.1** illustrates the effect of solution pH on the percentage removal of Hg(II) by mixed phase

Covellite at temperature of 25°C. In 100 ppm Hg(II) solution, it is clearly observed that initial solution pH has no effect on the percentage removal of Hg(II) in which ≈100% removal can be achieved. When Hg(II) concentration was increased to 250 ppm, similar case is observed from pH 1 – 7 in which constant Hg(II) removal of 95-99% is reached. However, as initial pH of Hg(II) solution is increased to 8 and 9, a significant drop of Hg(II) removal with values of ≈89.27% and ≈45.33% is detected respectively. This result shows that there is a decreased tendency for Hg(II) removal of mixed phase Covellite with solution pH elevation. In addition, the decreasing trend of Hg(II) removal efficiency at alkaline pH has become prominent at increasing Hg(II) concentration. With a better Hg(II) uptake at acidic condition, the initial solution pH used was decided to fix at 4 throughout the entire sorption studies. The fixing of pH 4 in further sorption studies aimed to avoid any unnecessary changes on CuS at extemene case i.e. pH 1 and to ensure maximum level of Hg(II) can be loaded onto mixed phase Covellite for solid phase investigation.

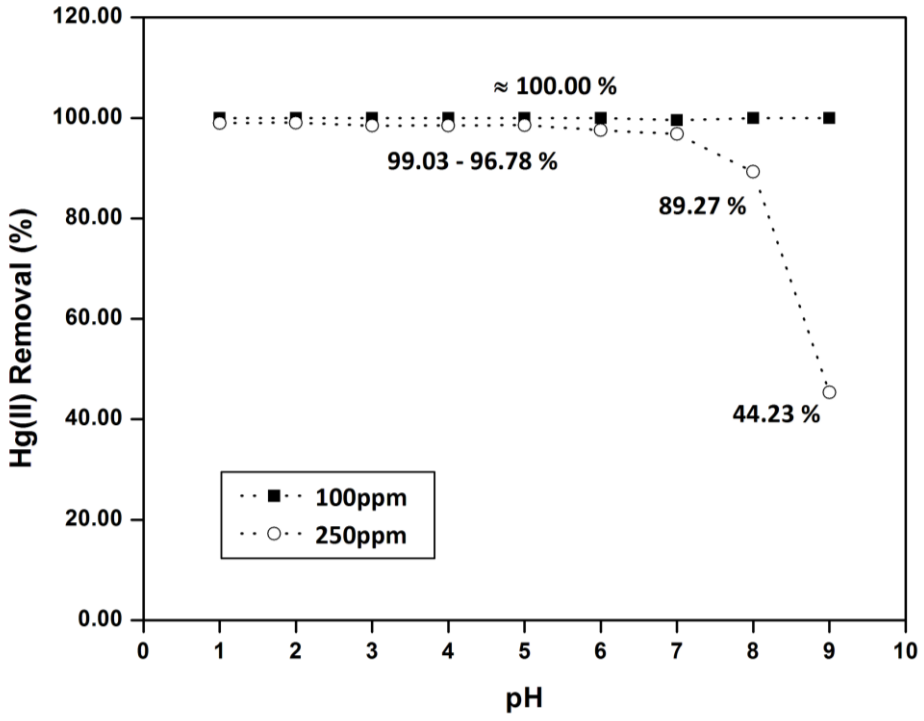

Figure 5.1. Effect of solution pH on the sorption of Hg(II) onto mixed phase Covellite.

5.2. Dynamic Modeling on Mercury Sorption Kinetic

5.2.1. Effect of Contact Time on Mercury Uptake

The effect of contact time on the Hg(II) removal was investigated using four Hg(II) solution of different concentrations, namely 100 ppm, 250 ppm, 400 ppm and 800 ppm at pH 4 and 25°C. The results are presented in **Figure 5.2**. Regardless of Hg(II) concentration used, it is observed that the sorption of Hg(II) onto mixed phase Covellite proceed in a two stage process *i.e.* a rapid initial uptake in the time region of approximately 200 mins followed by a slow removal which attain an equilibrium condition in approximately 400 minutes. The rapid uptake observed at the initial stage is typically due to the abundant availability of active sites on mixed phase Covellite which gradually got occupied with time. The decreasing removal rate, particularly towards the time approaching equilibrium, is mostly related to the decreased concentration of Hg(II) in the solid-liquid interface region as well as the reduced number of available active site for sorption of Hg(II) onto mixed phase Covelite as reaction time is prolonged. According to this result, the contact time was thus set at 15 hours (900 mins) for the entire sorption experiments in order to ensure the equilibrium conditions are established.

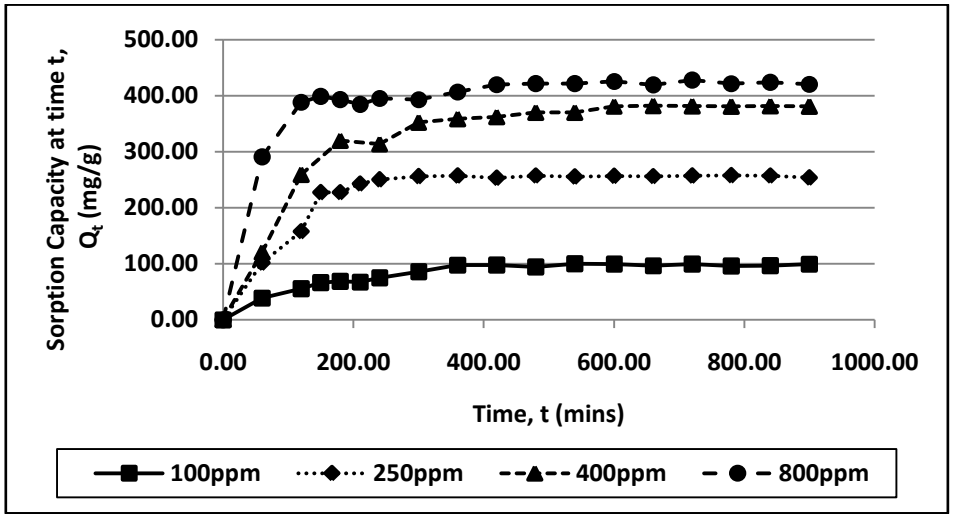

Figure 5.2. Effect of contact time on the sorption of Hg(II) onto mixed phase Covellite.

5.2.2. Elovich's Kinetic Model

Elovich's kinetic model or the Elovich equation is the rate equation, proposed by Roginsky and Zeldovich in 1934 to describe the adsorption kinetic of carbon monoxide onto manganese dioxide (Roginsky & Zeldovich, 1934). This model is one of the most useful models for describing activated chemical adsorption where this model takes into account of the chemical adsorption (Chemisorption) of adsorbate onto solid surface. Nevertheless, the desorption and dissociation of the chemical products from the surface back to the surrounding environment is not considered in the construction of this model. Thus, the sorption rate will decrease gradually due to an increase in surface coverage with time (Aharoni & Tompkins, 1970). **Figure 5.3** depicts the results in fitting the experimental sorption data with Elovich's kinetic model. The predicted initial sorption rate (a), the Elovich constant (b) as well as the evaluated correlation coefficient (R^2) are shown in Table **5.1**. From the fitting results, it is observed that the sorption data for the entire period of study is not fitted well to this model as all of the R^2 shown is less than the nominal value of good fit i.e. 0.9800 (Christian, 2003). This shows a strong indication in which this model is not appropriate in describing the sorption of Hg(II) onto mixed phase Covellite for the entire period of sorption time.

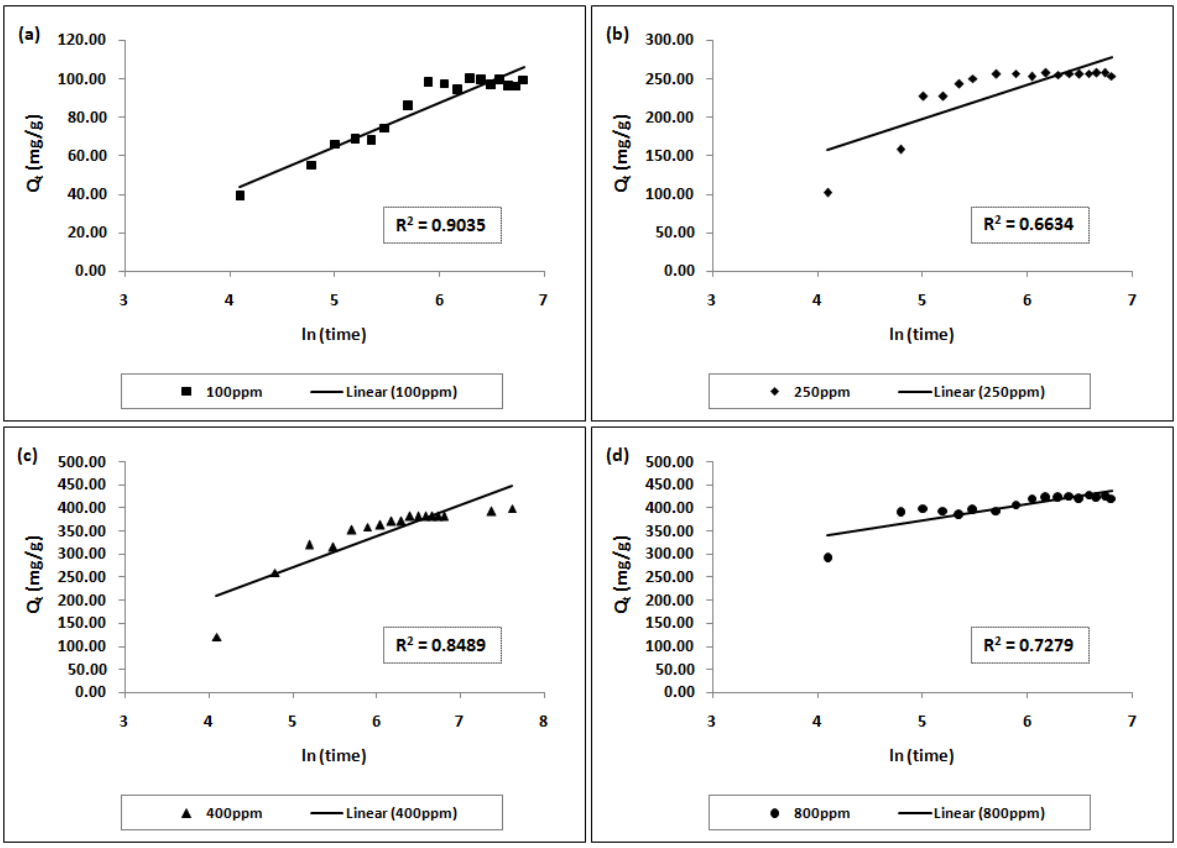

Figure 5.3. Elovich's kinetic plot for the sorption of (a) 100 ppm (b) 250 ppm (c) 400 ppm and (d) 800 ppm Hg(II) onto mixed phase Covellite.

Table 5.1. List of kinetic parameters evaluated using Elovich's kinetic model for the sorption of Hg(II) onto mixed phase Covellite.

Initial Hg(II) Concentration, C_0 (ppm)	Initial Sorption Rate, a (mg/(gmin))	Elovich Constant, b (g/mg)	Correlation Coefficient, R^2
100	0.0048	0.0435	0.9035
250	0.0129	0.0224	0.6634
400	0.0019	0.0121	0.8489
800	6.4461	0.0280	0.7279

5.2.3. Pseudo First-order Kinetic Model

The pseudo first-order kinetic model was first presented by Lagergren in describing the adsorption of oxalic acid and malonic acids onto charcoal (Lagergren, 1898). This model

considers the rate of sites occupation is proportional to the number of unoccupied sites. **Figure 5.4** illustrates the results in fitting the experimental sorption data with Lagergren's kinetic model. The predicted rate constants (k), equilibrium sorption capacity (Q_e) as well as the evaluated correlation coefficient (R^2) are shown in **Table 5.2**. It is seen that at all Hg(II) concentrations studied, most of the sorption data shows poor correlation coefficients ($R^2 < 0.9800$) when fitted with Lagregren's kinetic model. This implies that the sorption of Hg(II) onto mixed phase Covellite might not be represented well by Lagregren's kinetic model.

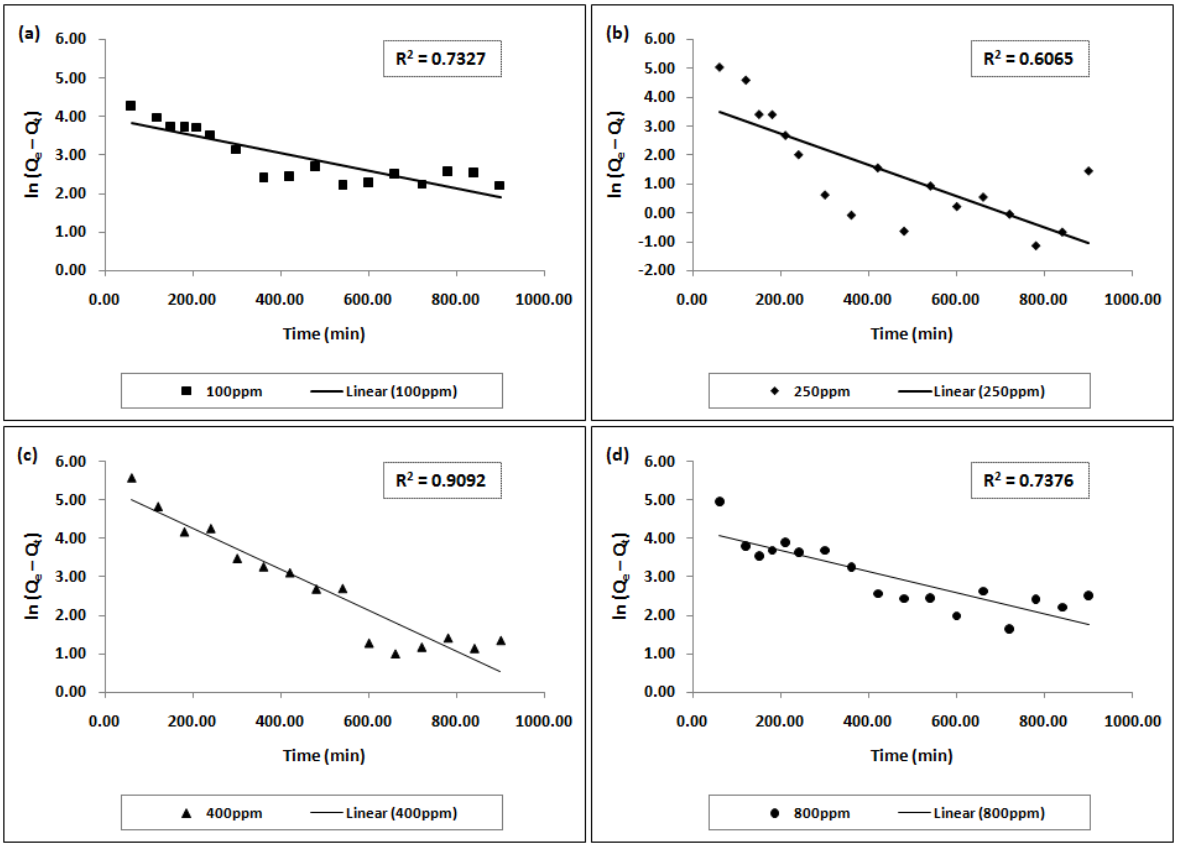

Figure 5.4. Pseudo first-order kinetic plot for the sorption of (a) 100 ppm (b) 250 ppm (c) 400 ppm and (d) 800 ppm Hg(II) onto mixed phase Covellite.

Table 5.2. List of kinetic parameters evaluated using pseudo first-order kinetic model for the sorption of Hg(II) onto mixed phase Covellite.

Initial Hg(II) Concentration, C_0 (ppm)	Sorption Capacity at equilibrium, Q_e (mg/g)	Rate Constant, k (l/min)	Correlation Coefficient, R^2
100	52.04	0.0023	0.7327
250	44.84	0.0054	0.6065
400	205.74	0.0053	0.9092
800	69.21	0.0028	0.7376

5.2.4. Pseudo Second-order Kinetic Model

The pseudo second-order kinetic model was first proposed by Blanchard et al. in describing the ion exchange reaction of heavy metal by natural zeolite (Blanchard, et al., 1984). The assumption behind this model is that the kinetic order of this reaction is two with respect to the number of adsorption site available for the exchange processes. In these studies, the fitting of sorption kinetic data, however, is carried out using Ho's linear pseudo second-order rate equation (Ho, 1995; Ho, Wase, & Forster, 1996) in which this is the most commonly applied form of the pseudo-second order kinetic model. The result of fitting experimental data with Ho's pseudo second-order model is shown in **Figure 5.5**. The predicted rate constants (k), equilibrium sorption capacity (Q_e) as well as the evaluated correlation coefficient (R^2) are shown in **Table 5.3**. It was found that all of the sorption data exhibit highest correlation coefficients ($R^2 > 0.9800$) when fitted with Ho's kinetic model regardless of the Hg(II) concentration and for sorption time applied. Thus, it is apparent that the kinetic data follows well to the pseudo-second order kinetic model in which the kinetic order should be two with respect to the overall order for the reaction.

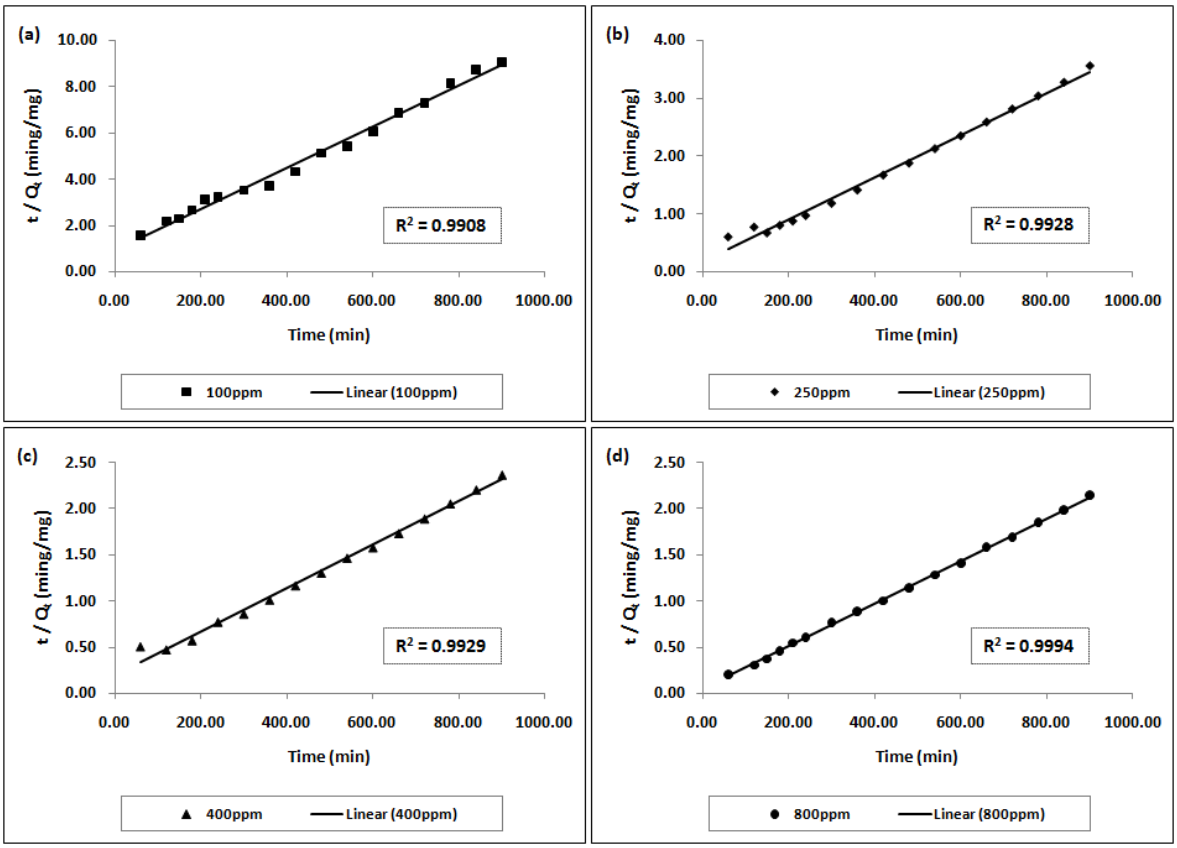

Figure 5.5. Pseudo second-order kinetic plot for the sorption of (a) 100 ppm (b) 250 ppm (c) 400 ppm and (d) 800 ppm Hg(II) onto mixed phase Covellite.

Table 5.3. List of kinetic parameters evaluated using pseudo second-order kinetic model for the sorption of Hg(II) onto mixed phase Covellite.

Initial Hg(II) Concentration, C_0 (ppm)	Sorption Capacity at equilibrium, Q_e (mg/g)	Rate Constant, k x 10^{-2} (g/(mgmin))	Correlation Coefficient, R^2
100	112.36	0.0086	0.9908
250	270.27	0.0084	0.9928
400	434.78	0.0027	0.9929
800	434.78	0.0109	0.9994

5.3. Interpretation on Sorption Isotherm

The capability of sorbent in removing the targeted sorbate is commonly evaluated by the maximum amount of sorbate that can be retained in the solid sorbent. In this case, the studies on the maximum sorption capacity of mixed phase Covellite in removing Hg(II) has been conducted under the variation of initial Hg(II) concentration in which the equilibrium data were collected and it was analyzed using linearized Langmuir and Freundlich isotherm models. The main reason for the extended use of these isotherm models is that they integrated with constants that are easily interpretable and the evaluation can be done without any advanced computational procedure. The linear least-squares method (correlation coefficient, R^2 evaluation) is used to verify the best fitted model since it is the most common method for fitting a straight line model with experimental data. The linear plot of Langmuir and Freundlich models at pH 4 and 25°C are shown in **Figure 5.6 (a)** and **(b)** respectively while the model constants of both Langmuir and Freundlich isotherms along with the correlation coefficient (R^2) are tabulated in **Table 5.4**. Among the sorption isotherm models, application of Langmuir isotherm equation in this study showed a reasonably good results with R^2 = 0.9999 compared to the R^2 = 0.8207 obtained in Freundlich isotherm equation. High correlation coefficient values (0.9999) for the Langmuir isotherm suggests that mixed phase Covellite must have a limited sorption capacity in which it is due to the monolayer coverage of Hg(II) on mixed phase Covellite. The maximum Hg(II) uptake upon complete saturation, Q_{max} which is estimated by Langmuir isotherm is found to be 416.67 mg Hg(II) / g of sorbent. With high amount of $CuSO_4$ (≈33.0%) passivated on the CuS sorbent, the Q_{max} determined for mixed phase Covellite is surprisingly high when compared to the Q_{max} determined for Pyrite, FeS_2 (Q_{max} = 1.23 mg/g) in which the experiments is also conducted in a similar manner i.e. an acidic condition of pH = 4.1 (Bower, et al., 2008).

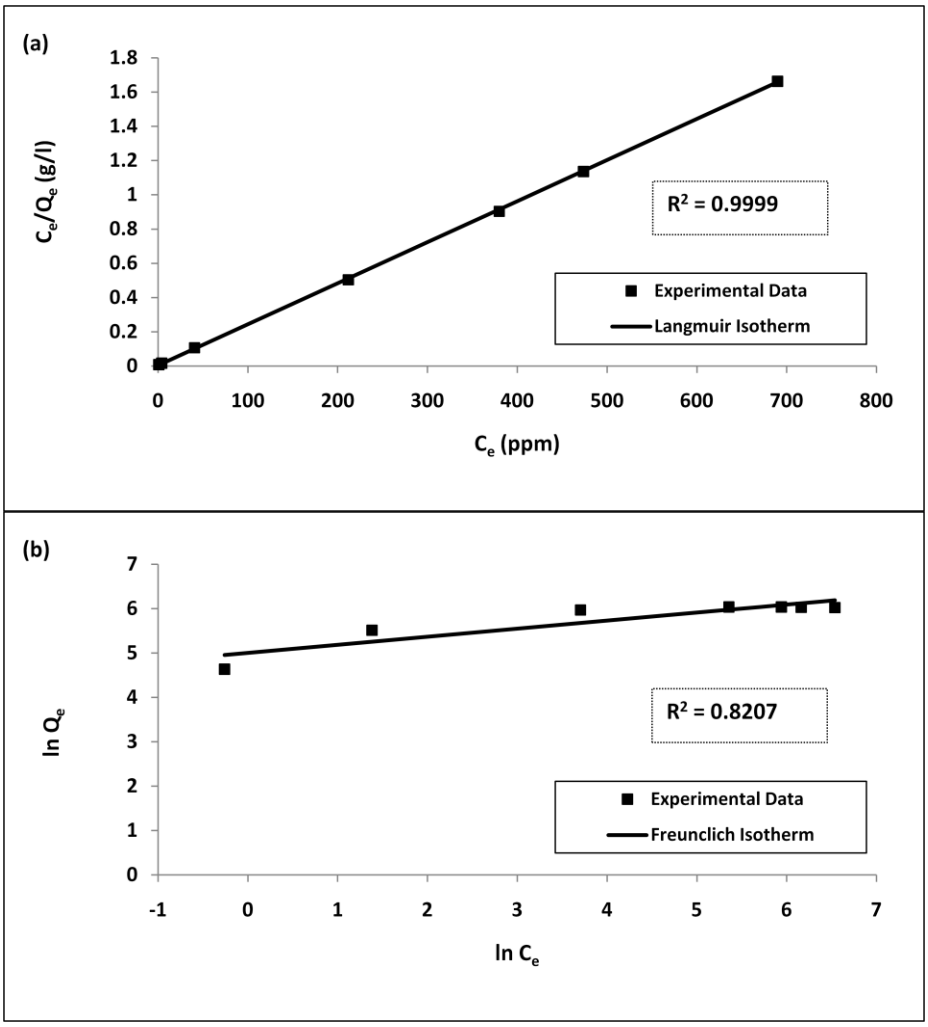

Figure 5.6. Fitting of equilibrium sorption data using
(a) Langmuir Isotherm (b) Freundlich Isotherm

Table 5.4. Langmuir and Freundlich Isotherm Constants and their corresponding Correlation Coefficients (R^2) for the sorption of Hg(II) onto mixed phase Covellite.

(a) Langmuir Isotherm		(b) Freundlich Isotherm	
R^2	0.9999	R^2	0.8207
K_a, (l/mg)	0.6486	K_F, (mg/g)(l/mg)$^{1/n}$	149.46
Q_{max}, (mg/g)	416.67	1/n	0.1812

5.4. Powder X-Ray Diffraction (PXRD) Analysis

The PXRD pattern of mixed phase Covellite used is displayed in **Figure 5.7**. From the data, two distinguished phases of crystalline compounds are identified from the diffractogram. The first compound is identified to be CuS in which all the characteristic peaks correspond well to the phase pure CuS in the space group of *P63/mmc* and is well indexed to hexagonal Covellite (PDF 00-006-0464, a = b = 3.79 Å, c = 16.34 Å). The second compound is found to be $CuSO_4.5H_2O$ in which all the characteristic peaks correspond well to the phase pure $CuSO_4.5H_2O$ in the space group of *P-1(2)* and is well indexed to triclinic Pentahydrate Copper Sulfate (PDF 01-077-1900, a = 6.12 Å, b = 10.72 Å, c = 5.97 Å). Rietveld refinement quantification analysis was done to quantify the phase composition of CuS in relative to $CuSO_4.5H_2O$ found in the sample. The Rietveld refinement fitting of the sample is displayed in **Figure 5.8** while the fitted parameters are illustrated in **Appendix A**. The result shows that the sample consisted of about 67% CuS in relative to 33% $CuSO_4.5H_2O$.

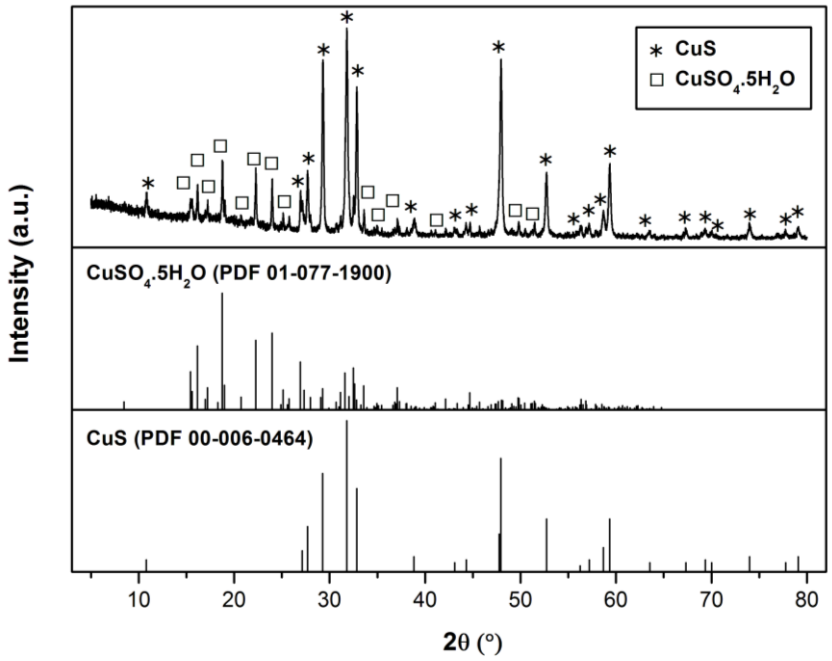

Figure 5.7. PXRD pattern of unreacted mixed phase Covellite.

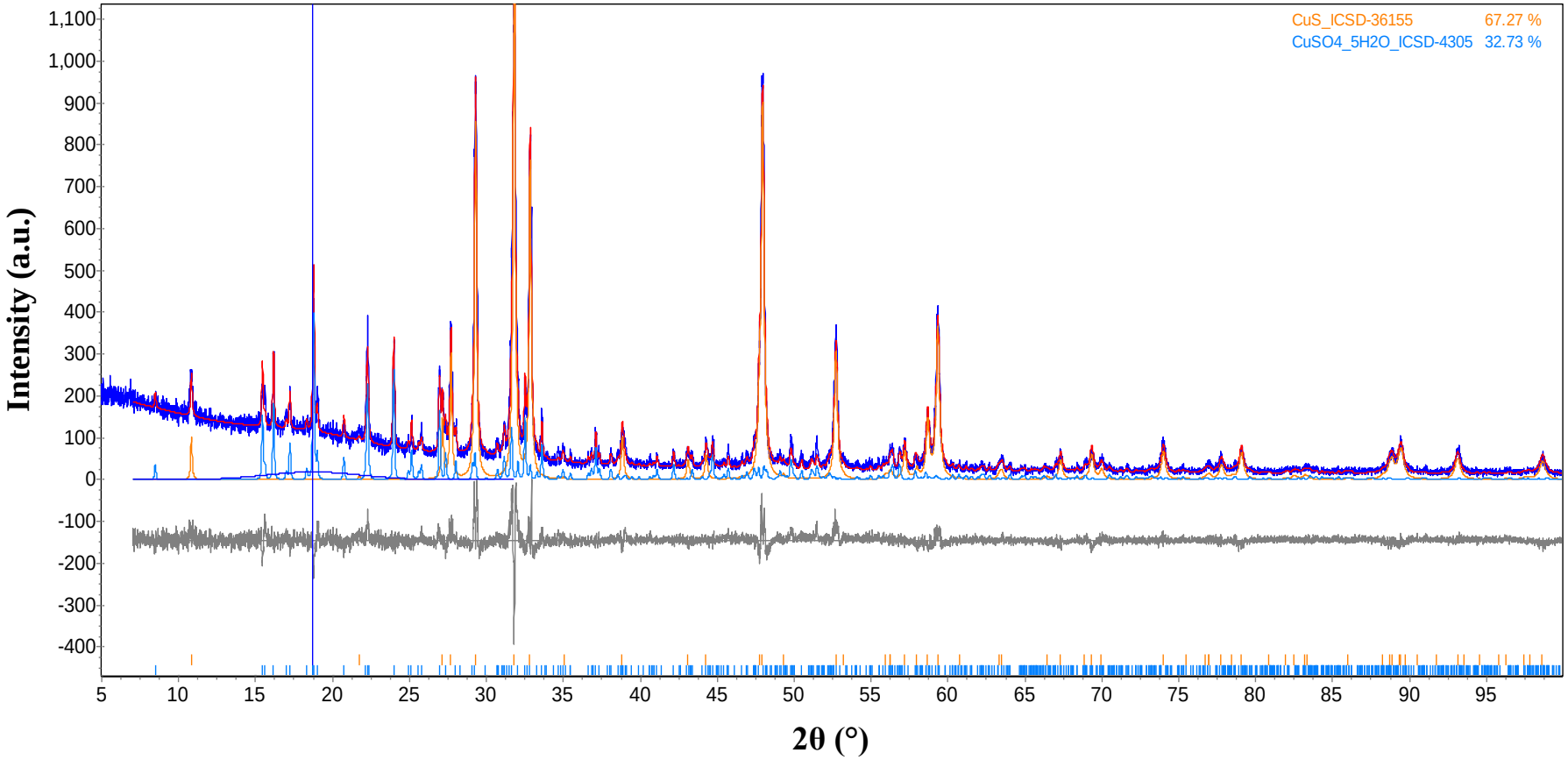

Figure 5.8. Rietveld refinement quantification analysis of CuS and $CuSO_4.5H_2O$ in unreacted mixed phase Covellite.

Figure 5.9 illustrates the PXRD pattern of reacted mixed phase Covellite under initial Hg(II) concentration of 250 ppm, initial solution pH of 4, reaction time of 15 hours and temperature of 25°C. From the diffractogram, it can be seen that the characteristic peaks of Covellite (CuS) phase are attested in the reacted powder in which large amount of unreacted CuS are present at the end of the reaction. In comparison to the PXRD pattern of unreacted mixed phase Covellite, the characteristic peaks of the triclinic $CuSO_4.5H_2O$ phase was found to be disappeared at the end of the reaction. Since triclinic $CuSO_4.5H_2O$ is highly soluble in water in which approximately 31.7g of $CuSO_4.5H_2O$ can dissolve completely in 100 ml of water at 0°C to yield ionic species of $Cu(H_2O)_6^{2+}$ and SO_4^{2-} (International Programme on Chemical Safety (IPCS), 2001), the disappearance of $CuSO_4.5H_2O$ phase from the PXRD pattern relates well to the dissolution process that occurs during the reaction. On the other hand, the powder diffraction pattern also shows some additional peaks which is crystalline in nature but the chemical identities of this compound is unidentified from the search and match library of Powder Diffraction File (PDF). The most intense peak of this unknown compound is located at $2\theta \approx 34.70°$. In combination to other unknown peaks, it is identified that this newly formed crystallite has some resemblance to $Hg_3S_2Cl_2$. Still, a detail matching analysis reveals that the reference pattern of $Hg_3S_2Cl_2$ cannot fits completely well to the unknown peaks in reacted mixed phase Covellite.

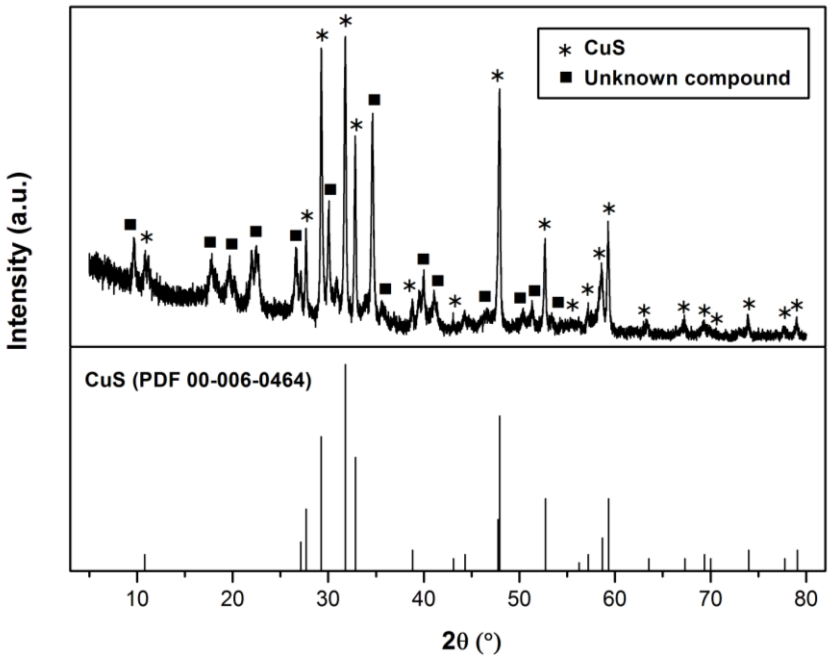

Figure 5.9. PXRD pattern of reacted mixed phase Covellite.

5.5. Field Emission Electron Microscopy and Energy Dispersive X-ray Spectroscopy (FESEM-EDX)

The morphology of unreacted mixed phase Covellite has been examined under the FESEM in which the results are depicted in **Figure 5.10 (a) – (c)**. From the low magnification FESEM image, it is observed that the mixed phase Covellite is comprised of highly agglomerated morphology. Meanwhile, it is observed that the agglomerated structure is actually composed of many hexagonal plates from the higher magnification FESEM images. The morphology of the mixed phase Covellite powder is found to be the same as the morphology of the pure phase Covellite powder detected in **Section 6.7.1**. This signifies that the transformation of CuS to $CuSO_4.5H_2O$ will not result in any morphology changes during the oxidation process. The elemental composition of the hexagonal plate morphology was analyzed using EDX. The EDX spectra of the hexagonal plate morphology and its respective elemental quantification under the electron gun accelerating voltage of 20kV are shown in **Figure 5.11**. From the results, it is found that the chemical

composition of the hexagonal plates is consisting mainly of copper (41.12%) and sulfur (40.10%) where significantly high amount of oxygen (18.78%) is also detected. Although high amount of oxygen is found on the hexagonal plates, the atomic ratio of Cu: S calculated is still 1: 1.03. This value agrees well to the ideal atomic ratio of Covellite (CuS) which is Cu: S = 1: 1. From the value of Cu: S = 1: 1.03 identified, it is obvious that the transformation of CuS to $CuSO_4.5H_2O$ does not altered the composition of copper and sulfur in the Covellite powder. The oxidation process will only lead to crystallographic changes from hexagonal phase CuS to triclinic phase $CuSO_4.5H_2O$ which can be identified by PXRD.

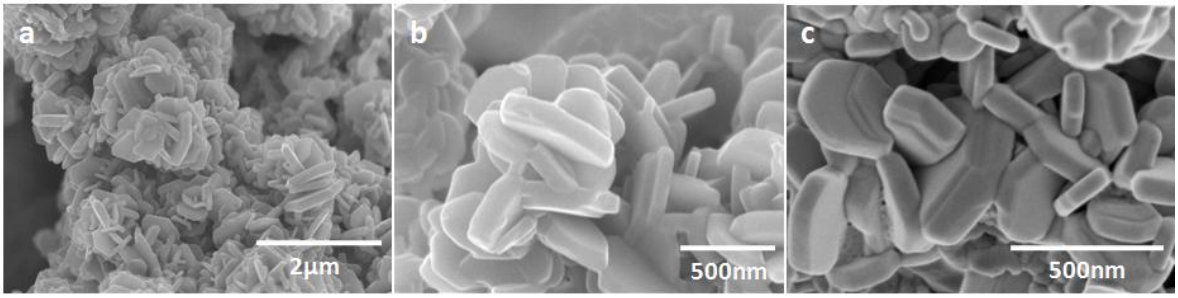

Figure 5.10. FESEM images of unreacted mixed phase Covellite with magnifications of (a) 20 000x (b) 60 000x and (c) 100 000x.

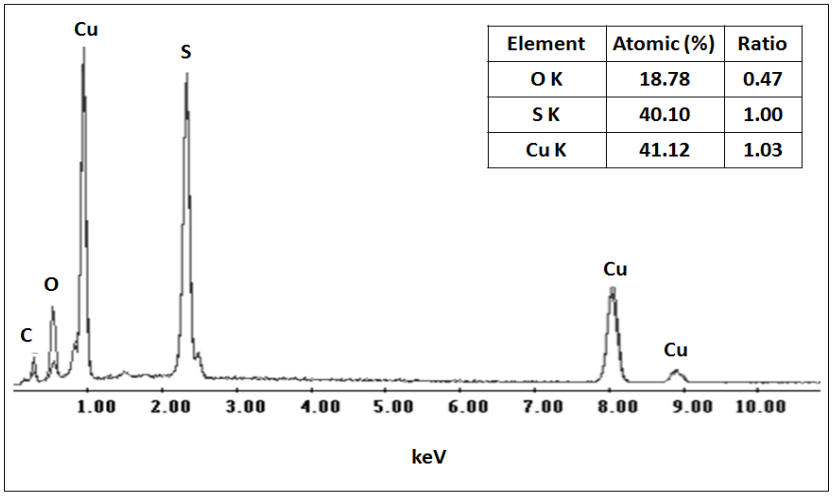

Element	Atomic (%)	Ratio
O K	18.78	0.47
S K	40.10	1.00
Cu K	41.12	1.03

Figure 5.11. EDX spectra of hexagonal plates and its respective elemental quantification result observed in unreacted mixed phase Covellite.

Figure 5.12 illustrates the morphology of the reacted mixed phase Covellite under initial Hg(II) concentration of 250 ppm, initial solution pH of 4, reaction time of 15 hours and temperature of 25℃. From **Figure 5.12 (a) and (b)**, it is identified that the initial agglomerated morphology of unreacted mixed phase Covellite remained at the end of the reaction. Nevertheless, it can be also observed that an additional formation of nanoscale needle like morphology namely nano-needle crystallites have grown on the initial hexagonal base material. From PXRD analysis earlier, it was detected that an extra unknown crystalline compound has formed on top of the hexagonal phase Covellite (CuS). Thus, it is strongly indicative the nano-needle crystallite identified herein correlates well with the unknown crystalline compound found previously. The chemical composition of the nano-needle crystallites is further analyzed using EDX. The EDX spectra of nano-needle crystallite and its respective elemental quantification result under the electron gun accelerating voltage of 20kV are shown in **Figure 5.13**. From the results, sulfur (43.12%) has contributed the highest amount among the elements found. This is followed by copper (37.51%), oxygen (11.01%) and a fairly low amount of mercury (6.35%) as well as chlorine (2.01%) detected in the morphology. The atomic ratio of Cu: S of the nano-needle morphology is calculated to be 0.87: 1 in contrast to the atomic ratio of Cu: S ≈ 1: 1 of unreacted mixed phase Covellite. In comparison of both of the values, it is apparent that the attachment of both mercury and chlorine onto the mixed phase Covellite has resulted in a loss of copper on the surface and additional growth of nano-needle crystallite on hexagonal plate morphology. Therefore, in order to obtain a comprehensive insight on the sorption of $HgCl_2$ onto the surface of mixed phase Covellite, surface sensitive tool *i.e* X-ray electron spectroscopy (XPS) will be used for further investigation.

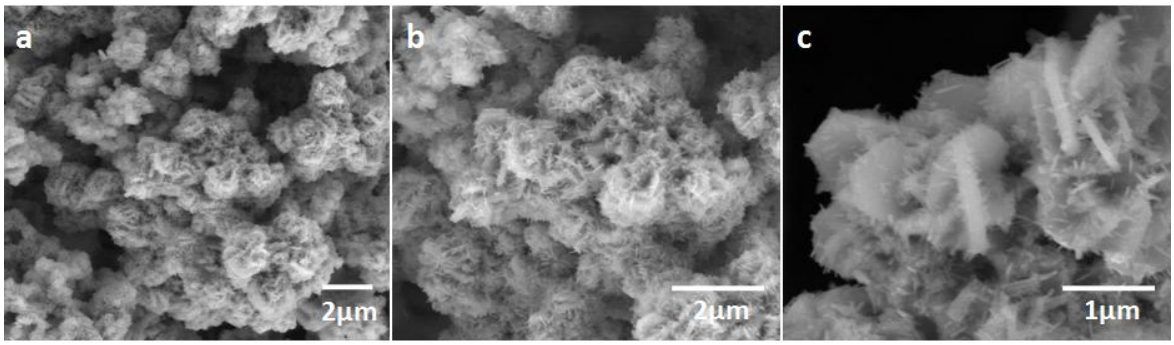

Figure 5.12. FESEM images of reacted mixed phase Covellite with magnifications of (a) 16 000x (b) 30 000x and (c) 60 000x.

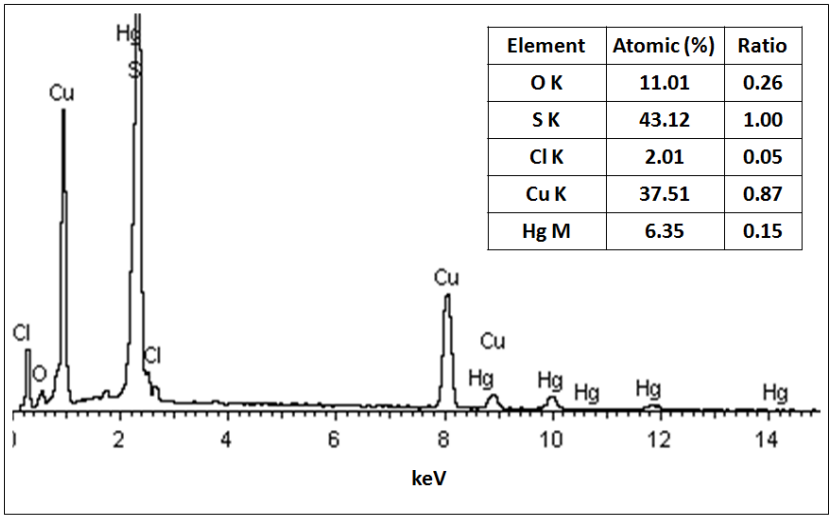

Figure 5.13. EDX spectra of nano-needle crystallite and its respective elemental quantification result observed in reacted mixed phase Covellite.

5.6. X-Ray Photoelectron Spectroscopy (XPS)

Unreacted and reacted mixed phase Covellite were characterized using XPS. The XPS survey scan spectra of unreacted mixed phase Covellite is shown in **Figure 5.14 (a)**. The important peaks of copper (Cu2p) and sulfur (S2p) are observed on the mixed phase Covellite surface. Their appearance is associated with a strong signal of O1s peaks at around 532eV. **Figure 5.14 (b)** depicts the XPS survey scan spectra of reacted mixed phase Covellite under initial Hg(II) concentration of 250 ppm, initial solution pH of 4, reaction time of 15 hours and temperature of 25°C. From the spectra, the presence of intense Hg4f

peaks at binding energy (B.E.) around 105eV confirms that Hg has been successfully sorbed onto the surface of mixed phase Covellite. Along with that, the sorption of Hg is also accompanied by the sorption of Cl^- onto the surface with Cl2p peaks observed at around 200eV. However, due to the intense signal of Hg4f peaks, no obvious changes is observed for the signal of Cu2p and S2p peaks in the XPS survey scan spectra.

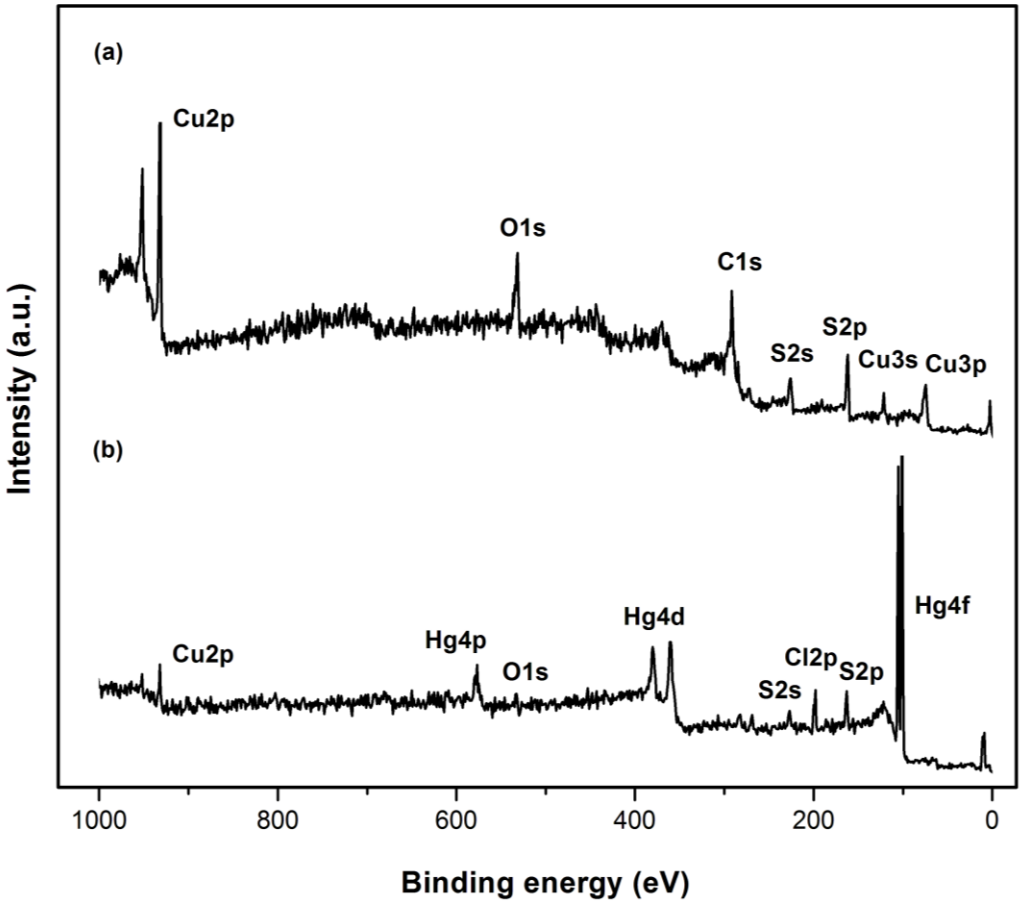

Figure 5.14. XPS survey scans of (a) unreacted and (b) reacted mixed phase Covellite.

Specific chemical states information for Hg, Cu, and S on the surface of unreacted and reacted mixed phase Covellite is available from the detail scan of Cu2p, S2p and Hg4f spectra. All the peaks de-convolution analysis has been carried out using a Gaussian-Lorentz (GL) function in CasaXPS software. In these studies, the detail scan of Cu2p, S2p and Hg4f spectra were collected at two kinetic energy (K.E.) *i.e* 200eV and 600eV to

investigate the distribution of chemical species at different depth condition. According to inelastic mean free path (IMFP) of electrons, variation on initial kinetic energy of the electron has a direct impact on the probability of the electron escape from each depth as well as frequency of detection of electrons from different depths in the solid. From the universal log-log plot of IMFP (nm) vs Energy (eV) as described in **Section 3.4.8**, the initial kinetic energy (K.E.) of electrons at 200eV gives ≈0.8 nm thickness of the surface information while for the initial kinetic energy (K.E.) of electrons at 600eV, it gives ≈1.0 nm thickness of the surface information.

The detail scans of $Cu2p_{3/2}$ spectra for unreacted and reacted mixed phase Covellite at K.E. of 200eV and 600eV are illustrated in **Figure 5.15** and **Figure 5.16** respectively. The main peaks of Cu(I) were detected at both B.E. around 932.35eV and 933.55eV (Goh, Buckley, & Lamb, 2006). The presence of these Cu(I) states in the spectra is consistent with the formation of CuS evidenced from the studies of XPS and X-ray absorption spectroscopy (XAS) (Goh, et al., 2006; Pattrick, et al., 1997). In addition, the real crystal structure of CuS was also determined as $(Cu)_3(S)(S_2)$ from single crystal experiment (Evans & Konnert, 1976). Thus, the two different Cu(I) state of CuS observed in XPS can be viewed as two different environment of Cu *i.e.* Cu-S and Cu-S_2 identified from single crystallography. From the figures, the signal of Cu(I) at B.E. around 933.55eV can be also related to Cu(II) species (B.E. around 933.50 – 934.00eV) (Fullston, Fornasiero, & Ralston, 1999; Lefèvre, Bessière, Ehrhardt, & Walcarius, 2003). This Cu(II) species is associated to the increased surface coverage of CuO upon oxidation of CuS (Fullston, et al., 1999). Besides, an additional peak is also identified at B.E. around 935eV. This main peak relates well to the feature of Cu(II) either in the form of $CuSO_3$, $CuSO_4$ or $Cu(OH)_2$ (Fullston, et al., 1999; Lefèvre, et al., 2003).

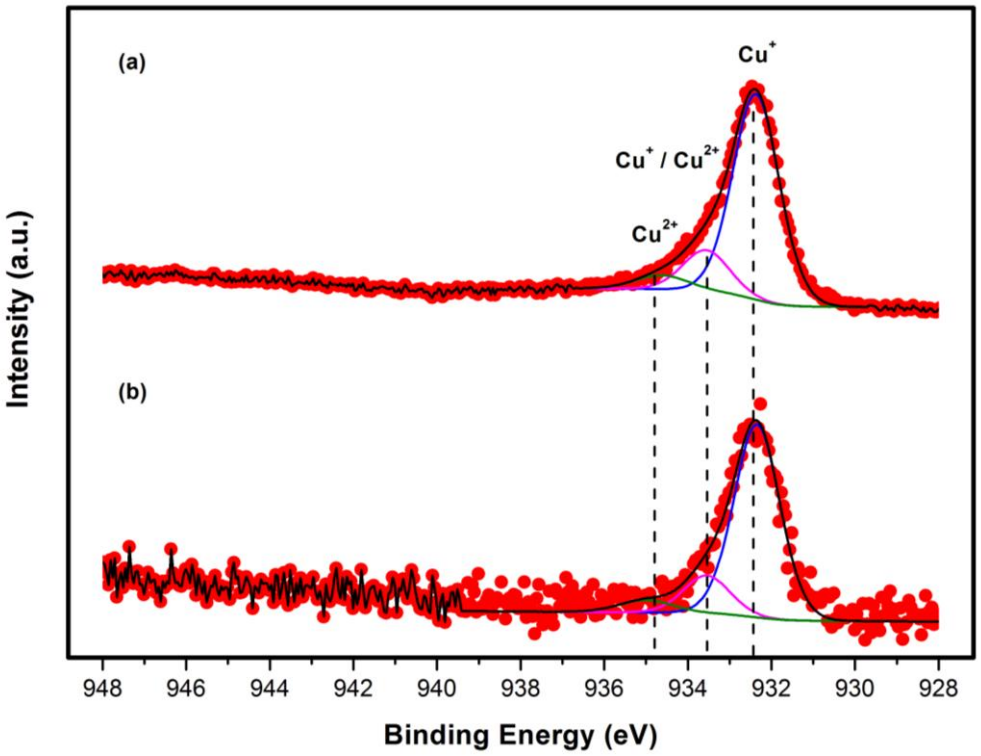

Figure 5.15. $Cu2p_{3/2}$ detail scans spectra of
(a) unreacted and (b) reacted mixed phase Covellite at K.E. of 200eV.

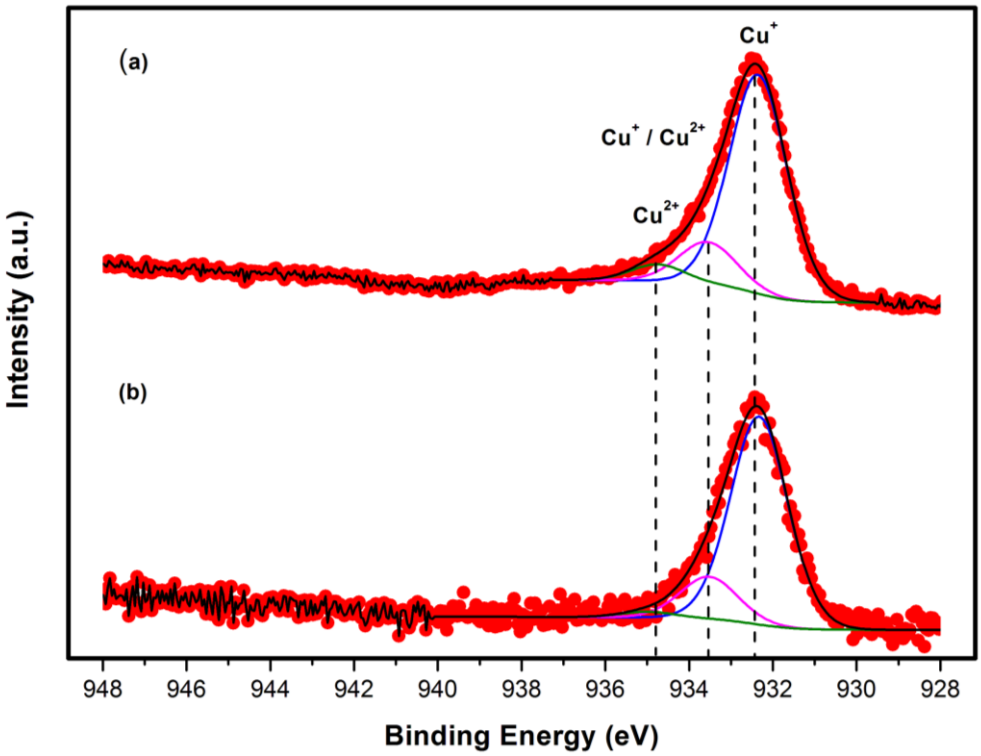

Figure 5.16. $Cu2p_{3/2}$ detail scans spectra of
(a) unreacted and (b) reacted mixed phase Covellite at K.E. of 600eV.

For reacted mixed phase Covellite, all signals of Cu(I) and Cu(II) are attested on Cu2p spectra regardless of the depth condition. Broadly speaking, the presence of these signals suggested that the sorption of Hg(II) onto mixed phase Covellite does not lead to any significant changes on the state of Cu. However, the dissolution of highly soluble $CuSO_3$ and $CuSO_4$ is occuring upon contact with water in which it is evidenced by their diminished signal in the S2p spectra of reacted mixed phase Covellite. In addition, CuO and $Cu(OH)_2$ can also remain on the surface mostly due to their relatively low solubility in water. It is noteworthy that the presence of CuO and $Cu(OH)_2$ on the surface can also play some role in complex Hg(II) since Fe-O compound such as Fe_3O_4 and FeOOH have also shown to be effective for Hg(II) removal (C. S. Kim, et al., 2004; Pan, et al., 2012).

Figure 5.17 and **Figure 5.18** depict the detail scans of S2p spectra for unreacted and reacted mixed phase Covellite at K.E. of 200eV and 600eV. In all cases, the S2p spectra shows an overlapped peak signal in which it is split by spin-orbit coupling into a doublet of $S2p_{1/2}$ and $S2p_{3/2}$ components. The components are separated by ≈1.20eV and have a theoretical $S2p_{1/2}$:$S2p_{3/2}$ area ratio of approximately 1:2 (Kurmaev, et al., 1998; Scofield, 1976). Comparing these two components, the B.E. of $S2p_{3/2}$ component provides useful information for specific sulfur chemical state identification. For unreacted mixed phase Covellite, an oxidized overlayer of SO_3 and SO_4 (with B.E. at ≈166.66eV and ≈168.74eV respectively) has been detected in covering the inner (K.E. of 600eV) and outer surface (K.E. of 200eV) (Moulder, Stickle, Sobol, & Bomben, 1992). The detection of oxidized overlayer of SO_4 correlates well to the triclinic $CuSO_4.5H_2O$ crystallite found in PXRD pattern of unreacted mixed phase Covellite.

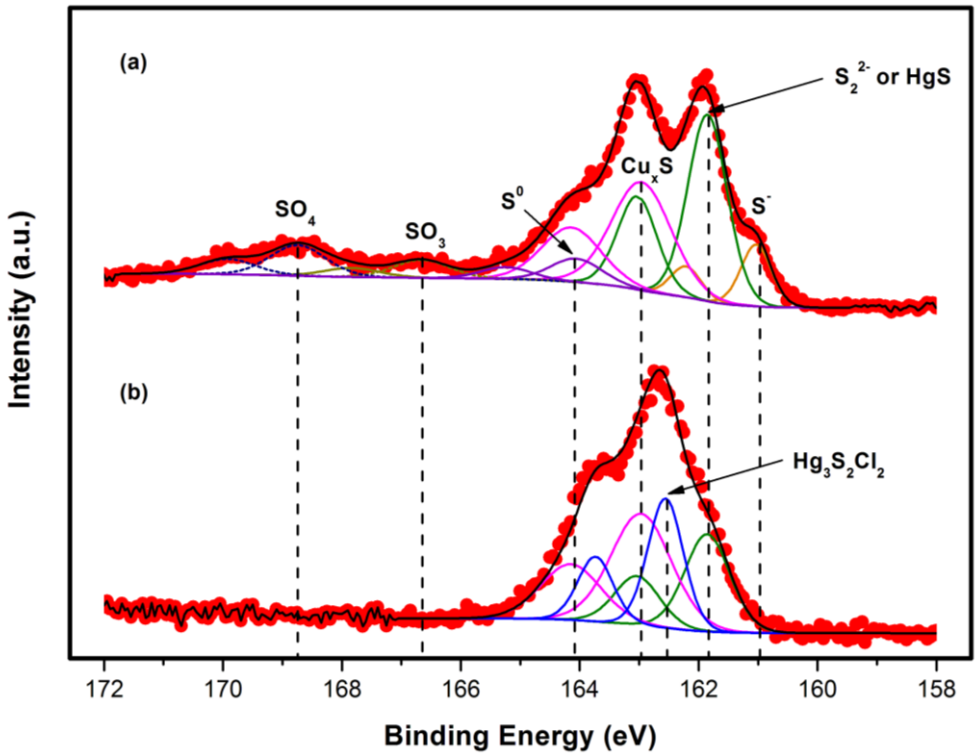

Figure 5.17. S2p detail scans spectra of
(a) unreacted and (b) reacted mixed phase Covellite at K.E. of 200eV.

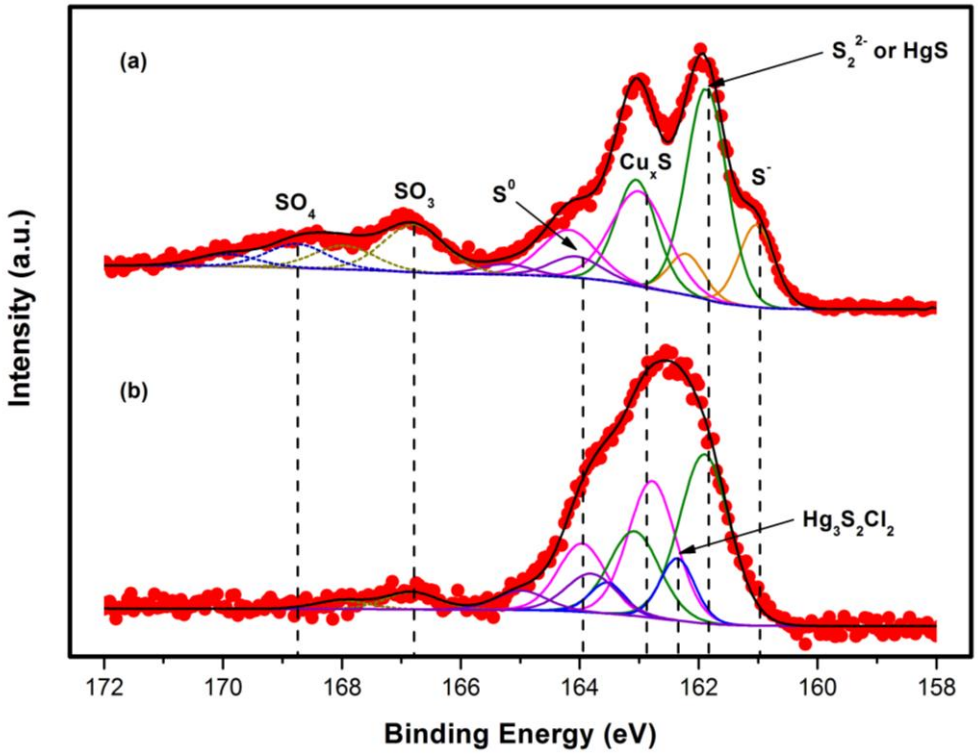

Figure 5.18. S2p detail scans spectra of
(a) unreacted and (b) reacted mixed phase Covellite at K.E. of 600eV.

For unreacted mixed phase Covellite, monosulfide (S^-) and disulfide (S_2^{2-}) species with B.E of ≈160.97eV and ≈161.85eV correspondingly are also found at both K.E. of 200eV and 600eV. These two sulfur species agrees well to the crystal structure of CuS in which it was found to compose of $Cu_3(S^-)(S_2^{2-})$ (Evans & Konnert, 1976; Goh, et al., 2006; Pattrick, et al., 1997). Besides, two other types of S species *i.e.* highly copper deficient nonstoichiometric sulfide, Cu_xS with $x < 2$ (B.E. at ≈162.96eV) (Kundu, Hasegawa, Terabe, Yamamoto, & Aono, 2008; Laajalehto, Kartio, & Nowak, 1994; Lefèvre, et al., 2003) and elemental sulfur, S^0 (B.E. at ≈164.06eV) (Moulder, et al., 1992) were also identified on the surface of unreacted mixed phase Covellite at both K.E. of 200eV and 600eV. These extra S species can be explained in views of the surface impurities that carried over from the reaction intermediate during synthesis of phase pure CuS.

For reacted mixed phase Covellite, absence of SO_3, SO_4, S^0 and S^- signals has been identified at K.E. of 200eV. Whilst at K.E. of 600eV, only the signal of SO_4 and S^- are missing. The loss of SO_3, SO_4 and S^0 signal from the surface is believed to be due to the dissolution process. The disappearance of SO_4 signal relates well to the high solubility of triclinic $CuSO_4.5H_2O$ in water. The detachment of both SO_3 and S^0 at K.E. of 200eV suggested that the dissolution process is preferably to occur at outer surface due to better exposure to the aqueous environment. Since Covellite (CuS) exhibits an exceptionally high solubility product in water ($K_{sp} = 8 \times 10^{-37}$) ("Solubility product constants," 2003), the loss of the S^- species from both of the inner and outer surface should not be due to any dissolution process. The S^- is acting as the responsible sulfur species for mercury complexation. In addition, the $S2p_{3/2}$ signal of copper deficient sulfide (Cu_xS) and disulfide (S_2^{2-}) are detected on both of the inner (K.E. of 600eV) and outer surface (K.E. of 200eV) of reacted mixed phase Covellite. The retention of Cu_xS and S_2^{2-} on reacted mixed phase

Covellite surface is unclear in this case. They might play the roles as spectator compounds or even in an indirect manner, might have certain ability in complexing aqueous mercury.

A special attention should be given to the signal of disulfide (S_2^{2-}) species. It is important to note that the chemical state of sulfur in cinnabar, HgS, exhibits the same B.E as disulfide (S_2^{2-}) at ≈161.85eV (Hyland, et al., 1990). The resolution is impossible by comparing the B.E values of the two species. The additional peak evolution (at B.E of ≈162.5eV) in the S2p spectra of reacted powder (K.E. at both 200eV and 600eV) shows significant finding on the sorption profile of mercury onto the mixed phase Covellite surface. The $S2p_{3/2}$ signal at B.E of ≈162.56eV corresponds well to the B.E. of $Hg_3S_2Cl_2$ (Hyland, et al., 1990). The $Hg_3S_2Cl_2$ compound, a double salt which shown earlier in Mellor et al. and Phillips & Kraus (Mellor, 1923; Harold O. Phillips & Kraus, 1965), is in fact a reaction product between HgS and $HgCl_2$. Similarly, the detection of this compound suggests that the sorption of mercury onto mixed phase Covellite surface should proceed firstly through the formation of HgS. The in-situ formation of HgS would further assist the sorption of $HgCl_2$ onto mixed phase Covellite surface.

The Hg4f detail scans spectra for reacted mixed phase Covellite is illustrated in **Figure 5.19**. Whilst, the reference B.E used for Hg compound determination is shown in **Table 5.5**. In general, the spectra consist of a two distinct, non-overlap spin-orbit coupling split peaks in which these peaks are identified as the $Hg4f_{5/2}$ and $Hg4f_{7/2}$ component. In contrast, the B.E. of $Hg4f_{7/2}$ component provides practical information for specific mercury chemical state identification. From the figures, characteristic peaks of Hg(II) were detected at both K.E of 200eV and 600eV. The signal at B.E. ≈100.90eV related well to the state of Hg(II) in $HgCl_2$, HgS and $Hg_3S_2Cl_2$. However, distinct identification among these species is impossible as they possess same B.E. The signal at B.E. ≈100.60eV linked well to the formation of HgO. Owing to the acidic solution used, the precipitation of HgO seems

unreasonable. Thus, its formation is mostly due to the reactions between Hg(II), $Cu(OH)_2$ and CuO. Nonetheless, the most important finding is that the +2 state of Hg persists throughout the reaction since Hg(II) salt *i.e.* $HgCl_2$ is used as the contaminant. Therefore, this confirmed the sorption of Hg(II) onto mixed phase Covellite at acidic pH does not involve any redox reaction that reduces the initial Hg^{2+} used to Hg^0 or Hg_2^{2+}.

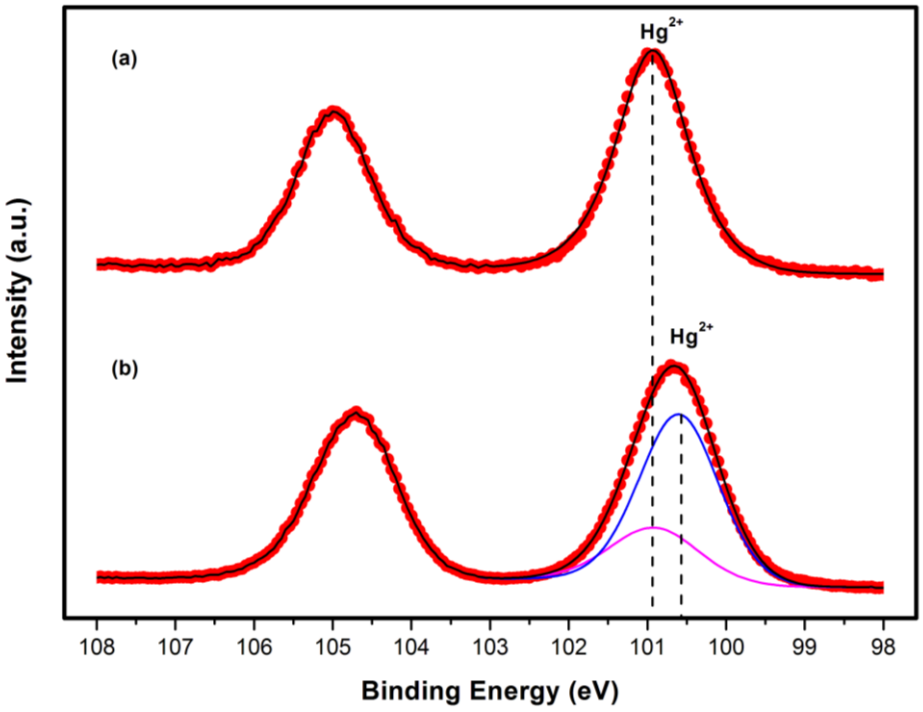

Figure 5.19. Hg4f detail scans spectra of reacted mixed phase Covellite at K.E. of (a) 200eV and (b) 600eV.

Table 5.5. Binding Energies (eV) of Hg $4f_{7/2}$ for selected standards and its references.

Standard	B.E. (eV) of Hg $4f_{7/2}$	References
$HgCl_2$	100.90	(Hyland, et al., 1990)
HgS	100.90	
$Hg_3S_2Cl_2$	100.90	
HgO	100.57	(Humbert, 1986)
Hg_2Cl_2	99.40	(Hyland, et al., 1990)
Hg^0	99.20	(Seals, Alexander, Taylor, & Dillard, 1973)

Apart from the peak de-convolution analysis, the peak areas quantification based on Cu2p, S2p, Hg4f, Cl2p and O1s detail scan spectra were also done to determine the surface atomic composition on unreacted and reacted mixed phase Covellite. The surface atomic composition at K.E. of 200eV and 600eV are normalized with respect to the sulfur in which the results are shown in **Table 5.6** and **Table 5.7** respectively. For unreacted mixed phase Covellite, high amount of sulfur in relative to copper is detected at both of the K.E. of 200eV and 600eV. This observation indicated that the sulfur rich termination rather than copper termination present dominantly on the unreacted powder surface. For reacted mixed phase Covellite, high amount of sulfur in relative to copper is again found at both of the K.E. of 200eV and 600eV. This clearly indicated that sulfur rich environment is conserved throughout the experiment even though the dissolution of sulfur species is identified from the S2p peak de-convolution analysis. In comparison of the amount of copper in unreacted and reacted mixed phase Covellite, a sharp decrease of copper content is observed at both of the K.E. of 200eV and 600eV. Considering that both leaching of copper and sulfur occurred during the reaction, this result strongly suggests that the amount of copper leached is significantly higher than the amount of sulfur leached from the surface. The sorption of Hg(II) onto mixed phase Covellite is therefore can be viewed as an ion-exchange process that involve the leaching of copper for mercury and retain the sulfur on the surface.

Table 5.6. XPS surface atomic compositions of unreacted and reacted mixed phase Covellite at K.E. of 200eV.

Sample	Quantification Ratio				
	S	Cu	Hg	Cl	O
Unreacted	1.00	0.73	0.00	0.00	1.11
Reacted	1.00	0.21	1.29	1.00	0.31

Table 5.7. XPS surface atomic compositions of unreacted and reacted mixed phase Covellite at K.E. of 600eV.

Sample	Quantification Ratio				
	S	Cu	Hg	Cl	O
Unreacted	1.00	0.44	0.00	0.00	0.47
Reacted	1.00	0.17	1.08	0.86	0.10

On the other hand, a notably high amount of mercury and chloride are also identified on the surface of reacted mixed phase Covellite regardless of the depth condition. For mercury, it has been recognized earlier from the S2p peak de-convolution analysis in which the negatively charged monosulfide (S^-) is responsible for mercury complexation. For chloride, two possible routes can be proposed to explain its presence onto the surface. Firstly, the sorption of chloride proceeds via the individual Cl^- species and adsorb onto the positively charged copper surface. Secondly, the sorption of chloride proceeds via the combined $HgCl_2$ species and adsorb onto negatively charged sulfide surface. Nevertheless, based on the quantification results, the first route seems to be impossible since only small amount of copper is found in the reacted sample. Therefore, the sorption of chloride must have a strong relationship to the sorption of mercury onto the surface in which a direct adsorption of $HgCl_2$ should occur during the reaction.

5.7. Summary

From Hg(II) uptake study, a steady decrease of mercury uptake with increasing solution pH was found when Hg(II) concentration is elevated. This result suggests the ineffective sorption of mercury onto mixed phase Covellite at alkaline pH. From the sorption kinetic studies at acidic pH i.e. pH 4, the data tend to fit well with Ho's pseudo second-order

kinetic model. The kinetic data indicated that the sorption of Hg(II) onto CuS at acidic pH should follows a second order reaction. Thus, two specific conditions must be fulfilled in order for the effective sorption of Hg(II) to happen. In addition, it was discovered that the sorption equilibrium data follows well with the Langmuir isotherm in which the monolayer coverage of Hg(II) is found to be ≈416.67 mg Hg(II) / g of sorbent. The unexpectedly high maximum sorption capacity of mixed phase CuS estimated showed CuS is a powerful sorbent for Hg(II) even in its severely oxidized state.

Solid characterization tools *i.e.* PXRD and FESEM-EDX were utilized to investigate the structural changes of mixed phase CuS before and after the reactions. From PXRD analysis, the dissolution of oxidized $CuSO_4$ phase has been detected in the reacted mixed phase Covellite. This indicated that the dissolution of $CuSO_4$ layer has re-activated the CuS surface for aqueous Hg(II) uptake. Thus, this suggested that the oxidation of pure phase CuS to 67% CuS and 33% $CuSO_4$ will not result in any significant performance declination in aqueous Hg(II) uptake. In addition, an unknown crystalline phase of mercury compound was found in reacted mixed phase Covellite. It was identified that this newly formed compound has some resemblance to $Hg_3S_2Cl_2$. Nevertheless, a detail matching analysis reveals that the reference pattern of $Hg_3S_2Cl_2$ cannot fits completely well to the unknown peaks in reacted mixed phase Covellite. From FESEM-EDX analysis, the additional formation of this compound was coupled with the growth of nano-needle crystallites on initial CuS hexagonal plates. Attempt has been tried to determine the chemical composition of the unknown morphology by EDX analysis but with no success. Hence, a more detail analysis is needed to solve the chemical identity of this unknown crystalline phase.

With the intention to obtain a more comprehensive insight on the sorption of $HgCl_2$ onto the 'real' surface of mixed phase CuS, surface sensitive XPS is used for further

investigation. From XPS analysis, both mercury and chloride are found on the inner (K.E. of 600eV) and outer (K.E. of 200eV) surface of mixed phase Covellite. The sorption of mercury and chloride is associated with the loss of Cu from the surface. This observation suggests that the ion-exchange sorption process which involves the substitution of Hg for Cu occurred on the surface during the reaction. From the S2p detail scan peak de-convolution analysis, it was identified that the monosulfide (S^-) species is responsible for mercury complexation. In addition, the formation of the double salt $Hg_3S_2Cl_2$, a reaction product between HgS and $HgCl_2$ is also found on both of the inner and outer surface. This shows that the sorption of mercury onto mixed phase Covellite surface should proceeds firstly through the complexation with monosulfide (S^-) in which it leads to the formation of cinnabar (HgS). The in-situ formation of HgS would then further assist the sorption of $HgCl_2$ onto mixed phase Covellite surface.

CHAPTER 6

HETEROGENEOUS AQUEOUS MERCURY COMPLEXATION – PURE PHASE COVELLITE

In the previous chapter, the potential ability of heavily oxidized Covellite, namely mixed phase Covellite in removing aqueous Hg(II) was demonstrated. The notably high Q_{max} found (416.67 mg Hg(II) / g of sorbent) suggests that the severely oxidized Covellite can be used in sequestrating high level of aqueous Hg(II). With the aid of solid characterization techniques, the incorporation of Hg(II) onto the crystal lattice of mixed phase Covellite was confirmed. Nevertheless, the full chemical identity of the mercury complexes sorbed is still unclear, the fate of Cu during the Hg(II) sorption and the interference of HgO formation during the experiment are also not considered in detail in the entire discussion. In this chapter, the studies of Hg(II) sorption onto Covellite surface was proceeded using the pure phase Covellite (CuS) powder. The hydrothermal synthesized CuS powder was well preserved in a N_2 environment to minimize surface oxidation. The sorption of Hg(II) onto pure phase Covellite are performed under the extended reaction parameters *i.e.* variation of solution pH, mercury concentration and solution temperature to deeply investigate the mercury uptake, copper leached and final solution pH resulted from Hg(II) sorption experiments. Furthermore, instead of assuming no HgO precipitation during the reaction, the interference of HgO precipitation for mercury uptake was also considered in prior to the real sorption experiment. With the support from solid characterization tools *i.e.* PXRD, FESEM-EDX, XPS, and HRTEM-EDX, the in depth analysis has finally leads to the identification of the mercury complexes sorbed as well as the reaction mechanism establishment for the sorption of Hg(II) onto CuS surface.

6.1. Reaction Parameters on Mercury Uptake

6.1.1 Precipitation of Mercury Oxide Compound

For any mercury related researches, mercury loss during the experiment has been a common issue in affecting the quality of the aqueous mercury data measured. The mercury loss issue is not limited to its high volatility to exist as atmospheric gas (UNEP Chemicals, 2002). Nevertheless, the loss of mercury can be also related to the transformation of different mercury species from one to another during a specific experimental condition. Undoubtedly, the latter case becomes particularly important when dealing to pH dependent experiment in which alkaline medium is required. The addition of alkaline solution into mercury containing media might precipitate out the mercury oxide (HgO) compounds and result in an inaccurate mercury data measured. Therefore, for solution phase mercury analysis, the mercury loss phenomenon needs to be considered carefully before any experiment. Understanding the optimum condition for retention of mercury in the solution is required to assure the safety of the working environment as well as to ensure the accuracy of the experimental data collected. Since solution pH plays the main parameter in controlling the stability and retention of mercury species, controlled experiments (without addition of Covellite powder) were conducted under the solution pH of 1, 4, 7, and 9 in Hg(II) concentration of 300 ppm, 400 ppm and 800 ppm at 25°C and 45°C for 15 hours shaking. These experiments were carried out to investigate the critical condition for HgO precipitation. The results of percentage Hg(II) recovery collected at 25°C and 45°C are depicted in **Figure 6.1** and **Figure 6.2** respectively.

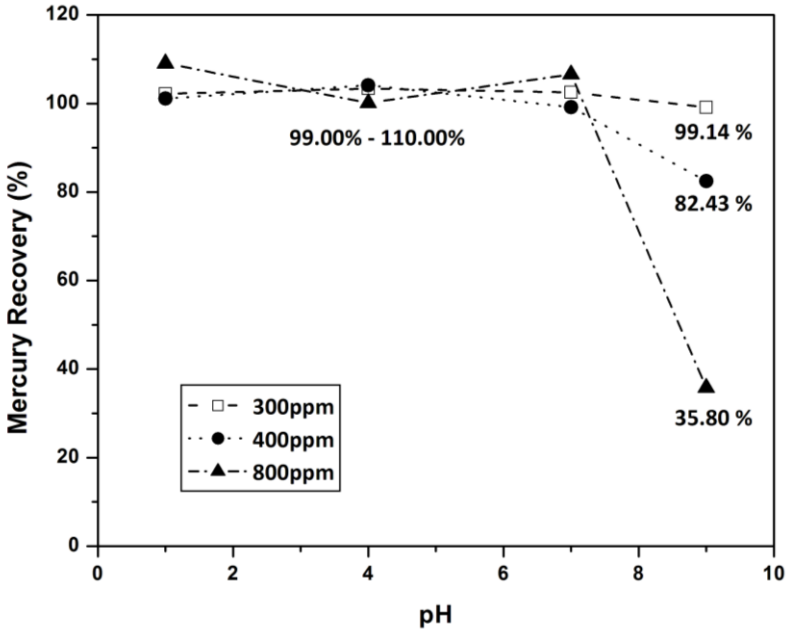

Figure 6.1. Effect of solution pH and mercury concentration on retention of aqueous Hg(II) in the solution at 25°C.

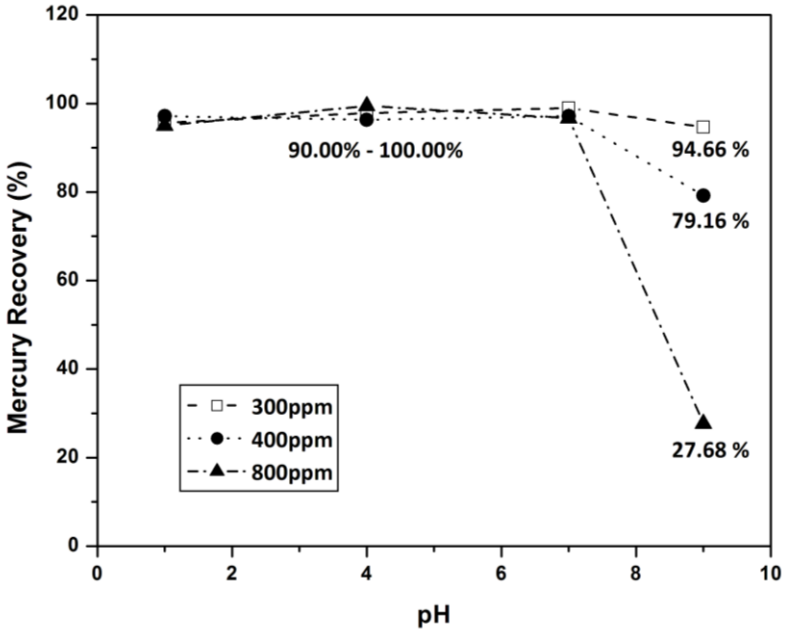

Figure 6.2. Effect of solution pH and mercury concentration on retention of aqueous Hg(II) in the solution at 45°C.

Regardless of the reaction condition used, fairly good mercury recoveries were achieved for all samples conducted at pH 1, 4, and 7. Effect of mercury concentration (≤ 800 ppm) and solution temperature (≤ 45°C) do not contribute much on the mercury loss

from pH 1 to 7. For pH 9 samples conducted in 300 ppm Hg(II) at both 25°C and 45°C, more than 90% mercury is recovered. However, as the Hg(II) concentration is increased to 400 ppm at both 25°C and 45°C, a sharp drop in % mercury recovery is detected. Same trend is observed for pH 9 samples conducted in 800 ppm at both 25°C and 45°C, the % of mercury recovered decreased significantly to less than 50%. From **Figure 6.3 (a)** and **(b)**, the decreased % of mercury recovered from pH 9 samples in 400 ppm and 800 ppm Hg(II) are associated by the suspension of red crystalline solid in the solution. The red crystalline solid is related to the HgO precipitation when supersaturation of $Hg(OH)_2$ is reached. From the images, the amount of HgO found also increases with Hg(II) concentration. The greater amount of HgO found can be actually reasoned to the kinetic factor in which the precipitation of HgO in 800 ppm sample occurred right after 3mins of N_2 purging while the precipitation of HgO in 400 ppm sample happened only after 15 hours of shaking.

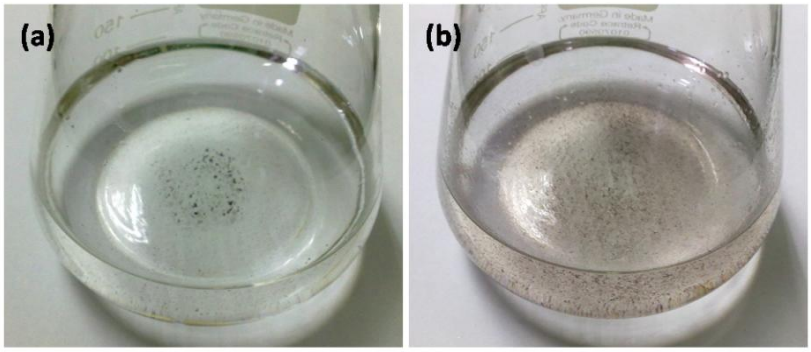

Figure 6.3. Precipitation of red crystalline solid in (a) 400 ppm and (b) 800 ppm Hg(II) solution.

6.1.2. Effect of Initial Solution pH and Mercury Concentration

Solution pH is known to be an important parameter that controls the sorption process of metal species onto mineral sulfides. A change of solution pH from acidic to alkaline condition had drastically increased the activity of pyrite (FeS_2) and pyrrhotite ($Fe_{1-x}S$) in removing Hg(II) (Bower, et al., 2008; Jean & Bancroft, 1986). **Figure 6.4** depicts the effect

of solution pH and mercury concentration on the percentage removal of Hg(II) by pure phase Covellite at temperature of 25°C under 15 hours of shaking. For reactions conducted in 50 ppm Hg(II), ≈100% Hg(II) removal is observed in all pH ranges investigated. No obvious effect of solution pH on the Hg(II) removal is seen at this concentration. For reactions performed in 150 ppm Hg(II), ≈100% Hg(II) removal is observed at pH 1 – 8 while a slight decrease of percentage Hg(II) removal (≈96%) is seen at pH 9. The slight decrease of percentage Hg(II) removal at pH 9 suggests that the sorption of Hg(II) onto Covellite can be inefficient at alkaline condition. As the Hg(II) concentration is increased to 250 ppm Hg(II), ≈100% Hg(II) removal is also observed at pH 1 – 6. However, a massive drop of Hg(II) removal (≈58%) starts to occur at pH 7. The percentage of Hg(II) removal continue to decline to ≈46% at pH 8 and ≈39% at pH 9. This observation again shows the ineffective sorption of Hg(II) onto Covellite specifically at pH 7 – 9 in which it has becomes more apparent when high concentration of Hg(II) is used.

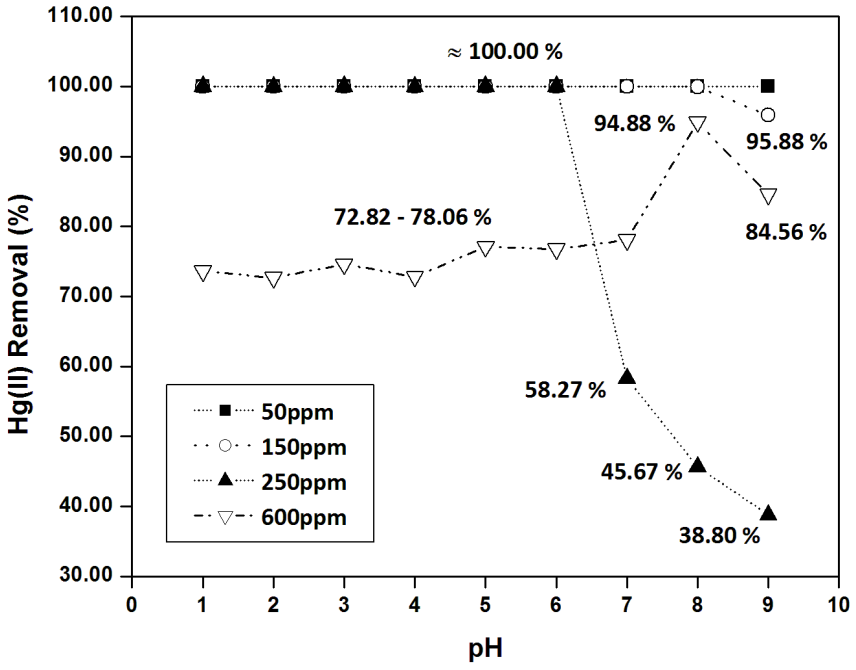

Figure 6.4. Effect of solution pH and mercury concentration on the sorption of Hg(II) onto pure phase Covellite.

Apart from the studies above, an additional study is done in 600 ppm Hg(II) to investigate the percentage mercury uptake under the interference of HgO precipitation. At pH 1 – 6, instead of showing ≈100% removal as shown in lower Hg(II) concentration, a consistent Hg(II) uptake of about 73% to 78% is observed from **Figure 6.4**. The constant Hg(II) uptake at these pH suggest that CuS is now saturated with Hg(II). An increase in Hg(II) concentration will not increase the amount of Hg(II) sorbed on Covellite surface. As the solution pH increases, a continuous increase of Hg(II) to 78% at pH 7, 95% at pH 8 and 85% at pH 9 are however found in 600 ppm Hg(II) series. The high mercury uptake at this pH values are associated with the identification of mixed black and red-orange colour powder in the supernatant solutions. In addition, the increasing trend of Hg(II) removal observed herein is also opposed to the ineffective Hg(II) sorption shown in 250 ppm Hg(II). These observations strongly suggest that an inversing trend of Hg(II) removal at pH 7 – 9 can be happened if precipitation of HgO occurred during the sorption experiment.

6.1.3. Effect of Initial Solution pH and Temperature

The ineffective sorption of Hg(II) onto CuS specifically at near neutral to alkaline pH (around pH 7 – 9) has been identified at 250 ppm Hg(II). Under the same reaction condition, the sorption experiment is expanded to 35°C and 45°C to investigate the effect of solution temperature on the sorption efficiency of Hg(II) at these pH ranges. **Figure 6.5** depicts the effect of solution pH and temperature on the percentage removal of Hg(II) by pure phase Covellite in 250 ppm Hg(II) under 15 hours of shaking. For reactions conducted at 25°C, ≈100% Hg(II) removal is observed at pH 1 – 6 while a massive drop of Hg(II) removal (≈58%) occurred at pH 7. The percentage of Hg(II) removal continue to drop to ≈46% at pH 8 and ≈39% at pH 9. For reactions performed at 35°C, ≈100% Hg(II) removal is also observed at pH 1 – 6. However, a significant increase in Hg(II) uptake is observed at

pH 7 and 8 in which ≈100% Hg(II) removal is reached. As the solution temperature is increased to 45°C, it is astounded that ≈100% Hg(II) removal is achieved at all pH range investigated. From these observations, the issue on ineffective sorption of Hg(II) onto Covellite surface specifically at pH 7 – 9 has been solved progressively with temperature elevation.

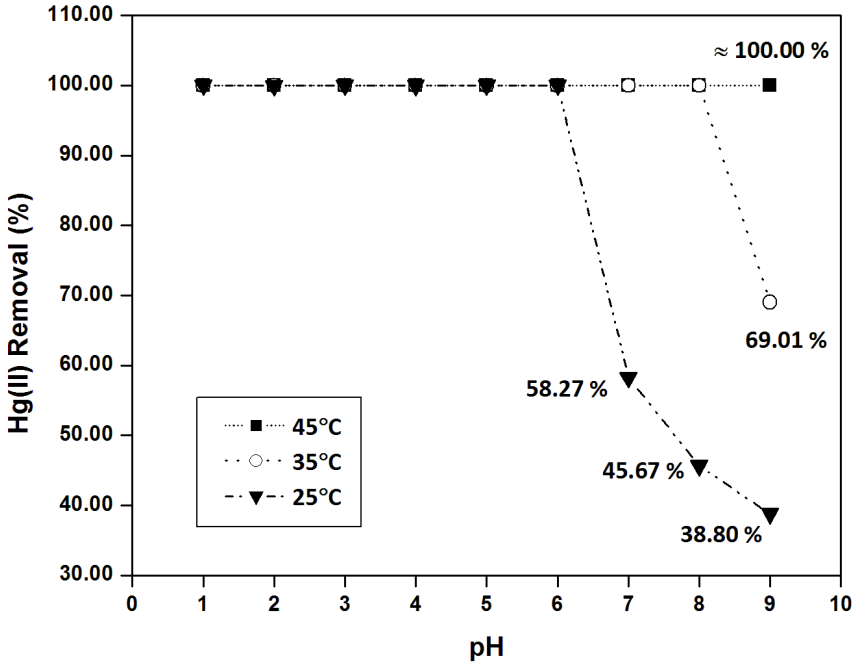

Figure 6.5. Effect of solution pH and temperature on the sorption of Hg(II) onto pure phase Covellite.

6.1.4. Discussion

Based on the HgO precipitation studies above, it is confirmed that despite of the Hg(II) concentration and solution temperature applied, the laboratory condition at pH 1 and 4 will not result in any significant HgO precipitation during the Hg(II) sorption experiment after 15 hours of shaking. A special attention is given to pH 7 in which the precipitation of HgO is also not detected in the concentration ranged studied. The clear precipitation of red HgO was in fact observed at higher mercury concentration, particularly above 1000 ppm Hg(II)

(Barriada, Herrero, Prada-Rodríguez, & Sastre de Vicente, 2008). For pH 9 condition, it is identified that there is increased risk in transforming the aqueous Hg(II) into the red crystalline HgO solid when more than 300 ppm of Hg(II) is used. In order to suppress the precipitation of red crystalline HgO during the real sorption experiment, the maximum concentration of Hg(II) solution used is recommended to be 300 ppm. By using Hg(II) solution with concentration less than 300 ppm for Hg(II) sorption experiments, the reliability of the mercury uptake data obtained can be reassured to be insignificantly affected by HgO precipitation. In contrast, by using Hg(II) solution with concentration more than 300 ppm for Hg(II) sorption experiments, the mercury uptake data measured can be highly interfered by HgO precipitation.

The dependence of sorption of Hg(II) onto Covellite surface as a function of pH is highly ruled by the mercury species in the solution and the chemical species present on Covellite surface. In view of the mercury species present in the solution, the speciation results were modeled using the Hydra-Medusa software which is freely available on Internet at http://www.kemi.kth.se/medusa. The speciation results simulated from the program is similar to the speciation calculated using with MINEQL (Schecher & McAvoy, 1992). The speciation calculation was carried out based on twice of the total chloride concentration to the total mercury concentration since the $HgCl_2$ has been used in the studies. **Figure 6.6 (a) – (d)** depicts the speciation diagram calculated for 50 ppm, 150 ppm, 250 ppm and 600 ppm Hg(II) at 25°C respectively. The main species that found in the pH range of 1 – 6 are $HgCl^+$, $HgCl_2$ and HgCl(OH) while $Hg(OH)_2$ and HgO are predicted at the near neutral to alkaline pH. Although HgO precipitation is expected from the speciation results, no clear indication of red crystalline HgO solid is observed during the real sorption experiments. The formation of red crystalline HgO precipitate is found merely in the pH 7 – 9 samples in 600 ppm Hg(II) solution. The mercury speciation calculation is thus acting

as a theoretical guideline in predicting the precipitation of HgO. The ideal way of estimating the HgO precipitation in the samples will still require the controlled HgO precipitation studies coupled with solid characterization analysis for the reacted sample obtained from the Hg(II) sorption experiments.

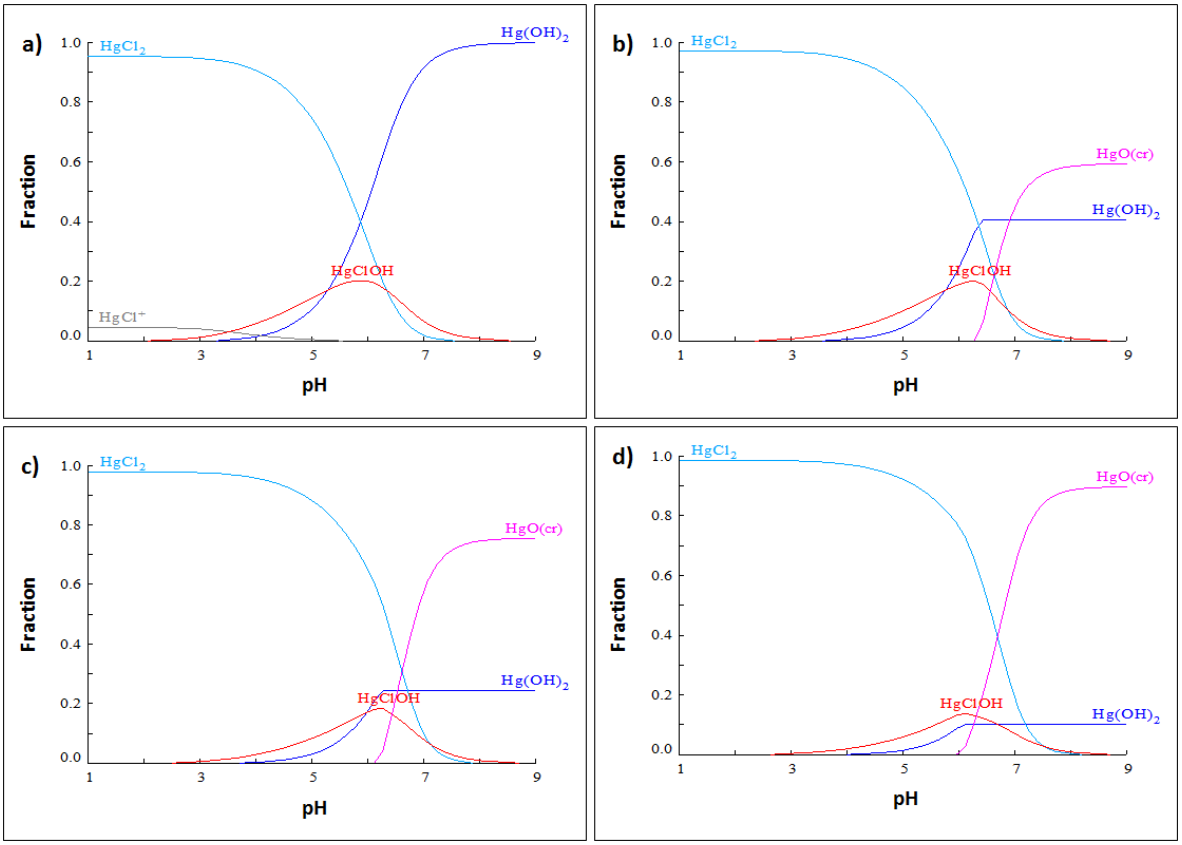

Figure 6.6. Mercury speciation at different solution pH calculated using (a) 50 ppm, (b) 150 ppm, (c) 250 ppm and (d) 600 ppm $HgCl_2$.

Despite of the Hg(II) concentration used, significant contribution of $HgCl^+$, HgCl(OH) and $HgCl_2$ species are identified in the pH range of 1.0 – 6.0. Their contribution, however, gradually decreases with increasing pH in the entire system. In **Figure 6.4**, reduced amount of mercury uptake has been detected at near neutral to alkaline pH (around pH 7 – 9). The trend of decreasing mercury uptake with increasing pH is found to be in line with the steady decrease of these mercury species in the solution. This observation strongly

suggests that the mercury uptake during the reaction is closely related to the dominance of $HgCl^+$, HgCl(OH) and $HgCl_2$ species in the solution. On the other hand, by excluding the precipitation of HgO in pH 7 – 9, it cannot be concluded that $Hg(OH)_2$ is not sorbed onto Covellite surface since certain degree of mercury uptake is observed from **Figure 6.4**. In fact, $Hg(OH)_2$ has been identified as the preferred adsorbing species during the sorption of Hg(II) onto pyrrhotite ($Fe_{1-x}S$) (Jean & Bancroft, 1986). Even with addition of large amount of NaCl during the reaction, highest mercury uptake is still observed at alkaline pH region where $Hg(OH)_2$ is dominant. Therefore, it is obvious that the sorption of $Hg(OH)_2$ onto Covellite surface cannot be underestimated. In current study, it is estimated that the sorption of $Hg(OH)_2$ onto Covellite surface is still occurring but its sorption efficiency is limited when compared to $HgCl^+$, HgCl(OH) and $HgCl_2$ species.

During the Hg(II) sorption studies, it has been identified that the issue of ineffective sorption of Hg(II) onto CuS at pH 7 – 9 can be overcome progressively via the reaction temperature elevation. In order to explain the change of mercury uptake at this pH region, it is important to identify the Hg(II) species present in the solution. From the chemical speciation diagram, $Hg(OH)_2$ is found out as the main contributing species that controlled the overall sorption at near neutral to alkaline pH region. For the sorption of $Hg(OH)_2$ species onto CuS, it is predicted that a relatively low rate of sorption has occurred during the reaction. Thus, a longer reaction time frame which is more than 15 hours at pH 7 – 9 is needed at 25°C to achieve a complete equilibration. In fact, it is renowned that the reaction rates double for every 10°C increase in temperature for most of the reactions. Therefore, the rate of $Hg(OH)_2$ sorbed onto CuS has been significantly increased via the reaction temperature elevation. This has finally led to a relatively fast rate of equilibration and consecutive increase of mercury uptake for near neutral to alkaline pH at higher temperature condition.

6.2. Reaction Parameters on Copper Leached

6.2.1. Dissolution of Covellite

In the process of studying the sorption of Hg(II) onto CuS, consideration on the stability of the powder in water is always an important measure. Although the solubility product of CuS (K_{sp} = 8 x 10^{-37}) ("Solubility product constants," 2003) suggests that the dissolution is highly impossible in water, the controlled studies is still needed to confirm the theoretical prediction. The controlled experiments have been performed under the variation of solution pH and temperature. Amount of Cu(II) leached from Covellite into the water is measured and the experimental results are illustrated in **Figure 6.7**. In general, it is identified that the maximum leaching of Cu(II) from Covellite occurred at pH 1 regardless of the solution temperature used. A consistent decrease of the Cu(II) leached to approximately zero percent is encountered when solution pH is further increased. From the trends described, it is clearly shows that the dissolution of Covellite in water is pH dependent in which its dissolution is feasible at acidic pH but remain intact at near neutral to alkaline pH.

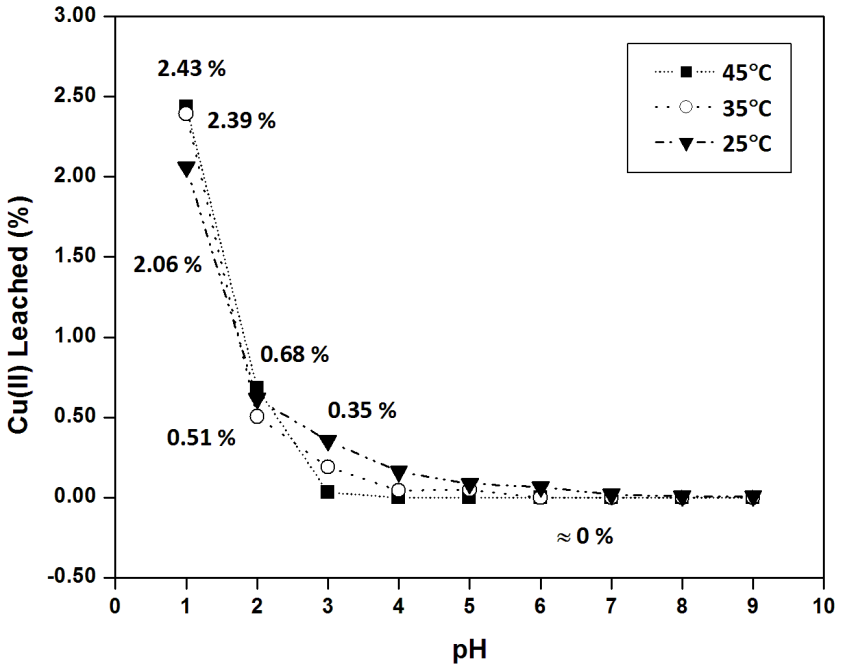

Figure 6.7. Controlled studies on dissolution of Covellite at different reaction temperature.

6.2.2. Effect of Initial Solution pH and Mercury Concentration

In view of the Hg(II) removal trends observed at different pH region, studies were conducted to investigate the amount of Cu(II) leached from Covellite during the Hg(II) sorption experiments. **Figure 6.8** shows the effect of solution pH and mercury concentration on the percentage leaching of Cu(II) by pure phase Covellite at temperature of 25°C under 15 hours of shaking. For reactions conducted in 50 ppm Hg(II), a steady decrease of percentage Cu(II) leached are observed at pH 1 – 5 (2.0% to 1.5%). The percentage Cu(II) leached continue to drop into 1.10% at pH 6, 0.40% at pH 7, as well as 0.20% at pH 8 and 9 correspondingly. For reactions conducted in 150 ppm Hg(II), similar observation is detected. The percentage of Cu(II) leached are found to decline from 6.60% to 3.60% at pH 1 – 6, 0.5% at pH 7, 0.2% at pH 8 and ≈0% at pH 9. As the Hg(II) concentration is increased to 250 ppm, the depreciating trend of Cu(II) leached is again observed. The percentage of Cu(II) leached are identified as 11.50% at pH 1 – 3, 9.18% to 7.46% at pH 4 – 6 and 1.22% to 0% at pH 7 – 9 in this series. Lastly, when the reaction is further extended to 600 ppm, the declining trend of Cu(II) leached persists. The percentage of Cu(II) leached are identified to be 14.00% at pH 1 – 3, 13.71 to 11.00% at pH 4 – 6 and 4.46% to 0% at pH 7 – 9 in this series. From these studies, the main trend observed in these experiments is that the percentage of Cu(II) leached decreases substantially with solution pH elevation until ≈0% is achieved at both pH 8 and 9. These observations strongly suggest that the leaching of Cu(II) is highly pH dependent even if the reactions is conducted in the presence of Hg(II). On the other hand, it is found out that at pH 1 – 7, an increase in the percentage of Cu(II) leached occurred when higher Hg(II) concentration solution is applied. These observations notably indicate that the percentage of Cu(II) leached during the reaction is closely related to the Hg(II) concentration used i.e. amount of Hg(II) present in the solution.

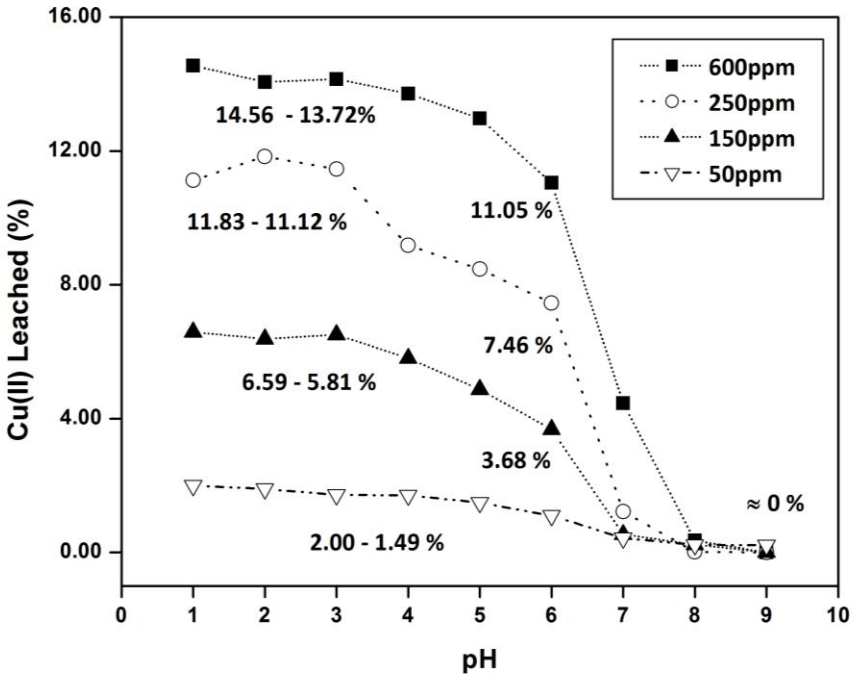

Figure 6.8. Effect of solution pH and mercury concentration on the leaching of Cu(II) during the sorption of Hg(II) onto pure phase Covellite.

Aside from the percentage of Cu(II) leached, a conversion ratio, $R_{conversion}$ which represent the number of moles of Hg(II) sorbed onto CuS to the number of moles of Cu(II) leached into the solution are calculated. **Table 6.1** tabulates all the $R_{conversion}$ values evaluated for the studies performed in 50 ppm, 150 ppm, 250 ppm and 600 ppm Hg(II) solutions. For reactions conducted in 50 ppm Hg(II), $R_{conversion}$ with value of 1 is identified at pH 1 and 2. The $R_{conversion}$ increase progressively with solution pH until a value of 9.24 is determined at pH 9 condition. For reactions conducted in 150 ppm Hg(II), similar observation has been detected. The $R_{conversion}$ begins with value of 1 at pH 1 and 2. The value increases with solution pH until a significantly high value of 1279.13 is detected at pH 9 condition. As the Hg(II) concentration is raised to 250 ppm, $R_{conversion}$ with value of 1.16 is found at pH 1. Likewise, the $R_{conversion}$ change in an appreciating manner with solution pH until a substantial increase at pH 8 and 9 is observed ($R_{conversion}$ of 320.13 and infinity are found respectively). Finally, when the reaction is further extended to 600 ppm,

the $R_{conversion}$ is again found to be increased with solution pH inclination until the value of infinity is found at pH 9. All these observations indicate that the $R_{conversion}$ i.e. the number of moles of Hg(II) sorbed onto CuS to the number of moles of Cu(II) leached into the solution is highly pH dependent in which it increases with solution pH elevation.

Table 6.1. $R_{conversion}$ values evaluated for the sorption studies performed in 50 ppm, 150 ppm, 250 ppm and 600 ppm Hg(II) solutions.

[Hg(II)] /pH	1	2	3	4	5	6	7	8	9
600 ppm	1.44	1.47	1.50	1.51	1.68	1.98	4.97	75.28	∞
250 ppm	1.16	1.10	1.14	1.42	1.53	1.74	6.17	320.13	∞
150 ppm	1.07	1.10	1.08	1.21	1.44	1.91	13.11	29.29	1279.13
50 ppm	1.02	1.07	1.19	1.19	1.36	1.85	4.73	8.66	9.24

6.2.3. Effect of Initial Solution pH and Temperature

From the studies above, it is identified that the percentage leaching of Cu(II) decreased significantly with solution pH. On top of that, remarkably high $R_{conversion}$ values are observed at pH 7 – 9. As a continuation from the previous studies, the the sorption experiment is further extended to 35°C and 45°C. **Figure 6.9** illustrates the effect of solution pH and temperature on the percentage leaching of Cu(II) by pure phase Covellite in 250 ppm Hg(II) under 15 hours of shaking. For reactions conducted at 25°C, the percentage of Cu(II) leached are identified as 11.50% at pH 1 – 3, 9.18% to 7.46% at pH 4 – 6 and 1.22% to 0% at pH 7 – 9. For reactions performed at 35°C, a declining manner of percentage Cu(II) leached is also detected. The percentage of Cu(II) leached has found to be 18.47% to 10.93% at pH 1 – 3, 9.46% to 6.36% at pH 4 – 6 and 4.26% to 0.09% at pH 7 – 9 in this series. As the reaction temperature is raised to 45°C, the decreasing trend of Cu(II) leached with solution pH persists. The percentage of Cu(II) leached are recognized

to be 18.35% to 15.06% at pH 1 – 3, 12.91% to 9.44% at pH 4 – 6 and 5.91% to 0.35% at pH 7 – 9 in this series. From these data, the depreciating trend of percentage Cu(II) leached with solution pH is again identified at different temperature condition. Nevertheless, it is observed that the percentage of Cu(II) leached at pH 1 – 9 has increases slightly with solution temperature elevation.

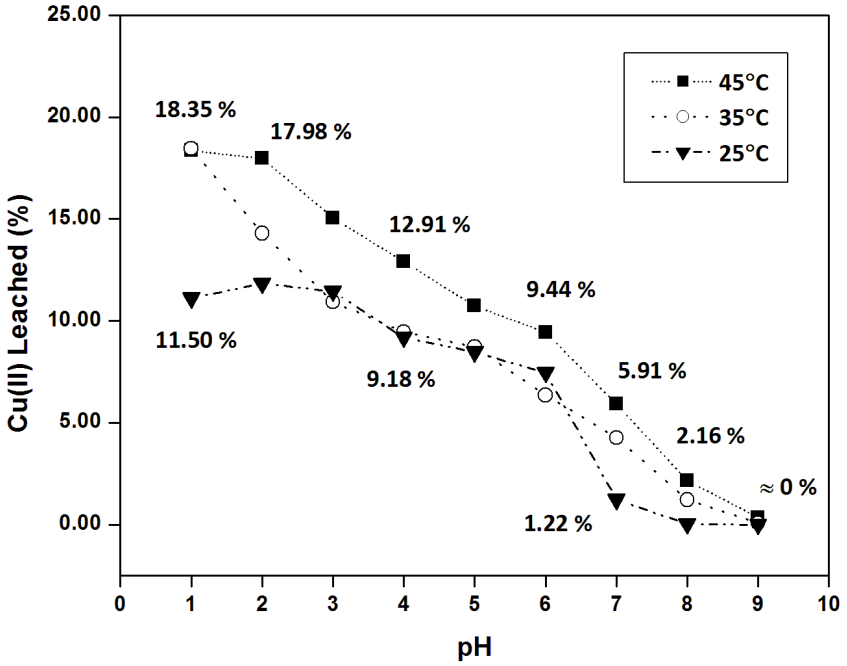

Figure 6.9. Effect of solution pH and temperature on the leaching of Cu(II) during the sorption of Hg(II) onto pure phase Covellite.

In addition to the percentage of Cu(II) leached analysis, the conversion ratio, $R_{conversion}$ which represent the number of moles of Hg(II) sorbed onto CuS to the number of moles of Cu(II) leached into the solution are also calculated for the reaction temperature data generated. **Table 6.2** tabulates all the $R_{conversion}$ values evaluated for the studies conducted at 25°C, 35°C and 45°C. For reactions carried out at 25°C, it has been shown that the $R_{conversion}$ with value of 1.16 is found at pH 1. The $R_{conversion}$ change in an appreciating manner with solution pH until a substantial increase at pH 8 and 9 is observed

($R_{conversion}$ of 320.13 and infinity are found respectively). For reactions performed at 35°C, the $R_{conversion}$ begins with value of 0.70 at pH 1. The value increases with solution pH until a significantly high value of 103.16 is detected at pH 9 condition. As the solution temperature is raised to 45°C, $R_{conversion}$ with value of 0.71 is found at pH 1. The $R_{conversion}$ is again detected to be increased with solution pH inclination until the value of about 37.37 is found at pH 9. From these analyses, the appreciating trend of $R_{conversion}$ with solution pH remained as the reaction is conducted at higher temperature. However, it can be also observed that the magnitude of $R_{conervsion}$ at pH 1 – 9 decreases consecutively with solution temperature elevation.

Table 6.2. $R_{conversion}$ values evaluated for the sorption studies conducted in 250 ppm Hg(II) solutions at 25°C, 35°C and 45°C.

[Hg(II)] /pH	1	2	3	4	5	6	7	8	9
45°C	0.71	0.73	0.86	1.01	1.22	1.38	2.21	6.03	37.37
35°C	0.70	0.91	1.19	1.37	1.49	2.05	3.05	10.67	103.16
25°C	1.16	1.10	1.14	1.42	1.53	1.74	6.17	320.13	∞

6.2.4. Discussion

From covellite dissolution studies, it is identified that dissolution of CuS in water decreases as pH increases. Maximum dissolution has occurred at pH 1 in which not more than 2.50% of Cu(II) is found in solution. This finding is consistent with the trends reported by Fullston et. al. in which the concentration of copper in solution resulted from dissolution of CuS increases with decreasing pH values (Fullston, 1998). For the studies carried out in the presence of Hg(II), it is found that the percentage of Cu(II) leached decreases gradually from pH 1 to 9 regardless of the Hg(II) concentration and reaction temperature applied in the experiments. It is also detected that the decreasing fashion of percentage Cu(II) leached

in the presence of Hg(II) is similar to the trend observed in controlled studies. Although a similar trend of Cu(II) leached is observed in both cases, it is wise to think that the leaching behaviour of CuS in contact with Hg(II) is different from Covellite dissolution. From the analysis of Cu(II) leached behaviour at solution pH of 1 – 7, the percentage of Cu(II) leached in real sorption studies is higher than the percentage of Cu(II) dissolved from Covellite in controlled studies. It can be also observed that the percentage of Cu(II) leached into solution increases when higher Hg(II) concentration is used. This observations provides useful insights for the sorption of Hg(II) onto CuS because extra Cu(II) leached from Covellite is evidenced during the reaction. Therefore, this confirmed that the ion exchange process is indeed taking place in controlling the sorption of Hg(II) onto CuS at solution pH of 1 – 7. The ion-exchange behaviour of CuS for Hg(II) has become more apparent when higher Hg(II) concentration or elevated amount of Hg(II) is present.

For the sorption of Hg(II) onto CuS at solution pH of 8 and 9, a relatively low percentage of Cu(II) leached has been detected. Thus, it is hard to use the Cu(II) leached data alone in describing the ion-exchange sorption of Hg(II) onto CuS at this pH region. As indicated earlier, remarkably high values of $R_{conversion}$ have been achieved at pH 8 and 9 when compared to pH 1 – 7. On the other hand, the magnitude of $R_{conversion}$ at pH 8 and 9 is also decreasing in a substantial manner as reaction temperature is elevated. The decrease in magnitude of $R_{conversion}$ can be rationalized clearly at pH 9 in which the values of $R_{conversion}$ has changed from infinity at 25°C into 103.16 at 35°C and finally drop to 37.37 at 45°C. Thus, it is apparent that an increase in reaction temperature has led to the increase leaching of Cu(II) with respect to the amount of Hg(II) sorbed. Therefore, this has indirectly revealed the occurrence of ion-exchange sorption of Hg(II) onto CuS at this pH region.

From the analysis above, the occurrence of ion-exchange process in dictating the sorption of Hg(II) onto CuS has been observed regardless of the reaction condition applied.

However, the decreasing trend of percentage Cu(II) leached and progressive increase of $R_{conversion}$ with solution pH elevation is still unjustified in the discussion. To explain this observations, it is considered that an in-situ re-adsorption of Cu(II) back onto the powder has been taken place in addition to the ion-exchange sorption of Hg(II) onto CuS. The ability of CuS powder in adsorbing Cu(II) increases with solution pH elevation. This Cu(II) adsorbing trend persists even if the reaction is conducted at higher temperature condition. In fact, HgS is found to be an effective scavenger in retaining aqueous Hg(II) (Hasany, et al., 1999). Therefore, it is believed the re-adsorption of Cu(II) back onto CuS powder can be also accounted for the systematic decrease of Cu(II) in solution as well as the increase of $R_{conversion}$ with solution pH elevation.

6.3. Reaction Parameters on Final Solution pH

6.3.1. Controlled Studies

In this section, the ability of CuS in changing the final solution pH is investigated. This study is particularly important because there is a possibility for the H^+ and OH^- to adsorb onto metal sulfide (Wolthers, Charlet, van Der Linde, Rickard, & van Der Weijden, 2005) and this information might provide useful insights on the sorption of Hg(II) onto CuS. **Figure 6.10** depicts the relation between the initial and final solution pH of the CuS suspensions in water at 25°C, 35°C and 45°C under 15 hours of shaking. For experiments conducted at initial solution pH of 1 – 4, it is observed that initial solution pH will not result in any significant changes in final solution pH. This observation persists even if the experiments were conducted at higher reaction temperature. For experiments performed at initial solution pH of 5, a slight drop of final solution pH is detected. The solution pH has decreased to value of about 4.5 at 25°C, value of about 4 at 35°C and 45°C respectively. As initial solution pH is further adjusted to 6 – 9, a huge decrease in final solution pH is found

regardless of the reaction temperature applied. For example, it can be observed that the final solution pH has decreased to value of 4.60 at pH 6, 4.71 at pH 7, 5.29 at pH 8 and 5.25 at pH 9 for experiment conducted at 25°C. The decrease of solution pH at initial solution pH of 5 – 9 suggests that the sorption of OH^- onto CuS might occurs when the experiments is performed without the presence of Hg(II). The sorption tendency of OH^- onto CuS also increases when elevated amount of OH^- is introduced to CuS.

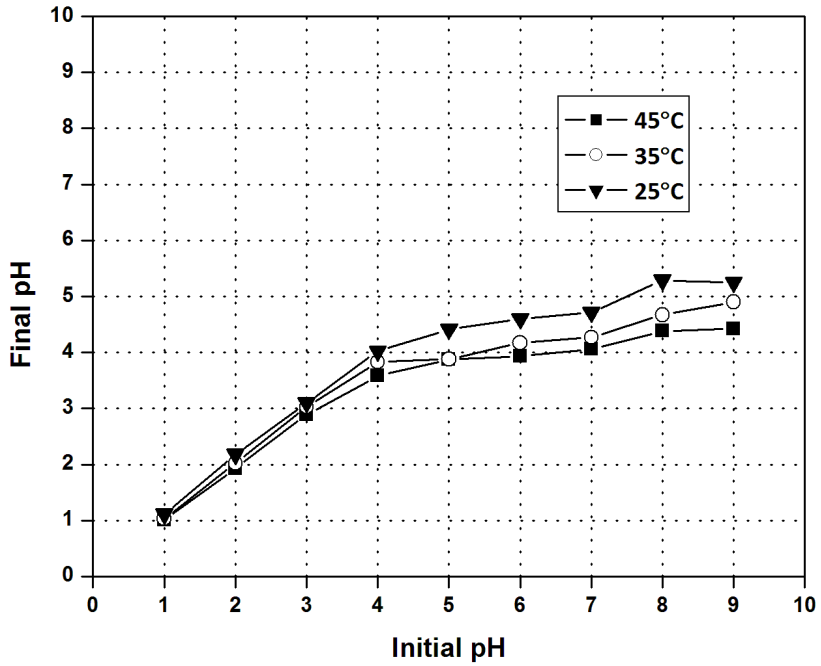

Figure 6.10. Controlled studies on the ability of Covellite in alternating final solution pH.

6.3.2. Effect of Initial Solution pH and Mercury Concentration

Given that CuS is a potential adsorbent for OH^- at pH 5 – 9, the sorption of OH^- onto CuS is also investigated via the solution pH changes studies conducted in the presence of Hg(II). The relation between the initial and final solution pH of the CuS suspensions in 50 ppm, 150 ppm, 250 ppm and 600 ppm Hg(II) at 25°C under 15 hours of shaking are illustrated in **Figure 6.11**. For reactions carried out at initial solution pH of 1 – 2 in 50 ppm Hg(II), it is observed that the final solution pH remains similar to the initial solution pH. No obvious

changes of final solution pH can be identified even if reaction the Hg(II) concentration is elevated. For reactions conducted at initial solution pH of 3 in 50 ppm Hg(II), no changes of final solution pH is again detected. However, a slight increase in final solution pH is identified when higher Hg(II) concentration is used.

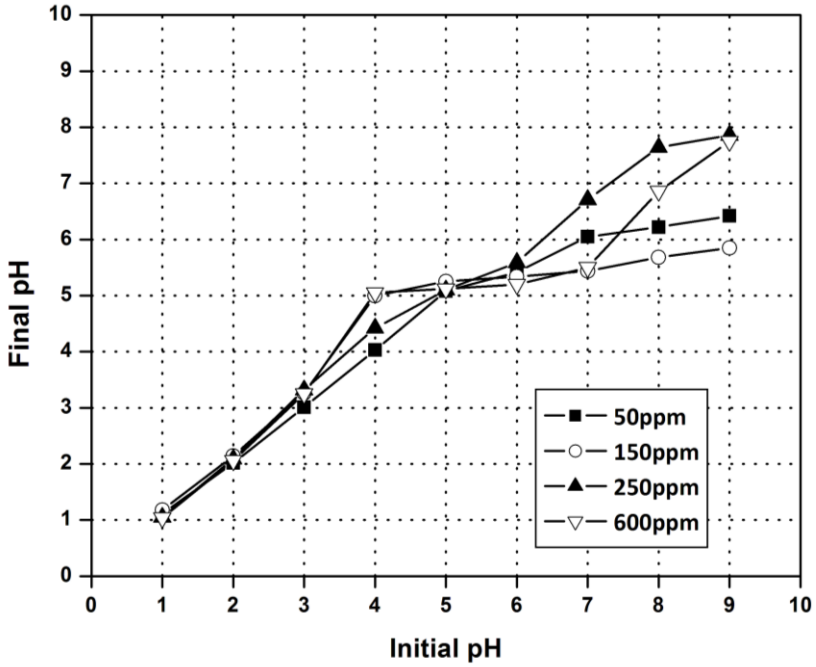

Figure 6.11. Effect of solution pH and mercury concentration on the final pH changes during the sorption of Hg(II) onto pure phase Covellite.

For reactions conducted at initial solution pH of 4 in 50 ppm Hg(II), the final solution pH also remains similar to the initial solution pH. Nevertheless, it is observed that the final solution pH in 50 ppm Hg(II) has increased to the value of about 5.00 in 150 ppm Hg(II), about 4.42 in 250 ppm Hg(II) and about 5.05 in 600 ppm Hg(II). This observation can be related to sorption of H^+ onto CuS and leads to an increase in the final solution pH being observed. On the other hand, as the initial solution pH is lifted to 5, the final solution pH is identified to be the same as initial solution pH regardless of the Hg(II) concentration used. At last, for the experiments conducted at initial solution pH of 6 – 9, a decrease in

final solution pH has been detected regardless of the Hg(II) concentration used. This show that the sorption of OH^- onto CuS is indeed occurring during the sorption of Hg(II) onto CuS. Nevertheless, the decrease in final solution pH found in this pH region is less than the pH changes detected in controlled studies. This indicates that the level of OH^- sorbed onto CuS in the present of Hg(II) is significantly lower to the case where Hg(II) is absent.

6.3.3. Effect of Initial Solution pH and Temperature

Figure 6.12 depicts the initial and final solution pH changes of the CuS suspensions in 250 ppm Hg(II) conducted at 25°C, 35°C and 45°C under 15 hours of shaking. At initial solution pH of 1 – 2 at 25°C, no obvious solution pH changes are detected. This observation persists even with reaction temperature elevation. As initial solution pH is tuned to pH 3 at 25°C, a slight increase in final solution pH (about 3.32) is observed. The increase in final solution pH becomes more obvious when reaction temperature is raised.

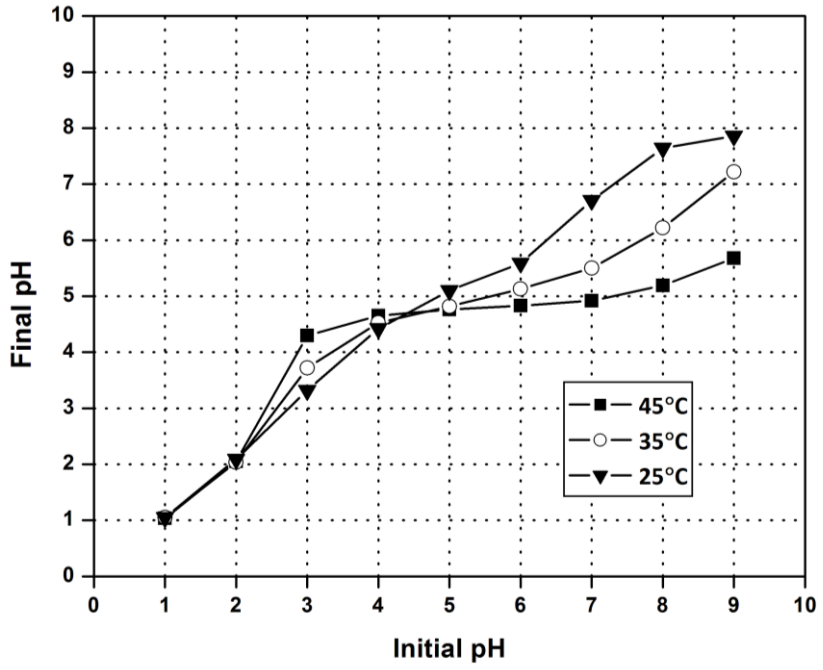

Figure 6.12. Effect of solution pH and temperature on the final pH changes during the sorption of Hg(II) onto pure phase Covellite.

For reaction conducted at initial solution pH of 4, the increase in final solution pH continues regardless of solution temperature used. The final solution pH is identified as about 4.42 at 25°C, about 4.53 at 35°C and 4.65 at 45°C. The increase in solution pH is considered to be the sorption of H^+ onto CuS. The decrease amount of H^+ in the solution has notably increases the final solution pH observed. As the initial solution pH is increased to 5 at 25°C, the final solution pH is identified to be the same as initial solution pH. Nevertheless, a slight decrease in solution pH is found when reaction is conducted at 35°C (about 4.82) and 45°C (about 4.76). Lastly, for the reaction conducted at initial solution pH of 6 – 9, a decrease in final solution pH has been detected. The depreciating trend becomes remarkably sharp when reaction temperature is raised. This clearly indicates that the occurrence of sorption of OH^- onto CuS is again confirmed at elevated reaction temperature. Nonetheless, the decrease in final solution pH found in this pH region is still less than the pH changes detected in the controlled studies. Even though the degree of OH^- adsorbed onto CuS is still lesser than in the case of controlled studies, it is found that OH^- adsorption affinity can be significantly increased when higher reaction temperature is used.

6.3.4. Discussion

At initial solution pH of 1 – 4, no notable solution pH changes are identified in the controlled studies. Whilst, for reactions conducted in the presence of Hg(II), an increase in final solution pH is observed at initial solution pH of 3 and 4. Apparently, sorption of Hg(II) onto CuS has resulted in an increase in final solution pH observed. The increase in final solution pH can be viewed as the decrease amount of H^+ ion present in the suspension. From Cu(II) leached analysis earlier, it is recognized that the ion-exchange process has been taken place in controlling the sorption of Hg(II) onto CuS. Thus, it reasonable to think that the ion-exchange sorption proceeds through the following manner:

$$CuS + 2H^+ \leftrightarrow Cu^{2+} + H_2S \quad (6.1)$$

$$H_2S + Hg^{2+} \leftrightarrow 2H^+ + HgS \quad (6.2)$$

As indicated in equations (6.1) and (6.2), it is observed that the H^+ ion is acting as the catalyst in the ion-exchange process. With the release of H^+ ion from the catalysis, the reaction is continued by the surface complexation of H^+ ion onto mineral sulfide surface. In actual fact, from zeta potential analysis of mineral sulfide, one may also conclude that the sulfide mineral surface is covered with sulfur-bearing species such as metal sulfide, metal-deficient sulfide or even polysulfide that can become charged by reacting with protons in a similar manner to metal oxide (de Bruyn & Agar, 1962):

$$–S^- + H^+ \leftrightarrow –SH \quad (6.3)$$

$$–SH + H^+ \leftrightarrow –SH_2^+ \quad (6.4)$$

in which –S denotes the active S species that present on the surface of metal sulfide, metal-deficient sulfide and polysulfide. For Covellite, it is reported that CuS surface is negatively charged when contact with water in N_2 environment (Fullston, et al., 1999). Even when solution pH is altered, no sign reversal of the zeta potential is observed which indicating that no iso-electric point (IEP) can be found. Thus, the negatively charged CuS surface supports the idea on the –S site as the sorption site for H^+ ions as described in equation (6.3) and (6.4). In the presence of ion-exchange process, the utilization of H^+ ion has tremendously raised the amount of H^+ ion in the vicinity of CuS as well as HgS. Subsequently, the probability and the amount of H^+ ion being trapped onto –S site increases as compared to the free H^+ ion in the solution. Therefore, it is clear that the sorption of Hg(II) onto CuS can play a vital role in increasing the tendency of H^+ ion adsorbed onto

mineral sulfide surface. This has lead to a significant increase in the final solution pH observed at the end of the reaction.

At initial solution pH of 5 – 9, a decrease in final solution pH has been detected in the controlled studies. The magnitude of decrease in final solution pH also increases with reaction temperature elevation. These observations can be interrelated to the decrease amount of OH^- present in the solution. With respect to the Covellite structure, it has been confirmed that CuS surface is composed of both of the –S site and –Cu site by XPS spectroscopy (Goh, et al., 2006). The present of –S site is responsible for the sorption of positively charged H^+ and Hg^{2+} ions whereas the existence of –Cu site is in charge for the trapping of negatively charged OH^- ion:

$$–SCu + OH^- \leftrightarrow –SCuOH^- \quad (6.5)$$

Indeed, the sorption of H^+ and OH^- ion onto mineral surface is also proposed by Schindler and Stumm et. al. as the surface complexation model and now it is widely used in treating the sorption data in mineral suspension (Brown, et al., 1998; M. Wang, Zhang, Hao, & Sun, 2011). Furthermore, it was also reported that the sulfide mineral surface can become increasingly covered with metal hydroxide and its oxide in alkaline media (Fullston, et al., 1999). Therefore, for the case of CuS, it is reasonable to consider that the surface complexation and oxidation process have consumed notably high amount of OH^- ions in the solution and its affinity increases with reaction temperature elevation. This explains the "pH buffering effect" of CuS at increasing solution pH which suppresses the rising amount of OH- ions present in the solution.

At initial solution pH of 5 – 9, it is also identified that the decrease in final solution pH occurred upon the sorption of Hg(II) onto CuS and the magnitude of decrease increases

with reaction temperature elevation. These observations are similar to the trend observed in controlled studies as well as the uptake of Pb^{2+} and Cd^{2+} onto FeS (Coles, Rao, & Yong, 2000). To explain the trends observed, it is again considered that the sorption of OH^- ions onto CuS surface is still occurring in the presence of Hg(II) and its affinity increases with reaction temperature elevation. Nonetheless, a surface adsorption model which is prompted by the interaction between hydrolyzed Hg(II) species and mineral surface can be possible for its contribution in further decreasing the amount of OH^- ions (James & Healy, 1972; MacNaughton & James, 1974):

$$Hg^{2+} + mH_2O \leftrightarrow Hg(OH)_m^{(2-m)+} + mH^+ \quad (6.6)$$

$$–CuS + Hg(OH)_m^{(2-m)+} \leftrightarrow –CuSHg(OH)_m^{(2-m)+} \quad (6.7)$$

$$–CuSHg(OH)_m^{(2-m)+} + OH^- \leftrightarrow –CuSHg(OH)_{m+1}^{(1-m)+} \quad (6.8)$$

As shown in equation (6.7), the complexation of Hg(II) proceed initially via the adsorption of hydrolyzed species i.e. $Hg(OH)_m^{(2-m)+}$ onto CuS. The adsorption of $Hg(OH)_m^{(2-m)+}$ species onto CuS can result in a positively charged surface that attract OH^- ion for further adsorption as indicated in equation (6.8). Although this explanation is logical in some extent to decrease the amount of OH^- ions present in the solution, it is believed that $Hg(OH)_m^{(2-m)+}$ species is also acting as the competitive species relative to OH^- ion in the sorption process. This can be realized in the case where a lesser magnitude of decrease in final solution pH is in fact observed when the experiment is conducted in the presence of Hg(II). The adsorption of $Hg(OH)_m^{(2-m)+}$ onto CuS species predominate compare to adsorption of OH^- ions. Thus, lower amount of OH^- ions is adsorbed onto CuS during the sorption of Hg(II) onto CuS. This has eventually led to higher final solution pH being detected at initial solution pH of 5 – 9 when Hg(II) is present.

6.4. Dynamic Modeling on Mercury Sorption Kinetic

6.4.1. Effect of Contact Time on Mercury Uptake

In view of the different trends of mercury uptake, copper leached and solution pH changes at acidic and alkaline pH, the kinetic investigations are conducted at two different solution pH i.e. pH 1 and 9. The time-dependent experiments carried out in 50 ppm, 150 ppm, and 250 ppm Hg(II) solutions at 25°C under solution pH of 1 are illustrated in **Figure 6.13**. At pH 1, it is observed that the sorption of Hg(II) onto CuS proceed rapidly at the first 100mins for all Hg(II) concentration studied. The reaction between Hg(II) and CuS seems to achieve the equilibration at about 300mins of contact time regardless of the Hg(II) concentration applied.

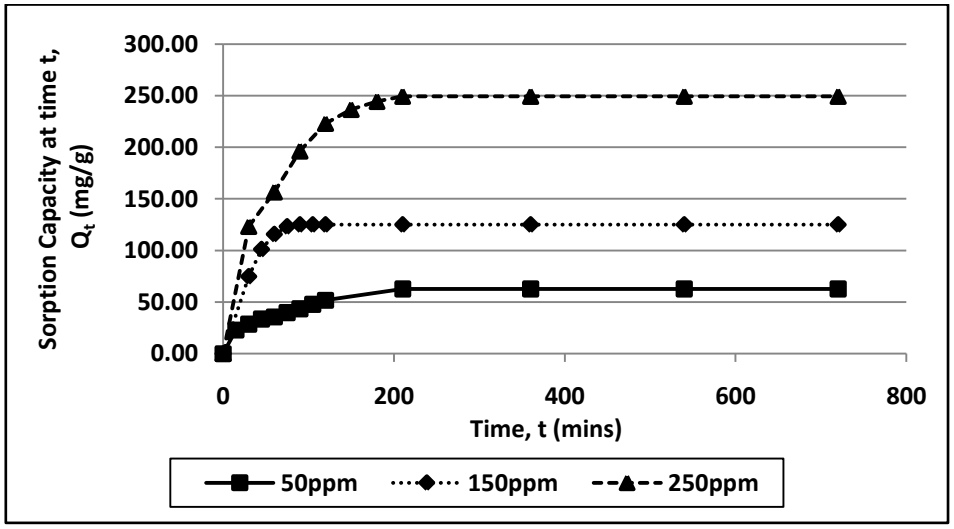

Figure 6.13. Effect of Contact Time on the sorption of Hg(II) onto pure phase Covellite under solution pH of 1 and temperature of 25°C.

Figure 6.14 depicts the kinetic experiments conducted in 50 ppm, 150 ppm, and 250 ppm Hg(II) solutions at 25°C under solution pH of 9. From the results, it is observed that the sorption of Hg(II) onto CuS begins quickly at the first 30mins for all Hg(II) concentration used. Nevertheless, it is identified that only the experiment performed in 50 ppm and 150 ppm Hg(II) can reach the equilibration within the time frame studied. For the

experiment conducted in 250 ppm Hg(II), it is detected that the experiment is not attaining equilibration in the time scale studied (900mins). The reactions performed in 250 ppm Hg(II) under solution pH of 9 will eventually require even longer reaction time to establish complete equilibration.

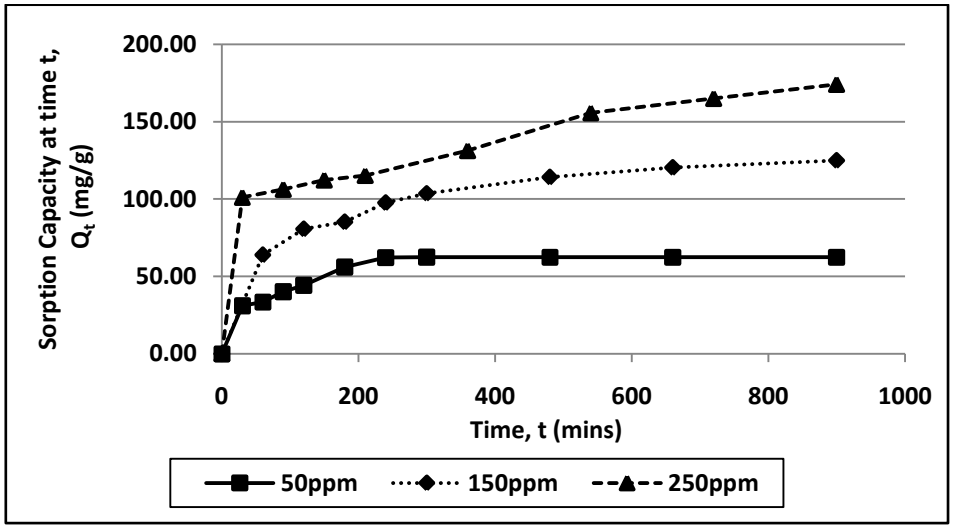

Figure 6.14. Effect of Contact Time on the sorption of Hg(II) onto pure phase Covellite under solution pH of 9 and temperature of 25°C.

Despite of the contact time studies at 25°C, the kinetic investigations were also extended to the reaction temperature of 35°C and 45°C. **Figure 6.15** depicted the kinetic data collected using 250 ppm Hg(II) solutions at 25°C, 35°C and 45°C under solution pH of 1. From the results, it is identified that the reaction conducted at 25°C is reaching the equilibration at about 210mins of contact time. However, a faster rate of equilibration is in fact observed as the reaction temperature is elevated to 35°C and 45°C. The time taken for complete equilibration has been shortened to 120mins and 90mins at 35°C and 45°C correspondingly.

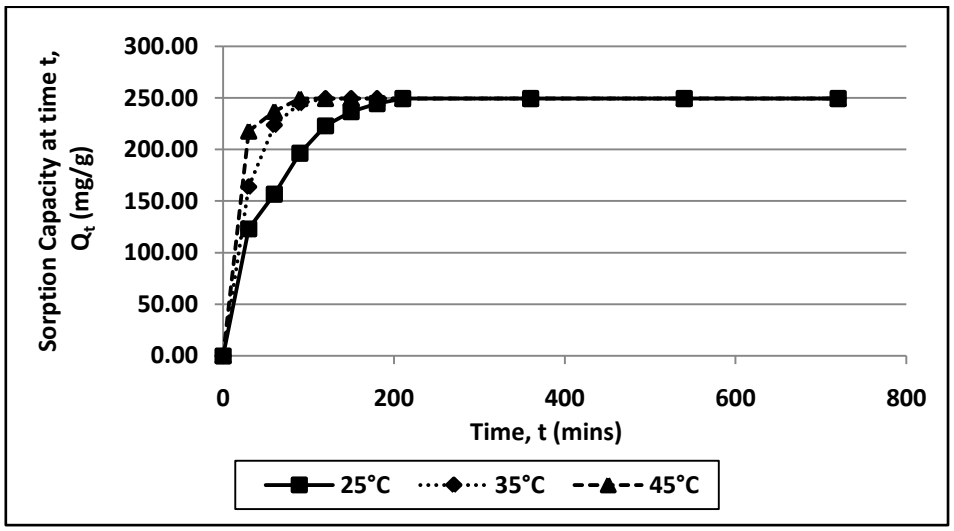

Figure 6.15. Effect of Contact Time on the sorption of Hg(II) onto pure phase Covellite at 25°C, 35°C and 45°C under solution pH of 1.

The kinetic experiments carried out using 250 ppm Hg(II) solutions at 25°C, 35°C and 45°C under solution pH of 9 are illustrated in **Figure 6.16**. From the previous Hg(II) concentration dependent kinetic results, it has been shown that the reaction carried out in 250 ppm Hg(II) solution at 25°C cannot attain the equilibration in the time frame studied (900mins). Nonetheless, it is detected that the equilibration rate for this particular reaction has been significantly increased when the reaction temperature is raised to 35°C and 45°C. The sorption of Hg(II) onto CuS has reached close to equilibration at about 900mins for reaction conducted at 35°C and more importantly, it establish the equilibration within 210mins for reaction performed at 45°C. Therefore, it is obvious that an increase of 10°C has reduced the time needed to establish equilibration. Thus, the reaction temperature elevation can ultimately lead to a faster sorption rate of Hg(II) onto CuS regardless of the solution pH applied.

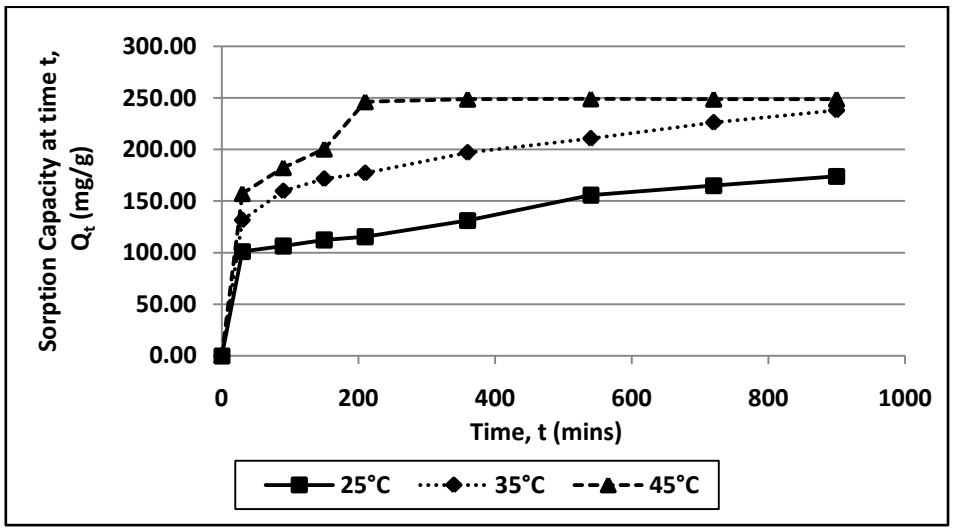

Figure 6.16. Effect of Contact Time on the sorption of Hg(II) onto pure phase Covellite at 25°C, 35°C and 45°C under solution pH of 9.

6.4.2. Elovich's Kinetic Model

For the sorption data collected, kinetic models are employed to investigate the sorption profile of aqueous Hg(II) onto solid CuS sorbent. **Figure 6.17** and **Figure 6.18** demonstrate the results of fitting experimental sorption data collected at 25°C under solution pH of 1 and 9 with Elovich's kinetic model respectively. The initial sorption rate (a), the Elovich constant (b) as well as the evaluated correlation coefficient (R^2) calculated via the fitting of sorption data at 25°C under solution pH of 1 and 9 are shown in **Table 6.3** and **Table 6.4** correspondingly. At pH 1, it is identified that the kinetic data obtained using various Hg(II) solutions at 25°C are not fitted well to this model with all of the R^2 shown is less than the nominal value of good fit i.e. 0.9800 (Christian, 2003). Similar results are also found at pH 9 in which poor R^2 value is again observed for the fitting of sorption data collected.

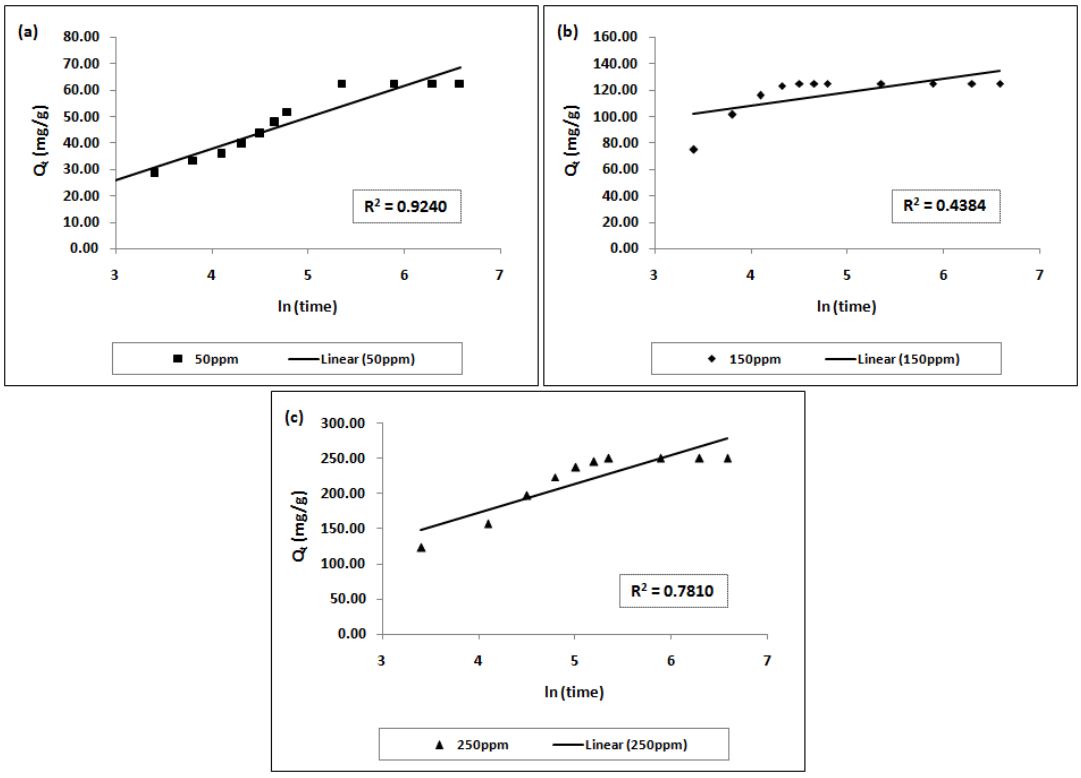

Figure 6.17. Elovich's kinetic plot for the sorption of (a) 50 ppm (b) 150 ppm and (c) 250 ppm Hg(II) onto pure phase Covellite under solution pH 1 and temperature of 25°C.

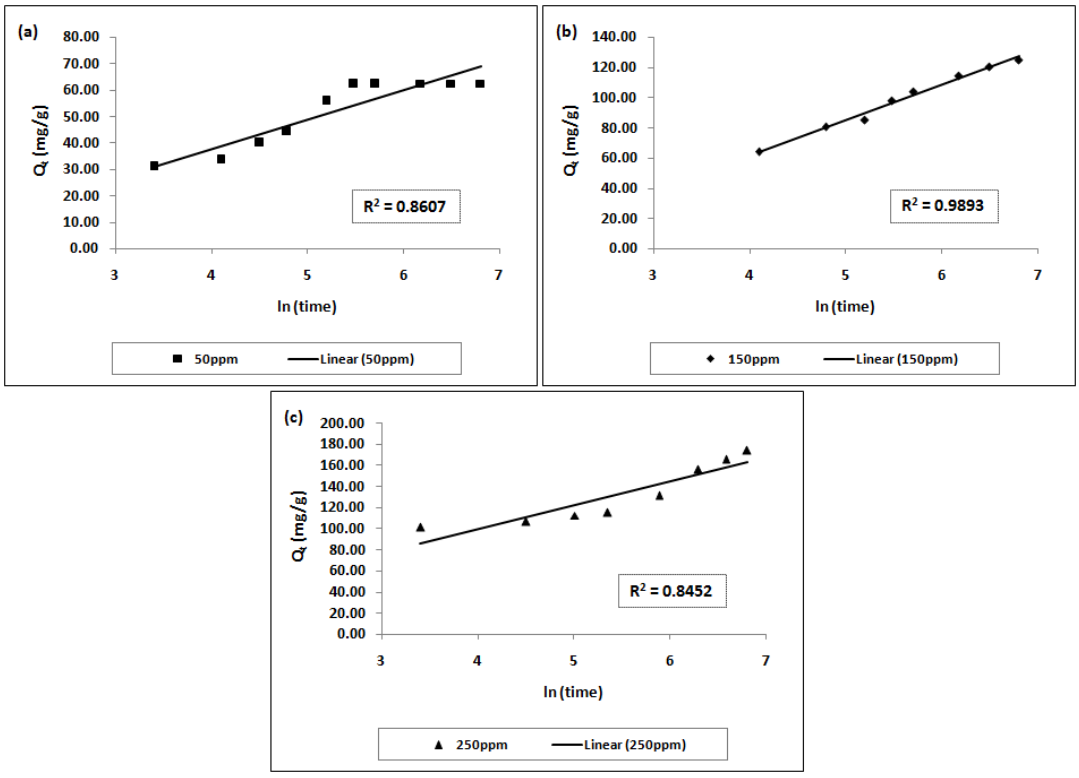

Figure 6.18. Elovich's kinetic plot for the sorption of (a) 50 ppm (b) 150 ppm and (c) 250 ppm Hg(II) onto pure phase Covellite under solution pH 9 and temperature of 25°C.

Table 6.3. List of kinetic parameters evaluated using Elovich's kinetic model for the sorption of Hg(II) onto pure phase Covellite at 50 ppm, 150 ppm and 250 ppm Hg(II) under solution pH 1 and temperature of 25°C.

Initial Hg(II) Concentration, C_0 (ppm)	Initial Sorption Rate, a (mg/(gmin))	Elovich Constant, b (g/mg)	Correlation Coefficient, R^2
50	5.2134	0.0841	0.9240
150	74.4820×10^2	0.0979	0.4384
250	52.7358	0.0247	0.7810

Table 6.4. List of kinetic parameters evaluated using Elovich's kinetic model for the sorption of Hg(II) onto pure phase Covellite at 50 ppm, 150 ppm and 250 ppm Hg(II) under solution pH 9 and temperature of 25°C.

Initial Hg(II) Concentration, C_0 (ppm)	Initial Sorption Rate, a (mg/(gmin))	Elovich Constant, b (g/mg)	Correlation Coefficient, R^2
50	5.8273	0.0892	0.8607
150	5.9390	0.0427	0.9893
250	32.0535	0.0438	0.8452

For the sorption data acquired using 250 ppm Hg(II) solutions at 25°C, 35°C and 45°C under solution pH of 1 and 9, the fitting results are depicted in **Figure 6.19** and **Figure 6.20** respectively. **Table 6.5** and **Table 6.6** shows the initial sorption rate (a), the Elovich constant (b) and correlation coefficient (R^2) calculated via the fitting of sorption data in both pH 1 and 9 at 25°C, 35°C and 45°C. In spite of the solution pH and temperature applied, it is detected that all of the R^2 value calculated is still less than 0.9800. It is obvious that all of the R^2 value calculated cannot be improved further even if higher reaction temperature is applied in the sorption studies.

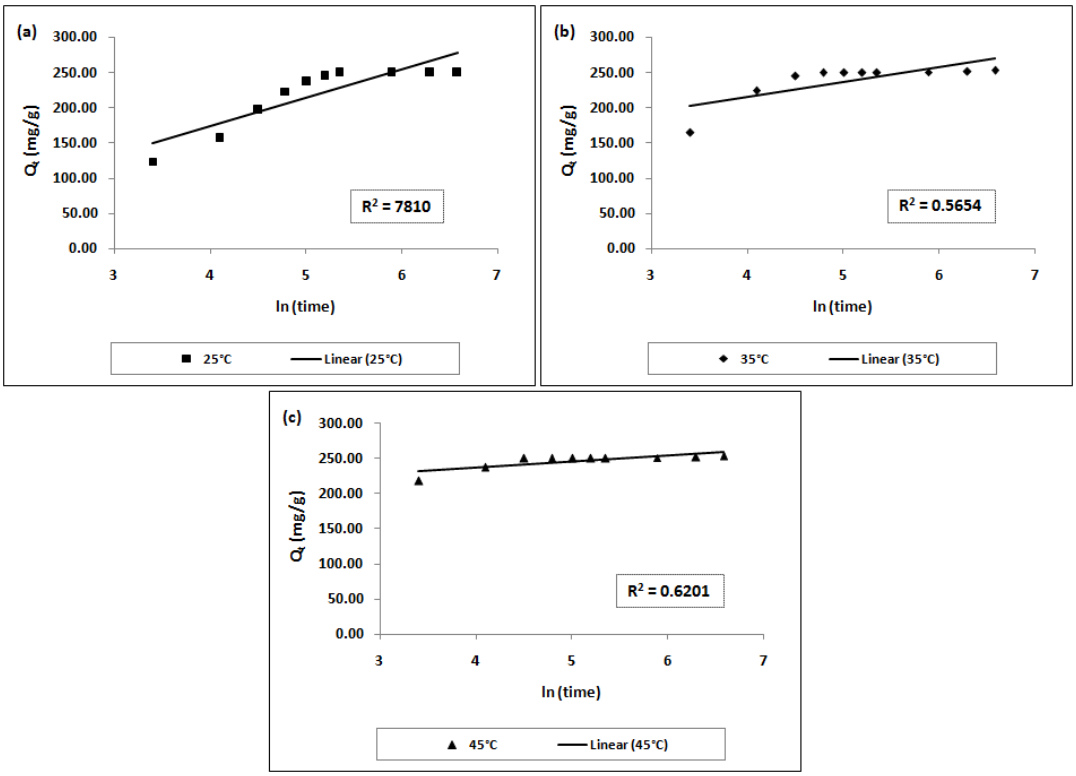

Figure 6.19. Elovich's kinetic plot for the sorption of 250 ppm Hg(II) onto pure phase Covellite at (a) 25°C (b) 35°C and (c) 45°C under solution pH 1.

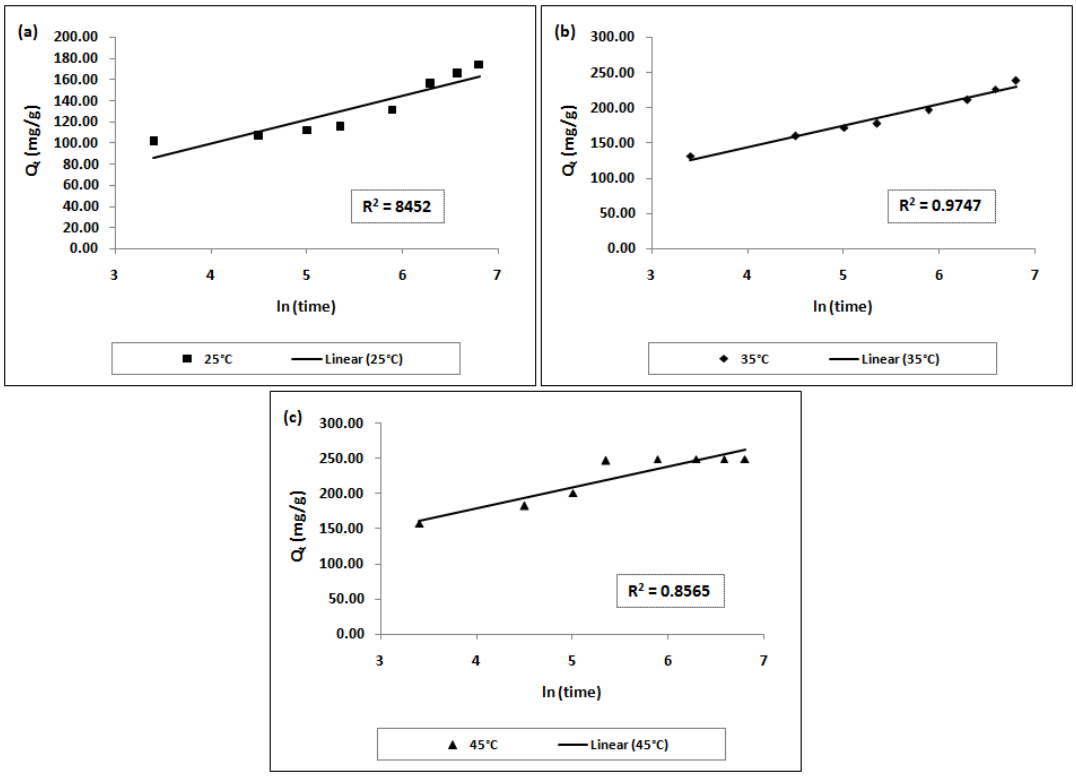

Figure 6.20. Elovich's kinetic plot for the sorption of 250 ppm Hg(II) onto pure phase Covellite at (a) 25°C (b) 35°C and (c) 45°C under solution pH 9.

Table 6.5. List of kinetic parameters evaluated using Elovich's kinetic model for the sorption of Hg(II) onto pure phase Covellite at 25°C, 35°C and 45°C under solution pH 1.

Reaction Temperature (°C)	Initial Sorption Rate, a (mg/(gmin))	Elovich Constant, b (g/mg)	Correlation Coefficient, R^2
25	52.7358	0.0247	0.7810
35	10.3513×10^{3}	0.0474	0.5654
45	14.4040×10^{10}	0.1167	0.6201

Table 6.6. List of kinetic parameters evaluated using Elovich's kinetic model for the sorption of Hg(II) onto pure phase Covellite at 25°C, 35°C and 45°C under solution pH 9.

Reaction Temperature (°C)	Initial Sorption Rate, a (mg/(gmin))	Elovich Constant, b (g/mg)	Correlation Coefficient, R^2
25	32.0535	0.0438	0.8452
35	61.5322	0.0327	0.9747
45	21.3984 x 10	0.0334	0.8565

6.4.3. Pseudo First-order Kinetic Model

Figure 6.21 and **Figure 6.22** illustrate the results in fitting the experimental sorption data collected at 25°C under solution pH of 1 and 9 with pseudo first-order (Lagergren's) kinetic model respectively. The predicted rate constants (k), equilibrium sorption capacity (Q_e) as well as the evaluated correlation coefficient (R^2) for solution pH 1 and 9 are shown in **Table 6.7** and **Table 6.8** correspondingly. At pH 1, it is observed that all of the R^2 value calculated is far less than 0.9800. Apparently, the bad R^2 value suggests that this model is not well in describing the sorption of Hg(II) onto CuS at acidic condition. At pH 9, it is found that poor R^2 value (about 0.8097) is observed for reactions conducted in 50 ppm. However, the R^2 value seem to be improved when the studies is carried out in 150 ppm (about 0.9974) and 250 ppm (about 0.9889) Hg(II) solutions.

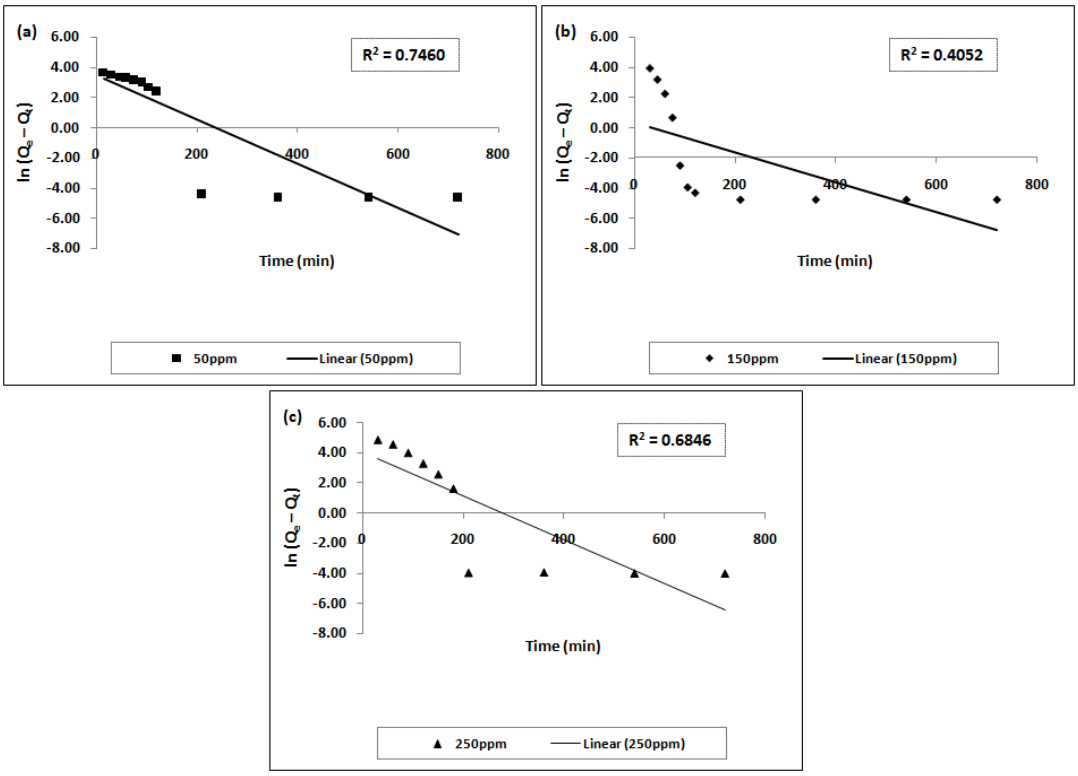

Figure 6.21. Lagergren's kinetic plot for the sorption of (a) 50 ppm (b) 150 ppm and (c) 250 ppm Hg(II) onto pure phase Covellite under solution pH 1 and temperature of 25°C.

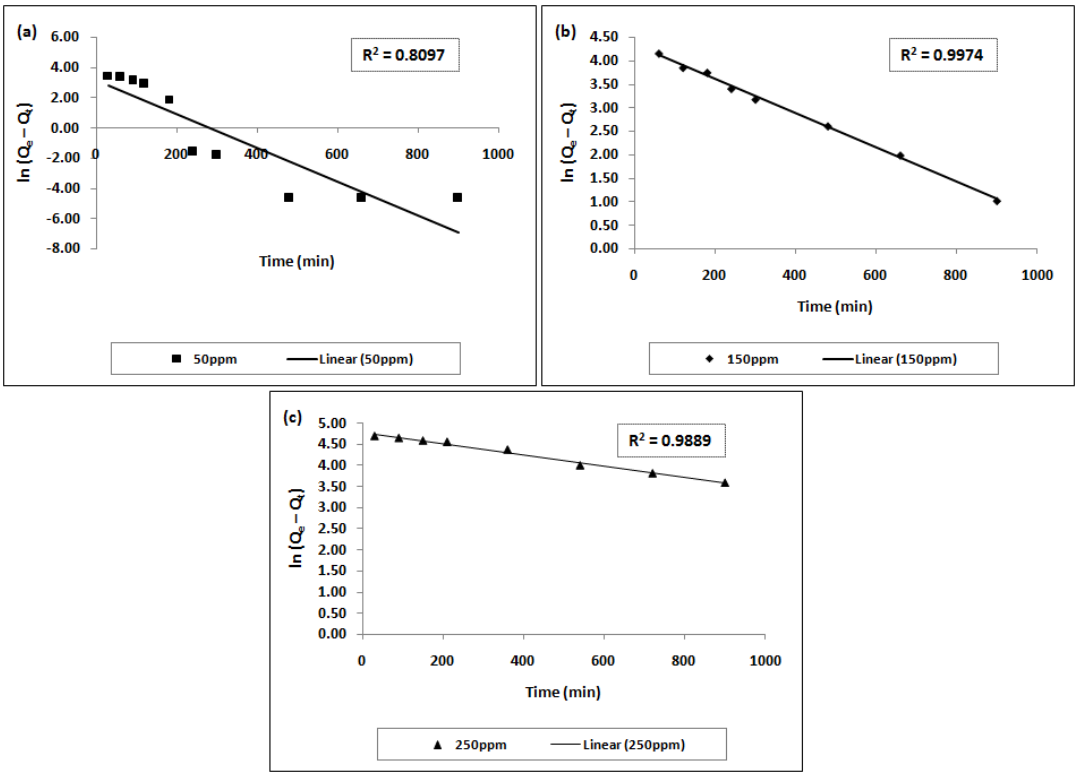

Figure 6.22. Lagergren's kinetic plot for the sorption of (a) 50 ppm (b) 150 ppm and (c) 250 ppm Hg(II) onto pure phase Covellite under solution pH 9 and temperature of 25°C.

Table 6.7. List of kinetic parameters evaluated using Lagergren's kinetic model for the sorption of Hg(II) onto pure phase Covellite at 50 ppm, 150 ppm and 250 ppm Hg(II) under solution pH 1 and temperature of 25°C.

Initial Hg(II) Concentration, C_0 (ppm)	Sorption Capacity at equilibrium, Q_e (mg/g)	Rate Constant, k (l/min)	Correlation Coefficient, R^2
50	31.16	0.0147	0.7460
150	1.35	0.0099	0.4052
250	56.14	0.0145	0.6846

Table 6.8. List of kinetic parameters evaluated using Lagergren's kinetic model for the sorption of Hg(II) onto pure phase Covellite at 50 ppm, 150 ppm and 250 ppm Hg(II) under solution pH 9 and temperature of 25°C.

Initial Hg(II) Concentration, C_0 (ppm)	Sorption Capacity at equilibrium, Q_e (mg/g)	Rate Constant, k (l/min)	Correlation Coefficient, R^2
50	23.46	0.0112	0.8097
150	76.42	0.0037	0.9974
250	118.89	0.0013	0.9889

The fitting results for the sorption data collected using 250 ppm Hg(II) solutions at 25°C, 35°C and 45°C under solution pH of 1 and 9 are depicted in **Figure 6.23** and **Figure 6.24** respectively. The predicted rate constants (k), equilibrium sorption capacity (Q_e) as well as the evaluated correlation coefficient (R^2) at 25°C, 35°C and 45°C under solution pH of 1 and 9 are shown in **Table 6.9** and **Table 6.10** correspondingly. In general, poor R^2 values are observed for almost all of the kinetic data fitted. Notably good R^2 values of about 0.9889 and 0.9893 are only found for the kinetic data collected at 25°C and 35°C under solution pH of 9. From the analysis, the kinetic data shows some correlation with Lagergren's kinetic model. Nevertheless, this model is still insufficient in describing the sorption kinetic behavior of Hg(II) onto Covellite at various reaction condition.

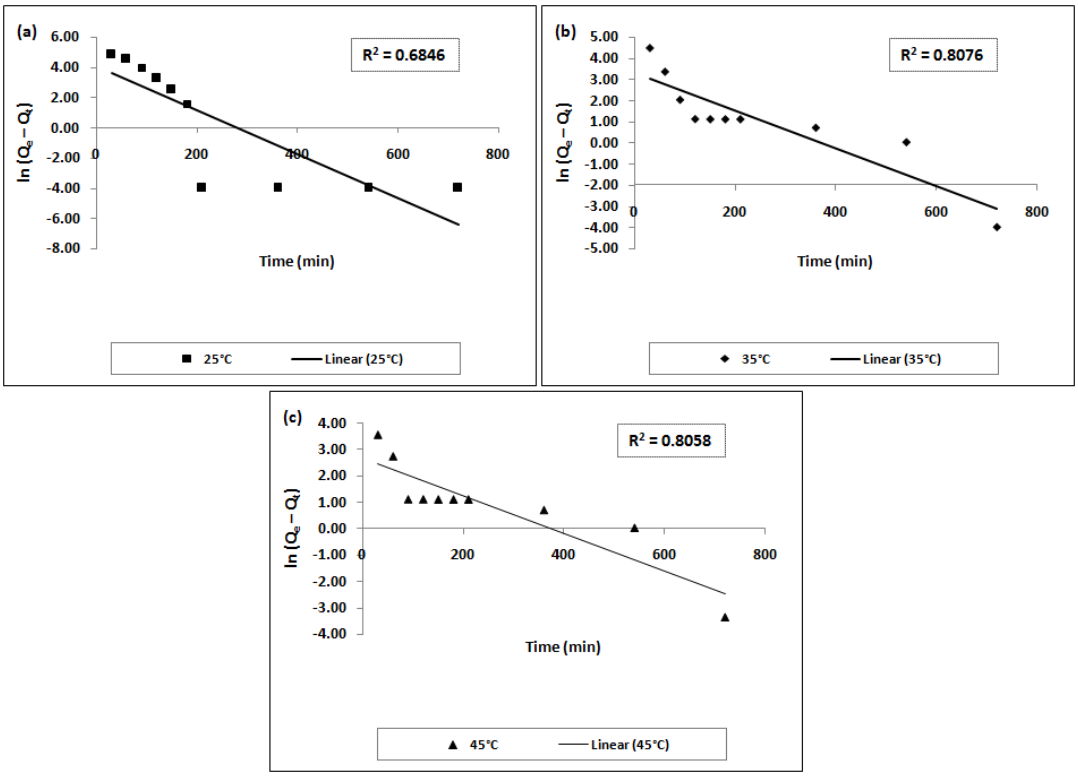

Figure 6.23. Lagergren's kinetic plot for the sorption of 250 ppm Hg(II) onto pure phase Covellite at (a) 25°C (b) 35°C and (c) 45°C under solution pH 1.

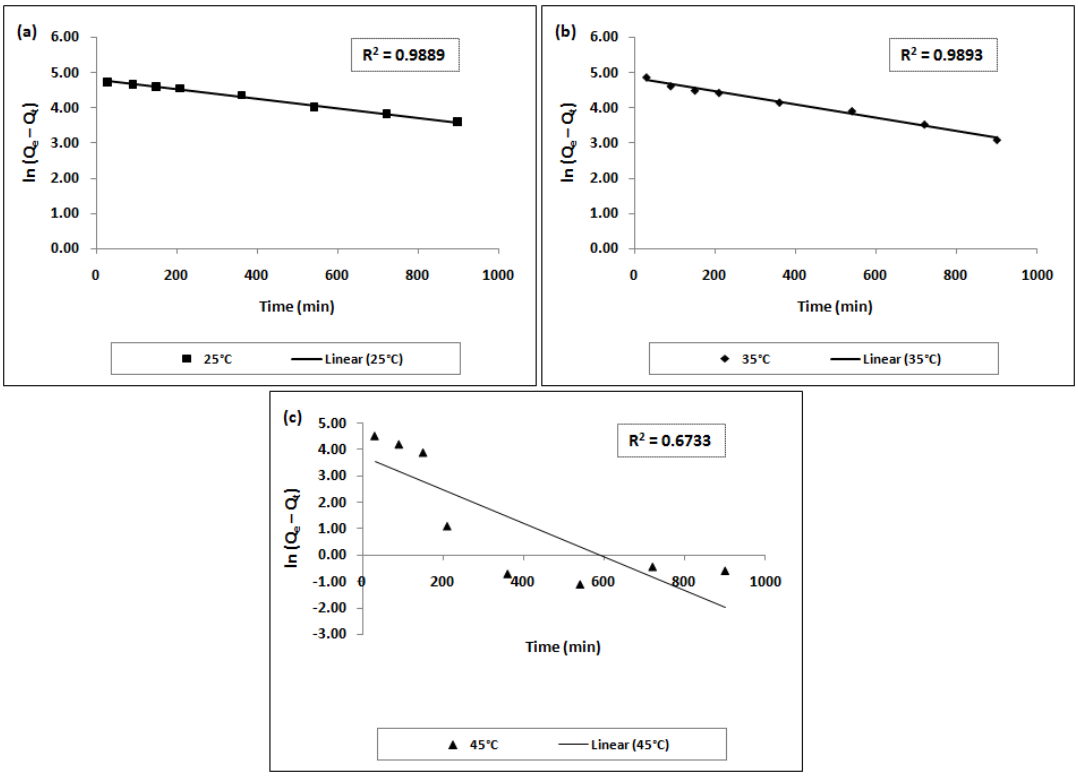

Figure 6.24. Lagergren's kinetic plot for the sorption of 250 ppm Hg(II) onto pure phase Covellite at (a) 25°C (b) 35°C and (c) 45°C under solution pH 9.

Table 6.9. List of kinetic parameters evaluated using Lagergren's kinetic model for the sorption of Hg(II) onto pure phase Covellite at 25°C, 35°C and 45°C under solution pH 1.

Reaction Temperature (°C)	Sorption Capacity at equilibrium, Q_e (mg/g)	Rate Constant, k (l/min)	Correlation Coefficient, R^2
25	56.14	0.0145	0.6846
35	26.66	0.0089	0.8076
45	14.69	0.0072	0.8058

Table 6.10. List of kinetic parameters evaluated using Lagergren's kinetic model for the sorption of Hg(II) onto pure phase Covellite at 25°C, 35°C and 45°C under solution pH 9.

Reaction Temperature (°C)	Sorption Capacity at equilibrium, Q_e (mg/g)	Rate Constant, k (l/min)	Correlation Coefficient, R^2
25	118.89	0.0013	0.9889
35	124.95	0.0019	0.9893
45	42.16	0.0064	0.6733

6.4.4. Pseudo Second-order Kinetic Model

The results in fitting the experimental sorption data collected at 25°C under solution pH of 1 and 9 with pseudo second-order (Ho's) kinetic model are shown in **Figure 6.25** and **Figure 6.26** respectively. The predicted rate constants (k), equilibrium sorption capacity (Q_e) as well as the evaluated correlation coefficient (R^2) for solution pH 1 and 9 are shown in **Table 6.11** and **Table 6.12** correspondingly. At pH 1, it is observed that all of the R^2 values evaluated are more than 0.9800. This shows that the kinetic data are well fitted with Ho's kinetic model. At pH 9, high R^2 values of 0.9966, 0.9984 and 0.9850 are found for reactions conducted in 50 ppm, 150 ppm and 250 ppm Hg(II) solutions correspondingly. Although there is a slight decrease of R^2 value observed in 250 ppm Hg(II) solution, Ho's kinetic model still shows good result in describing the sorption kinetic profile at 25°C.

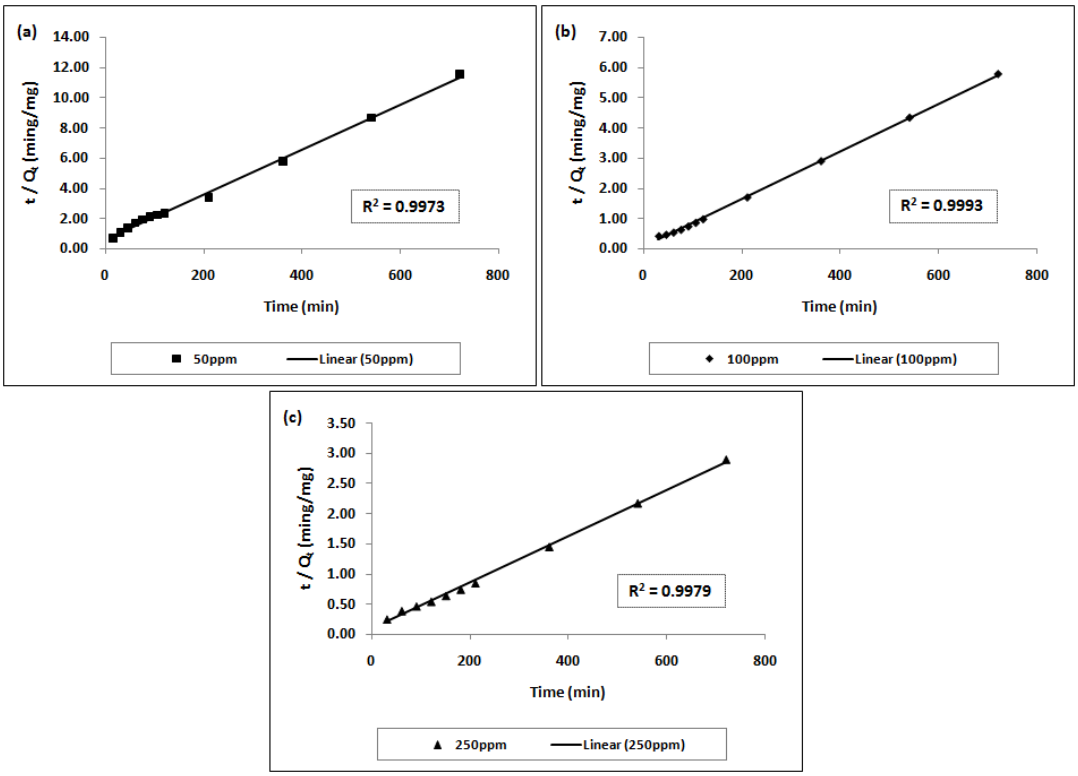

Figure 6.25. Ho's kinetic plot for the sorption of (a) 50 ppm (b) 150 ppm and (c) 250 ppm Hg(II) onto pure phase Covellite under solution pH 1 and temperature of 25°C.

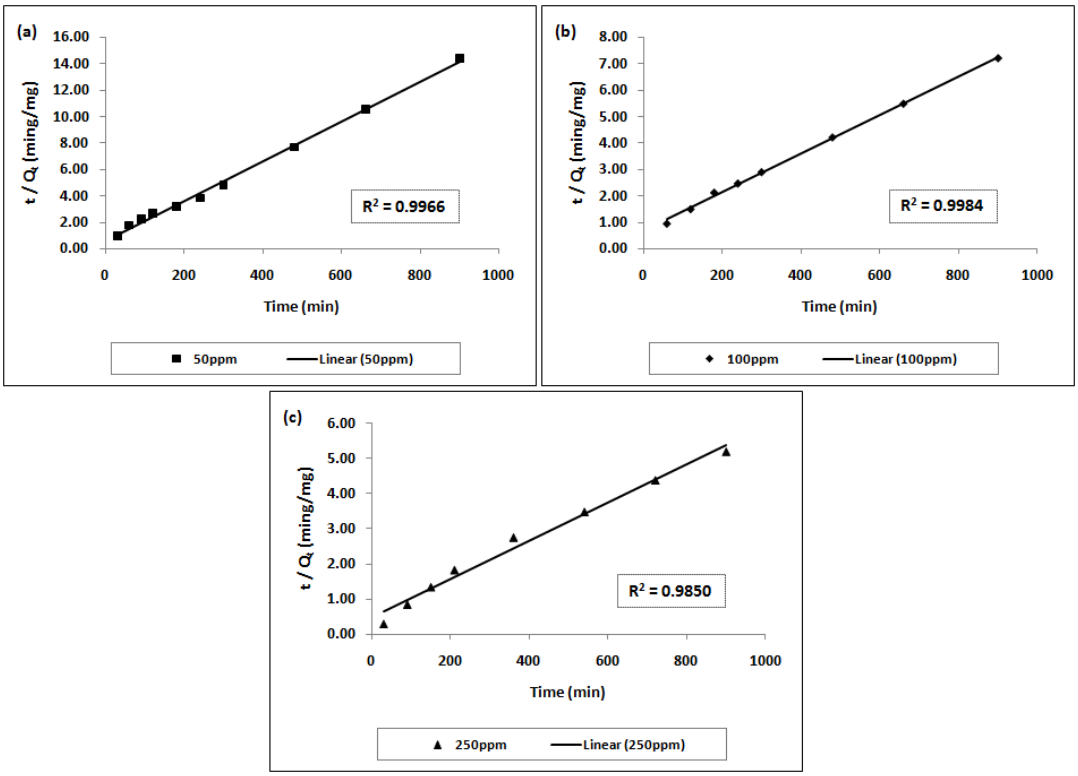

Figure 6.26. Ho's kinetic plot for the sorption of (a) 50 ppm (b) 150 ppm and (c) 250 ppm Hg(II) onto pure phase Covellite under solution pH 9 and temperature of 25°C.

Table 6.11. List of kinetic parameters evaluated using Ho's kinetic model for the sorption of Hg(II) onto pure phase Covellite at 50 ppm, 150 ppm and 250 ppm Hg(II) under solution pH 1 and temperature of 25°C.

Initial Hg(II) Concentration, C_0 (ppm)	Sorption Capacity at equilibrium, Q_e (mg/g)	Rate Constant, $k \times 10^{-2}$ (g/(mgmin))	Correlation Coefficient, R^2
50	67.11	0.0373	0.9973
100	126.58	0.1308	0.9993
250	263.16	0.0162	0.9979

Table 6.12. List of kinetic parameters evaluated using Ho's kinetic model for the sorption of Hg(II) onto pure phase Covellite at 50 ppm, 150 ppm and 250 ppm Hg(II) under solution pH 9 and temperature of 25°C.

Initial Hg(II) Concentration, C_0 (ppm)	Sorption Capacity at equilibrium, Q_e (mg/g)	Rate Constant, $k \times 10^{-2}$ (g/(mgmin))	Correlation Coefficient, R^2
50	66.23	0.0369	0.9966
100	136.99	0.0081	0.9984
250	185.19	0.0062	0.9850

Figure 6.27 and **Figure 6.28** depict the results in fitting the experimental sorption data collected using 250 ppm Hg(II) solutions at 25°C, 35°C and 45°C under solution pH of 1 and 9 with pseudo second-order (Ho's) kinetic model respectively. The predicted rate constants (k), equilibrium sorption capacity (Q_e) and the evaluated correlation coefficient (R^2) for solution pH 1 and 9 are shown in **Table 6.13** and **Table 6.14** correspondingly. Regardless of solution pH, it is observed that the reaction temperature elevation has again increased the R^2 value from 25°C to 45°C. From Ho's kinetic model fitting analysis, it is identified that good R^2 value are found for all of the kinetic data collected regardless of Hg(II) concentration, solution temperature and pH region applied. This implies that Ho's kinetic model is best in describing the kinetic profile of sorption of Hg(II) onto Covellite.

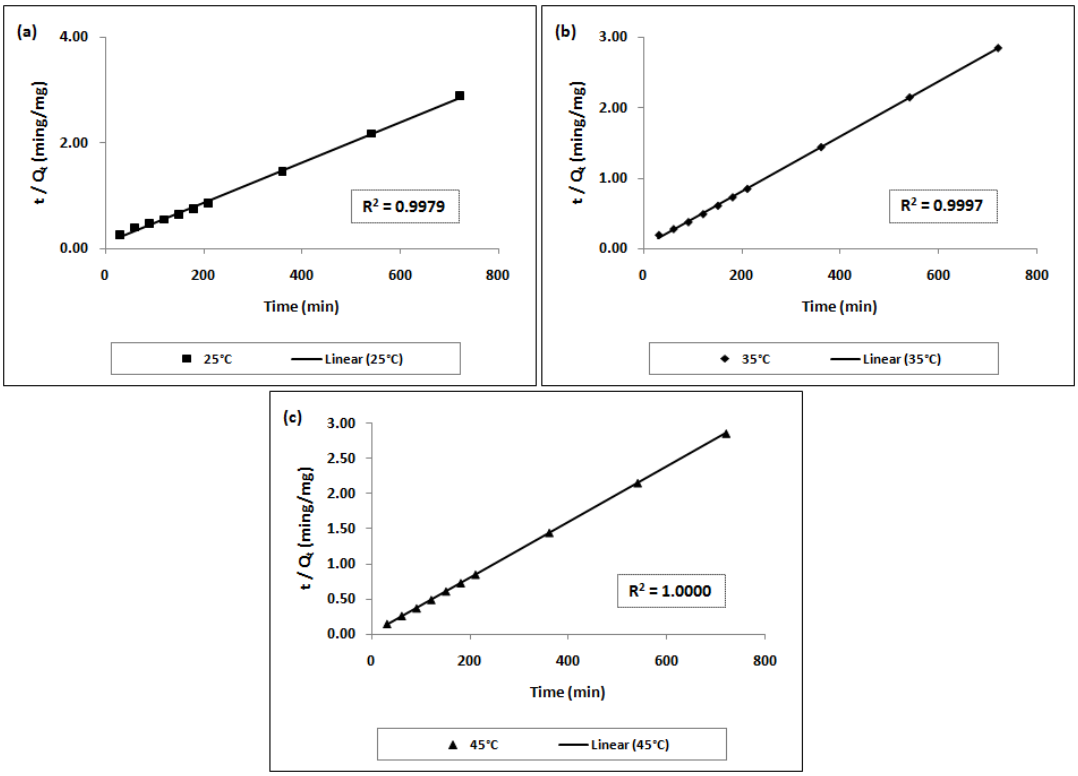

Figure 6.27. Ho's kinetic plot for the sorption of 250 ppm Hg(II) onto pure phase Covellite at (a) 25°C (b) 35°C and (c) 45°C under solution pH 1.

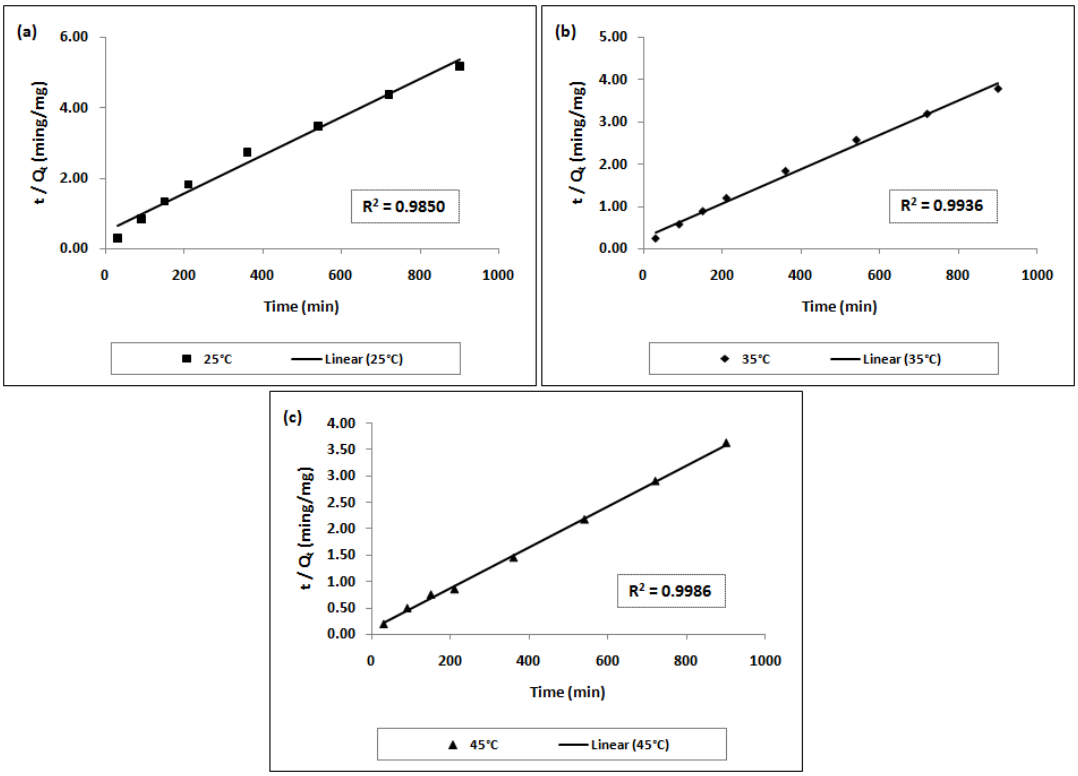

Figure 6.28. Ho's kinetic plot for the sorption of 250 ppm Hg(II) onto pure phase Covellite at (a) 25°C (b) 35°C and (c) 45°C under solution pH 9.

Table 6.13. List of kinetic parameters evaluated using Ho's kinetic model for the sorption of Hg(II) onto pure phase Covellite at 25°C, 35°C and 45°C under solution pH 1.

Reaction Temperature (°C)	Sorption Capacity at equilibrium, Q_e (mg/g)	Rate Constant, $k \times 10^{-2}$ (g/(mgmin))	Correlation Coefficient, R^2
25	263.16	0.0162	0.9979
35	256.41	0.0578	0.9997
45	256.41	0.1237	1.0000

Table 6.14. List of kinetic parameters evaluated using Ho's kinetic model for the sorption of Hg(II) onto pure phase Covellite at 25°C, 35°C and 45°C under solution pH 9.

Reaction Temperature (°C)	Sorption Capacity at equilibrium, Q_e (mg/g)	Rate Constant, $k \times 10^{-2}$ (g/(mgmin))	Correlation Coefficient, R^2
25	185.19	0.0062	0.9850
35	243.90	0.0067	0.9936
45	256.41	0.0159	0.9986

6.4.5. Discussion

In general, the uptake of mercury onto Covellite has been observed to occur in a two stage process regardless of the reaction condition employed. The first stage is consisted of the rapid sorption of Hg(II) onto CuS which occurred in the initial time frame of 100mins. After that, the reactions is continued by the slow uptake of Hg(II) approaching equilibrium. The initial rapid uptake of Hg(II) onto Covellite is probably due to the high concentration gradient of Hg(II) in the bulk solution as well as the abundant availability of the active sites on Covellite. As a result, large amount of Hg(II) from the bulk solution diffuse in a fast rate into the solid-liquid interface and sorbed onto the active S site of Covellite. Nevertheless, it is also noted that the saturation of Hg(II) complexes on Covellite can be achieved when reaction time is prolonged. This has led to a notably low amount of active site available for

Hg(II) sorption and finally a slow uptake of Hg(II) is observed at the time approaching equilibrium.

In comparing the sorption kinetic profile of Hg(II) onto CuS at 25°C under solution pH 1 and 9, the former has achieved complete equilibration within 720mins whereas the latter requires longer reaction time i.e. more than 900mins to establish complete equilibration at higher Hg(II) concentration. To explain the discrepancy of sorption rate observed, it is first considered the type of Hg(II) species present at different solution pH. From the chemical speciation diagram of $HgCl_2$ in water (**Figure 6.6)**, chlorine containing Hg(II) species i.e. $HgCl_2$, $HgCl^+$ and HgCl(OH) exist predominantly at acidic to near neutral pH region. Whist, $Hg(OH)_2$ is the only species present at near neutral to alkaline pH region. For the sorption of Hg(II) onto CuS, it is believed that a better interaction of chlorine containing Hg(II) with CuS has happened during the reaction. This has increased the overall sorption rate of Hg(II) onto CuS at pH 1. On the other hand, the slower sorption rate of Hg(II) onto CuS at pH 9 can be also correlated to the competitive adsorption of OH^- onto CuS in which the adsorption of OH^- has been identified at pH 5 – 9 (**Section 6.3.4)**. Furthermore, the adsorption of OH^- can also lead to subsequent formation of $Cu(OH)_2$ and CuO on CuS surface (Fullston, et al., 1999). Therefore, it is expected that both of the competitive adsorption of OH^- and its subsequent formation of $Cu(OH)_2$ and CuO can significantly decreased the sorption rate of Hg(II) onto CuS at pH 9.

Even though a slow rate of mercury uptake has been observed at 25°C under solution pH 9, it is important to note that the sorption rate of Hg(II) onto CuS can be increased significantly when reaction temperature is elevated. For reaction performed at 25°C, it is identified that the contact time of more than 900mins is required for complete equilibration. For reaction carried out at 35°C, the mercury uptake has reached close to equilibration at about 900mins of contact time. When solution temperature is finally

elevated to 45°C, the reaction seems to establish the equilibration within 210mins of contact time. These observations agrees well with the Arrhenius's law for rate of reaction in which reaction rates for many reactions double for every 10°C increase in reaction temperature. Therefore, it is indicative that at alkaline pH region, the rate of $Hg(OH)_2$ sorbed onto CuS can be successively increased via the reaction temperature elevation in which this has led to a shorter equilibration time being observed. Last but not least, the increase in sorption rate with solution temperature elevation has also indirectly explained the progressive increase in mercury uptake at solution pH 7 – 9 with reaction temperature that identified earlier in **Section 6.1.3**.

The sorption data collected at different Hg(II) concentration, solution temperature under solution pH of 1 and 9 have been fitted with three different two parameters linear kinetic model *i.e.* Elovich's kinetic model, Lagergren's pseudo first-order kinetic model and Ho's pseudo second-order kinetic model. From the fitting analysis of Elovich's kinetic model, it is found out that the kinetic data obtained are not fitted well to this model in which all of the R^2 shown is less than the nominal value of good fit i.e. 0.9800. In fact, the applicability of this model in analyzing the sorption data has been discussed (Plazinski, Rudzinski, & Plazinska, 2009) and this equation is somehow restricted to the initial time of sorption. For longer time of adsorption, this model has neglected the rate of simultaneously occurring desorption. Although effort has been tried in modifying Elovich equation using fundamental SRT (Statistical Rate Theory) approach for sorption kinetic data evaluation (Plazinski, et al., 2009; Rudzinski & Plazinski, 2009), the improved rate equation is still complex and it required advanced mathematical program for further data assessment.

From the fitting analysis of Lagergren's pseudo first-order kinetic model, it is identified that the fitting of kinetic data with this model is still poor. Again, this model fail to describe the rate of sorption of Hg(II) onto Covellite at different Hg(II) concentration,

solution temperature and pH region in which all of the R^2 shown is than the nominal value of good fit i.e. 0.9800. In discussing the utilization of this model in analyzing sorption kinetic data, Ho and McKay have previously reported the sorption kinetic of basic dyes from aqueous solution onto sphagnum moss peat. From their studies, the sorption kinetic data follows the Lagergren's model only for the rapid initial phase that occurs for a contact time of 0 – 30 minutes (Ho & McKay, 1998b). The use of Lagergren's kinetic model in fitting experimental data has once again reviewed (Ho & McKay, 1998a). Indeed, most of literature data shows the similar limitation of Lagergren's model in describing their sorption kinetic system in which this model is restricted to a limited fraction of the reaction range. In addition, the equilibrium sorption capacity (Q_e) in the form of log (Q_e) is actually an adjustable parameter and often, it is found not equal to the intercept of a plot of log ($Q_e - Q_t$) vs t. Therefore, this is apparent that Lagergren's kinetic model is not appropriate in describing the kinetic profile of sorption of Hg(II) onto Covellite for the entire sorption period *i.e.* contact time of 900mins (15 hours).

From the fitting analysis of Ho's pseudo second-order kinetic model, it is identified that all of the R^2 shown is greater than the nominal value of good fit i.e. 0.9800. Apparently, this is the most suitable model among the three in describing the sorption kinetic of Hg(II) onto Covellite. In actual fact, the pseudo second-order kinetic model has been used by Blanchard et al. to correlate the rate of ion exchange reaction of heavy metal onto natural zeolite (Blanchard, et al., 1984). The assumption behind this model is that the kinetic order of this reaction is two with respect to the number of adsorption site available for the exchange processes. Thus, in order to link the relationship of the kinetic data collected with this model, it is considered that the kinetic order should be two with respect to the overall order for the reaction. However, for the sorption mechanism establishment, the studies from solid characterization techniques are still strongly needed to answer these questions.

6.5. Interpretation on Sorption Isotherm

6.5.1. Fitting of Isotherm Model

The loading of Hg(II) onto CuS at different Hg(II) concentration has been modeled using sorption isotherm models. Since highest mercury uptake efficiency has been observed at acidic pH and there is a increased tendency for HgO to precipitate in concentrated Hg(II) solutions at alkaline pH, the sorption isotherms were only measured under solution pH 1 condition. The linear plot of Langmuir and Freundlich models at 25°C, 35°C and 45°C under solution pH 1 are shown in **Figure 6.29 (a)** and **(b)** respectively while the model constants of both Langmuir and Freundlich isotherms along with the correlation coefficient (R^2) are tabulated in **Table 6.15**. From the analysis, it is identified that the fitting of sorption data with Freundlich model shows poor R^2 value of about 0.9483, 0.9214 and 0.8726 at reaction temperature of 25°C, 35°C and 45°C correspondingly. However, notably high R^2 values are obtained when the sorption data were fitted with Langmuir model in which R^2 values of about 0.9985, 0.9960 and 0.9952 has been observed at solution temperature of 25°C, 35°C and 45°C respectively. These results strongly suggest that the experimental data collected at 25°C, 35°C and 45°C agrees well with the Langmuir isotherm, assuming that all of the sorption sites have equal energy (Langmuir, 1916). From Langmuir isotherm, the maximum loading of Hg(II) onto CuS upon complete saturation, Q_{max} is found to be 434.78 mg Hg(II) / g of sorbent at 25°C. Nonetheless, as reaction temperature is raised to 35°C and 45°C, it is observed that the Q_{max} has increased to 460.83 mg/g and 520.83 mg/g respectively.

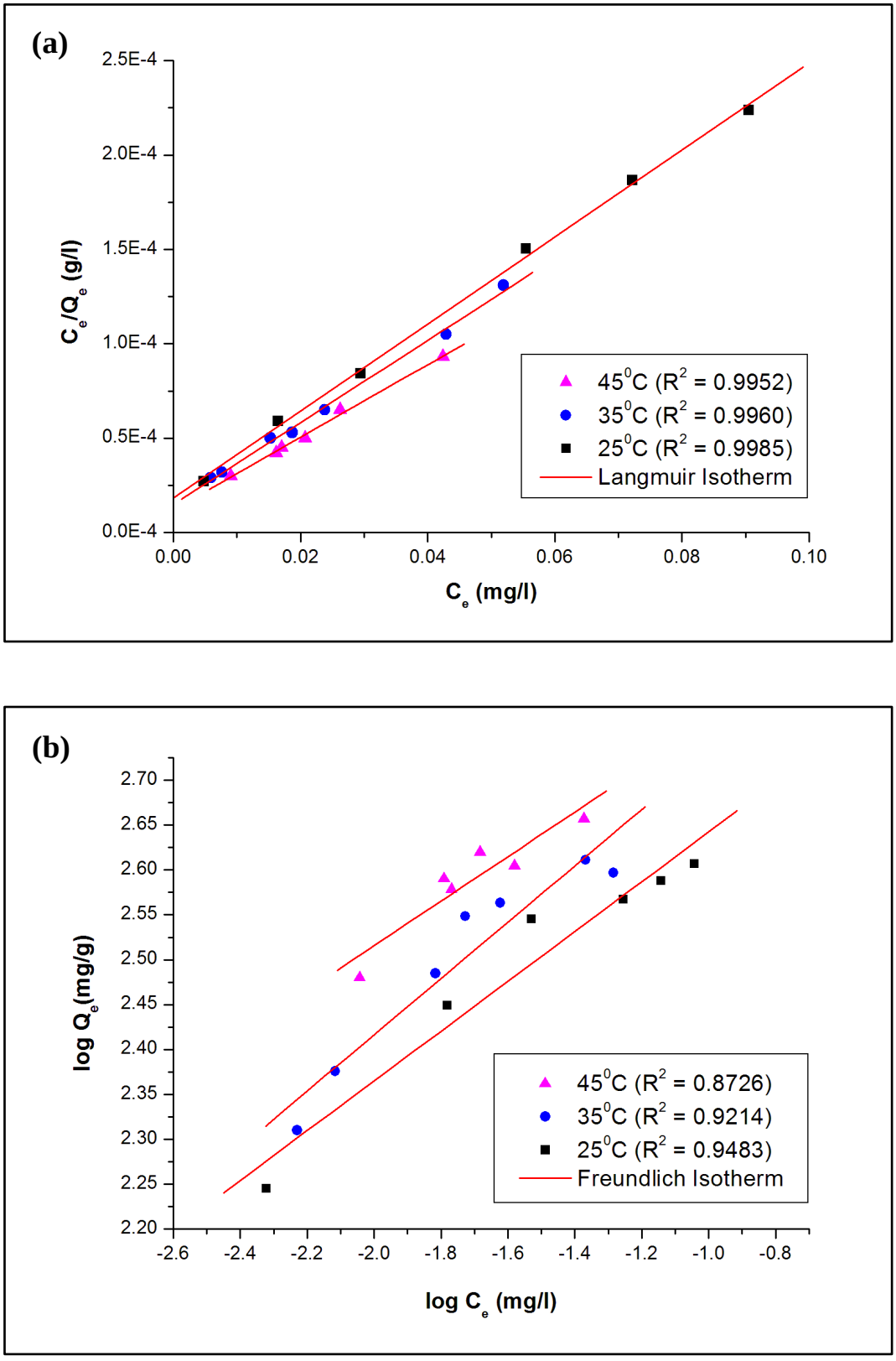

Figure 6.29. Fitting of equilibrium sorption data using (a) Langmuir Isotherm (b) Freundlich Isotherm.

Table 6.15. Langmuir and Freundlich Isotherm Constants and their corresponding Correlation Coefficients (R^2) for the sorption of Hg(II) onto pure phase Covellite.

(a) Langmuir Isotherm			
Constants	Temperature (°C)		
	25	35	45
R^2	0.9985	0.9960	0.9952
K_a, (l/mg)	124.84	145.76	160.30
Q_{max}, (mg/g)	434.78	460.83	520.83

(b) Freundlich Isotherm			
Constants	Temperature (°C)		
	25	35	45
R^2	0.9483	0.9214	0.8726
K_F, $(mg/g)(l/mg)^{1/n}$	831.38	1106.37	1027.07
1/n	0.2774	0.3137	0.2479

6.5.2. Specific Surface Area Analysis

In Langmuir isotherm, monolayer coverage is resulted during the maximum sorption of solute molecule onto the solid sorbent. The value on the maximum sorption is the ultimate sorption capacity at high concentration and it can be used to estimate the specific surface area, $S_{specific}$ of CuS using the following equation:

$$S_{specific} = \frac{Q_{max} N A}{M} \qquad (6.9)$$

where $S_{specific}$ is the specific surface area in m^2/g CuS, Q_{max} is the maximum monolayer sorption capacity in g Hg(II)/g CuS, N is Avogadro's constant (6.02×10^{23} particles/mol), A is the cross-sectional area of Hg(II) in m^2 (4.23×10^{-20}), and M is the molecular weight

of Hg(II) (200.59 g/mol). The evaluated results using Q_{max} found at reaction temperature of 25°C, 35°C and 45°C are shown in **Table 6.16**. In general, it is detected that the specific surface area of CuS increases with the reaction temperature elevation. This observation is somehow predicted since the equation used for calculating specific surface area, $S_{specific}$, involves the Q_{max} value in which this value also increases at higher reaction temperature.

Table 6.16. Specific surface area evaluated for pure phase Covellite at different reaction temperature.

Constants	Temperature (°C)		
	25	35	45
$S_{specific}$ (m^2/g)	55.20	58.50	66.12

6.5.3. Isotherm Shape Factor Analysis

The effect of isotherm shape can be used to predict the favorability of a sorption process in both the fixed-bed (Webi & Chakravort, 1974) and batch sorption system (Poots, McKay, & Healy, 1978). According to Hall et. al. (Hall, Eagleton, Acrivos, & Vermeulen, 1966), the essential features of the Langmuir isotherm can be expressed in a dimensionless constant which is defined by the following relationship:

$$K_R = \frac{1}{1 + K_a C_0} \qquad (6.10)$$

where K_R is the dimensionless separation factor, C_0 is the initial concentration (mg/l) and K_a is the Langmuir constant (l/mg). The parameter K_R shows the shape of isotherm based on **Table 6.17**. The relationship between the parameter K_R and C_0 are illustrated in **Figure 6.30**. From the data, all of the K_R calculated show positive value that are far less than unity and it decreases as initial Hg(II) concentration increases. Moreover, the values of K_R also

decrease as reaction temperature is elevated. Thus, it is indicative that the sorption of Hg(II) onto CuS is more favorable at higher initial Hg(II) concentration, not to mention that the process also becomes even more favorable when reaction temperature is elevated.

Table 6.17. The shape of isotherm based on the value of separation factor, K_R.

Values of K_R	Type of isotherm
$K_R > 1$	Unfavorable
$0 < K_R \leq 1$	Favorable
$K_R = 0$	Irreversible

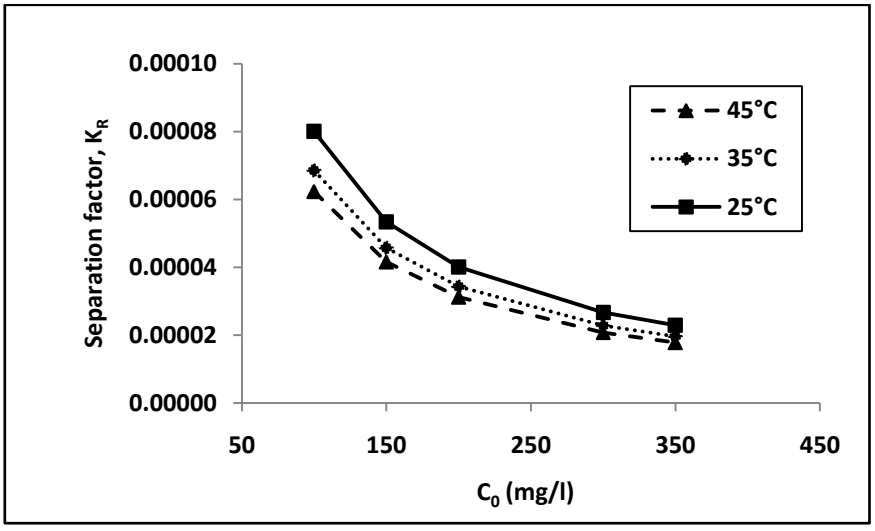

Figure 6.30. Plot of K_R against initial Hg(II) concentration at various reaction temperature.

6.5.4. Evaluation of Thermodynamic Parameters

In the investigation of certain material as potential sorbent, both of the energy and entropy changes must be considered to evaluate the process's spontaneity. The thermodynamic parameters, Gibb's free energy change, $\Delta G°$, for the sorption of Hg(II) onto CuS is calculated using the equation below:

$$\Delta G° = - RT\ln K_a \qquad (6.11)$$

where R is the universal gas constant (8.314 J/mol K), T is the absolute temperature in K and K_a is the Langmuir constant in l/mg. **Table 6.18** shows the Gibb's free energy change, ΔG° calculated from equation 6.11. From the results, it is observed that negative values of ΔG° are obtained at all of the solution temperature applied. The negative values of ΔG° confirm the feasibility of sorption of Hg(II) onto CuS. This indicates the spontaneous nature and high preference of Hg(II) to sorb onto CuS. In addition, it is also seen that the negative values of ΔG° increases with reaction temperature elevation. This observation shows that the sorption of Hg(II) onto CuS has become even more favorable when higher reaction temperature is employed in the system.

Table 6.18. Thermodynamic parameters evaluated for the sorption of Hg(II) onto pure phase Covellite.

Temperature (°C)	ΔG° (kJ/mol)	ΔH° (kJ/mol)	ΔS° (kJ/mol K)
25	-25.09	9.83	0.1170
35	-26.33		
45	-27.44		

For the enthalpy change, ΔH° and entropy change, ΔS°, the relationship shown in equation 6.12 has been used for their determination. A straight line plot of Gibb's free energy change, ΔG°, versus temperature, T (**Figure 6.31**) would give the intercept of enthalpy change, ΔH° and slope of entropy change, ΔS° during the evaluation.

$$\Delta G^\circ = \Delta H^\circ - T\Delta S^\circ \qquad (6.12)$$

From the analysis, positive enthalpy change, ΔH° = 9.83 kJ/mol has been identified. This implies that an endothermic reaction which absorb heat from the environment occurred

during the sorption of Hg(II) onto CuS. On the other hand, positive entropy change, $\Delta S°$ = 0.1170 kJ/mol K is also detected from the evaluation. The positive change in $\Delta S°$ reflects that increasing randomness at the solid/liquid interface has happened during the sorption of Hg(II) onto CuS.

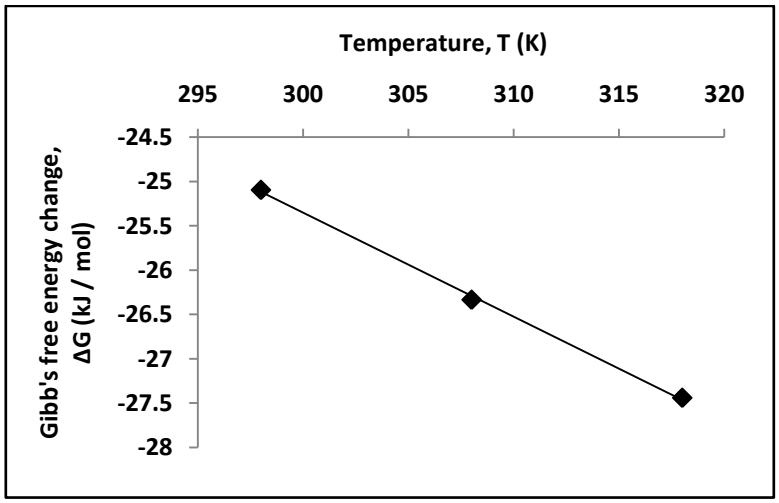

Figure 6.31. Plot of Gibb's free energy change, $\Delta G°$, versus temperature, T.

6.5.5. Discussion

From the isotherm studies, it is identified that the sorption of Hg(II) onto CuS at 25°C, 35°C and 45°C under solution pH 1 follows well with the Langmuir isotherm with all of the R^2 value greater than 0.9800. As a result, it can be assumed that all of the sorption sites on CuS are energetically homogeneous and identical in which only one Hg(II) can accommodate one specific sorption site. This has resulted in single adsorption layer i.e monolayer adsorption being observed at the contact time reaching complete equilibration (Langmuir, 1916, 1917, 1918). The maximum loading of Hg(II) onto CuS upon saturation, Q_{max} which is estimated from Langmuir model is found to be 434.78 mg Hg(II) / g of sorbent at 25°C. This observation is similar to the maximum sorption capacity found for heavily oxidized CuS in the previous chapter (416.67mg/g), suggesting that the passivation

of CuS by $CuSO_4$ does not affect much on the maximum capacity of CuS in scavenging Hg(II) at acidic condition. Furthermore, the Q_{max} of CuS is found to be greater than Q_{max} of other un-modified and modified metal oxide and metal sulfide reported in the literature (see **Table 6.19**). This finding clearly demonstrates that CuS tend to has stronger affinity towards Hg(II) trapping when compared to other metal oxide and metal sulfide materials.

Table 6.19. Maximum sorption capacity of metal oxide and sulfide in scavenging Hg(II).

Sorbent material	Maximum sorption capacity (mg/g)	Reference
Single phase Covellite (CuS)	434.78	Present work
Zinc and Tin sulfide chalcogel	280.83 – 339.00	(Oh, et al., 2011)
Mercapto-functionalized Fe_3O_4 polymers	256.40	(Pan, et al., 2012)
Polyacrylamide-grafted iron(III) oxide	155.01	(Manju, et al., 2002)
Thiol-functionalized zeolite and Portland cement	89.32	(X.-Y. Zhang, et al., 2009)
Natural zeolites	57.50	(Chojnacki, et al., 2004)
Fe(III) / Cr(III) hydroxide	37.30	(Namasivayam & Senthilkumar, 1997)
Fe_3O_4 nano-particles modified with 2-mercaptobenzothiazole (MIOPs)	0.59	(Parham, et al., 2012)
MgO impregnated volcanic ash soil-ceramic	0.27	(Bhakta & Munekage, 2011)
Pyrite, FeS_2	0.12	(Bower, et al., 2008)
Mercury sulfide (HgS)	0.17×10^{-5}	(Hasany, et al., 1999)

From the maximum sorption capacity analysis, it is detected that the Q_{max} value has increased to 460.83 mg/g and 520.83 mg/g when the isotherm studies are carried out at

35°C and 45°C respectively. Obviously, this result indicates that the reaction temperature elevation has a propensity to increase the maximum sorption capacity of sorbent in which this is also commonly found in solution phase sorbent investigation (Ho, Huang, & Huang, 2002; Hosseini-Bandegharaei, et al., 2011; Inbaraj & Sulochana, 2006; Wajima & Sugawara, 2011). In order to explain the trend observed, it is first considered that a swelling effect within the inner structure of CuS arises when the reaction temperature is lifted (El-Shafey, 2010; Tiwari, Ghosh, Rupainwar, & Sharma, 1993). The swelling of CuS has increased the surface area of CuS as well as open up the internal pore structure of CuS in enabling more Hg(II) to further penetrate and adsorbed during the reaction. In addition, it is possible to think that the reaction temperature elevation has also led to the new active sorption site generation (Ho & Wang, 2008; Khalid, Ahmad, Kiani, & Ahmed, 1999). The creation of new active site together with the pre-existing ones in the powder has remarkably increased the amount of mercury loaded onto CuS at higher reaction temperature.

Presuming that monolayer sorption coverage occurred during the sorption of Hg(II) onto CuS, the value on the maximum sorption capacity, Q_{max} has been used in calculating the specific surface area, $S_{specific}$ of CuS at different reaction temperature. From the analysis, $S_{specific}$ with values of 55.22, 58.53 and 66.15 m^2/g are evaluated for reaction carried out at temperature of 25°C, 35°C and 45°C respectively. The increase of $S_{specific}$ with reaction temperature is due to the increase of maximum sorption capacity used in the calculation. Alternatively, the surface area of CuS is also determined from the *Brunnauer-Emmet-Teller* (BET) gas sorptometry measurement in which the N_2 adsorption and desorption isotherm is illustrated in **Appendix B**. The BET surface area of CuS was evaluated to be 15 m^2/g while the total pore volume was determined to be 0.029 cm^3/g. In contrast, it is identified that the Langmuir monolayer sorption isotherm gives bigger value than the BET multilayer sorption isotherm. This observation can be considered uncommon since surface area

calaculated from BET multilayer isotherm would always give higher surface area than Langmuir monolayer isotherm. Nonetheless, the opposite trend observed clearly suggested the occurrence of other crystallite growth reactions which can increase the surface area of CuS. Undeniably, the increase of surface area of CuS upon Hg(II) sorption has also become one of the aims that needed to be solved via studies of solid characterization techniques.

Apart from the surface area analysis, it was found that the maximum sorption capacity of CuS in removing Hg(II) is notably high when compared to other sorbent materials studied in the literature. **Table 6.20** shows the maximum sorption capacity as well as the surface area of different sorbent materials in scavenging Hg(II). From the findings, it is observed that high surface area materials like activated carbon, silica and their derivatives do not correlate well with the high sorption capacity in adsorbing Hg(II). On the contrary, it is recognized that only those material that are functionalized with thiourea, sulfur or sulfide will have high affinity towards Hg(II) immobilization even if the surface area is not high in the system. This phenomenon is in good agreement with the hard soft acid base theory proposed by Pearson et. al. (Pearson, 1963) in which the soft acid, Hg(II) tends to interact well with soft base, S in any reaction. Thus, it is apparent that CuS is an effective sorbent material in scavenging Hg(II) with astounding maximum sorption capacity of 434.78 mg/g despite of the low surface area possessed in its internal structure.

Table 6.20. Sorbent materials of different surface area and maximum sorption capacity in scavenging Hg(II).

Sorbent material	BET Surface Area ($m^{2/}g$)	Maximum sorption capacity (mg/g)	Reference
Activated carbon from rice husk	2786	555.60	(Song, Zhang, Yan, Jiang, & Xie, 2012)
Thiol containing ethene bridged mesoporous silica	1182	64.19	(De Canck, Lapeire, De Clercq, Verpoort, & Van Der Voort, 2010)
Activated carbon from furfural	1100	174.00	(Yardim, et al., 2003)
2-mercaptobenzothiazole-modified mesoporous silica	885	26.08	(Pérez-Quintanilla, et al., 2006)
Tin sulfide chalcogels	520	280.83	(Oh, et al., 2011)
Benzoylthiourea-modified mesoporous silica	505	1343.95	(Olkhovyk, et al., 2004)
Pyridine, dimethyl sulfoxide and 3 - aminopropyltriethoxysilane modified clay	198	355.04	(Guerra, Viana, & Airoldi, 2009).
Polyacrylamide-grafted iron (III) oxide	97	155.01	(Manju, et al., 2002)
Chitin isolated from crab	82	70.00	(Barriada, et al., 2008)
Natural zeolites	75	57.50	(Chojnacki, et al., 2004)
Thiourea-modified magnetic chitosan	62	625.20	(L. Zhou, Wang, Liu, & Huang, 2009)
Sulfur-impregnated activated carbons from coal	50	254.35	(Wajima & Sugawara, 2011)
Granular bentonite	24	1.70	(Fernandez-Nava, Ulmanu, Anger, Maranon, & Castrillon, 2011)
Single phase Covellite (CuS)	15	434.78	Present work

From the isotherm shape factor and Gibb's free energy analysis, the results show that the sorption of Hg(II) onto CuS is spontaneous and its favourability increases with reaction temperature elevation. Thus, it is indicative that CuS is a good sorbent for mercury especially dealing to highly contaminated Hg(II) system when high solution temperature is applied in the treatment. The enthalpy change of reaction (ΔH°) is determined to be 9.83 kJ/mol. The positive ΔH° observed implies that this particular sorption process is endothermic reaction. Nevertheless, it is important to note that not all of the mercury sorption systems were endothermic in which exothermic reactions are also identified in the case for polyurethane (Mufazzal Saeed, Moosa Hasany, & Ahmed, 1999), activated carbon (Mohan, Gupta, Srivastava, & Chander, 2000) and demineralized lignite coal (Eligwe, Okolue, Nwambu, & Nwoko, 1999). The entropy change of reaction (ΔS°) is evaluated to be 0.1170 kJ/mol K. Since entropy is defined as the degree of chaos in a system, the positive ΔS° reveals that the increasing randomness at the solid/liquid interface occurred during the reaction. This also suggests that some structural changes in both of the mercury and sorbent could be taken place during the sorption process (Ho & Wang, 2008; Manohar, Anoop Krishnan, & Anirudhan, 2002).

6.6. Powder X-Ray Diffraction (PXRD) Analysis

6.6.1. Characteristic of Pure Phase Covellite

The PXRD pattern of pure phase Covellite used is depicted in **Figure 6.32**. All the characteristic peaks in this pattern correspond well to the hexagonal phase copper sulfide (Covellite, CuS) in the space group of *P63/mmc* which can be well indexed to PDF 00-006-0464 with a = b = 3.79Å and c = 16.34Å. The diffractogram exhibits no PXRD peaks arising from oxidized product of $CuSO_4.5H_2O$ as well as impurities of CuO, S, and other Cu_xS. This denotes high purity of the CuS powder synthesized via the facile hydrothermal

batch route developed during the initial stage of these studies. Furthermore, the relative peaks intensity of the sample match well to the relative peaks intensity of the reference. This indicates that no significant preferential orientation growth of CuS crystallite present in the pure phase Covellite powder employed.

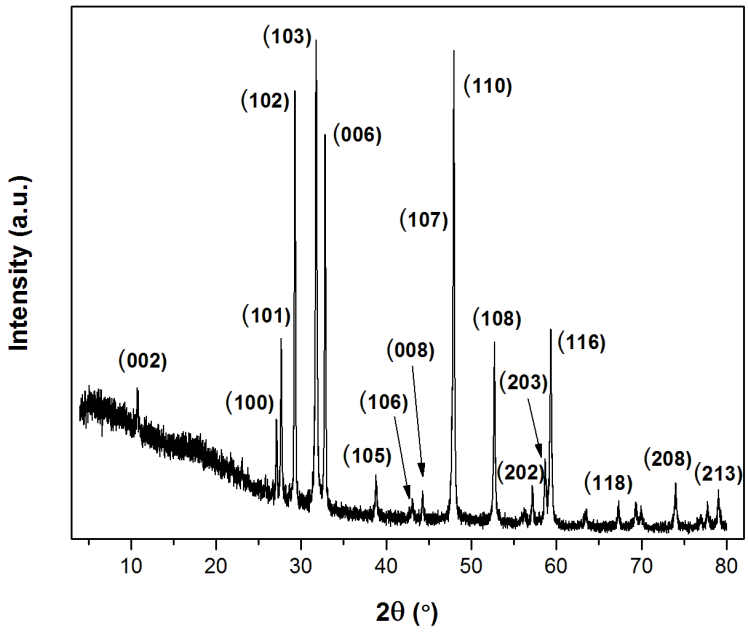

Figure 6.32. PXRD pattern of unreacted pure phase Covellite.

6.6.2. Formation of Mercury Sulfide

The PXRD patterns of Hg(II) reacted Covellite samples using different initial Hg(II) concentration and temperature of 25°C, 35°C and 45°C are illustrated in **Figure 6.33 – 6.38** respectively. **Figure 6.39** depicts the matching result on one of the PXRD pattern using powder diffraction file (PDF) database. It is noticed that Covellite (CuS) phase is attested in the powder upon the end of reaction. Nonetheless, additional diffraction peaks are also detected at $2\theta \approx 26.40°$ and 43.70° for most of the PXRD patterns. These diffraction peaks are found to agree well with the cubic phase mercury sulfide (Metacinnabar, β-HgS) in the space group of *F-43m* with PDF 01-089-0432 and a = b = c = 5.85Å when compared to hexagonal phase mercury sulfide (α-HgS, space group of hP6 and P3221).

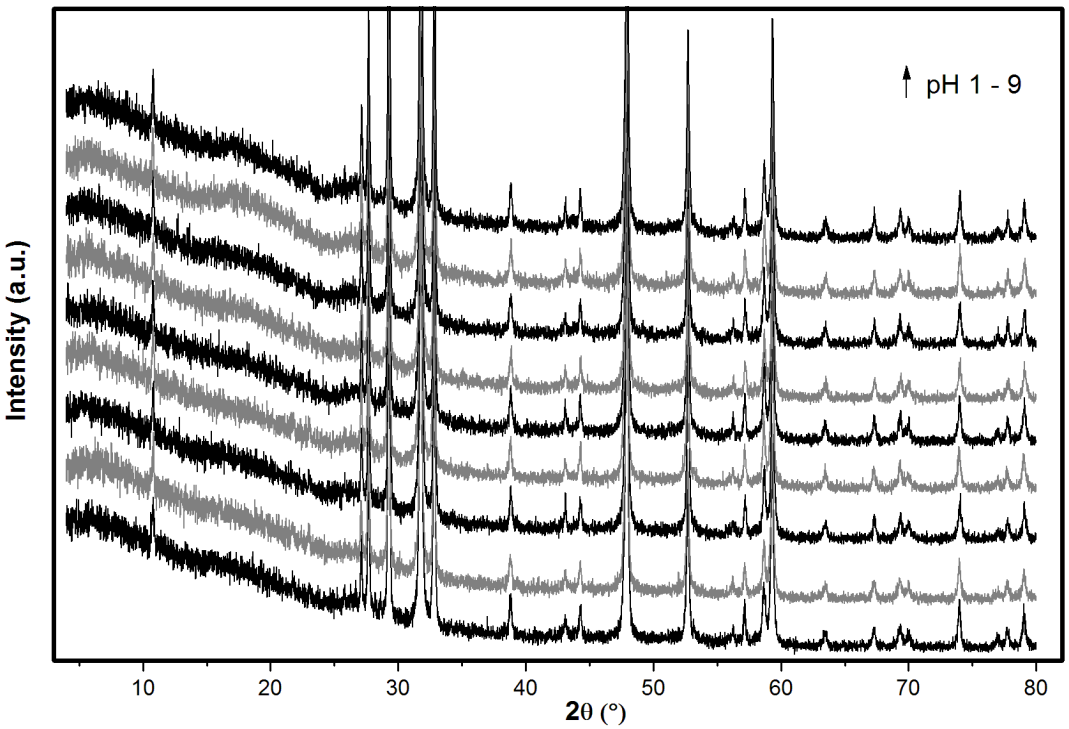

Figure 6.33. PXRD pattern of reacted pure phase Covellite under reaction condition of 50 ppm Hg(II), pH 1 – 9 and temperature of 25°C.
↑ pH 1 – 9 denotes pH value increases in ascending order from bottom to top.

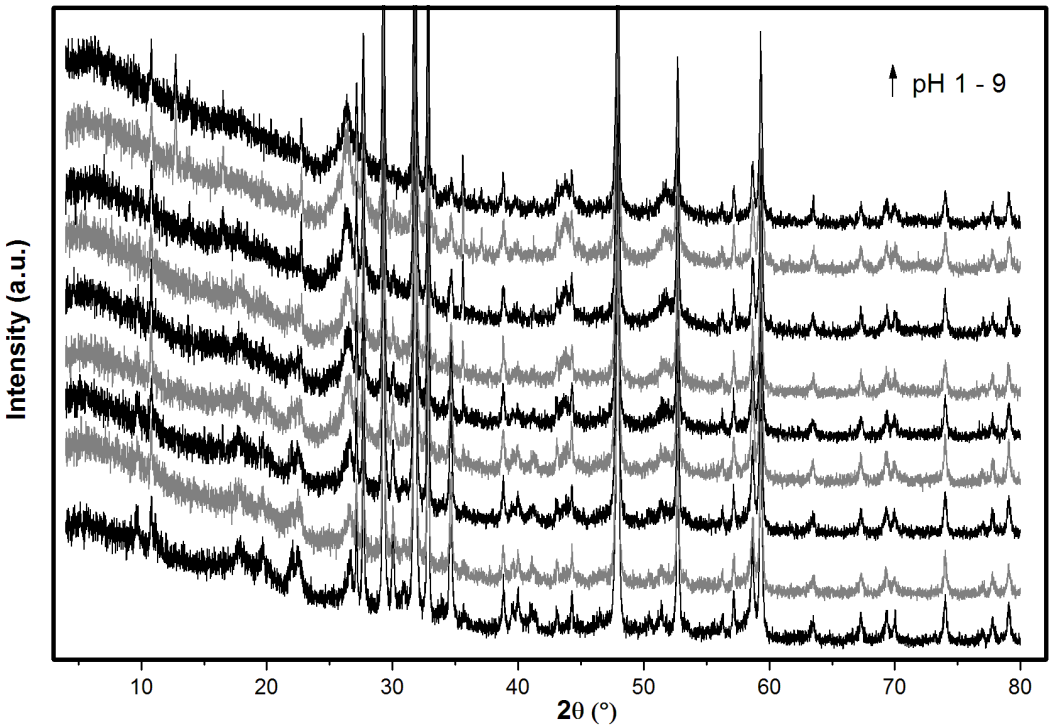

Figure 6.34. PXRD pattern of reacted pure phase Covellite under reaction condition of 150 ppm Hg(II), pH 1 – 9 and temperature of 25°C.
↑ pH 1 – 9 denotes pH value increases in ascending order from bottom to top.

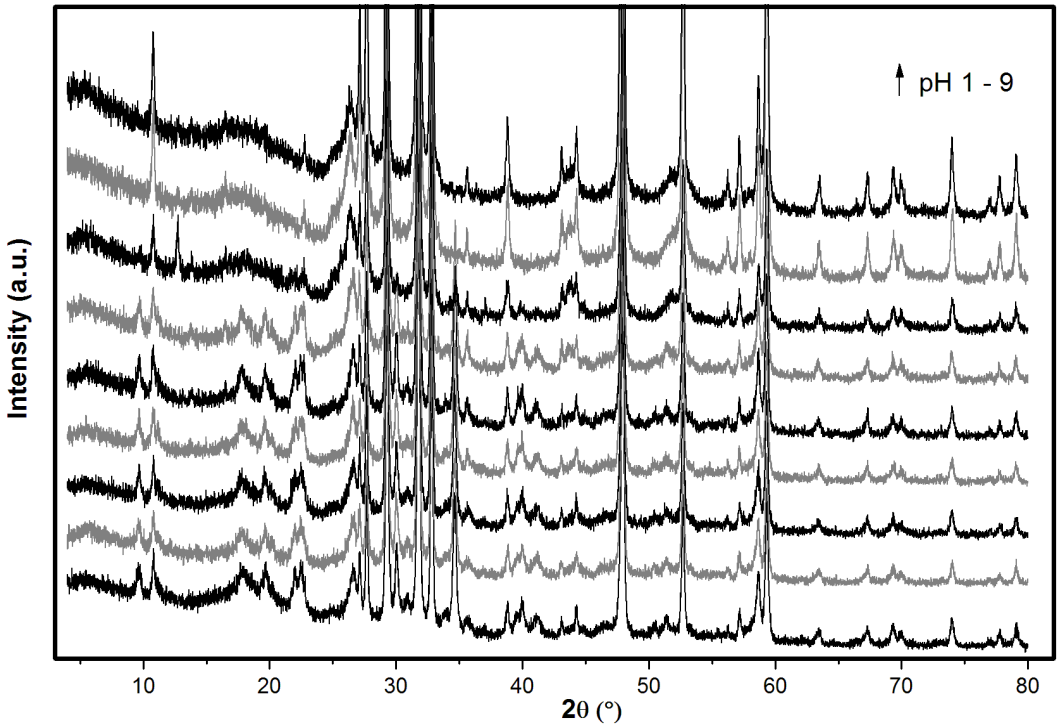

Figure 6.35. PXRD pattern of reacted pure phase Covellite under reaction condition of 250 ppm Hg(II), pH 1 – 9 and temperature of 25°C.
↑ pH 1 – 9 denotes pH value increases in ascending order from bottom to top.

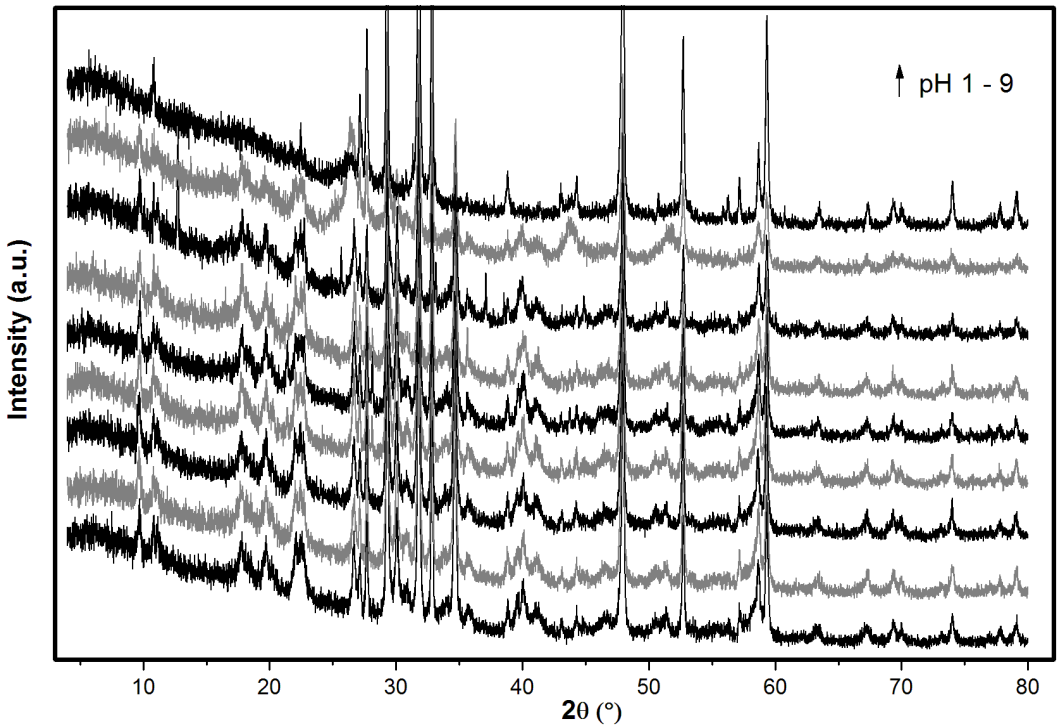

Figure 6.36. PXRD pattern of reacted pure phase Covellite under reaction condition of 600 ppm Hg(II), pH 1 – 9 and temperature of 25°C.
↑ pH 1 – 9 denotes pH value increases in ascending order from bottom to top.

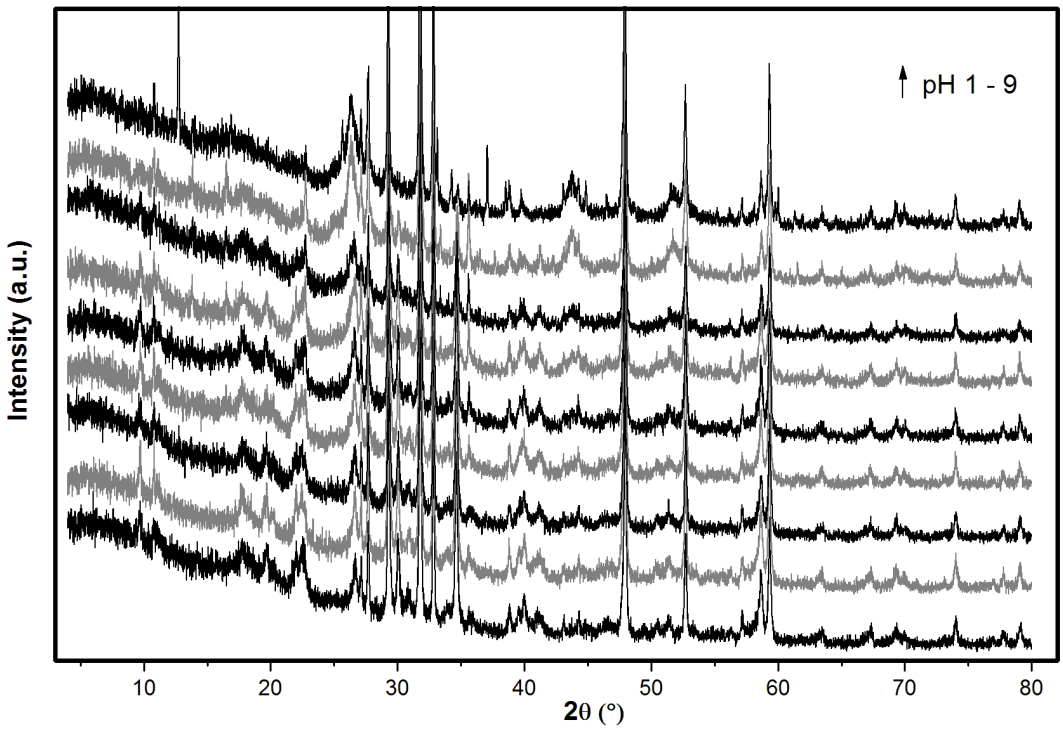

Figure 6.37. PXRD pattern of reacted pure phase Covellite under reaction condition of 250 ppm Hg(II), pH 1 – 9 and temperature of 35°C.
↑ pH 1 – 9 denotes pH value increases in ascending order from bottom to top.

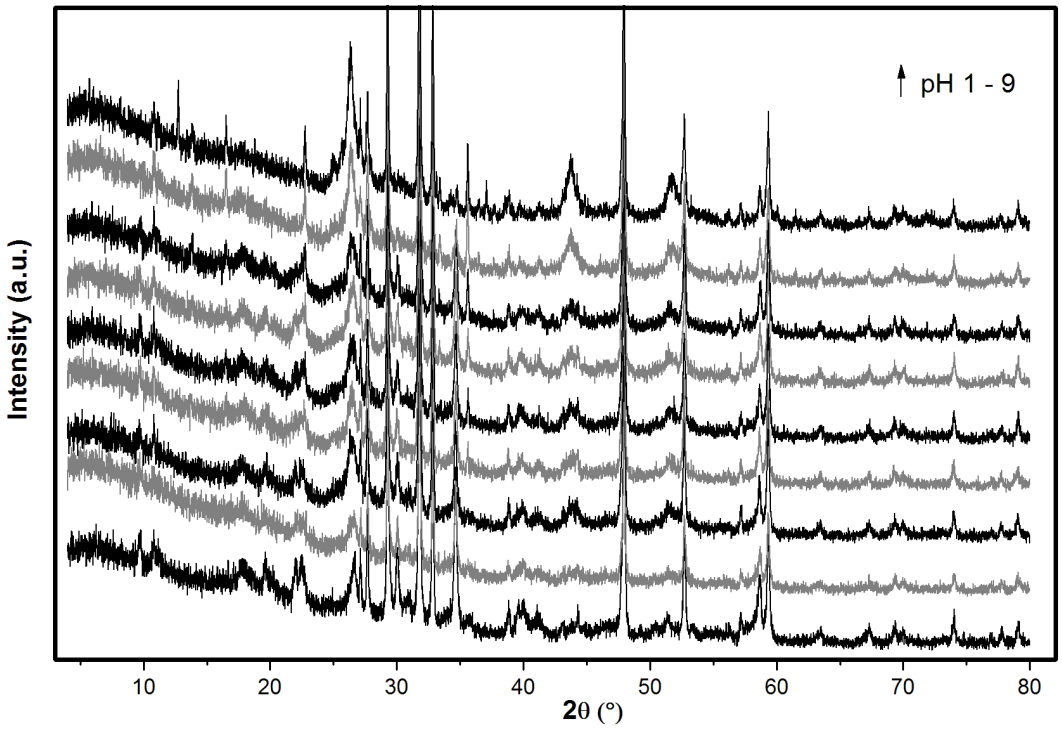

Figure 6.38. PXRD pattern of reacted pure phase Covellite under reaction condition of 250 ppm Hg(II), pH 1 – 9 and temperature of 45°C.
↑ pH 1 – 9 denotes pH value increases in ascending order from bottom to top.

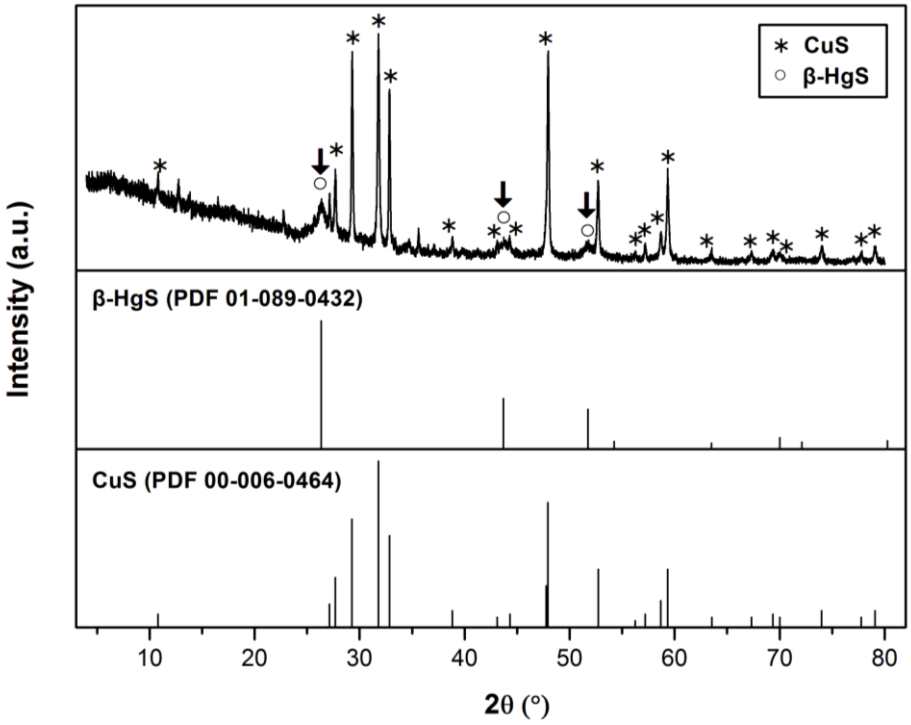

Figure 6.39. β-HgS identification on PXRD pattern of reacted pure phase Covellite under reaction condition of 150 ppm Hg(II), pH 9 and temperature of 25°C.
↓ denotes the diffraction peaks of β-HgS.

The identification on formation of β-HgS is also extended to other diffractograms at different reaction conditions and its results are shown in **Table 6.21** and **Table 6.22**. From the analysis, it is detected that the mercury uptake via β-HgS formation is feasible at almost all reaction conditions used except for the reactions conducted in extreme Hg(II) concentration i.e. using 50 ppm and 600 ppm Hg(II) solutions. In 50 ppm Hg(II) solutions, the PXRD pattern at solution pH 1 – 9 resembled the initial PXRD pattern of Covellite in which no significant additional diffraction peaks are observed. In 600 ppm Hg(II) solutions, the absence of β-HgS is found at solution pH 1 – 3. Nonetheless, by looking at the PXRD patterns of samples conducted using 600 ppm Hg(II) solutions at solution pH 1 – 3 (**Figure 6.38**, the lowest most three PXRD patterns), we identified that the missing of β-HgS phase is accompanied by the significant appearance of other diffraction peaks ($2\theta \approx 18.01°$, 19.88°, 22.50° and 34.70°) in the diffractograms.

Table 6.21. Identification of β-HgS on PXRD patterns at different initial Hg(II) concentration and solution pH under temperature of 25°C.

[Hg(II)]/ppm	pH								
	1	2	3	4	5	6	7	8	9
600	×†	×	×	✓	✓	✓	✓	✓	✓
250	✓††	✓	✓	✓	✓	✓	✓	✓	✓
150	✓	✓	✓	✓	✓	✓	✓	✓	✓
50	×	×	×	×	×	×	×	×	×

† × denotes the absence of β-HgS.
†† ✓ denotes the presence of β-HgS.

Table 6.22. Identification of β-HgS on PXRD patterns at different reaction temperature and solution pH using 250 ppm aqueous Hg(II).

Temp/°C	pH								
	1	2	3	4	5	6	7	8	9
45	✓††	✓	✓	✓	✓	✓	✓	✓	✓
35	✓	✓	✓	✓	✓	✓	✓	✓	✓
25	✓	✓	✓	✓	✓	✓	✓	✓	✓

†† ✓ denotes the presence of β-HgS.

6.6.3. Formation of Mercury Sulfide Chloride

Beside the formation of bare HgS, the mercury uptake onto Covellite can also be correlated to the formation of copper and chloride containing mercury sulfide. As a result, the PXRD pattern depicted in **Figure 6.33 – 6.38** are again matched with orthorhombic phase copper mercury sulfide chloride (CuHgSCl), tetragonal phase copper dimercury disulfide chloride ($CuHg_2S_2Cl$) and cubic phase mercury sulfide chloride ($Hg_3S_2Cl_2$). From the analysis, it is identified that the diffraction peaks at $2\theta \approx 18.01°$, 19.88°, 22.50° and 34.70° are similar to the diffraction peaks observed in reacted mixed phase Covellite (**Figure 5.9**). Nontheless, these peaks cannot be matched well with copper containing mercury sulfide i.e. CuHgSCl and $CuHg_2S_2Cl$. These diffraction peaks shows some resemblance to the cubic phase of

mercury sulfide chloride ($Hg_3S_2Cl_2$, space group of *Pm*-3n, PDF 01-087-1667 with a = b = c = 18.28Å) where the matching result is shown in **Figure 6.40**. From the analysis, it can be observed that peaks matching only look superficially good in which some peaks agree well with $Hg_3S_2Cl_2$ reference pattern while matching of some peaks are clearly off. Hence, this indicates that the reference pattern of $Hg_3S_2Cl_2$ is again unsatisfactory in explaining the unknown peaks in mercury reacted Covellite powder. The examination of the unknown phase is further performed using the monoclinic phase mercury sulfide bromide ($Hg_3S_2Br_2$, space group of *C2/m*, PDF 01-087-1050 with a = 17.58Å, b = 8.98Å, c = 10.10Å) where the matching result is depicted in **Figure 6.41**. From the analysis, it is astounded to see that the unknown peaks match considerably well with the reference pattern of $Hg_3S_2Br_2$ although no Br element is present in the powder.

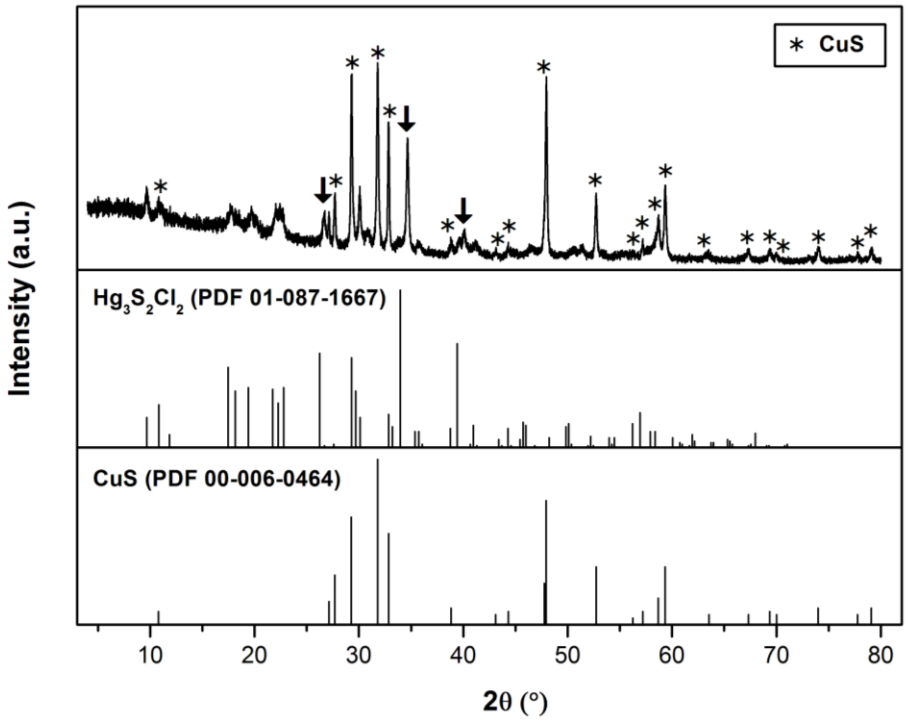

Figure 6.40. Matching of $Hg_3S_2Cl_2$ on PXRD pattern of reacted pure phase Covellite under reaction condition of 600 ppm Hg(II), pH 2 and temperature of 25°C.
↓ denotes the mismatch of diffraction peaks between the sample and cubic phase $Hg_3S_2Cl_2$.

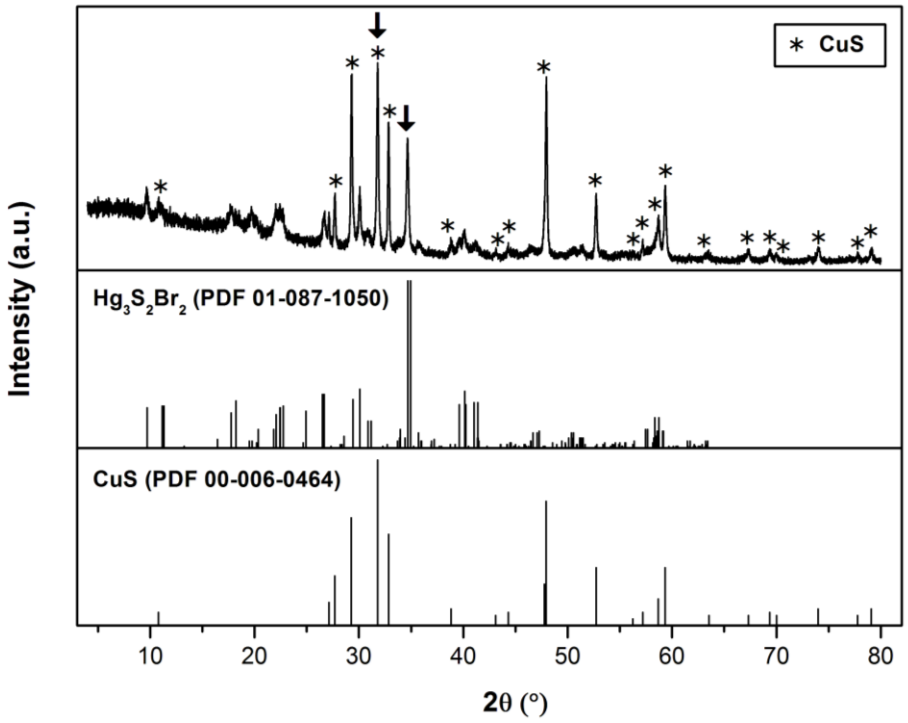

Figure 6.41. Matching of $Hg_3S_2Br_2$ on PXRD pattern of reacted pure phase Covellite under reaction condition of 600 ppm Hg(II), pH 2 and temperature of 25°C.
↓ denotes the peak of CuS and unknown phase used for quantification ratio analysis.

With the intention to confirm the peaks fitness between the unknown and monoclinic phase $Hg_3S_2Br_2$, the PXRD pattern was subjected to Rietveld refinement in which the crystal model of monoclinic phase $Hg_3S_2Br_2$ was used in the evaluation. The corresponding Rietveld refinement result is illustrated in **Figure 6.42** whereas the fitted parameters are documented in **Appendix C**. From the calculated model, the position of the simulated peaks matched perfectly well to the position of the unknown peaks in the diffractogram. The only mismatch found is owing to the slight different in the intensity between the unknown and simulated peaks. This implies a notably good fit of crystal structure between the unknown compound and $Hg_3S_2Br_2$. Therefore, the unknown compound is determined to be monoclinic phase $Hg_3S_2Cl_2$ in which it is labeled as m-$Hg_3S_2Cl_2$ in the entire discussion.

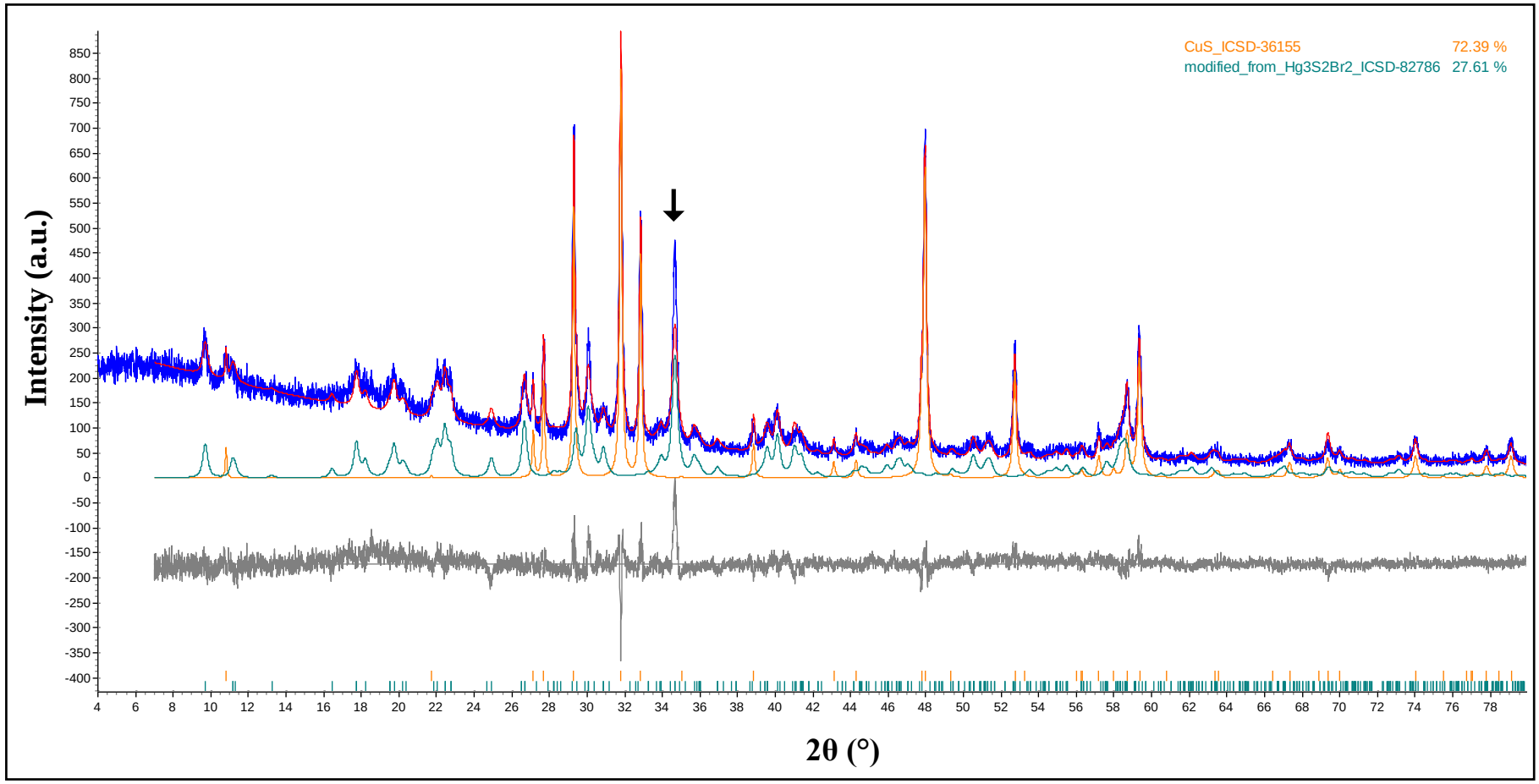

Figure 6.42. Rietveld refinement analysis on PXRD pattern of reacted pure phase Covellite under reaction condition of 600 ppm Hg(II), pH 2 and temperature of 25°C using the monoclinic phase $Hg_3S_2Br_2$.
↓ denotes the mismatch of diffraction peaks intensity between the sample and monoclinic phase $Hg_3S_2Br_2$.

The compositional analysis on the formation of m-$Hg_3S_2Cl_2$ phase during the mercury uptake onto CuS has been carried out using the quantification ratio between the peak area of m-$Hg_3S_2Cl_2$ at $2\theta \approx 34.70°$ relative to peak area of CuS at $2\theta \approx 31.80°$ (The peaks are indicated by ↓ in **Figure 6.41**). The peak area of the phases and its evaluation which determined from diffractograms of **Figure 6.33 – 6.38** are shown in **Appendix D**.

The peak area ratio calculated at different solution pH and Hg(II) concentrations are depicted in **Figure 6.43 (a) – (d)** correspondingly. In 50 ppm Hg(II) solutions, no m-$Hg_3S_2Cl_2$ phase is detected from the PXRD patterns (**Figure 6.33**) regardless of solution pH applied. In 150 ppm Hg(II) solutions, the detection of m-$Hg_3S_2Cl_2$ phase is found but it decreases progressively as solution pH increases. In 250 ppm Hg(II) solutions, m-$Hg_3S_2Cl_2$ phase is found at pH 1 – 6 in which it is depicted by a constant plateau line in **Figure 6.43 (c)**. However, the formation of m-$Hg_3S_2Cl_2$ phase has declined at pH 7 until no detection at pH 8 and 9. In 600 ppm Hg(II) solutions, the peak area ratio analysis reveals that the formation of m-$Hg_3S_2Cl_2$ phase can be increased gradually at pH 1 – 7. Even so, the m-$Hg_3S_2Cl_2$ phase has again decreases at pH 8 and until no detection at pH 9.

The peak area ratio calculated at different solution pH and reaction temperature using 250 ppm Hg(II) solutions are illustrated in **Figure 6.44 (a) – (c)** respectively. At 25°C, a consistent detection of m-$Hg_3S_2Cl_2$ phase is found at pH 1 – 6 in which it is accompanied by a constant plateau of peak area ratio. Nevertheless, the constant plateau on the formation of m-$Hg_3S_2Cl_2$ phase has declined consistently at pH 7 until no detection at pH 8 and 9. At 35°C, a steady decrease on the peak area ratio is found at pH 1 – 7 which suggests a gradual decrease on the formation of m-$Hg_3S_2Cl_2$ phase in this pH range. This is followed by a sharp drop on formation of m-$Hg_3S_2Cl_2$ phase at pH 8 and 9. At 45°C, a huge decrease of peak area ratio is observed at pH 2 – 3 and 7 – 9. This observation again indicates the decreasing trend on formation of m-$Hg_3S_2Cl_2$ with increasing solution pH.

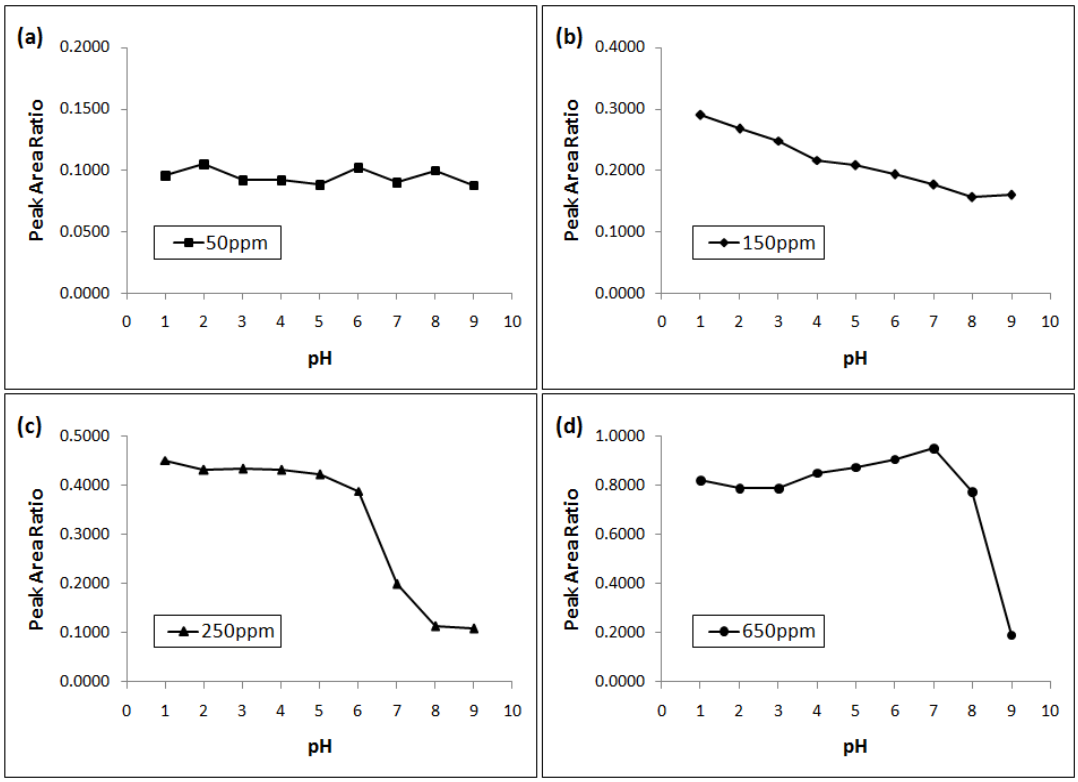

Figure 6.43. Peak area ratio of m-$Hg_3S_2Cl_2$:CuS calculated for the sorption of (a) 50 ppm (b) 150 ppm (c) 250 ppm and (d) 600 ppm Hg(II) onto pure phase Covellite.

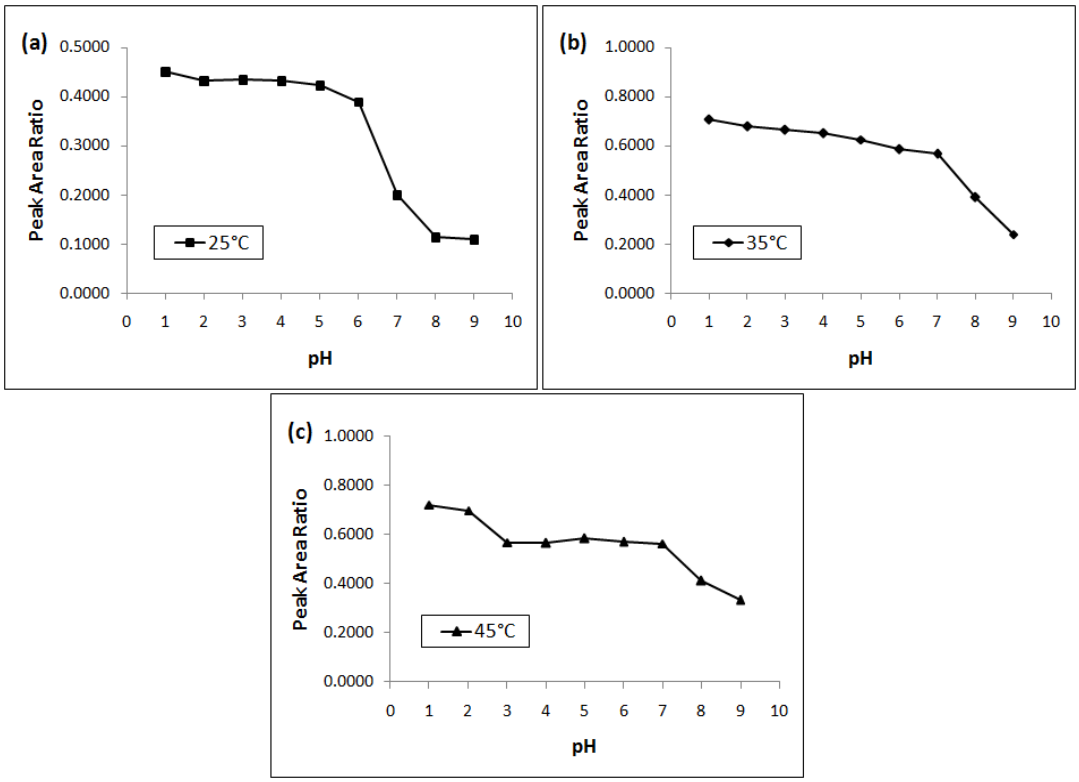

Figure 6.44. Peak area ratio of m-$Hg_3S_2Cl_2$:CuS calculated for sorption of 250 ppm Hg(II) onto pure phase Covellite at (a) 25°C (b) 35°C and (c) 45°C.

6.6.4. Precipitation of Mercury Oxide Compound

For reaction conducted using 600 ppm Hg(II) solutions, detail analysis reveals that a moderately weak diffraction is also observed at $2\theta \approx 22.40°$ in 600 ppm Hg(II) solution, pH 9 diffractogram (**Figure 6.45**). From the search and match analysis, this diffraction peak can be considered as a main representative signal of mercury oxide chloride, $HgCl_2.3HgO$ with PDF 00-001-0456.

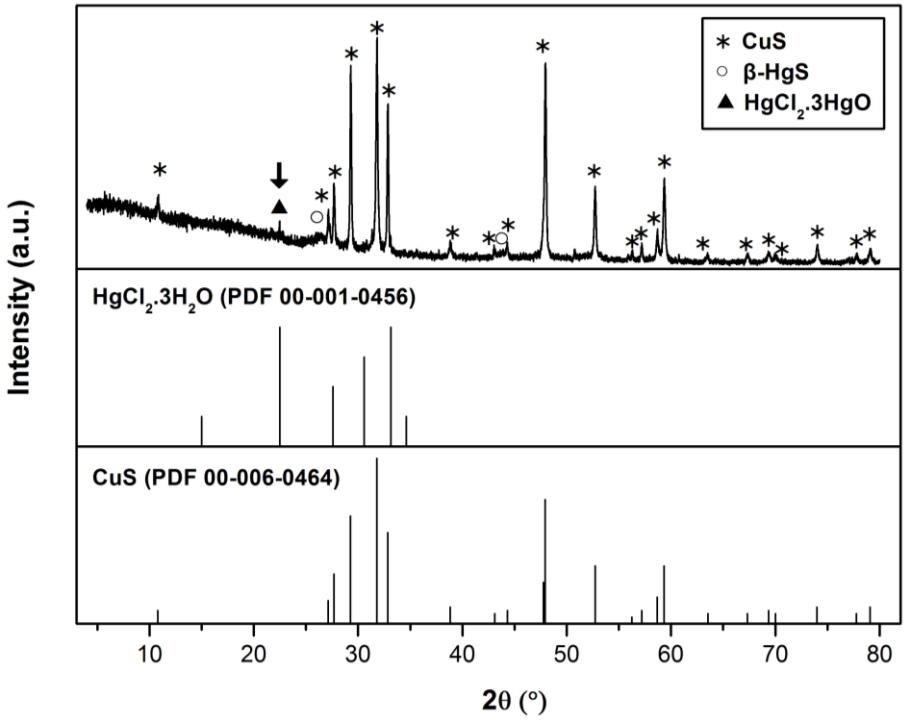

Figure 6.45. Matching of $HgCl_2.3HgO$ on PXRD pattern of reacted Covellite under reaction condition of 600 ppm Hg(II), pH 9 and temperature of 25°C.
↓ denotes the main diffraction peaks of $HgCl_2.3HgO$.

6.6.5. Formation of Copper Sulfate Hydroxide and its Hydrate

The PXRD patterns of reacted samples (**Figure 6.33 – 6.38**) are again analyzed to identify the potential copper compounds formed during the sorption of Hg(II) onto Covellite. **Figure 6.46** and **Figure 6.47** illustrate the search and match result using the PXRD pattern of reacted Covellite under reaction condition of 250 ppm Hg(II), pH 9 and temperature of 45°C. From **Figure 6.46**, It is observed that the diffraction peak at 2θ ≈ 13.88°, 16.55°, 22.80° and 35.61° matched well with the monoclinic phase copper sulphate hydroxide, $Cu_4(SO_4)(OH)_6$ (Bronchantite-M) in the space group of *p21/a* with PDF 00-043-1458 and a = 13.11Å, b = 9.85Å, c = 6.02Å. Moreover, from **Figure 6.47**, the diffraction peaks at 2θ ≈ 12.66°, 34.48° and 36.89° also found to agree well with the monoclinic phase copper sulphate hydroxide hydrate, $Cu_4(SO_4)(OH)_6(H_2O)$ (Posnjakite) in the space group of *Pa* with PDF 01-083-1410 and a = 10.58Å, b = 6.35Å, c = 7.86Å.

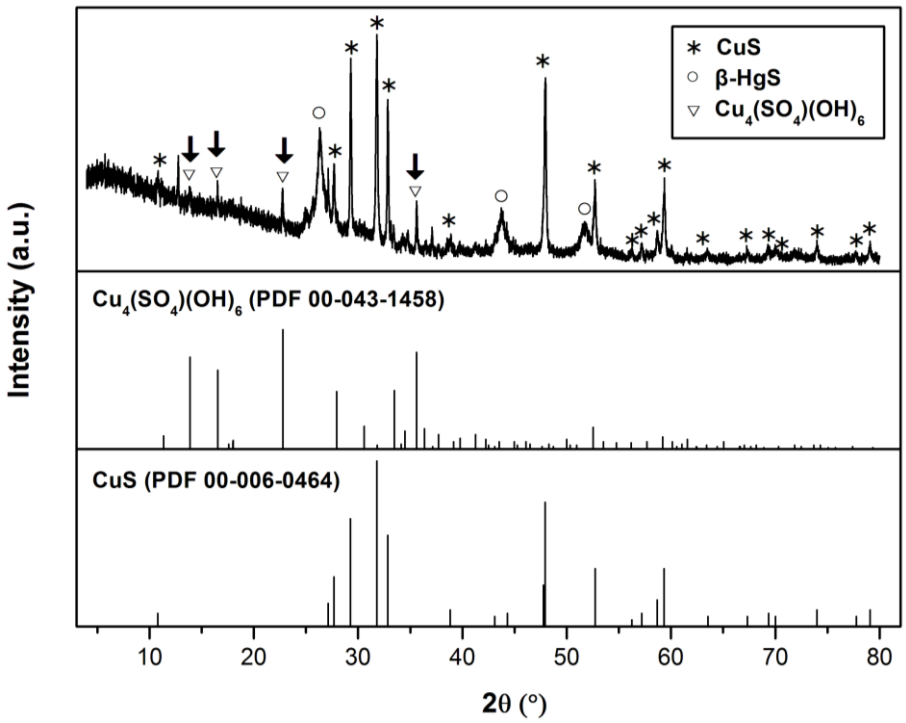

Figure 6.46. Matching of $Cu_4(SO_4)(OH)_6$ on PXRD pattern of reacted Covellite under reaction condition of 250 ppm Hg(II), pH 9 and temperature of 45°C.
↓ denotes the main diffraction peaks of $Cu_4(SO_4)(OH)_6$.

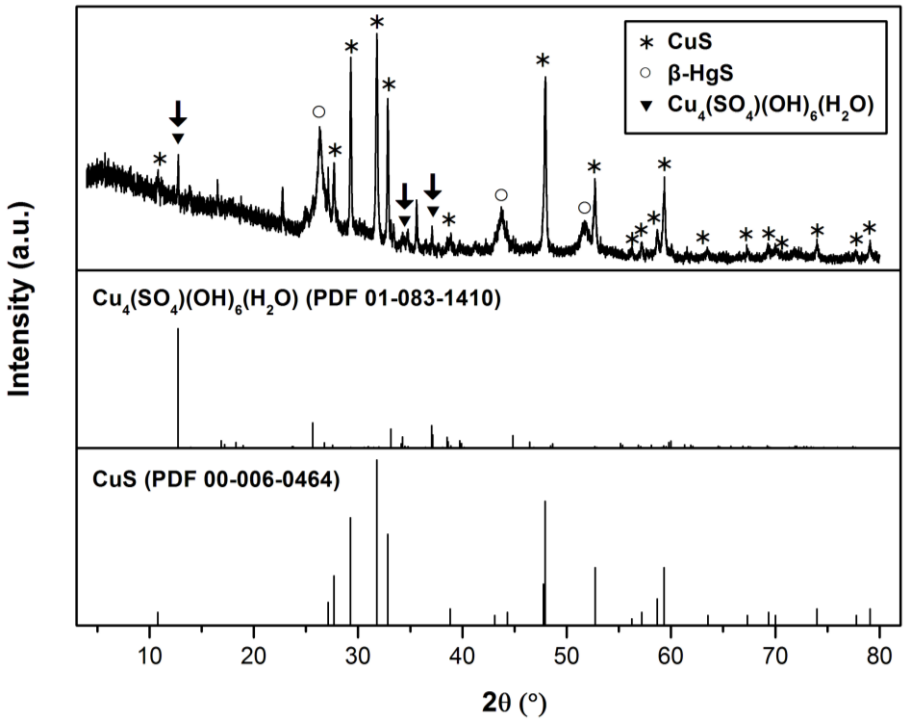

Figure 6.47. Matching of $Cu_4(SO_4)(OH)_6(H_2O)$ on PXRD pattern of reacted Covellite under reaction condition of 250 ppm Hg(II), pH 9 and temperature of 45°C.
↓ denotes the main diffraction peaks of $Cu_4(SO_4)(OH)_6$.

The identification results of $Cu_4(SO_4)(OH)_6$ and $Cu_4(SO_4)(OH)_6(H_2O)$ on all of the PXRD patterns for reactions performed at 25°C are tabulated in **Table 6.23** and **Table 6.24**. From the PXRD patterns, it is noticed that $Cu_4(SO_4)(OH)_6$ is easier to detect than $Cu_4(SO_4)(OH)_6(H_2O)$. Therefore, only the formation of $Cu_4(SO_4)(OH)_6$ will be described in this section. In 50 ppm Hg(II) solutions, the PXRD patterns resembled the initial PXRD pattern of Covellite in which no additional diffraction peaks are observed. In 150 ppm Hg(II) solutions, the formation of $Cu_4(SO_4)(OH)_6$ is only identified at pH 7 – 9. When the Hg(II) concentration is increased to 250 ppm, the formation has been extended to pH 4 – 9. In 600 ppm Hg(II) solutions, the formation of $Cu_4(SO_4)(OH)_6$ is observed at pH 6 – 8. From the appealing observations, the formation of $Cu_4(SO_4)(OH)_6$ has frequently occurred at reactions conducted in near neutral to alkaline solution pH i.e. 6 – 9.

Table 6.23. Identification of $Cu_4(SO_4)(OH)_6$ on PXRD patterns at different initial Hg(II) concentration and solution pH under temperature of 25°C.

[Hg(II)]/ppm	pH								
	1	2	3	4	5	6	7	8	9
600	×†	×	×	×	×	✓††	✓	✓	×
250	×	×	×	✓	✓	✓	✓	✓	✓
150	×	×	×	×	×	×	✓	✓	✓
50	×	×	×	×	×	×	×	×	×

† × denotes the absence of $Cu_4(SO_4)(OH)_6$.
†† ✓ denotes the presence of $Cu_4(SO_4)(OH)_6$.

Table 6.24. Identification of $Cu_4(SO_4)(OH)_6(H_2O)$ on PXRD patterns at different initial Hg(II) concentration and solution pH under temperature of 25°C.

[Hg(II)]/ppm	pH								
	1	2	3	4	5	6	7	8	9
600	×†	×	×	×	×	×	✓††	×	×
250	×	×	×	×	×	×	✓	✓	✓
150	×	×	×	×	×	×	×	✓	✓
50	×	×	×	×	×	×	×	×	×

† × denotes the absence of $Cu_4(SO_4)(OH)_6(H_2O)$.
†† ✓ denotes the presence of $Cu_4(SO_4)(OH)_6(H_2O)$.

The identification results of $Cu_4(SO_4)(OH)_6$ and $Cu_4(SO_4)(OH)_6(H_2O)$ on all of the PXRD for reactions performed at different reaction temperature using 250 ppm Hg(II) are tabulated in **Table 6.25** and **Table 6.26**. At 25°C, it has been described earlier that the formation of $Cu_4(SO_4)(OH)_6$ has happened at pH 4 – 9. When reaction temperature is elevated to 35°C, the formation of $Cu_4(SO_4)(OH)_6$ remained at pH 6 – 9 while it disappear at pH 4 and 5. At 45°C, the formation of $Cu_4(SO_4)(OH)_6$ is once again observed at pH 4 – 9. From the analysis, the formation tendency of $Cu_4(SO_4)(OH)_6$ at solution pH 4 and 5 is revealed when reaction temperature is increased. This indicates that the formation of $Cu_4(SO_4)(OH)_6$ is feasible when the reactions are performed at acidic pH.

Table 6.25. Identification of $Cu_4(SO_4)(OH)_6$ on PXRD patterns at different reaction temperature and solution pH using 250 ppm Hg(II).

Temp/°C	pH								
	1	2	3	4	5	6	7	8	9
45	×†	×	×	✓††	✓	✓	✓	✓	✓
35	×	×	×	×	×	✓	✓	✓	✓
25	×	×	×	✓	✓	✓	✓	✓	✓

† × denotes the absence of $Cu_4(SO_4)(OH)_6$.
†† ✓ denotes the presence of $Cu_4(SO_4)(OH)_6$.

Table 6.26. Identification of $Cu_4(SO_4)(OH)_6(H_2O)$ on PXRD patterns at different reaction temperature and solution pH using 250 ppm Hg(II).

Temp/°C	pH								
	1	2	3	4	5	6	7	8	9
45	×†	×	×	×	×	×	×	×	✓††
35	×	×	×	×	×	×	×	×	✓
25	×	×	×	×	×	×	✓	✓	✓

† × denotes the absence of $Cu_4(SO_4)(OH)_6(H_2O)$.
†† ✓ denotes the presence of $Cu_4(SO_4)(OH)_6(H_2O)$.

To further investigate the formation of $Cu_4(SO_4)(OH)_6$ and $Cu_4(SO_4)(OH)_6(H_2O)$, the PXRD pattern for Covellite used in controlled studies (**Section 6.2.1**) has been collected and analyzed. **Figure 6.48 – 6.50** illustrates the PXRD patterns for controlled studies performed at 25°C, 35°C and 45°C respectively. Regardless of reaction temperature applied, it is observed that the PXRD patterns are made up of the diffraction peaks of CuS in which no noticeable diffraction peaks resulted from other crystallite phases is identified. This information is crucial because this proves that the formation of $Cu_4(SO_4)(OH)_6$ and $Cu_4(SO_4)(OH)_6(H_2O)$ is impossible without the presence of Hg(II). Therefore, the formation of $Cu_4(SO_4)(OH)_6$ and $Cu_4(SO_4)(OH)_6(H_2O)$ is highly related and dependent on the sorption of Hg(II) onto Covellite.

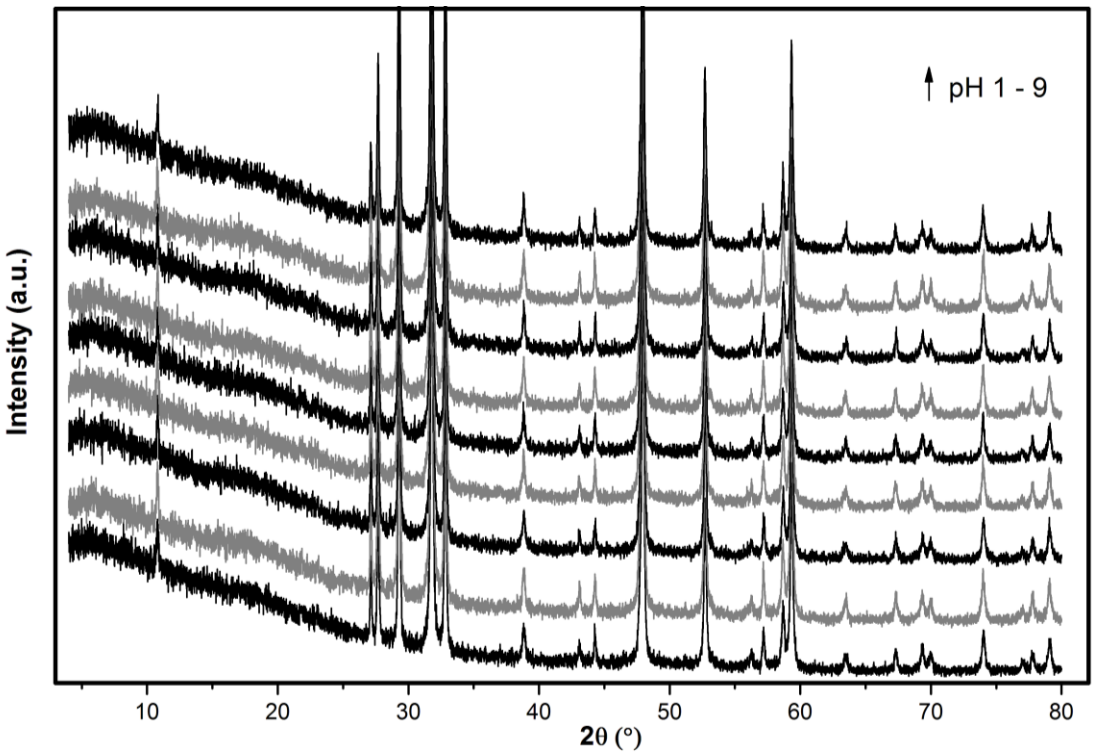

Figure 6.48. PXRD pattern of reacted pure phase Covellite without the presence Hg(II), pH 1 – 9 and temperature of 25°C.

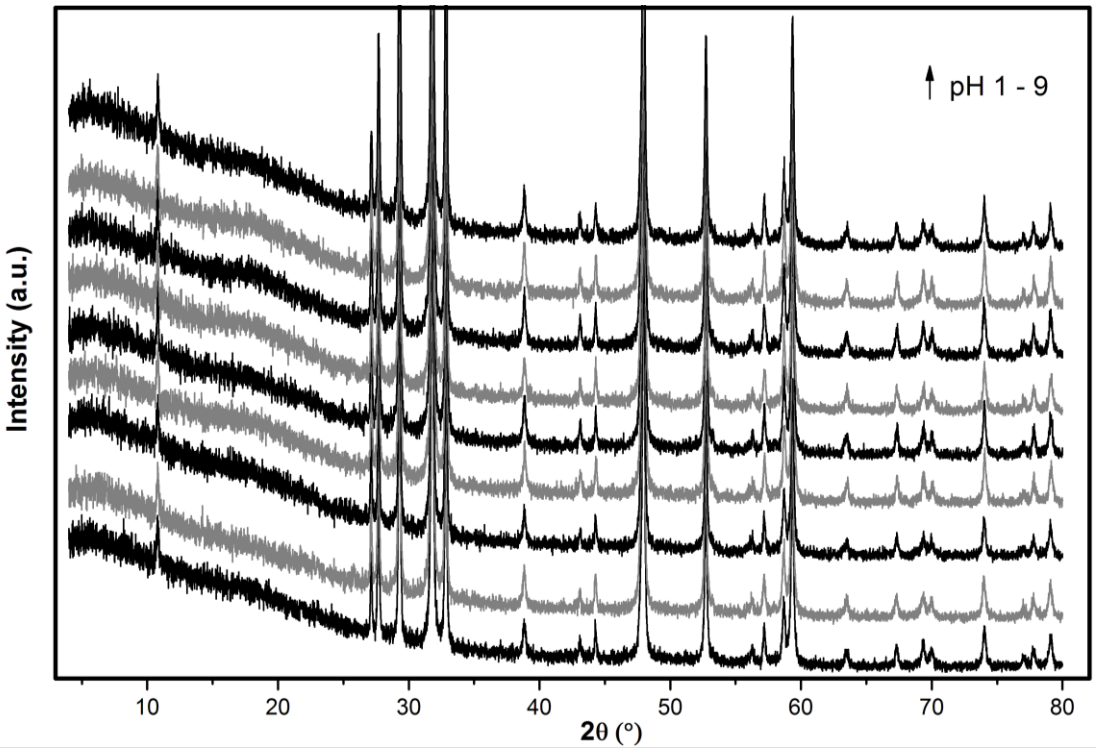

Figure 6.49. PXRD pattern of reacted pure phase Covellite without the presence Hg(II), pH 1 – 9 and temperature of 35°C.

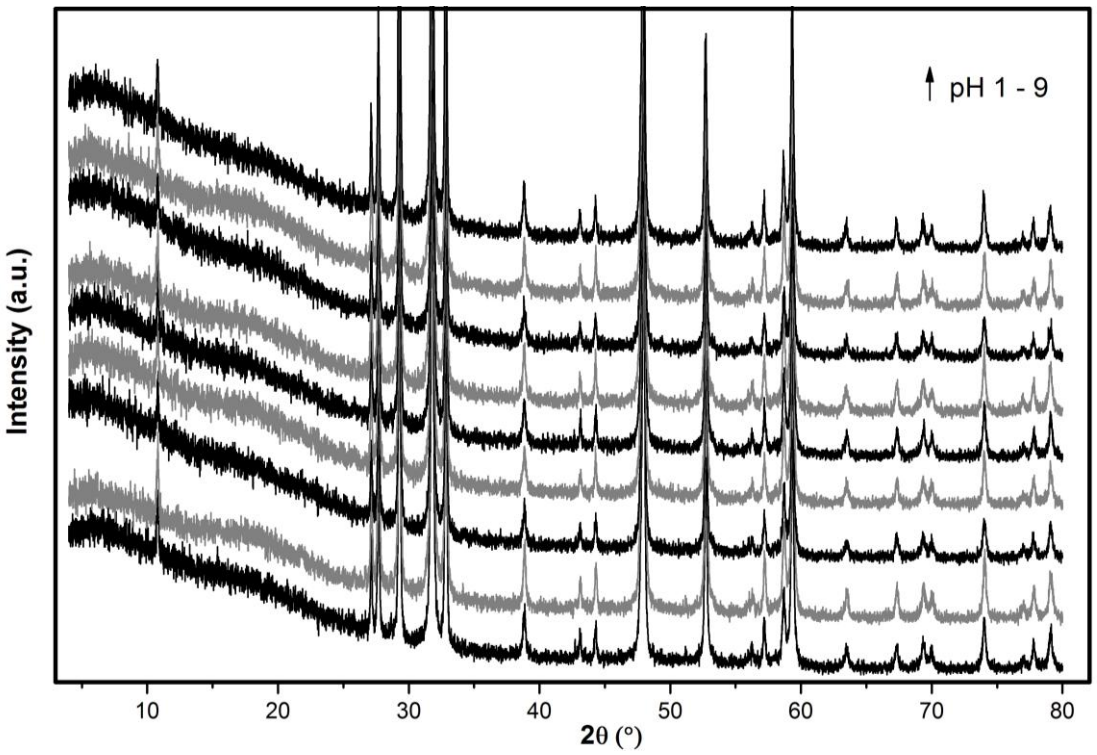

Figure 6.50. PXRD pattern of reacted pure phase Covellite without the presence Hg(II), pH 1 – 9 and temperature of 45°C.

6.6.6. Discussion

From PXRD analysis, several type of mercury compounds have been detected upon sorption of Hg(II) onto CuS. The first compound is related to cubic phase mercuric sulfide (β-HgS) in which its formation is also observed in the case for sorption of Hg(II) onto FeS (Jeong, et al., 2007; J. Liu, et al., 2008). In comparison to other studies conducted for the sorption of Hg(II) onto copper sulfide (Martellaro, et al., 2001; Moore, et al., 2000; Harold O. Phillips & Kraus, 1965; C.-C. Wu & Yang, 1976), the finding reported herein has for the first time provided strong evidence for the Hg(II) uptake follows the formation of cubic phase β-HgS rather than hexagonal phase α-HgS although the latter adopt a similar lattice system as hexagonal phase CuS. The second compound identified is associated to mercuric sulfide chloride or specifically m-$Hg_3S_2Cl_2$. A great attention is given to this compound because its PXRD pattern matches well with the PXRD pattern of m-$Hg_3S_2Br_2$ in

preference to the PXRD pattern of cubic phase $Hg_3S_2Cl_2$. In fact, the building of $Hg_3S_2Cl_2$ with monoclinic crystal structure seems reasonable as Cl^- and Br^- are very similar in size with ionic radii of Cl^- = 181pm and Br^- = 196pm (Shannon, 1976). Cl^- and Br^- should be interchangeable towards the formation of both cubic and monoclinic type of $Hg_3S_2X_2$ (X = Cl and Br). Indeed, presence of Cl in the crystal lattice of $Hg_3S_2Br_2$ is also identified by Pervukhina et. al. in crystal phase of monoclinic $Hg_3S_2Cl_{1.5}Br_{0.5}$ and cubic $Hg_3S_2Cl_{1.54}Br_{0.46}$ (Pervukhina, Vasil'ev, Magarill, Borisov, & Naumov, 2006). Therefore, this shows a high possibility for the formation of m-$Hg_3S_2Cl_2$ rather than the conventional cubic phase $Hg_3S_2Cl_2$ which reported in the powder diffraction file (PDF) database. In addition, mercury oxide chloride, $HgCl_2$.3HgO was also detected. This compound is composed of two salt components i.e. $HgCl_2$ and HgO in which its presence is also found during the sorption of Hg(II) onto Mackinawite, FeS at alkaline pH (Jeong, et al., 2007).

The identification of these mercury compounds has provided important insight in explaining the mercury uptake trend that observed earlier. In **Section 6.1.2**, ≈100% Hg(II) removal has been observed in 50 ppm Hg(II) solutions regardless of solution pH applied. Nonetheless, the PXRD patterns at solution pH 1 – 9 resembled the initial PXRD pattern of Covellite in which no significant additional diffraction peaks are observed. Thus, it suggested that the formation of mercury complexes is still minimal and it is beyond the L.O.D of PXRD technique. In 150 ppm Hg(II) solutions, ≈100% Hg(II) removal was identified at pH 1 – 8 and it is followed by a small decrease of Hg(II) removal (≈96%) at pH 9. The PXRD analysis shows that the Hg(II) uptake trends are associated with the constant appearance of β-HgS and a gradual decrease of m-$Hg_3S_2Cl_2$ with increasing solution pH. When the Hg(II) concentration is elevated to 250 ppm, ≈100% Hg(II) uptake is observed at pH 1 – 6 while the drop of Hg(II) uptake (≈58%) has started at pH 7 instead of pH 9. From PXRD analysis, the Hg(II) uptake trends are again coupled with the regular

appearance of β-HgS and a progressive decrease of m-$Hg_3S_2Cl_2$ with solution pH elevation. These observations suggest that the progressive decrease of m-$Hg_3S_2Cl_2$ can has a positive relationship with the drop of Hg(II) uptake at increasing solution pH. In view of $Hg_3S_2Cl_2$, this compound is commonly recognized as a double salt and it is formed through the reaction between HgS and $HgCl_2$ (Mellor, 1923; Harold O. Phillips & Kraus, 1965). Since both HgS and $HgCl_2$ are the main constituents in the compound, the formation of HgS and presence of $HgCl_2$ in the solution can affect highly on the formation of $Hg_3S_2Cl_2$ during the reaction. From the mercury speciation diagram calculated earlier (**Figure 6.6**), it was detected that the dominancy of $HgCl_2$ species gradually decreases with increasing pH in the entire system. Thus, it is reasonable to think that the decrease of $HgCl_2$ species at increasing solution pH has limited the formation of m-$Hg_3S_2Cl_2$ at near neutral to alkaline pH. Therefore, together with the formation of β-HgS, the preferential formation of m-$Hg_3S_2Cl_2$ has increased the Hg(II) uptake at pH 1 – 6 while the lacking on formation of m-$Hg_3S_2Cl_2$ has decreased the Hg(II) uptake at pH 7 – 9.

In 600 ppm Hg(II) solutions, mercury uptake of 72.82 – 78.06% were identified at pH 1 – 7 while an increase mercury uptake of 94.88% and 84.56% were detected at pH 8 and 9. For the phase of β-HgS, PXRD analysis revealed that its formation has disappeared at pH 1 – 3 but it become visible again at pH 4 – 9. For the phase of m-$Hg_3S_2Cl_2$, a gradual increase is in fact observed at pH 1 – 7 although it decreases again at pH 8 and until no detection at pH 9. With respect to the trend of mercury uptake and crystallites formation observed, it is estimated that an extensive growth of m-$Hg_3S_2Cl_2$ has occurred at pH 1 – 3. The rapid growth of m-$Hg_3S_2Cl_2$ has outpaced the formation of β-HgS. This has resulted in the fully conversion of β-HgS to m-$Hg_3S_2Cl_2$ and thus the disappearance of β-HgS peaks in the PXRD patterns. On the other hand, the consistent increase of m-$Hg_3S_2Cl_2$ at pH 1 – 7 is unexpectedly opposite to the decrease formation of m-$Hg_3S_2Cl_2$ observed in 150 ppm and

250 ppm Hg(II) solutions. Nevertheless, this observation can be still explained by looking into the insight of solution pH changes studies shown earlier. In **Section 6.3.2**, it is detected that the sorption of OH^- onto CuS can occur at initial solution pH of 5 – 9 in which this has decreased the final suspension pH to 5 – 6. It is important to note that the drop of final solution pH to 5 – 6 has undeniably increased the amount of $HgCl_2$ present in the solution according to the mercury speciation diagram shown in **Figure 6.6 (d)**. Apparently, the increase amount of $HgCl_2$ has enhanced the growth of m-$Hg_3S_2Cl_2$ on CuS in which this has lead to a gradual increase of m-$Hg_3S_2Cl_2$ observed in the PXRD patterns. Besides, the formation of mercury oxide chloride, $HgCl_2$.3HgO was also found at pH 9 in the reactions conducted under 600 ppm Hg(II) concentration. The formation of mercury oxide chloride, $HgCl_2$.3HgO is associated with the appearance of mixed black and red-orange colour powder in the supernatant solutions. Undoubtedly, the precipitation of mercury oxide chloride is largely responsible for the increased mercury uptake observed at alkaline solution pH (**Figure 6.4**).

In **Section 6.1.3**, it has been identified that the low Hg(II) uptake at pH 7 and pH 8 (25°C) has been elevated to ≈100% at 35°C whereas the low Hg(II) uptake at pH 9 (25°C) has been shot up to ≈100% at 45°C. From PXRD analysis, the trends identified are again connected with a steady appearance of β-HgS and a gradual decrease of m-$Hg_3S_2Cl_2$ with increasing solution pH. Although the Hg(II) uptake at neutral to alkaline pH is restricted by the formation of m-$Hg_3S_2Cl_2$, the results above indicate that the Hg(II) uptake at neutral to alkaline pH can be still increased systematically through the reaction temperature elevation. To explain the trends observed, it is considered that the rate of β-HgS formation has accelerated significantly at higher temperature. This reason is supported by the kinetic investigation shown in **Section 6.4.1** where the time needed for complete equilibration at pH 9 is indeed shorten at elevated temperature. Therefore, it is conclusive that in 15 hours

reaction time, the mercury uptake at neutral to alkaline pH is strictly governed by the rate of β-HgS formation. Thus, increasing reaction temperature can notably boost up the loading of Hg(II) onto CuS at neutral to alkaline pH.

Apart from the mercury compounds, copper sulfate hydroxide, $Cu_4(SO_4)(OH)_6$ and its hydrate, $Cu_4(SO_4)(OH)_6(H_2O)$ were also found from PXRD pattern of reacted Covellite. In 50 ppm Hg(II) solutions, the formation of $Cu_4(SO_4)(OH)_6$ is undetectable regardless of solution pH used. This finding shows that the amount of $Cu_4(SO_4)(OH)_6$ was still low and it is again beyond the L.O.D of PXRD technique. In 150 ppm, 600 ppm Hg(II) solutions and reaction temperature 35°C, the formation of $Cu_4(SO_4)(OH)_6$ is only restricted in the pH range of 6 – 9. Nevertheless, the formation of $Cu_4(SO_4)(OH)_6$ has been extended to pH 4 – 9 when either Hg(II) concentration is increased to 250 ppm or reaction temperature is raised to 45°C. This indicated that $Cu_4(SO_4)(OH)_6$ occurred consistently at pH 6 – 9 in which there is also chances for the formation of $Cu_4(SO_4)(OH)_6$ to extend to pH 4 – 5. To further examine the formation of $Cu_4(SO_4)(OH)_6$ and its hydrate, the Covellite powder used in controlled studies (**Section 6.2.1**) were subjected to PXRD analysis. From the results, the formation of $Cu_4(SO_4)(OH)_6$ and its hydrate is undetectable when Hg(II) is absent. This implies that the formation of $Cu_4(SO_4)(OH)_6$ and $Cu_4(SO_4)(OH)_6(H_2O)$ depends strongly on the ion-exchange process of Hg(II) onto CuS in which large amount of Cu(II) needed to be displaced from CuS to facilitate the formation.

In view of the trend of Cu(II) leached found in **Section 6.2.2** and **Section 6.2.3**, the amount of Cu(II) present in the solution has declined gradually with solution pH elevation until ≈0% at pH 9. For the increase tendency of the $Cu_4(SO_4)(OH)_6$ formation with solution pH, its detection is consistent with the trend of Cu(II) leached identified. This signifies that the formation of $Cu_4(SO_4)(OH)_6$ is mainly responsible for the Cu(II) uptake during the sorption of Hg(II) onto Covellite. On the other hand, it is also observed in **Section 6.3.2**

that the final suspension pH has decreased to 5 – 6 when the reactions are conducted at initial solution pH of 5 – 9. For the formation of one mole of $Cu_4(SO_4)(OH)_6$, up to six mole of OH^- will be consumed in the reaction. Apparently, formation of $Cu_4(SO_4)(OH)_6$ is highly accountable for the decrease in final solution pH observed. Thus, this signifies that sorption of OH^- onto Covellite powder can occur during the uptake of Hg(II) onto CuS.

6.7. Field Emission Electron Microscopy and Energy Dispersive X-ray Spectroscopy (FESEM-EDX) Analysis

6.7.1. Characteristic of Pure Phase Covellite

The morphology of the pure phase Covellite (CuS) was examined under FESEM in which the results are depicted in **Figure 6.51**. From **Figure 6.51 (a)**, the powder was identified to consist of an aggregated morphology. Nonetheless, it is clearly shown that the powder exhibits particles with hexagonal plate structure when the images are focused at higher magnification i.e. **Figure 6.51 (b) and (c)**. The hexagonal shape plates are assembled, interlaced and perpendicular to one another, showing a mean edge length of 1 – 1.5 µm and an average thickness of approximately 50 – 100 nm. The chemical composition of the hexagonal plates was further quantified using EDX. The EDX spectra of the hexagonal plate and its respective elemental quantification under the electron gun accelerating voltage of 20kV are shown in **Figure 6.52**. From the analysis, the hexagonal plate is identified to compose only of Cu and S in which no notable contamination from other element can be detected. In addition, the atomic ratio of Cu: S is also calculated to be 1: 1.04. The atomic ratio of Cu: S evaluated (1: 1.04) is consistent with the ideal nominal stoichiometric ratio of covellite (Cu: S = 1: 1) where it is in good agreement with the pure phase Covellite (CuS) found by PXRD analysis.

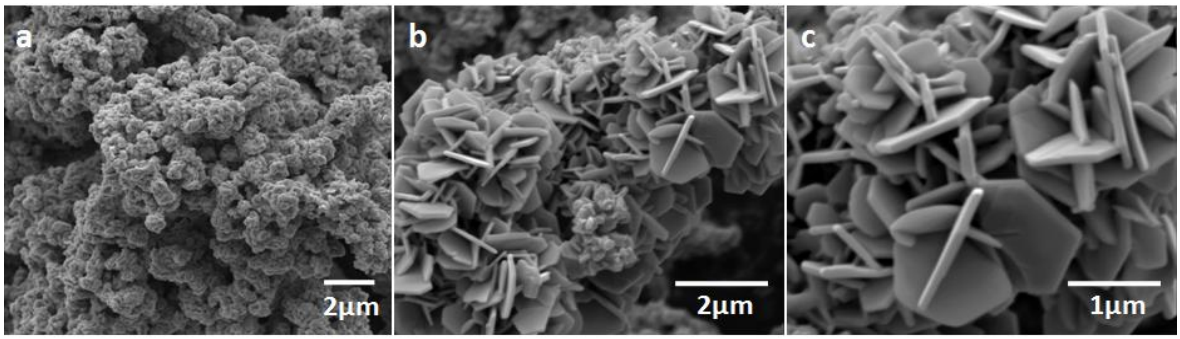

Figure 6.51. FESEM images of unreacted pure phase Covellite with magnifications of (a) 15 000x (b) 30 000x and (c) 60 000x.

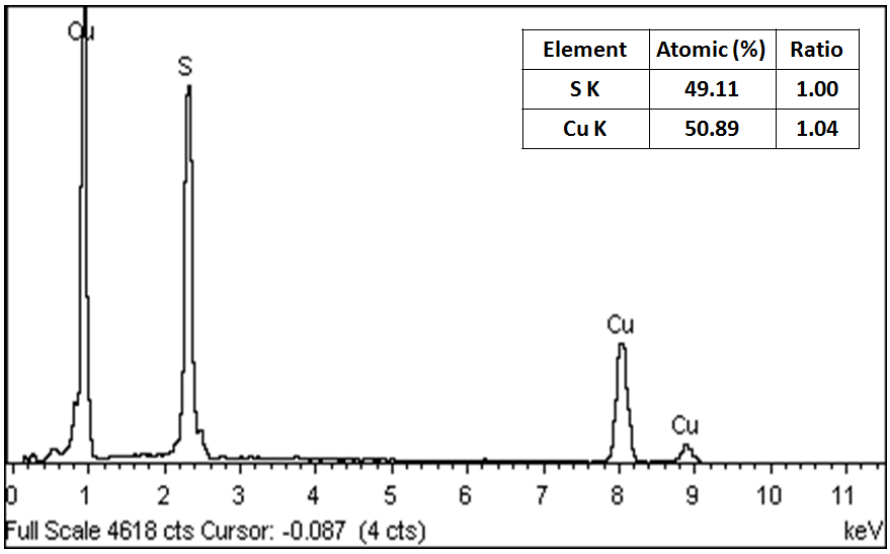

Figure 6.52. EDX spectra of hexagonal plates and its respective elemental quantification result observed in unreacted pure phase Covellite.

6.7.2. Growth of Nano-needle Crystallite

The morphology of the reacted pure phase Covellite at Hg(II) concentration of 50 ppm, 150 ppm, 250 ppm and 600 ppm under solution pH 1 and temperature of 25°C was examined using FESEM in which the results are depicted in **Figure 6.53 (a) – (d)** respectively. In 50 ppm Hg(II) solution, no obvious changes is detected on the reacted pure phase Covellite powder. The initial "hexagonal plates" morphology observed in unreacted pure phase Covellite remained as in the case of reacted pure phase Covellite. When Hg(II) concentration is increased to 150 ppm, 250 ppm and 600 ppm, it is identified that the initial

hexagonal plate morphology has become hardly found in the powder. The morphology is seemed to be dominated by some nanosize ranged needle like architecture namely nano-needle crystallite. They are identified to be grown on top of the hexagonal plates from **Figure 6.53 (c) (i)**. The chemical composition of the nano-needle crystallite was also analyzed using EDX. The EDX spectra of nano-needle crystallite at different Hg(II) concentration and its respective elemental quantification under the electron gun accelerating voltage of 20kV are shown in **Figure 6.54**. From the results, it can be seen that both of the copper and sulfur contributed the most to the overall atomic composition. The elemental composition is then followed by oxygen, mercury and chloride in which their content is far lesser compared to copper and sulfur present in the system.

The morphology of the reacted pure phase Covellite at Hg(II) concentration of 250 ppm under solution pH 1 and temperature of 25, 35 and 45°C are illustrated in **Figure 6.55 (a) – (c)** correspondingly. From the analysis, the morphology of the reacted pure phase Covellite powder is again covered mainly by the nano-needle crystallite. In addition, the growth of nano-needle crystallite has also resulted in the initial "hexagonal plates" diminished significantly. The chemical composition of the nano-needle crystallite was again analyzed using EDX. The EDX spectra of nano-needle crystallite at different reaction temperature and its respective elemental quantification under the electron gun accelerating voltage of 20kV are shown in **Figure 6.56**. From the results, it can be observed that the nano-needle crystallite is mostly composing of copper and sulfur. The amount of mercury and chloride found is also systematically increased via the temperature elevation. The results identified herein suggest that that the growth of nano-needle crystallite is highly due to the sorption of mercury and chloride onto the pure phase Covellite system.

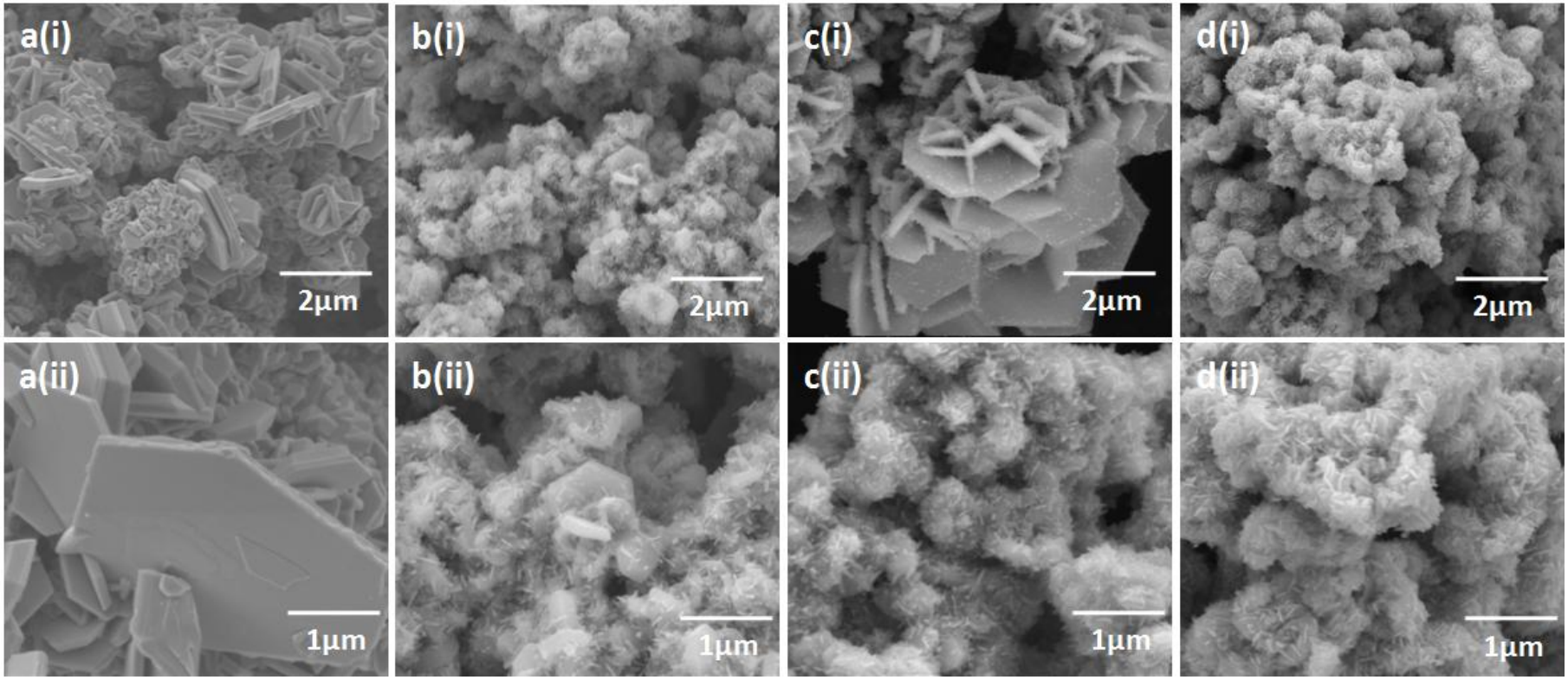

Figure 6.53. FESEM images of reacted pure phase Covellite at Hg(II) concentration of (a) 50 ppm (b) 150 ppm (c) 250 ppm (d) 600 ppm under solution pH 1, temperature of 25°C with magnifications of (i) 30 000x and (ii) 60 000x.

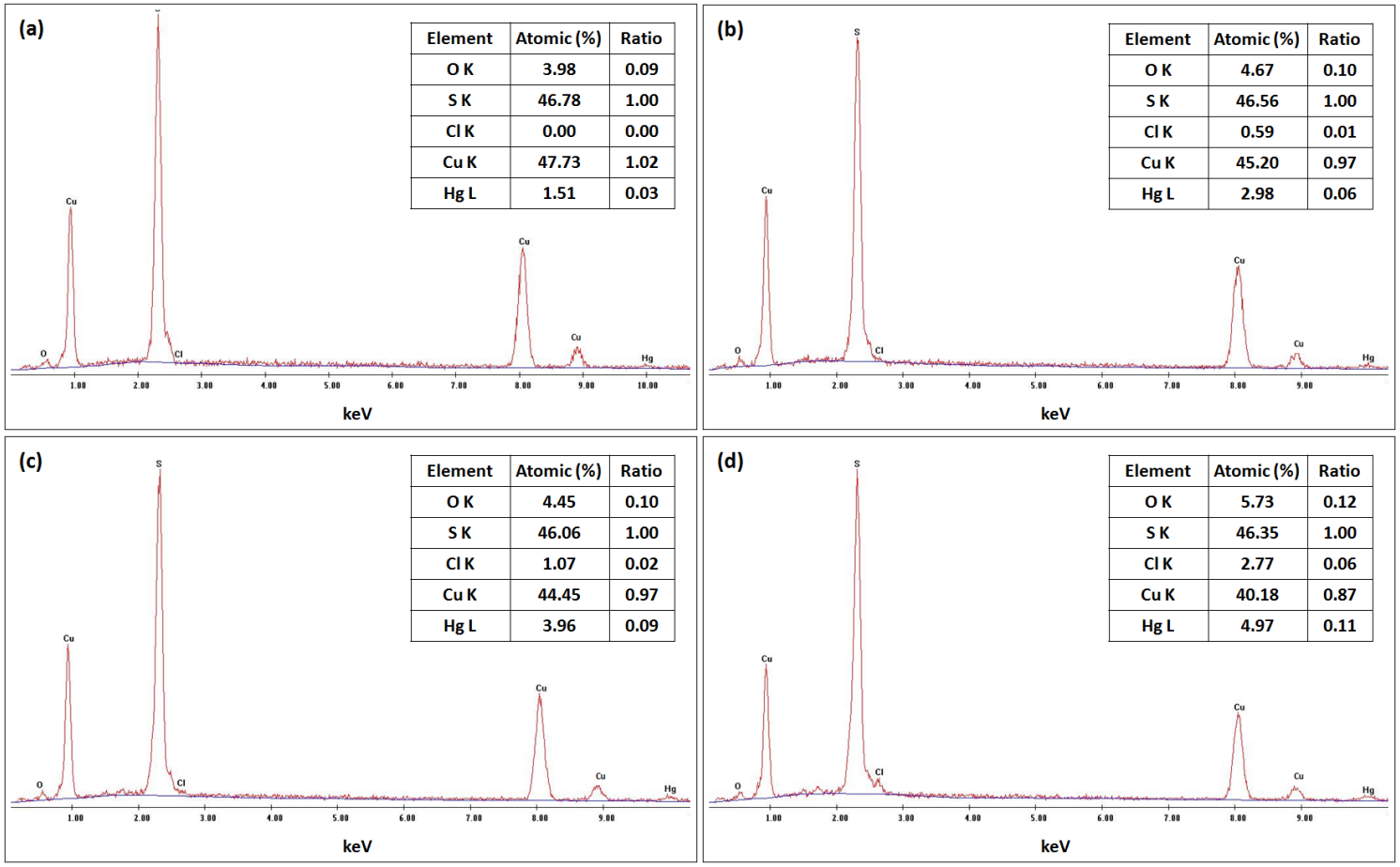

Figure 6.54. EDX spectra of nano-needle crystallite and its respective elemental quantification result at Hg(II) concentration of (a) 50 ppm (b) 150 ppm (c) 250 ppm (d) 600 ppm under solution pH 1 and temperature of 25°C.

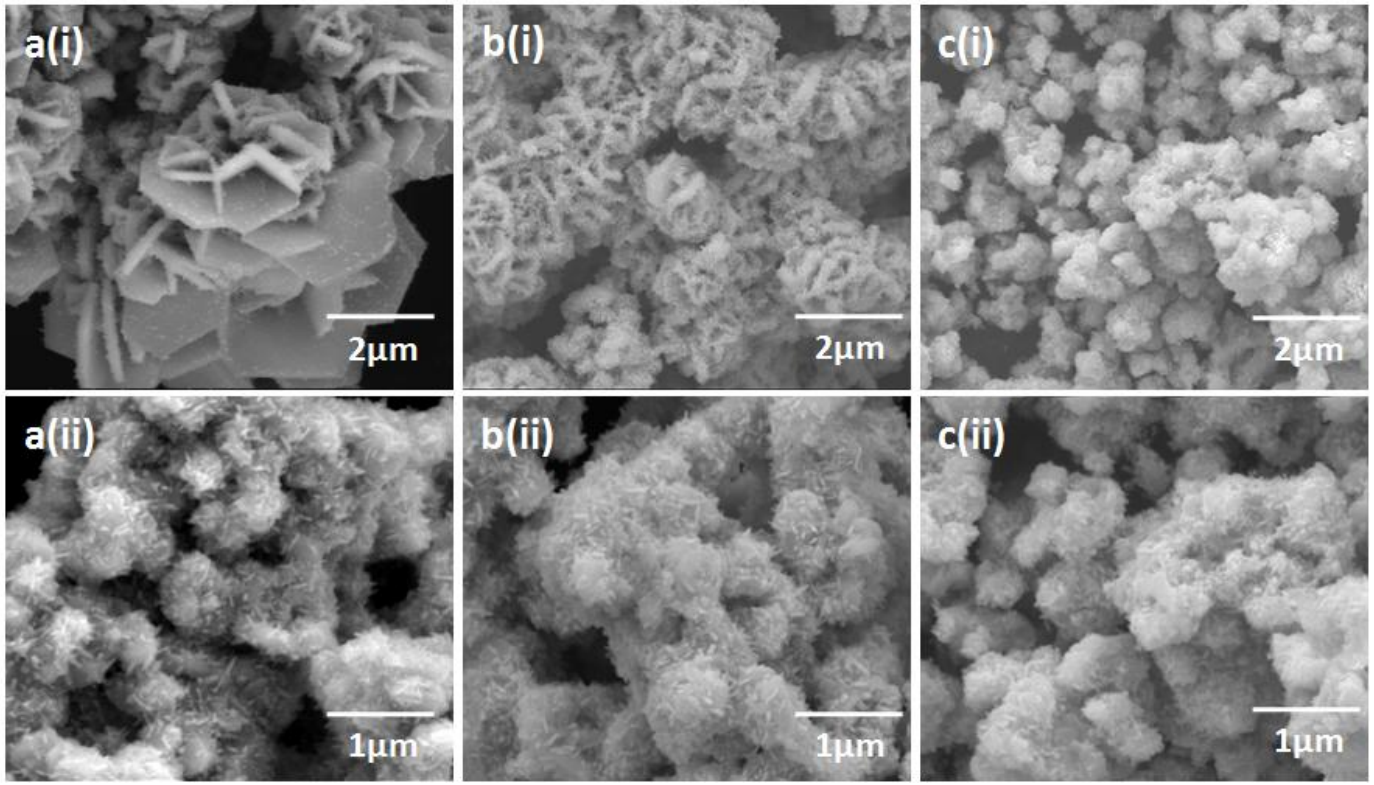

Figure 6.55. FESEM images of reacted pure phase Covellite at Hg(II) concentration of 250 ppm under solution pH 1 and temperature of (a) 25°C (b) 35°C (c) 45°C with magnifications of (i) 30 000x and (ii) 60 000x.

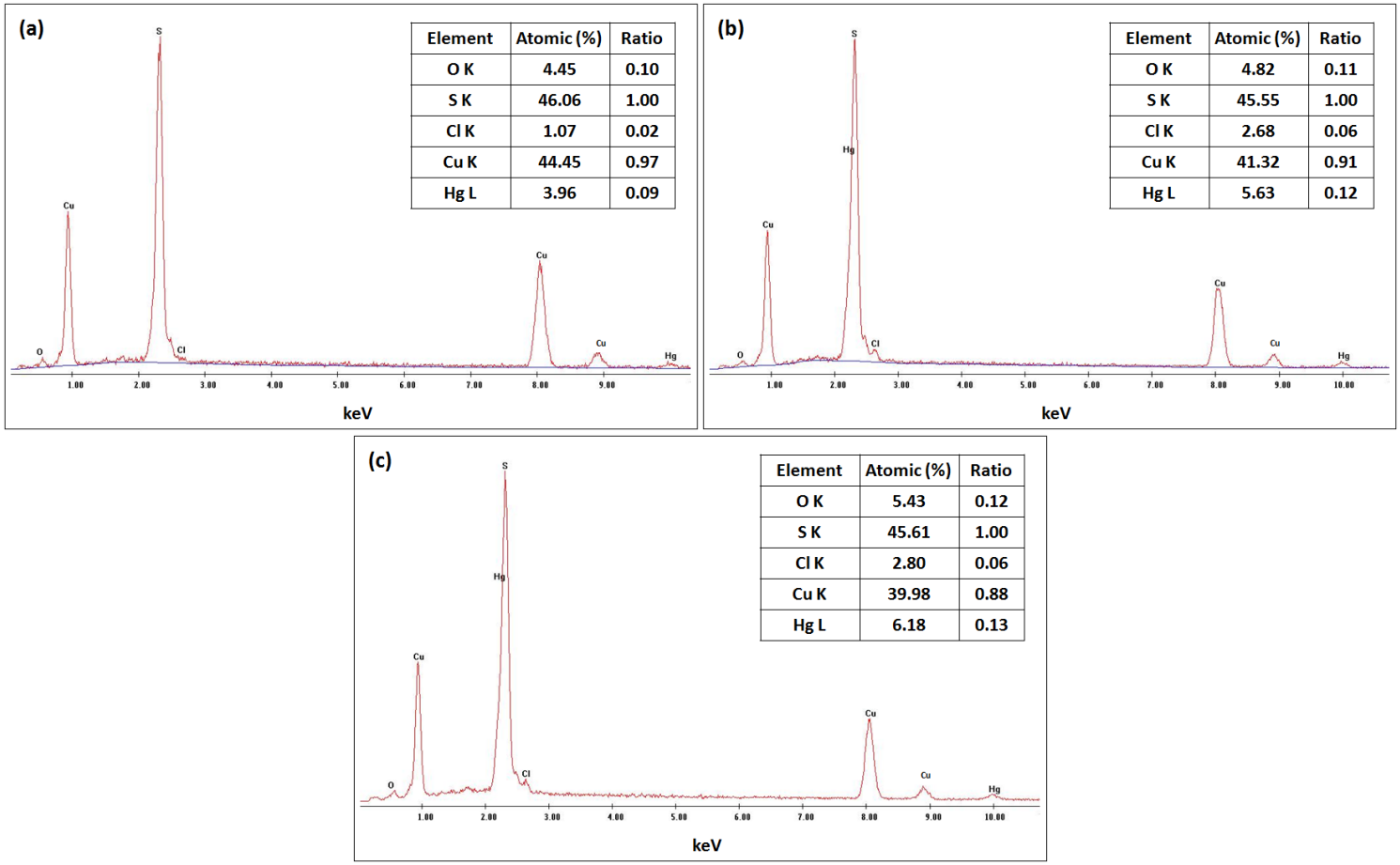

Figure 6.56. EDX spectra of nano-needle crystallite and its respective elemental quantification result at Hg(II) concentration of 250 ppm under solution pH 1 and temperature of (a) 25°C (b) 35°C and (c) 45°C.

6.7.3. Growth of Platelet Crystallite

The morphology of the reacted pure phase Covellite at Hg(II) concentration of 50 ppm, 150 ppm, 250 ppm and 600 ppm under solution pH 9 and temperature of 25°C was examined using FESEM in which the results are illustrated in **Figure 6.57 (a) – (d)** respectively. In 50 ppm Hg(II) solution, no obvious changes is detected on the reacted pure phase Covellite powder. The initial "hexagonal plates" morphology identified in unreacted pure phase Covellite remained as in the case of reacted pure phase Covellite. When Hg(II) concentration is increased to 150 ppm, 250 ppm and 600 ppm, the appearance of initial hexagonal plates morphology is again observed in the reacted pure phase Covellite powder. Nonetheless, an extra platelet like morphology i.e. platelet crystallite is also found in the powder in which it is indicated by the black arrow in the FESEM images. The platelet morphology adopted the micrometer ranged particle size and is bigger as compared to the initial hexagonal plates. In addition, this platelet crystallite seems to be "grown in between" rather than "grown on" the hexagonal plates. The relatively large size and well separated form of this platelet crystallite have made them easily distinguished from the initial CuS hexagonal plates. The chemical composition of this platelet crystallite was analyzed using EDX. The EDX spectra of platelet crystallite at different Hg(II) concentration and its respective elemental quantification under the electron gun accelerating voltage of 20kV are shown in **Figure 6.58**. From the results, it can be seen that copper shows the highest contribution in the content. This is associated with significant amount of oxygen and sulfur, followed by small amount of mercury and chloride present in the system.

The morphology of the reacted pure phase Covellite at Hg(II) concentration of 250 ppm under solution pH 9 and temperature of 25, 35 and 45°C are illustrated in **Figure 6.59 (a) – (c)** correspondingly. The analysis shows that the platelet crystallite morphology is again found between the hexagonal plates at all temperature employed. From **Figure 6.59**

(b) and (c), it can be seen that the growth of this platelet crystallite also has become more extensive when reaction temperature is raised to 35 and 45°C. The chemical composition of the platelet crystallite was also analyzed using EDX. The EDX spectra of platelet crystallite at different reaction temperature and its respective elemental quantification under the electron gun accelerating voltage of 20kV are shown in **Figure 6.60**. From the results, high amount of copper and sulfur is again found in the crystallite. However, the oxygen has contributed the most as reaction temperature increased. These results indicate that the platelet crystallite is mainly made up of copper, sulfur and oxygen where minor amount of mercury and chloride can be also present.

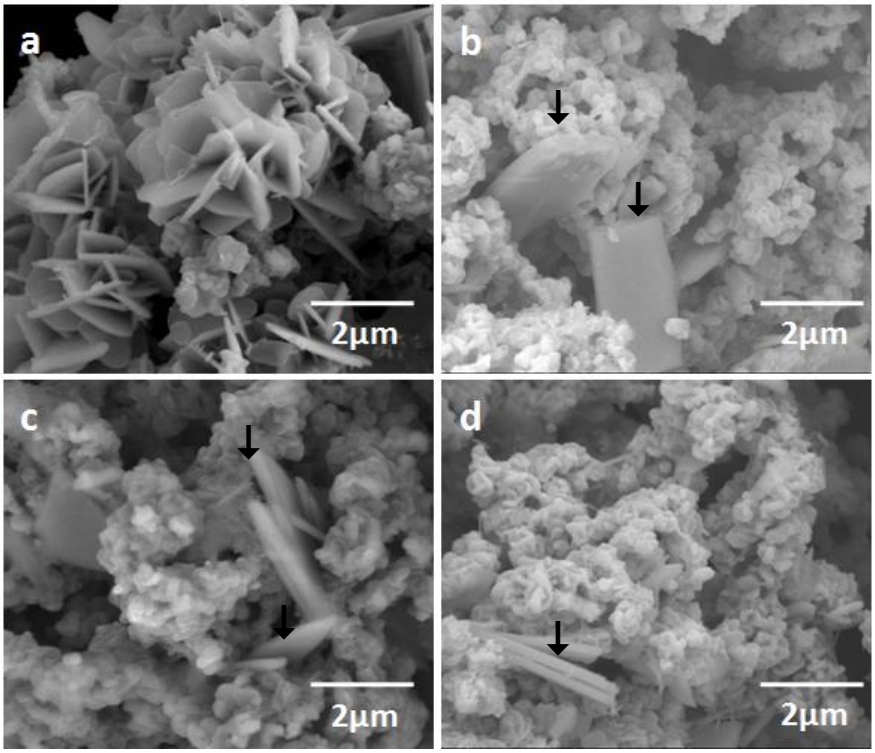

Figure 6.57. FESEM images of reacted pure phase Covellite at Hg(II) concentration of (a) 50 ppm (b) 150 ppm (c) 250 ppm (d) 600 ppm under solution pH 9 and temperature of 25°C.
↓ denotes the growth of platelet crystallite.

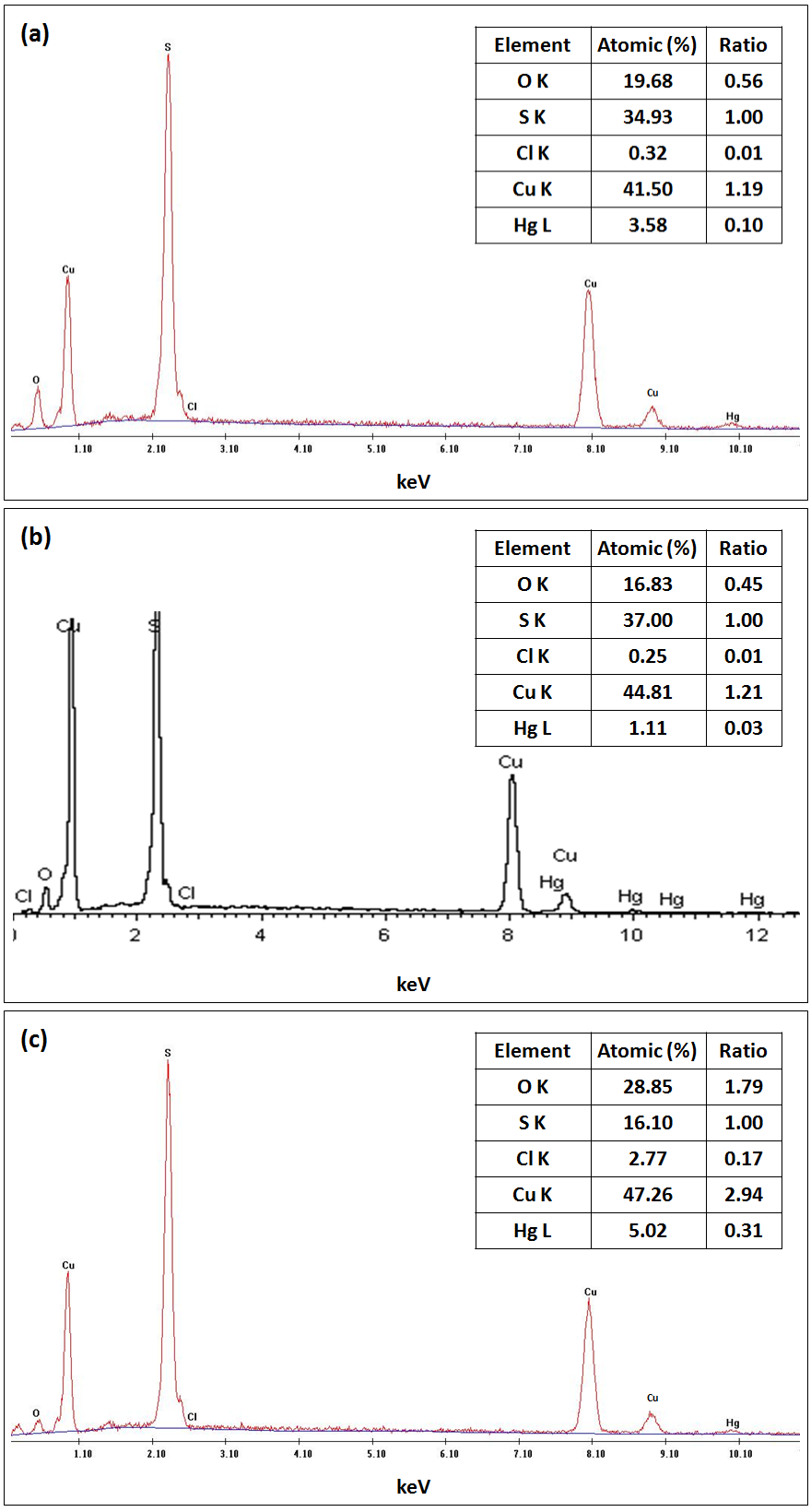

Figure 6.58. EDX spectra of platelet crystallite and its respective elemental quantification result at Hg(II) concentration of (a) 150 ppm (b) 250 ppm (c) 600 ppm under solution pH 9 and temperature of 25°C.

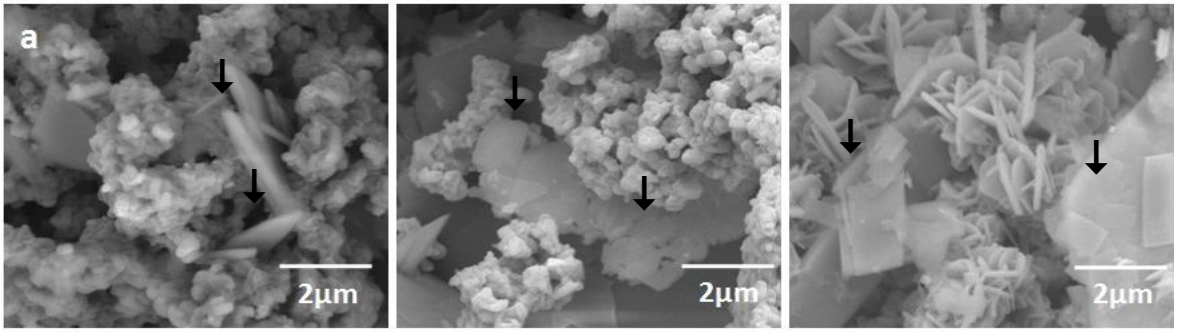

Figure 6.59. FESEM images of reacted pure phase Covellite at Hg(II) concentration of 250 ppm under solution pH 9 and temperature of (a) 25°C (b) 35°C and (c) 45°C. ↓ denotes the growth of platelet crystallite.

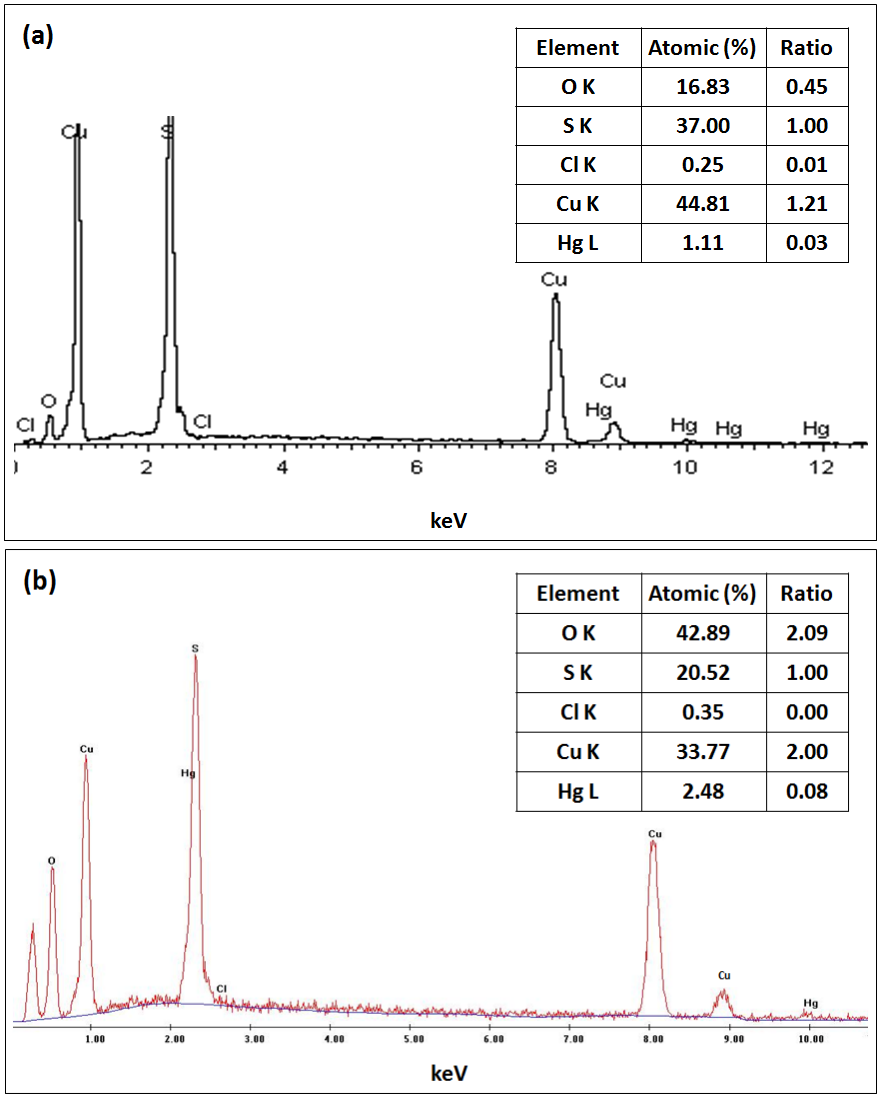

Figure 6.60. EDX spectra of platelet crystallite and its respective elemental quantification result at Hg(II) concentration of 250 ppm under solution pH 9 and temperature of (a) 25°C and (b) 35°C

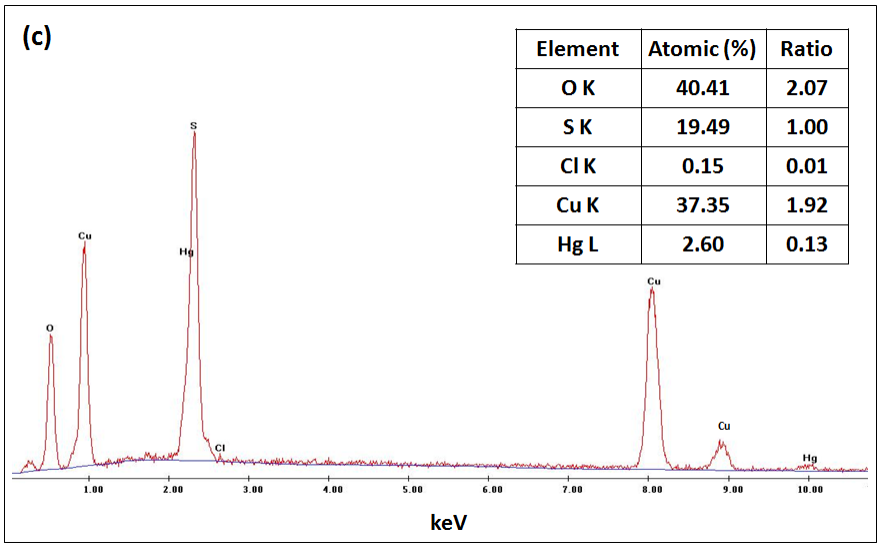

Figure 6.60. EDX spectra of platelet crystallite and its respective elemental quantification result at Hg(II) concentration of 250 ppm under solution pH 9 and temperature of (a) 25°C (b) 35°C and (c) 45°C (Continued).

6.7.4. Identification of Mercury Containing Crystallite via BSE Technique

The morphology of the reacted pure phase Covellite in 600 ppm Hg(II) under solution pH 8 and 9 at temperature of 25°C were examined using the FESEM where the results are depicted in **Figure 6.61 (a) and (b)** respectively. For both of the sample, the same FESEM image has been taken using different electron detection techniques i.e. secondary electron (SE) and backscattered electron (BSE) modes in the electron microscope. The FESEM image taken under the SE and BSE mode are denoted by SE and BSE image correspondingly. From both of the SE and BSE images, no information on the morphology changes of the reacted pure phase Covellite can be observed via the low magnification focus (100x). Nevertheless, it is astounded to see that there are some additional remarkably bright and shining particles from the BSE images. Attempts has been tried to increase the magnification of the respective SE and BSE images to 500x in which the results are depicted in **Figure 6.62**. From the FESEM images, it is observed that this bright and shining particle does not attain to any particular shape of morphology. The particle is found

to be agglomerated as a clump of crystallite at pH 8 whereas it is identified as crystallite of platelet shape at pH 9.

The chemical composition of these bright crystallites was analyzed using EDX. The EDX analysis has been performed using the elemental mapping technique under the electron gun accelerating voltage of 20kV. The elemental map of reacted pure phase Covellite in 600 ppm Hg(II) under solution pH 8 and 9 at temperature of 25°C are illustrated in **Figure 6.63 and Figure 6.64** respectively. For the reacted sample collected at pH 8, it can be observed that Hg and Cl have distributed homogeneously throughout the powder. It can also see that the bright crystallite is quite concentrated with Hg when compared to other site in the morphology. Nonetheless, no information can obtained for the bright crystallite regarding the composition of oxygen element due to its weak mapping. For the reacted sample collected at pH 9, it can be identified that Cl shows more homogeneous distribution compared to Hg. However, it can be clearly observed that Hg is far more concentrated on the bright crystallites in contrast to other site in the morphology. The elemental map again shows weak contribution of oxygen element on the bright crystallite. This indicates that the bright crystallite is chiefly composed of mercury and it might be free from the companion of oxygen element in its chemical composition.

On a separate note, spot EDX analysis were also carried out to confirm the chemical composition of the bright crystallite. **Figure 6.65 and 6.66** depicted the EDX spectra of the bright crystallite in 600 ppm Hg(II) under solution pH 8 and 9 at temperature of 25°C correspondingly. From both of the results, it is identified that the bright crystallite is indeed compose of a high content of Hg. It is astounded to see that the amount of Hg found is higher than the amount of Cu and S present in the bright crystallite. In addition, the presence of chlorine element in the bright crystallite is also verified via the spot EDX analysis. The amount of chlorine found in this case is significantly higher than the amount

of chlorine detected in the nano-needle crystallite shown previously (See **Section 6.7.2**). Nevertheless, a special attention is actually given to the oxygen element. A high contribution of oxygen is in fact identified in the bright crystallite although it is undetectable via the mapping analysis. It can be seen that the oxygen has contributed the most in the sample collected at pH 9. Thus, the results strongly suggest that the bright crystallite is eventually a mercury, oxygen and chloride containing compound looking at the elemental content found.

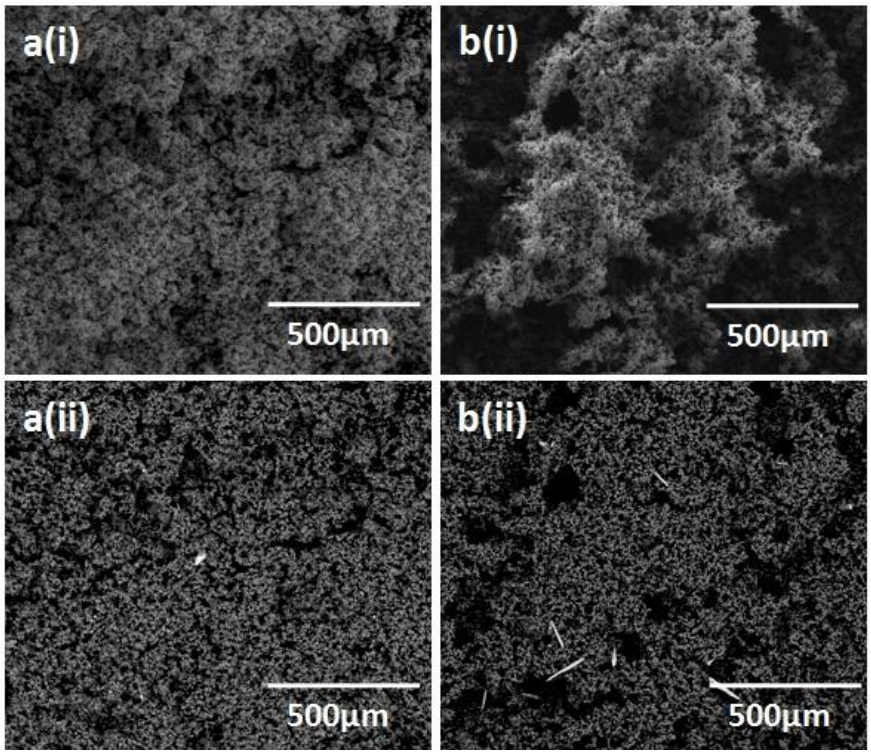

Figure 6.61. FESEM images of reacted pure phase Covellite at Hg(II) concentration of 600 ppm, temperature of 25°C under solution (a) pH 8 and (b) pH 9. The image is taken with e^- detection mode of (a) (i) Secondary electron (SE) and (ii) Backscattered electron (BSE) with magnification of 100x.

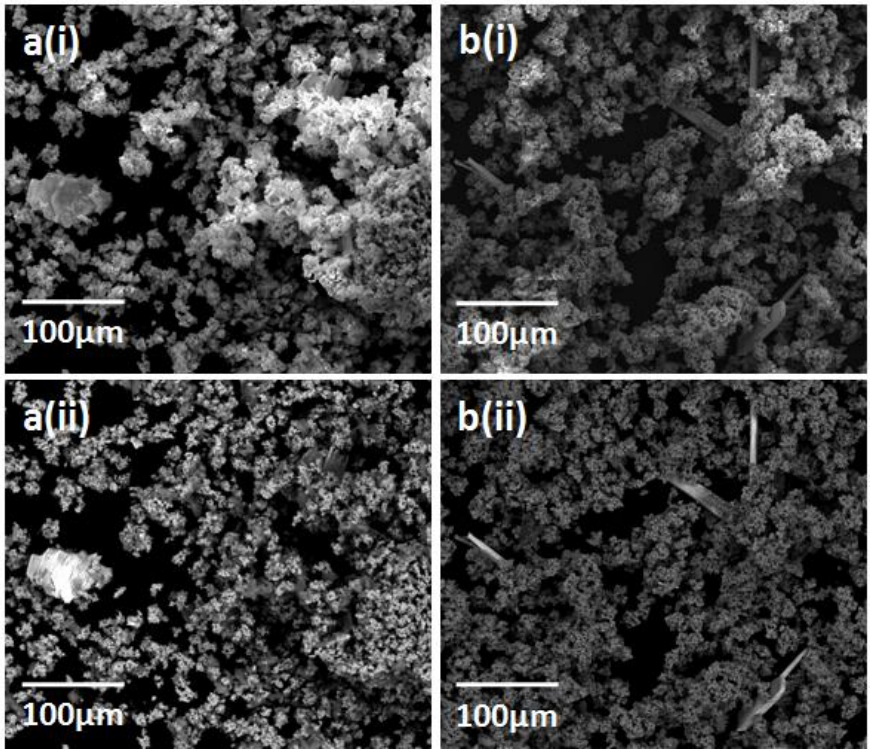

Figure 6.62. FESEM images of reacted pure phase Covellite at Hg(II) concentration of 600 ppm, temperature of 25°C under solution (a) pH 8 and (b) pH 9. The image is taken with e^- detection mode of (a) (i) Secondary electron (SE) and (ii) Backscattered electron (BSE) with magnification of 500x.

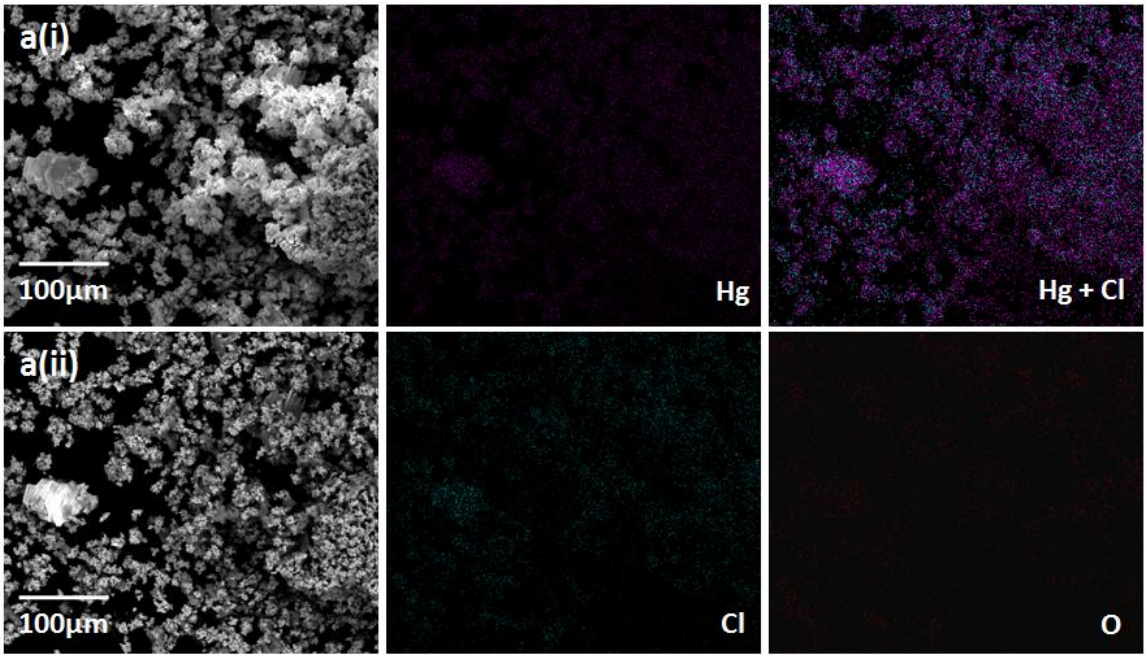

Figure 6.63. EDX mapping of reacted pure phase Covellite in 600 ppm Hg(II) under solution pH 8 at temperature of 25°C. The image is taken with e^- detection mode of (a) (i) Secondary electron (SE) and (ii) Backscattered electron (BSE) with magnification of 500x.

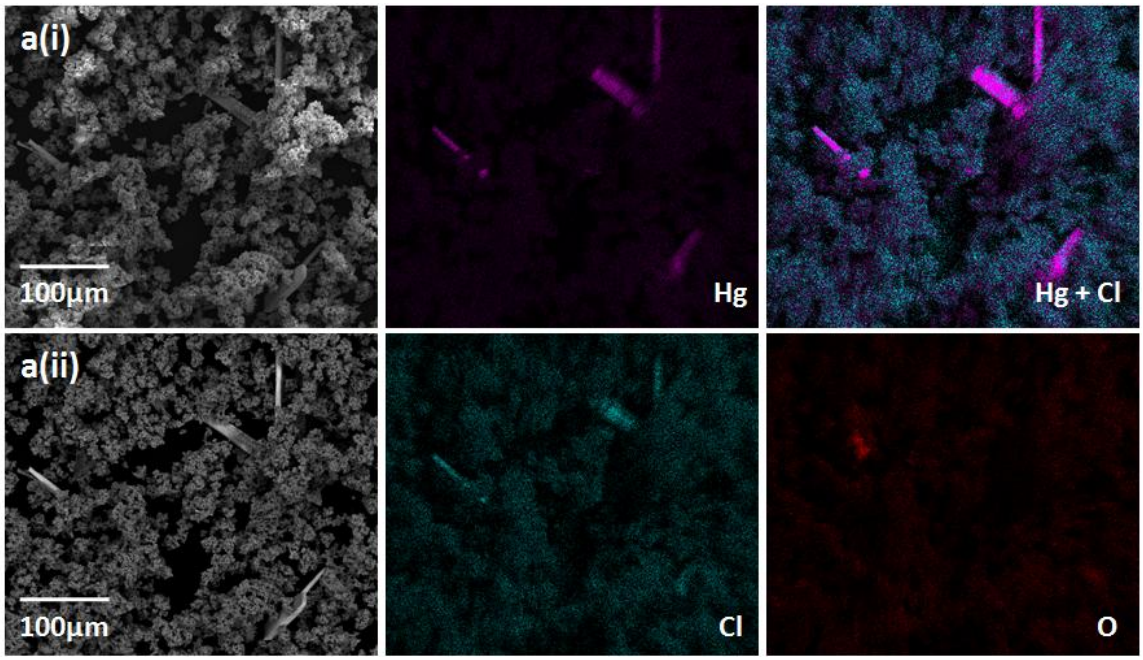

Figure 6.64. EDX mapping of reacted pure phase Covellite in 600 ppm Hg(II) under solution pH 9 at temperature of 25°C. The image is taken with e^- detection mode of (a) (i) Secondary electron (SE) and (ii) Backscattered electron (BSE) with magnification of 500x.

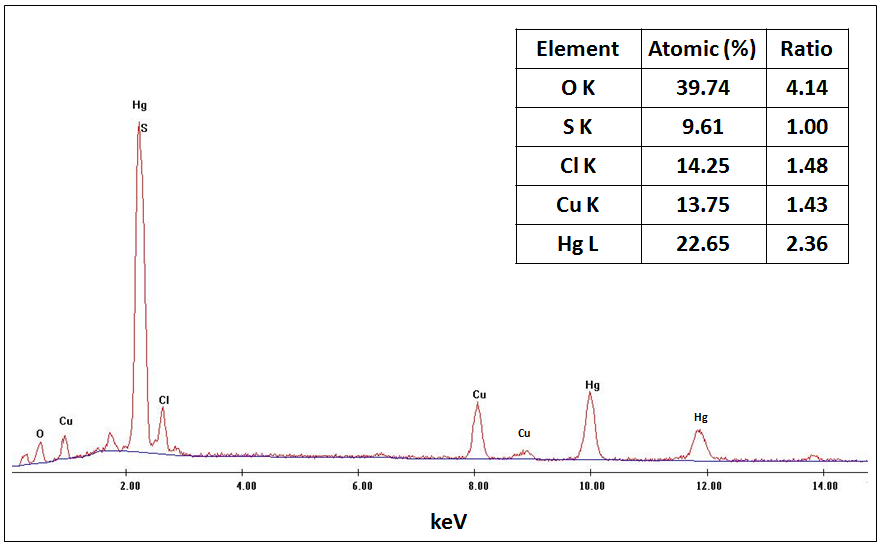

Element	Atomic (%)	Ratio
O K	39.74	4.14
S K	9.61	1.00
Cl K	14.25	1.48
Cu K	13.75	1.43
Hg L	22.65	2.36

Figure 6.65. EDX spectra of bright crystallite and its respective elemental quantification result in 600 ppm Hg(II) under solution pH 8 at temperature of 25°C.

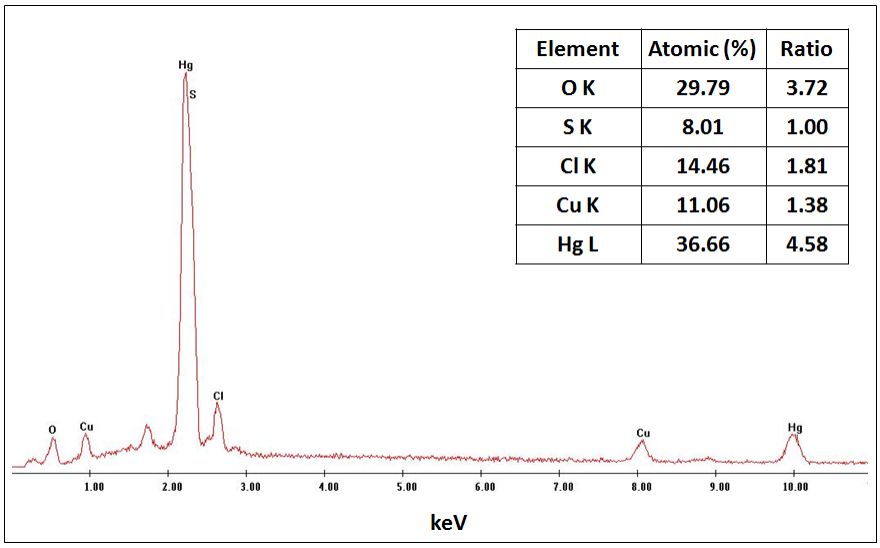

Figure 6.66. EDX spectra of bright crystallite and its respective elemental quantification result in 600 ppm Hg(II) under solution pH 9 at temperature of 25°C.

6.7.5. Discussion

For reactions performed at pH 1, the initial hexagonal plate morphology observed in unreacted pure phase Covellite has become hardly found in the reacted pure phase Covellite. This is associated by the appearance of nanosize ranged needle like architecture namely nano-needle crystallite which grow on the initial hexagonal plates. From PXRD analysis, β-HgS and m-$Hg_3S_2Cl_2$ have been detected in almost all of the reactions conducted at pH 1. This suggests that the growth of nano-needle crystallite can be closely related to the formation of these two compounds. In order to differentiate which compound corresponds to the growth of nano-needle crystallite, it is vital to first look at the PXRD pattern for reaction conducted in 600 ppm Hg(II) under solution pH 1 (**Section 6.6.2**). At this particular reaction condition, it is observed that no β-HgS is present in the reacted pure phase Covellite although a 100% Hg(II) removal is reached (**Section 6.1.2**). The high mercury uptake is actually coupled with the formation of m-$Hg_3S_2Cl_2$ in the reacted powder. This observation signifies that m-$Hg_3S_2Cl_2$ is the sole product in governing the high mercury uptake observed. More importantly, the formation of m-$Hg_3S_2Cl_2$ also correlated

well with the growth of nano-needle crystallite in reacted pure phase Covellite. On the other hand, EDX analysis was also conducted to determine the elemental composition of the nano-needle crystallite. From the analysis, it is identified that both Hg and Cl are present in the nano-needle crystallite in which their content has increased simultaneously with the raise of Hg(II) concentration and reaction temperature during the experiments. This result suggests that the growth of nano-needle crystallite is highly related to the sorption of Hg and Cl. This finding again supported the fact that the growth of nano-needle agrees well with the formation of m-$Hg_3S_2Cl_2$ compared to β-HgS.

For reactions carried out at pH 1, it has been also discussed earlier in **Section 6.5.5** that the Langmuir monolayer sorption isotherm gives bigger surface area value, $S_{specific}$ in contrast to the BET multilayer sorption isotherm. This observation is thought of uncommon since surface area calculated from BET multilayer isotherm would always give higher surface area than Langmuir monolayer isotherm. From FESEM analysis, it can be observed that an additional formation of nano-needle crystallite has actually grown on the initial CuS hexagonal plate morphology. Apparently, the growth of these nano-needle crystallites can notably increase the overall surface area of reacted CuS when compared to the unreacted CuS. Therefore, the formation of additional morphology in the CuS has directly explained the discrepancy of surface area calculated using BET and Langmuir approach.

For reactions carried out at pH 9, the initial hexagonal plate morphology observed in unreacted pure phase Covellite has remained in the reacted pure phase Covellite. Nevertheless, an additional platelet like morphology i.e. platelet crystallite is also detected in the powder. This platelet crystallite seems to be “grown in between” rather than “grown on” the hexagonal plates. This indicates that this platelet crystallite should be a separated form of morphology which is not developed from the initial hexagonal plates. From PXRD analysis, β-HgS and $Cu_4(SO_4)(OH)_6$ have been detected in almost all of the reactions

conducted at pH 9. This suggests that the growth of platelet crystallite can be significantly linked to the formation of these two compounds. With the aim to distinguish the compound corresponds to the growth of platelet crystallite, EDX analysis has been performed to determine the chemical content of this platelet crystallite. From the analysis, it is identified that the amount of Cu, S, Hg, Cl and O found is not consistent for all the samples examined. However, it can be observed that the platelet crystallite will always consists of a high amount of Cu, S and O. This observation has become prominent as reaction temperature increases. Apparently, the high amount of Cu, S and O detected agrees well with the formation of $Cu_4(SO_4)(OH)_6$. This finding strongly suggested the growth of platelet crystallite relates well to the formation of $Cu_4(SO_4)(OH)_6$ in reacted pure phase Covellite.

For reactions conducted at pH 8 and 9 in 600 ppm Hg(II), the initial hexagonal plate morphology observed in unreacted pure phase Covellite has remained in the reacted pure phase Covellite. Nonetheless, some additional remarkably bright and shining particles were also identified via the BSE technique. From the FESEM images, it is observed that this bright and shining particle does not attain to any particular shape of morphology. The particle is found to be agglomerated as a clump of crystallite at pH 8 whereas it is identified as crystallite of platelet shape at pH 9. This observation strongly suggests that the bright and shining particles are again not developed from the initial CuS hexagonal plates. Instead they are rather a type of precipitation product which formed during the sorption of Hg(II) onto CuS. From PXRD analysis, β-HgS and $HgCl_2.3HgO$ have been detected in reactions conducted at pH 9. This suggests that the growth of these bright and shining particles can be considerably connected to the formation of these two compounds. With the aim to distinguish the compound corresponds to the growth of these bright particles, EDX analysis has been performed to determine their chemical content. From the mapping analysis, it is confirmed that the bright crystallite is concentrated with Hg and Cl when compared to other

site in the morphology. Furthermore, the spot EDX analysis revealed that the bright crystallite is consisted of a huge amount of oxygen when compared to other element detected. These results indicate that the bright crystallite is actually a mercury, oxygen and chloride containing compound in which it is consistent with $HgCl_2.3HgO$ identified from PXRD analysis. Therefore, this finding verified the precipitation of $HgCl_2.3HgO$ during the sorption of Hg(II) onto CuS. The precipitation of $HgCl_2.3HgO$ happened when the amount of Hg(II) present has exceed the saturation limit of mercury oxide at alkaline pH (see mercury speciation diagram in **Section 6.1.4**).

6.8. X-ray Photoelectron Spectroscopy (XPS) Analysis

6.8.1. Survey Scans of Unreacted and Reacted Covellite at pH 1 and 9

Apart from the experiments conducted in 50 ppm, 150 ppm, 250 ppm and 600 ppm Hg(II), a separate experiment was also performed in 100 ppm Hg(II) at 25°C under solution pH of 1 and 9 using freshly prepared pure phase Covellite. The unreacted and reacted CuS using the aforementioned reaction conditions were further characterized using XPS. The XPS survey scan spectra of unreacted pure phase Covellite is shown in **Figure 6.67 (a)**. Both of the Cu2p and S2p peaks are clearly observed on the Covellite surface indicating the presence of Cu and S elements. Their appearance is also coupled with a small fraction of O1s peak at around 532eV which suggests that a low level of oxygen might be present on the unreacted CuS surface. **Figure 6.67 (b)** depicts the XPS survey scan spectra of reacted pure phase Covellite at pH 1. From the spectra, it is identified that the mercury has been successfully incorporated onto the surface lattice of CuS owing to the presence of intense Hg4f peak at around 105eV. The sorption of Hg is also accompanied by the sorption of Cl onto the surface with Cl2p peaks observed at around 200eV. The XPS survey scan spectra of reacted pure phase Covellite at pH 9 is illustrated in **Figure 6.67 (c)**. From the spectra, it

is again observed that the mercury has been successfully attached onto the surface lattice of CuS with the identification of intense Hg4f peak at around 105eV. Nevertheless, the sorption of Cl onto CuS seems to be minor when looking at the relative peaks intensity of Cu2p vs Cl2p. On top of that, the sorption of Hg is also associated by a higher amount of oxygen when comparing the relative peaks intensity of Cu2p vs O1s for both CuS sample reacted at pH 1 and 9. These finding has provided an important preliminary elemental profile before and after the sorption of Hg(II) onto CuS.

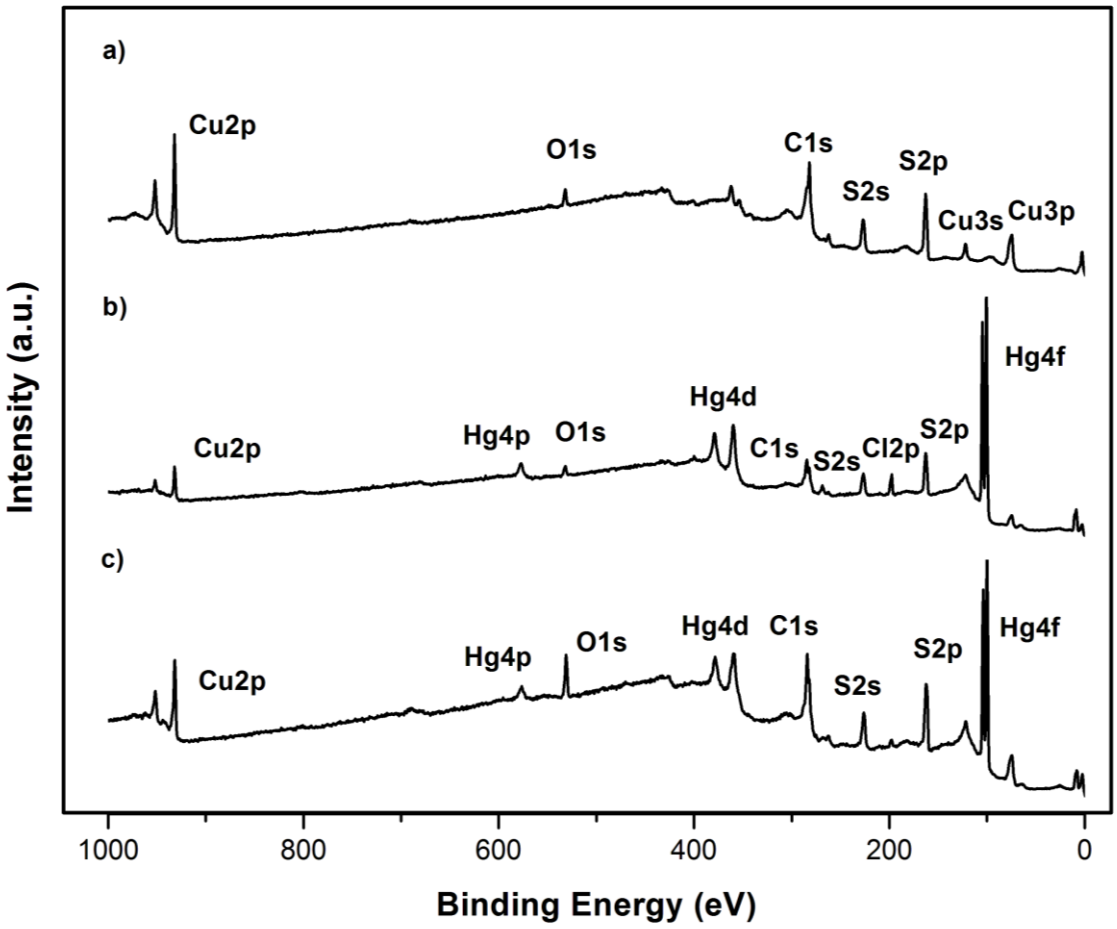

Figure 6.67. XPS survey scans of pure phase Covellite under reaction condition of (a) unreacted (b) reacted at pH 1 and (c) reacted at pH 9.

6.8.2. Elemental States in Unreacted and Reacted Covellite at pH 1 and 9

a) Copper

All the peaks de-convolution analysis has been performed using a Gaussian-Lorentz (GL) function in CasaXPS software. The detail scans of Cu2p, S2p and Hg4f spectra were collected at two kinetic energy (K.E.) *i.e* 200eV and 600eV to examine the distribution of chemical species at different depth condition. According to inelastic mean free path (IMFP) of electrons, variation on initial kinetic energy of the electron has a direct impact on the probability of the electron escape from each depth as well as frequency of detection of electrons from different depths in the solid. From the universal log-log plot of IMFP (nm) vs Energy (eV) as described in **Section 3.4.8**, the initial kinetic energy (K.E.) of electrons at 200eV gives ≈0.8 nm thickness of the surface information while for the initial kinetic energy (K.E.) of electrons at 600eV, it gives ≈1.0 nm thickness of the surface information.

The detail scans of $Cu2p_{3/2}$ spectra for unreacted and reacted pure phase Covellite at pH 1 and 9 at K.E. of 200eV and 600eV are illustrated in **Figure 6.68** and **Figure 6.69** respectively. For unreacted pure phase Covellite, all of the collected spectra shows the characteristic peak of Cu(I) with B.E. at around 932.35eV and 933.55eV (peaks separation of 1.20eV) (Goh, et al., 2006). The presence of these Cu(I) states in the spectra is consistent with the formation of CuS evidenced from the studies of X-ray photoelectron (XPS) and X-ray absorption spectroscopy (XAS) (Goh, et al., 2006; Pattrick, et al., 1997). In addition, the real crystal structure of CuS was also determined as $(Cu)_3(S)(S_2)$ from single crystal experiment (Evans & Konnert, 1976). Thus, the two different Cu(I) state of CuS observed in XPS can be viewed as two different environment of Cu *i.e.* Cu-S and Cu-S_2 identified from single crystallography. From the figures, the signal of Cu(I) at B.E. around 933.55eV can be also related to Cu(II) species (B.E. around 933.50 – 934.00eV) (Fullston, et al., 1999; Lefèvre, et al., 2003). This Cu(II) species is associated to the CuO formation upon slight

oxidation of CuS (Fullston, et al., 1999). Besides, an additional peak is also identified at B.E. around 935eV. This main peak relates well to the feature of Cu(II) either in the form of $CuSO_3$ or $Cu(OH)_2$ (Fullston, et al., 1999; Lefèvre, et al., 2003).

For reacted Covellite at pH 1, the signals of Cu(I) and Cu(I)/Cu(II) are attested in the $Cu2p_{3/2}$ spectra regardless of depth condition. Whilst, the signal of Cu(II) (B.E. around 935eV) is detected to be diminished notably in the $Cu2p_{3/2}$ spectra at both K.E of 200eV and 600eV. The decrease in the Cu(II) signal is mostly due to the dissolution of $CuSO_3$ upon contact with water in acidic condition in which it is evidenced by their diminished signal in the S2p spectra of reacted pure phase Covellite at pH 1. Therefore, the remaining signals of Cu(I), Cu(I)/Cu(II) and Cu(II) shows that CuS, $Cu(OH)_2$ as well as CuO can be still present on the surface upon sorption of Hg(II) onto CuS at pH 1.

For reacted Covellite at pH 9, all signals of Cu(I) and Cu(II) are found on the $Cu2p_{3/2}$ spectra regardless of depth condition. In general, the presence of these signals suggested that the sorption of Hg(II) onto pure phase Covellite at pH 9 does not lead to any obvious changes on the state of Cu. However, a special interest is given to the signal of Cu(I)/Cu(II) and Cu(II) at B.E. around 933.50 – 934.00eV and 935.00eV respectively. It is because the dissolution of highly soluble $CuSO_3$ is occuring upon contact with water in which it is evidenced by their diminished signal in the S2p spectra of reacted pure phase Covellite at pH 9. CuO and $Cu(OH)_2$ can also remain on the surface mostly due to their relatively low solubility in alkaline condition. Moreover, the formation of Cu(II) compound such as $Cu_4(SO_4)(OH)_6$ were also detected from PXRD patterns at pH 4 – 9 (**Section 6.6.5**). Thus, it is indicative that the attested signals of Cu(I), Cu(I)/Cu(II) and Cu(II) should be the results of dissolution of $CuSO_3$ and the presence of CuS, $Cu_4(SO_4)(OH)_6$, $Cu(OH)_2$ as well as CuO on the surface at pH 9.

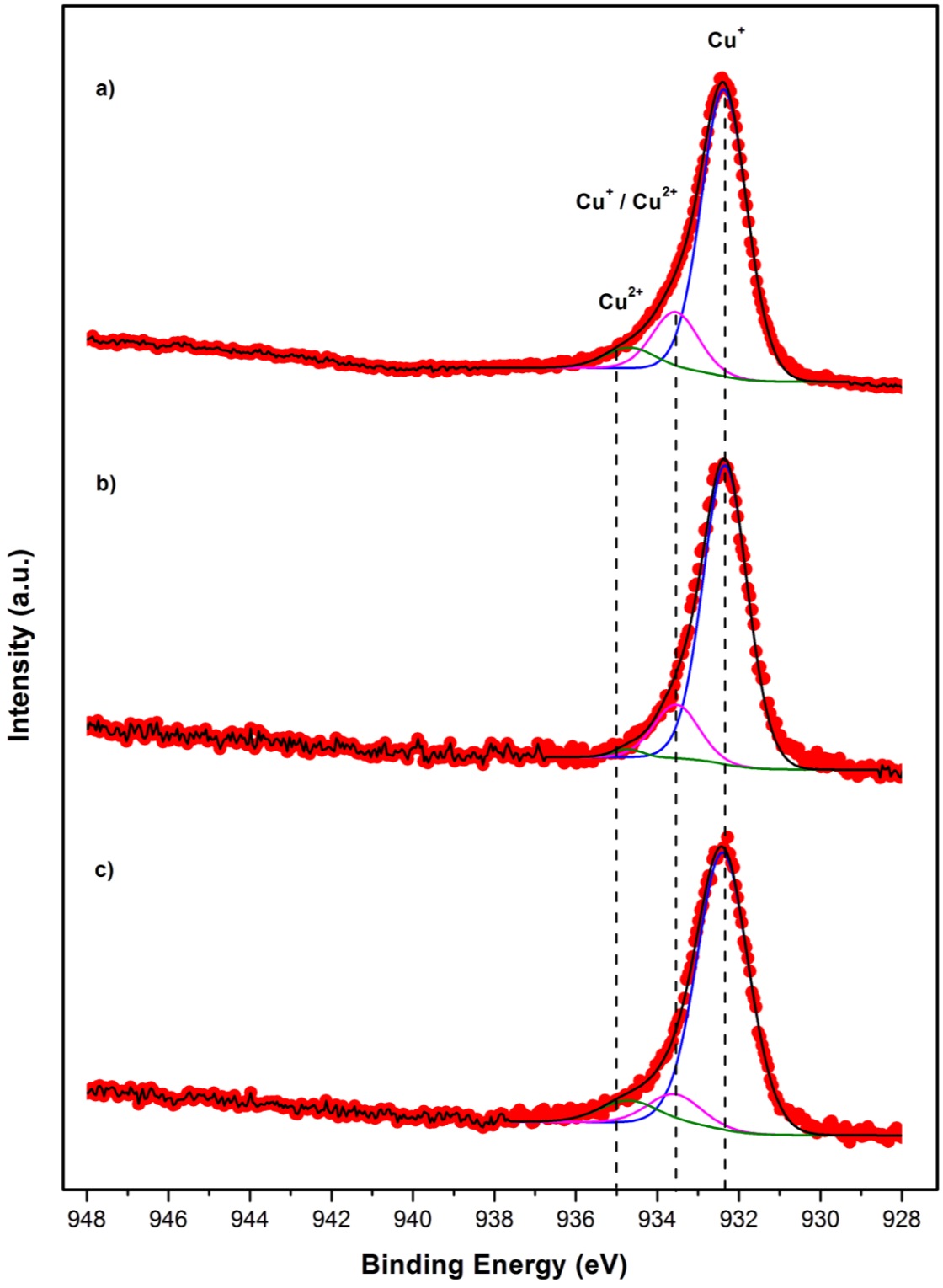

Figure 6.68. $Cu2p_{3/2}$ detail scans spectra of pure phase Covellite under reaction condition of (a) unreacted (b) reacted at pH 1 and (c) reacted at pH 9 at K.E. of 200eV.

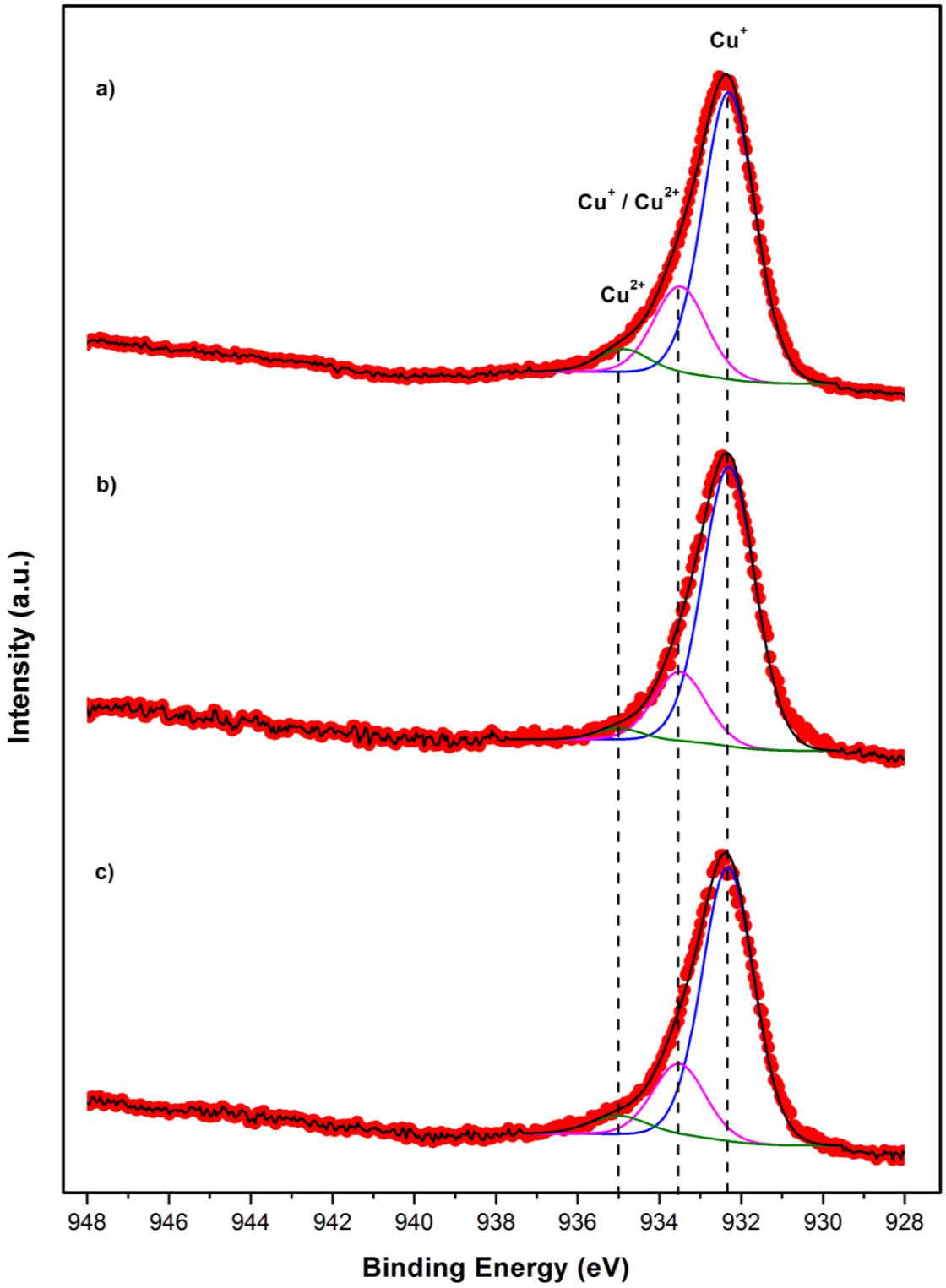

Figure 6.69. $Cu2p_{3/2}$ detail scans spectra of pure phase Covellite under reaction condition of (a) unreacted (b) reacted at pH 1 and (c) reacted at pH 9 at K.E. of 600eV.

b) Sulfur

The detail scans of S2p spectra for unreacted and reacted pure phase Covellite at pH 1 and 9 at K.E. of 200eV and 600eV are shown in **Figure 6.70** and **Figure 6.71** correspondingly. In all cases, the S2p spectra shows an overlapped peak signal in which it is split by spin-orbit coupling into a doublet of $S2p_{1/2}$ and $S2p_{3/2}$ components (Kurmaev, et al., 1998; Scofield, 1976). In contrast, the B.E. of $S2p_{3/2}$ component provides practical information for specific sulfur chemical state identification. For unreacted Covellite, it was found that no oxidized layer of SO_3 and SO_4 with B.E. at ≈166.66eV and ≈168.74eV respectively are detected at the outer surface (K.E. of 200eV) (Moulder, et al., 1992). This indicates the employment of N_2 passivation method is effective in preventing the attack of atmospheric oxygen towards CuS (P. L. Yap, et al., 2012). Nevertheless, from **Figure 6.71 (a)**, it was identified that a small fraction of SO_3 is detected at the inner surface of unreacted Covellite (K.E. of 600eV). The formation of SO_3 species is most probably due to the oxidation of CuS by crystalline H_2O or trapped O_2 which is not preventable during the normal vacuum drying and storage of CuS. At both K.E. of 200eV and 600eV, the sulfur species of monosulfide (S^-) and disulfide (S_2^{2-}) species were also found at the B.E of ≈160.97eV and ≈161.85eV correspondingly. These two sulfur species agrees well to the crystal structure of CuS in which it was found to compose of $Cu_3(S^-)(S_2^{2-})$ instead of simple ions like Cu^{2+} and S^{2-} (Evans & Konnert, 1976; Goh, et al., 2006; Pattrick, et al., 1997). Furthermore, two other types of S species *i.e.* highly copper deficient nonstoichiometric sulfide, Cu_xS with $x < 2$ (B.E. at ≈162.96eV) (Kundu, et al., 2008; Laajalehto, et al., 1994; Lefèvre, et al., 2003) and elemental sulfur, S^0 (B.E. at ≈164.06eV) (Moulder, et al., 1992) were also detected on the surface of unreacted Covellite (both K.E. of 200eV and 600eV). These extra S species can be explained in views of the surface impurities that carried over from the reaction intermediate during synthesis of phase pure CuS.

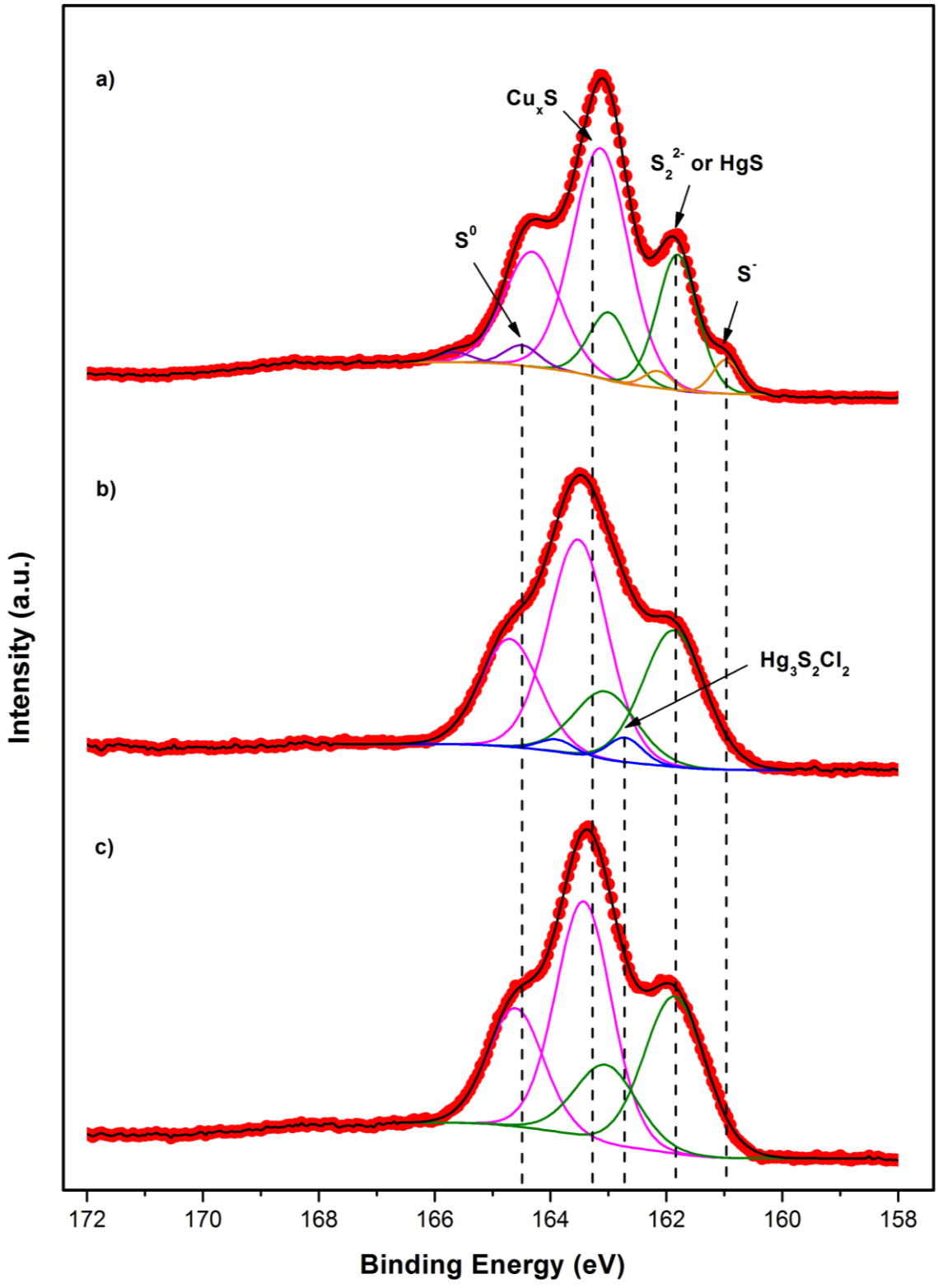

Figure 6.70. S2p detail scans spectra of pure phase Covellite under reaction condition of (a) unreacted (b) reacted at pH 1 and (c) reacted at pH 9 at K.E. of 200eV.

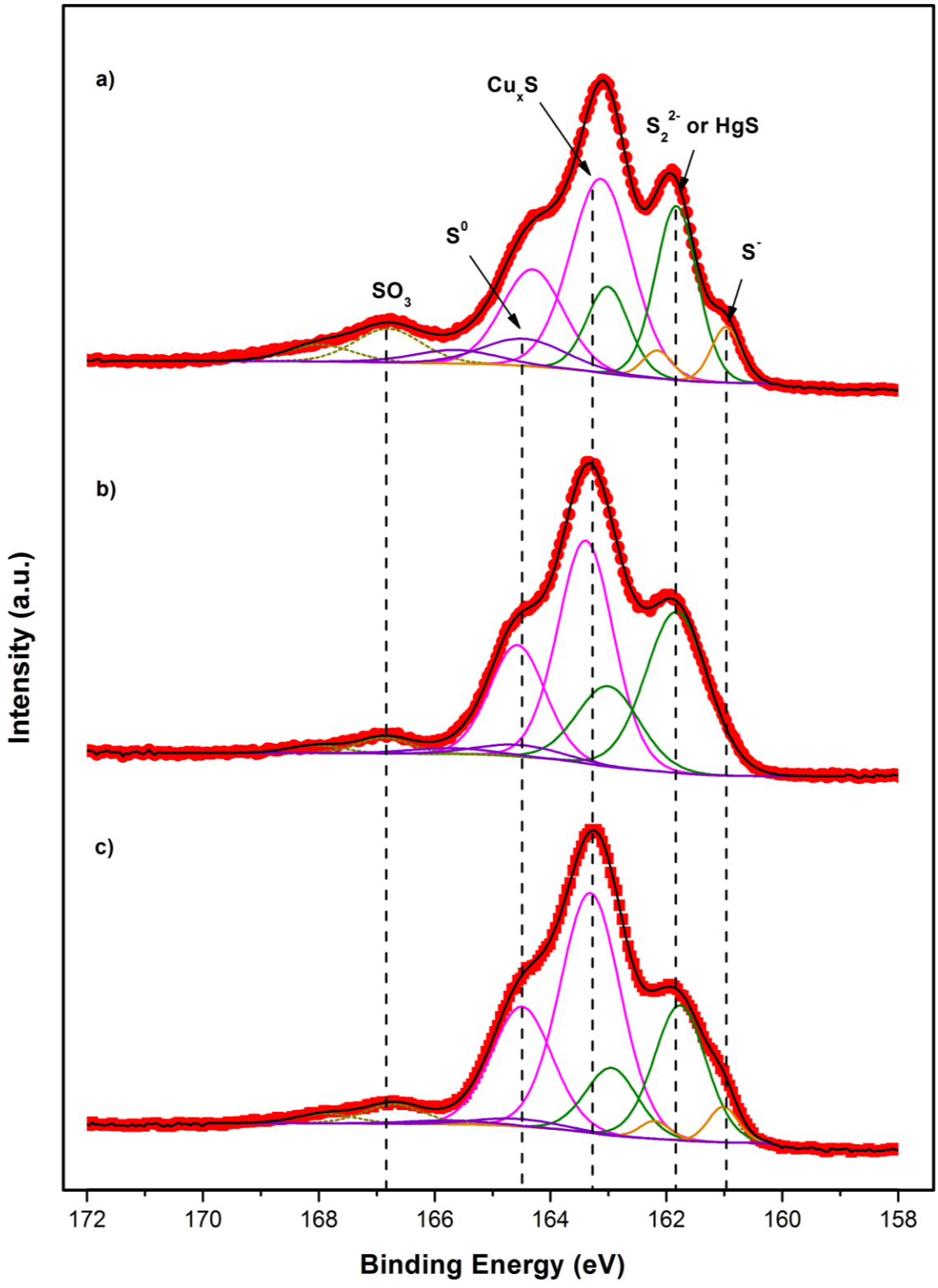

Figure 6.71. S2p detail scans spectra of pure phase Covellite under reaction condition of (a) unreacted (b) reacted at pH 1 and (c) reacted at pH 9 at K.E. of 600eV.

For reacted Covellite at pH 1, the first observation is coupled to the diminished signal of SO_3 at K.E. of 600eV. This implied that the dissolution of $CuSO_3$ has occurred upon the sorption of Hg(II) onto CuS. In addition, monosulfide (S^-) and elemental sulfur (S^0) species have disappeared in the spectra at K.E. of 200eV wheras only the signal of monosulfide (S^-) is absent in the spectra at K.E. of 600eV. The loss of S^0 signal is believed to be due to the dissolution process. This process is preferably to occur at outer surface due to better exposure to the aqueous environment. The disappearance of S^- cannot be due to the the dissolution process since CuS exhibits an exceptionally high solubility product in water (K_{sp} = 8 x 10^{-37}) ("Solubility product constants," 2003). Thus, the loss of S^- signal suggests that this species can be the responsible sulfur species for mercury complexation. On top of that, the $S2p_{3/2}$ signal of copper deficient sulfide (Cu_xS) and disulfide (S_2^{2-}) are also detected on both of the inner and outer surface. The retention of Cu_xS and S_2^{2-} are unclear in this case. However, they might play the roles as spectator compounds or even in an indirect manner, possess certain ability in complexing aqueous mercury.

A special attention should be given to the signal of disulfide (S_2^{2-}) species since the chemical state of sulfur in cinnabar, HgS, exhibits the same B.E as disulfide (S_2^{2-}) at ≈161.85eV (Hyland, et al., 1990). The resolution is impossible by comparing the B.E values of the two species. On the other hand, an additional peak evolution (B.E of ≈162.5eV) is also observed in the S2p spectra of reacted powder at pH 1 at the outer surface (K.E. of 200eV). The $S2p_{3/2}$ signal at B.E of ≈162.56eV corresponds well to the B.E. of $Hg_3S_2Cl_2$ (Hyland, et al., 1990) in which this compound has been described earlier as a reaction product between HgS and $HgCl_2$ by Mellor et al. and Phillips et al. (Mellor, 1923; Harold O. Phillips & Kraus, 1965). The identification of this compound is also confirmed by the diffraction peaks of m-$Hg_3S_2Cl_2$ in its respective PXRD pattern (**Appendix E**). Moreover, this is coupled with the growth of nano-needle crystallite on

reacted Covellite from the FESEM image (**Appendix F**). Thus, the detection of m-$Hg_3S_2Cl_2$ on reacted Covellite via XPS technique again proved the presence of $Hg_3S_2Cl_2$ on reacted Covellite surface. Its existence in the powder strongly suggests that the sorption of Hg(II) onto CuS at acidic pH can proceed via the formation of m-$Hg_3S_2Cl_2$.

For reacted Covellite at pH 9, the diminished signal of SO_3 is again observed at K.E. of 600eV, suggesting that the dissolution of $CuSO_3$ is also possible in alkaline condition. In contrast, monosulfide (S^-) and elemental sulfur (S^0) species have completely disappeared in the XPS spectra at K.E. of 200eV whereas the signal of monosulfide (S^-) and elemental sulfur (S^0) species are only slightly reduced in the XPS spectra at K.E. of 600eV. The loss of S^0 signal from the surface is believed to be due to the dissolution process. The higher detachment of S^0 at K.E. of 200eV compared to K.E. of 600eV indicated that the dissolution process is preferably to occur at outer surface due to better exposure to the aqueous environment. The disappearance of S^- cannot be due to the the dissolution process since CuS exhibits an exceptionally high solubility product in water (K_{sp} = 8 x 10^{-37}) ("Solubility product constants," 2003). Thus, the loss and reduced S^- signal at both K.E. of 200eV and K.E of 600eV suggests that this species can be the responsible sulfur species for mercury complexation. Furthermore, the $S2p_{3/2}$ signal of copper deficient sulfide (Cu_xS) and disulfide (S_2^{2-}) are also detected on both of the inner (K.E. of 600eV) and outer surface (K.E. of 200eV) of reacted Covellite at pH 9. The retention of Cu_xS and S_2^{2-} are again unclear in this case. They might play the roles as spectator compounds or even in an indirect manner, possess certain ability in complexing aqueous mercury. Moreover, the presence of disulfide (S_2^{2-}) signal also indicates that surface HgS might be formed during the reaction. It is because the chemical state of sulfur in disulfide (S_2^{2-}) exhibits the same B.E as cinnabar, HgS at ≈161.85eV (Hyland, et al., 1990).

c) Mercury

The Hg4f detail scans spectra for reacted pure phase Covellite at pH 1 and 9 at K.E. of 200eV and 600eV are depicted in **Figure 6.72** and **Figure 6.73** respectively. Meanwhile, the reference B.E. used for the Hg compound determination is shown in **Table 6.27**. In general, the spectra consist of a two distinct, non-overlap spin-orbit coupling split peaks in which these peaks are identified as the $Hg4f_{5/2}$ and $Hg4f_{7/2}$ component. In contrast, the B.E. of $Hg4f_{7/2}$ component provides practical information for specific mercury chemical state identification.

For reacted Covellite at pH 1, the main peaks of Hg(II) have been detected at both K.E. of 200eV and 600eV. The Hg(II) signal identified at K.E. of 200eV corresponded well to the state of Hg(II) in $HgCl_2$, HgS and $Hg_3S_2Cl_2$. However, distinct identification among these species is impossible as they possess same B.E. The Hg(II) signal identified at K.E. of 600eV related well to both state of Hg(II) in $HgCl_2$, HgS, $Hg_3S_2Cl_2$ as well as the state of Hg(II) in HgO. A special attention is given to the formation of HgO since its precipitation is unreasonable at solution pH 1. Thus, the formation of HgO can be most probably due to the reactions between Hg(II) and oxygen containing copper species *i.e.* $Cu(OH)_2$ and CuO in which interaction of Hg-O-Cu is expected from the reactions.

For reacted Covellite at pH 9 and K.E. of 200eV, the characteristic peaks of Hg(II) have been detected. From **Figure 6.72 (b)**, it can be observed that the Hg(II) signal is largely contributed by the formation of HgO. The large contribution of HgO species at pH 9 can be correlated well to the precipitation of HgO when supersaturation of $Hg(OH)_2$ is reached (see **Figure 6.6**). In addition, the formation of HgO can be also due to the reactions between Hg(II), surface $Cu(OH)_2$ and CuO in which interaction of Hg-O-Cu is expected from the reactions. On the other hand, a small fraction of $HgCl_2$, HgS and $Hg_3S_2Cl_2$ signal was also detected on the reacted Covellite surface at K.E. of 200eV. The identification of

$HgCl_2$, HgS and $Hg_3S_2Cl_2$ species have clearly suggested that the reaction can also proceed through the complexation with the S species present on CuS surface.

For reacted Covellite at pH 9 and K.E. of 600eV, the main peaks of Hg(II) state in HgO is again detected. The formation of HgO can be largely due to (i) the precipitation of HgO when supersaturation of $Hg(OH)_2$ is reached and (ii) the reactions between Hg(II), surface $Cu(OH)_2$ and CuO species. However, a great interest is actually given to the peak at B.E around 99.96eV in which this peak is found to relate closely to the Hg(I) state in Hg_2Cl_2. The formation of Hg_2Cl_2 seems not impossible since it was also detected that in the sorption studies of Hg(II) onto FeS (Jeong, et al., 2007).

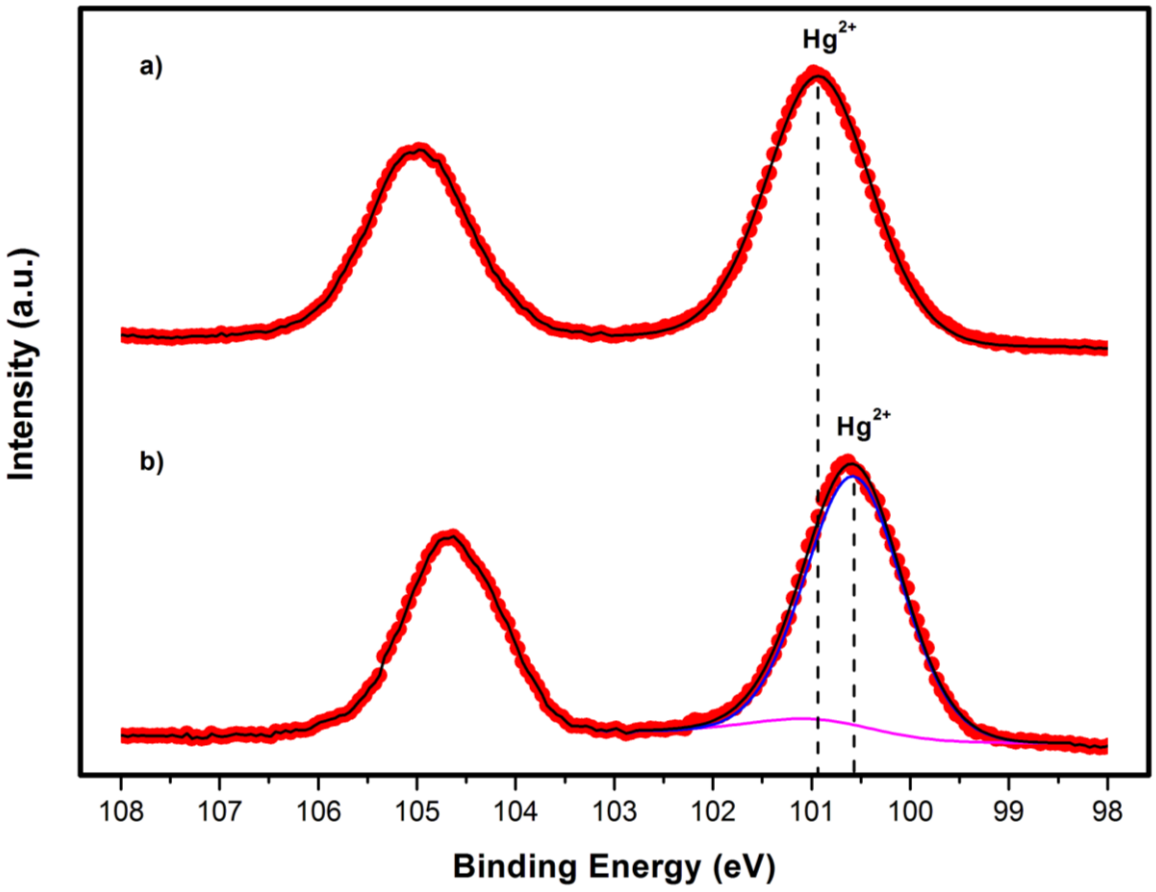

Figure 6.72. Hg4f detail scans spectra of reacted pure phase Covellite under reaction condition of (a) pH 1 and (b) pH 9 at K.E. of 200eV.

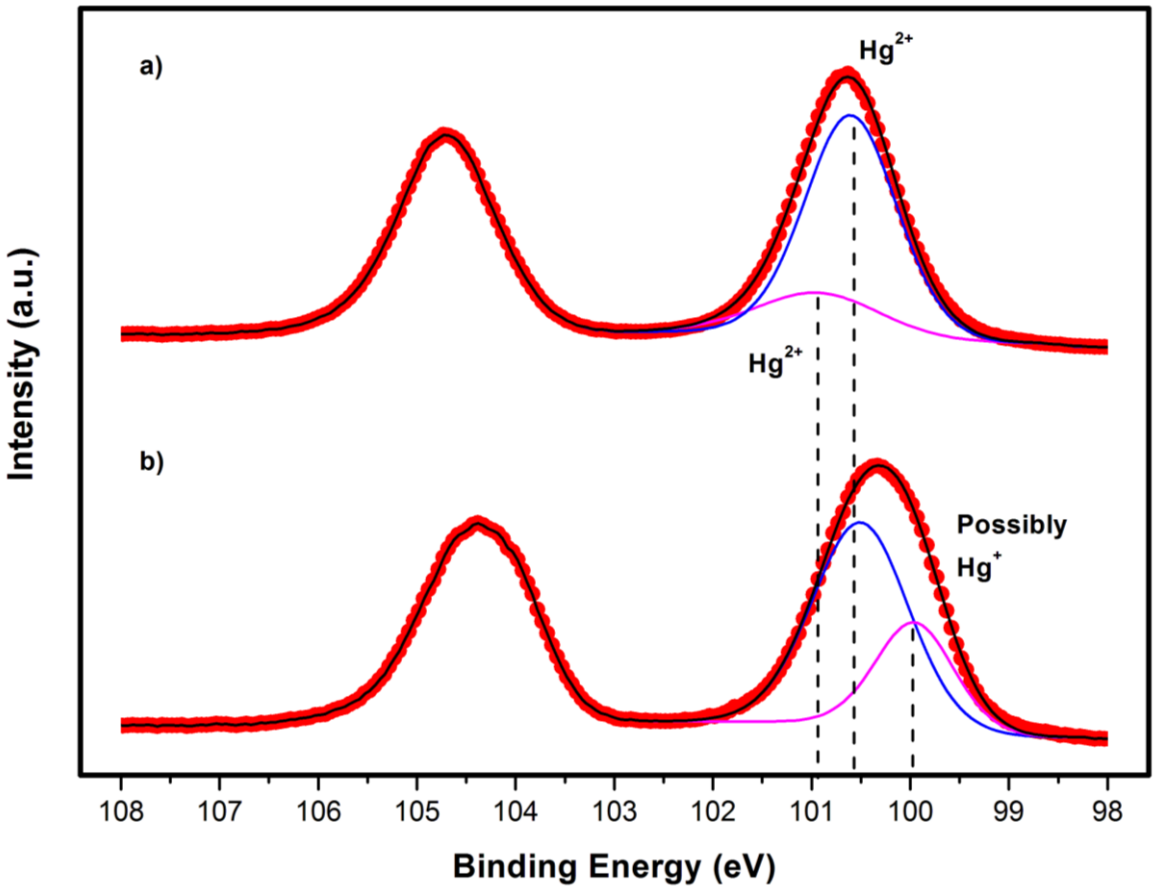

Figure 6.73. Hg4f detail scans spectra of reacted pure phase Covellite under reaction condition of (a) pH 1 and (b) pH 9 at K.E. of 600eV.

Table 6.27. Binding Energies (eV) of Hg $4f_{7/2}$ for selected standards and its references.

.

Standard	B.E. (eV) of Hg $4f_{7/2}$	References
$HgCl_2$	100.90	(Hyland, et al., 1990)
HgS	100.90	
$Hg_3S_2Cl_2$	100.90	
HgO	100.57	(Humbert, 1986)
Hg_2Cl_2	99.40	(Hyland, et al., 1990)
Hg^0	99.20	(Seals, et al., 1973)

The formation of Hg_2Cl_2 from the initial $HgCl_2$ can be explained via the electrochemistry approach. The reduction of Hg^{2+} to Hg_2^{2+} with its respective half cell potential is shown as below:

$$2Hg^{2+} + 2e^- \leftrightarrow Hg_2^{2+} \qquad E°/V = +0.91 \qquad (6.13)$$

The first plausible explaination for the formation of Hg_2Cl_2 is the oxidation of hyxroxide ion at alkaline pH:

$$4OH^- \leftrightarrow 2H_2O + O_2 + 4e^- \qquad E°/V = -0.40 \qquad (6.14)$$

and overall reaction:

$$2Hg^{2+} + 4OH^- \leftrightarrow Hg_2^{2+} + 2H_2O + O_2 \qquad \Delta E°/V = +0.51 \qquad (6.15)$$

This lead to $\Delta G° = -196.8$ kJ/mol ($\Delta G° = -n\Delta E°F$ with n is the number of moles of electrons involved and F is the Faraday constant). The negative $\Delta G°$ signifies the feasibility of the reduction of Hg(II) to Hg(I) to occur at alkaline pH.

In addition, the reduction of $HgCl_2$ to Hg_2Cl_2 can be also due to the oxidation of CuS at alkaline media. The stepwise oxidation of CuS to $CuSO_4$ with its respective half cell potential is shown as the following:

$$CuS \leftrightarrow 2S + 2e^- + Cu^{2+} \qquad E°/V = +0.43 \qquad (6.16)$$

$$S + 6OH^- \leftrightarrow SO_3^{2-} + 4e^- + 3H_2O \qquad E°/V = +0.66 \qquad (6.17)$$

$$SO_3^{2-} + OH^- \leftrightarrow SO_4^{2-} + H_2O + 2e^- \qquad E°/V = +0.93 \qquad (6.18)$$

From the equation above, it can be observed that the reduction of Hg(II) to Hg(I) in equation 6.13 can lead to a positive $\Delta E°$ and subsequently a negative $\Delta G°$ regardless of which reaction pair from equation 6.16 to 6.18 is used. Thus, this again signifies the feasibility of the reduction of Hg(II) to Hg(I) to occur at alkaline pH. On the other hand, the presence of Hg(I) state on CuS surface also shows that a concurrent oxidation of Cu(I) to Cu(II) should has occurred as indicated by equation 6.16. The reaction between free Cu^{2+} and OH^- on the surface vicinity of CuS has resulted in the formation of $Cu(OH)_2$:

$$Cu^{2+} + 2OH^- \leftrightarrow Cu(OH)_2 \quad (6.19)$$

Further dissociation of H_2O from $Cu(OH)_2$ can also lead to the formation of CuO:

$$Cu(OH)_2 \leftrightarrow CuO + H_2O \quad (6.20)$$

In fact, it was also reported by Fullston et al. that CuS surface can become increasingly covered with $Cu(OH)_2$ and CuO upon oxidation in alkaline media (Fullston, et al., 1999). Thus, the presence of Hg(I) on CuS surface has indirectly revealed the in-situ transformation of CuS to $Cu(OH)_2$ and CuO as well as the subsequent Hg(II) uptake at highly alkaline condition (pH 9) via the reduction of $HgCl_2$ to Hg_2Cl_2.

6.8.3. Quantification of Copper, Sulfur, Oxygen, Mercury and Chlorine in Unreacted and Reacted Covellite at pH 1 and 9

Apart from the peak de-convolution analysis, the peak areas quantification based on Cu2p, S2p, O1s, Hg4f and Cl2p detail scan spectra were also done to determine the surface atomic composition on unreacted and reacted pure phase Covellite. The surface atomic

composition at K.E. of 200eV and 600eV are normalized with respect to the sulfur in which the results are shown in **Table 6.28** and **Table 6.29** respectively. For unreacted pure phase Covellite, high amount of S in relative to Cu is detected at both of the K.E. of 200eV and 600eV. This indicated that the dominance of S rich rather than Cu rich termination on the unreacted CuS surface. For reacted mixed phase Covellite at pH 1 and 9, a sharp decrease of Cu is observed at both K.E. of 200eV and 600eV upon the Hg(II) sorption. Considering that leaching of Cu and S both occurred during the reaction, this result strongly suggests that the amount of Cu leached is notably higher than the amount of S leached from the surface. Thus, the sorption of Hg(II) onto CuS surface is apparently consisted of an ion-exchange process that involve the leaching of Cu for Hg but retain S on the surface.

Table 6.28. XPS surface atomic compositions of unreacted and reacted pure phase Covellite at K.E. of 200eV.

Sample	Quantification Ratio				
	S	Cu	Hg	Cl	O
Unreacted	1.00	0.29	0.00	0.00	0.16
Reacted at pH 1	1.00	0.12	0.34	0.18	0.12
Reacted at pH 9	1.00	0.14	0.22	0.05	0.16

Table 6.29. XPS surface atomic compositions of unreacted and reacted pure phase Covellite at K.E. of 600eV.

Sample	Quantification Ratio				
	S	Cu	Hg	Cl	O
Unreacted	1.00	0.28	0.00	0.00	0.08
Reacted at pH 1	1.00	0.13	0.30	0.10	0.06
Reacted at pH 9	1.00	0.15	0.16	0.03	0.10

In addition, relatively higher Hg/S and Cl/S ratio is also observed at pH 1 in contrast to pH 9 although similar Cu/S ratio is observed at both pH 1 & 9 regardless of the depth condition. These results indicate that an additional Hg(II) sorption process which does not sacrifices the Cu-S bonding might occur at pH 1 regardless of depth condition. This finding is in good agreement with the formation of m-$Hg_3S_2Cl_2$ in which its formation has increased the loading of Hg(II) onto CuS but prevented further leaching of Cu(II) from the surface. This has compensated back the similar Cu/S ratio at both pH 1 and 9 despite the higher ratio of Hg/S and Cl/S found at pH 1.

Moreover, it is identified that the relative amount of O present on reacted CuS at pH 9 and K.E. of 200eV remained similar to unreacted CuS. More importantly, the relative amount of O present on reacted CuS at pH 9 and K.E. of 600eV has increased slightly when compared to unreacted CuS. The similar and increase amount of O at pH 9 is actually not correlated well to the decreased in SO_3 species identified earlier. Thus, this suggested that an extra reaction that captures oxygen onto CuS has occured during the Hg(II) sorption process. In order to explain this observation, it is considered that an in situ transformation of CuS to $Cu(OH)_2$ and CuO has happened on the surface in alkaline media. Therefore, the oxidation process has directly increased the amount of oxygen present on the reacted CuS.

The peak areas quantification for specific composition of different S species were also carried out based on the S2p detail scan spectra of unreacted and reacted pure phase Covellite. The surface composition of specific S species at K.E. of 200eV and 600eV are normalized with respect to the copper deficient sulfide (Cu_xS) in which the results are shown in **Table 6.30** and **Table 6.31** respectively. For reacted pure phase Covellite, a reduction of monosulfide (S^-) species is observed regardless of the pH and depth condition. This signifies the role of monosulfide (S^-) as the active S species for Hg(II) complexation. On the other hand, the reduction of monosulfide (S^-) is also associated with the evolution of

$Hg_3S_2Cl_2$ and the increased signal of S_2^{2-} in the XPS spectra. This shows that monosulfide (S^-) can be fully converted to $Hg_3S_2Cl_2$ and S_2^{2-} upon the sorption of Hg(II) onto CuS. Nonetheless, a special attention is in fact given to S_2^{2-} since it exhibits the same B.E. as HgS at ≈161.85eV (Hyland, et al., 1990). The resolution is impossible by comparing the B.E. values of these two species. From the specific quantification ratio of S_2^{2-} to Cu_xS, it can be observed that the ratio has been increased notably in almost all of the reaction condition applied. This strongly suggested that an additional evolution of HgS might be occurring in responding to the increased signal of disulfide (S_2^{2-}) at B.E. ≈161.85eV. Thus, the quantification analysis of specific S species has indirectly provided an important strategy in differentiating HgS from S_2^{2-} despite their similar B.E in the XPS spectra.

Table 6.30. XPS surface specific S species compositions of unreacted and reacted pure phase Covellite at K.E. of 200eV.

Sample	Quantification Ratio					
	Cu_xS	S^-	$(S_2)^{2-}$ / HgS	$Hg_3S_2Cl_2$	S^0	SO_3
Unreacted	1.00	0.07	0.42	0.00	0.05	0.00
Reacted at pH 1	1.00	0.00	0.67	0.07	0.00	0.00
Reacted at pH 9	1.00	0.00	0.73	0.00	0.00	0.00

Table 6.31. XPS surface specific S species compositions of unreacted and reacted pure phase Covellite at K.E. of 600eV.

Sample	Quantification Ratio					
	Cu_xS	S^-	$(S_2)^{2-}$ / HgS	$Hg_3S_2Cl_2$	S^0	SO_3
Unreacted	1.00	0.14	0.61	0.00	0.19	0.19
Reacted at pH 1	1.00	0.00	0.81	0.00	0.08	0.07
Reacted at pH 9	1.00	0.07	0.48	0.00	0.04	0.08

6.9. High Resolution Transmission Electron Microscopy and Energy Dispersive X-ray Spectroscopy (HRTEM-EDX) Analysis

6.9.1. Characteristic of Pure Phase Covellite

The insight of the pure phase CuS hexagonal plate used was also examined using TEM and HRTEM analyses in which the results are illustrated in **Figure 6.74**. From **Figure 6.74 (a)**, it vividly shows the stack layers orientation of many CuS plates with hexagonal structure. The observation of hexagonal shaped particle from TEM analysis agrees well with the morphology determined from FESEM images. **Figure 6.74 (b)** depicts the HRTEM image of the hexagonal shaped particle. From the well resolved 2D lattice fringes of the CuS hexagonal plate measured, two adjacent lattice spacings of 0.19 nm and 0.33 nm have been identified from the image. It is important to note that both of the lattice spacings of 0.19 nm and 0.33 nm relate well to the {110} and {100} lattice plane of hexagonal CuS respectively. A Fast Fourier Transform (FFT) pattern of the as-synthesized CuS hexagonal plate is also captured in **Figure 6.74 (c)**. The ordered hexagonal-like spot arrays visibly illustrated in the FFT pattern again confirmed the formation of CuS with hexagonal lattice structure and shape. All these results strongly signify the single crystallinity of the CuS hexagonal plates used in the mercury sorption studies.

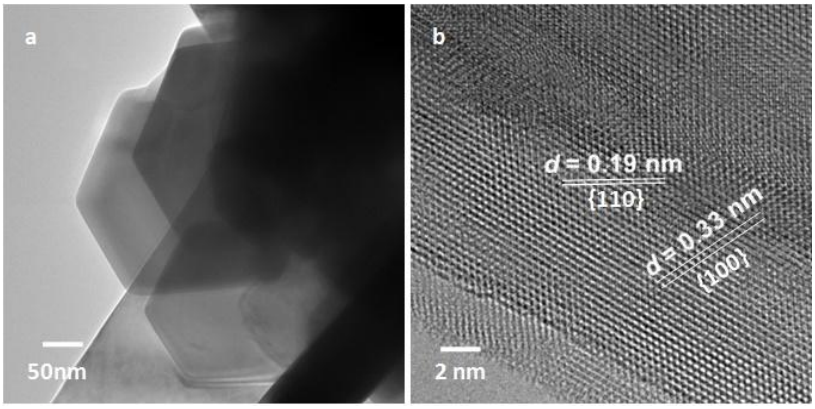

Figure 6.74. TEM image (a), HRTEM image with incident beam from the <001 > direction (b) and Fast Fourier Transform (FFT) pattern of CuS hexagonal plates.

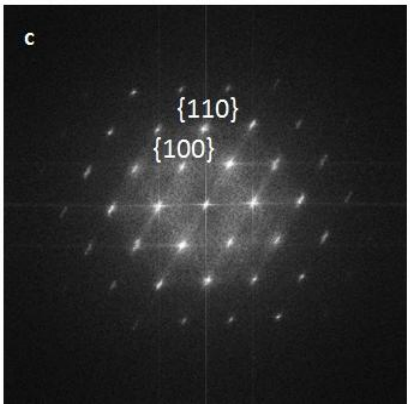

Figure 6.74. TEM image (a), HRTEM image with incident beam from the <001 > direction (b) and Fast Fourier Transform (FFT) pattern (c) of CuS hexagonal plates (Continued).

6.9.2. Characteristic of Reacted Covellite at pH 1

The reacted CuS collected using experiment performed in 100 ppm Hg(II) at 25°C under solution pH 1 was characterized using TEM techniques. **Figure 6.75 (a)** and **(b)** depict the low magnification TEM image of the respective reacted CuS. From the images, it can be seen that the reacted powder is still agglomerated in nature upon the sorption of Hg(II). Nonetheless, it can be observed that there is some growth of distinct rod like morphology on the edges of the initial CuS hexagonal base material. This morphology has been named as nano-needle crystallite from FESEM images and not to mention that it was also correlated to the growth of m-$Hg_3S_2Cl_2$ from PXRD analysis. The high magnification TEM image of this particular nano-needle crystallite is illustrated in **Figure 6.75 (c)**. From the image, it is found that the reacted powder has suffered a loss in the nano-needle morphology in which this is an apparent result of electron beam damage. Thus, this implies that the nano-needle crystallite is very likely to be unstable towards the focus of high density electron flux.

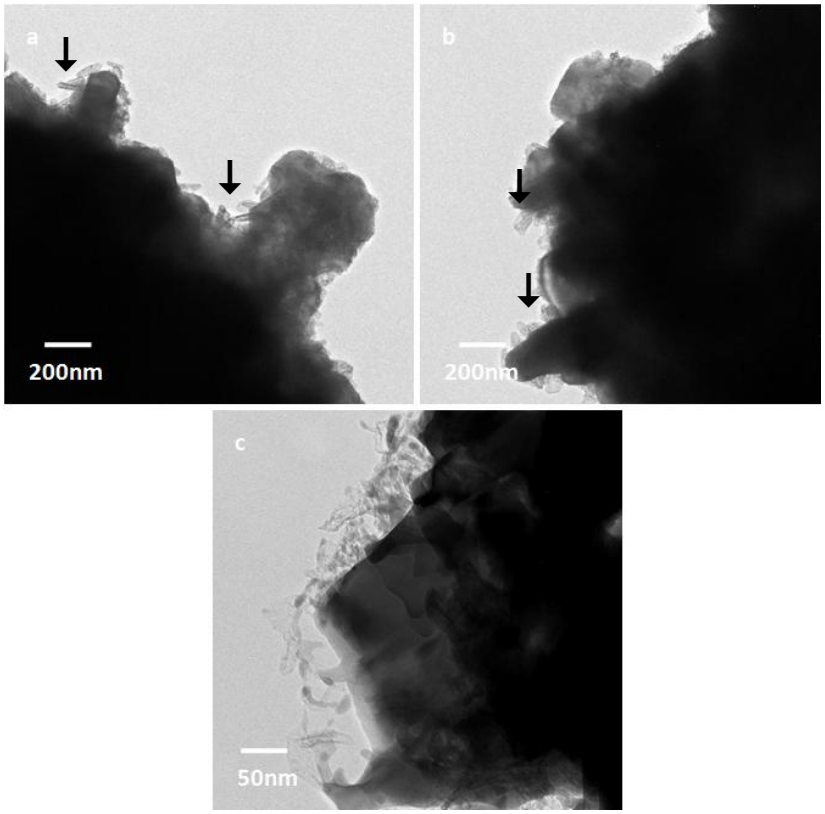

Figure 6.75. Low magnification TEM image 1 (a), low magnification TEM image 2 (b), and high magnification TEM image (c) of reacted CuS at pH 1.
↓ denotes the nano-needle crystallite which damage under the exposure of electron beam.

With the intention to investigate further, a time dependent experiment was also conducted using the low magnification TEM to study the characteristic of these nano-needle crystallites under the exposure of electron beam. **Figure 6.76 (a) – (f)** shows the TEM images of reacted CuS at pH 1 captured at different contact time with constant electron flux. From **Figure 6.76 (a)**, the initial CuS base material is indeed covered by a high amount of nano-needle crystallite. This nano-needle crystallite is mainly dark in color when compared to the initial CuS base material. As the contact time prolonged to 100s, it can be seen that the nano-needle like morphology has disappeared progressively. This observation has eventually verified the unstable nature of nano-needle crystallite under the electron beam. More importantly, the destruction of this nano-needle morphology can also

turn out to be even faster when the image is captured under higher magnification mode of TEM i.e. higher density of electron flux is bombarded onto this specific sample.

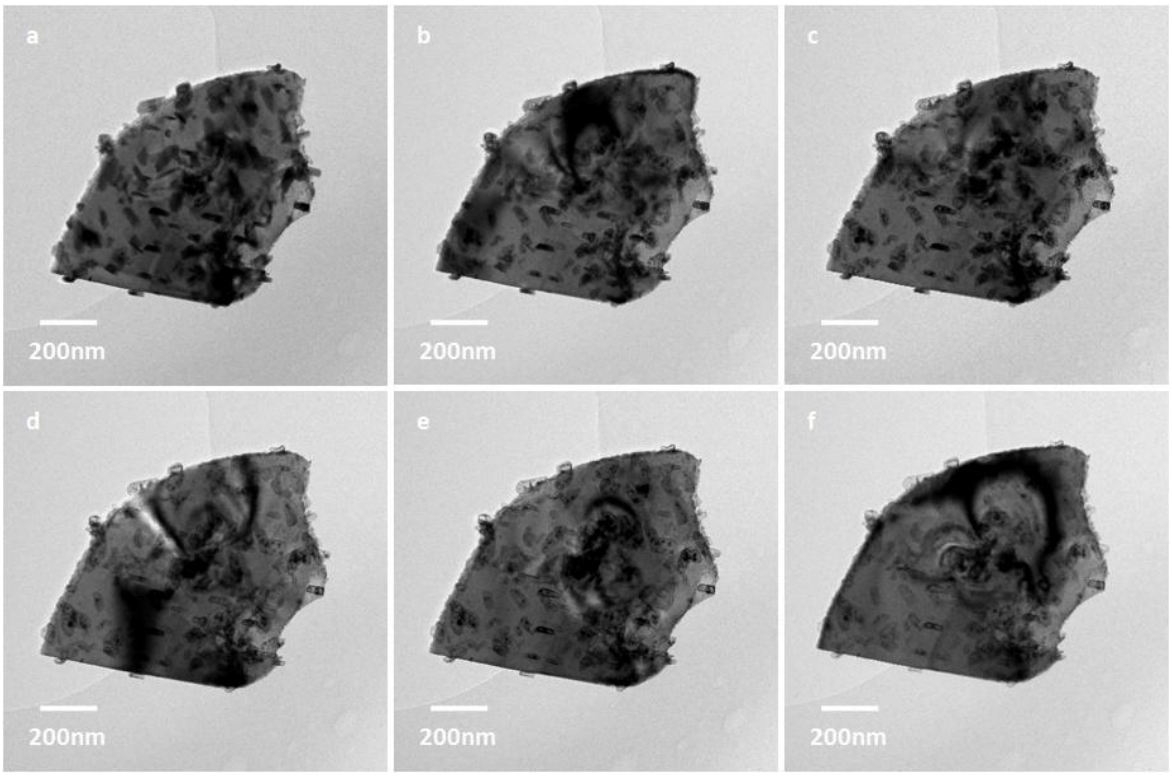

Figure 6.76. Low magnification TEM image of reacted CuS at pH 1 captured at time of (a) 0s, (b) 30s, (c) 45s, (d) 60s, (e) 75s, and (f) 100s.

Although the nano-needle crystallites tend to damage under a long exposure time of electron beam, attempt was also tried to determine their chemical composition using EDX analysis. The EDX analysis has been performed using the elemental mapping technique under the electron gun accelerating voltage of 20kV. The elemental map of reacted pure phase Covellite in 100 ppm Hg(II) under solution pH 1 at temperature of 25°C is illustrated in **Figure 6.77**. From the elemental maps, it can be observed that Cu and S are homogeneously distributed on the initial CuS base material. Nevertheless, the elemental map shows that the Hg is mostly concentrated on the edge region of CuS. The pre-concentration of Hg at the edge region of CuS is due to the outcome of the loss of nano-

needle crystallite during the mapping collection. The destruction of nano-needle crystallites have resulted in some stable leftover mercury compound in which this compound has shrunk and led to the higher Hg concentration being detected at the edge region of CuS.

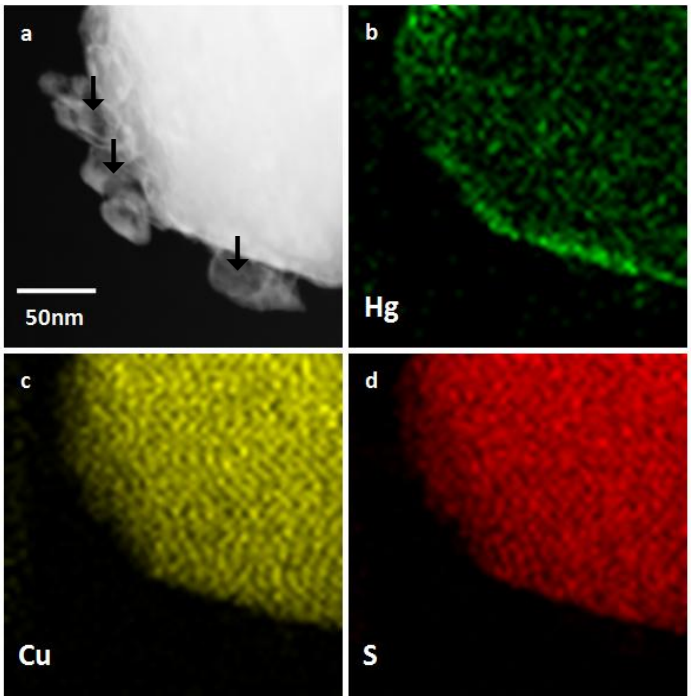

Figure 6.77. EDX mapping of nano-needle crystallite in reacted Covellite under reaction condition of 100 ppm Hg(II)solution, pH 1 at temperature of 25°C.
↓ denotes the nano-needle crystallite which damage under the exposure of electron beam.

Figure 6.78 depicts the HRTEM image of the leftover compound upon the destruction of nano-needle crystallite. From the well resolved 2D lattice fringes of the leftover compound, lattice spacing of 0.34 nm has been identified. It is important to note that the lattice spacing of 0.34 nm measured agrees satisfactorily to the {111} lattice plane of cubic phase mercury sulfide (Metacinnabar, β-HgS). This result strongly suggests that the nano-needle crystallite is the formation of bare $Hg_3S_2Cl_2$ in which it is a reaction product between HgS and $HgCl_2$. The destruction of nano-needle crystallite under the electron beam has finally led to the stable compound of HgS being retained in the reacted CuS while $HgCl_2$ was evaporated to the vacuum during the electron bombardment.

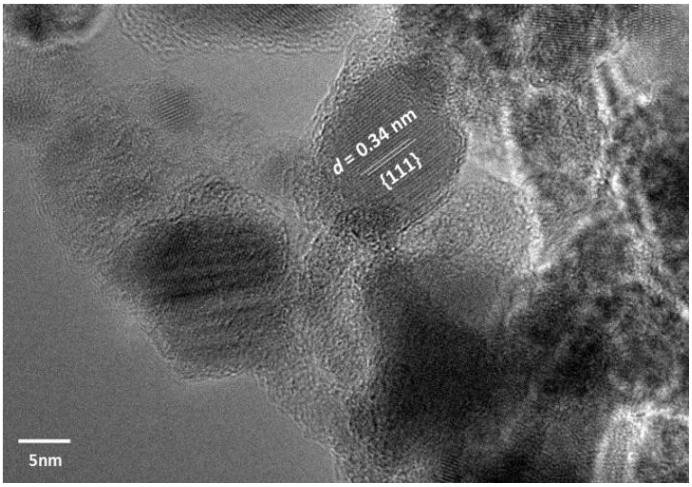

Figure 6.78. HRTEM image of leftover compound upon the destruction of nano-needle crystallite.

6.9.3. Characteristic of Reacted Covellite at pH 9

The reacted CuS collected using experiment performed in 100 ppm Hg(II) at 25°C under solution pH 9 was characterized using TEM technique. **Figure 6.79 (a)** and **(b)** depict the low and high magnification TEM image of the respective reacted CuS. From the images, it is again observed that the reacted powder is still agglomerated in nature upon the sorption of Hg(II). However, it can be identified that the hexagonal base structure of CuS remained. More importantly, a relatively thicker and darker region is also found at the edges of the hexagonal plates. Attempts have been tried in determine the chemical composition of this darker edge region using EDX analysis. The EDX spectra collected under the electron gun accelerating voltage of 20kV for the darker edge and brighter internal hexagonal plate region are illustrated in **Figure 6.79 (b) (i)** and **(ii)** correspondingly. Meanwhile, the elemental map of the combined external and internal hexagonal plate region under the electron gun accelerating voltage of 20kV is depicted in **Figure 6.80**. At the darker edge region, both Cu and S are identified in which it is also followed by a high concentration of Hg. At the brighter internal hexagonal plate side, it can be observed that only Cu and S are found where Hg is considered to be untraceable. Apparently, the darker edge region is the

results of the sorption of Hg(II) onto CuS. Thus, this suggests that the sorption of Hg(II) onto CuS should be started at the outermost edge region of CuS hexagonal plate. This information strongly implies that the higher the edge length of CuS hexagonal plate, the more superior will be for the ability of CuS hexagonal plate in scavenging Hg(II).

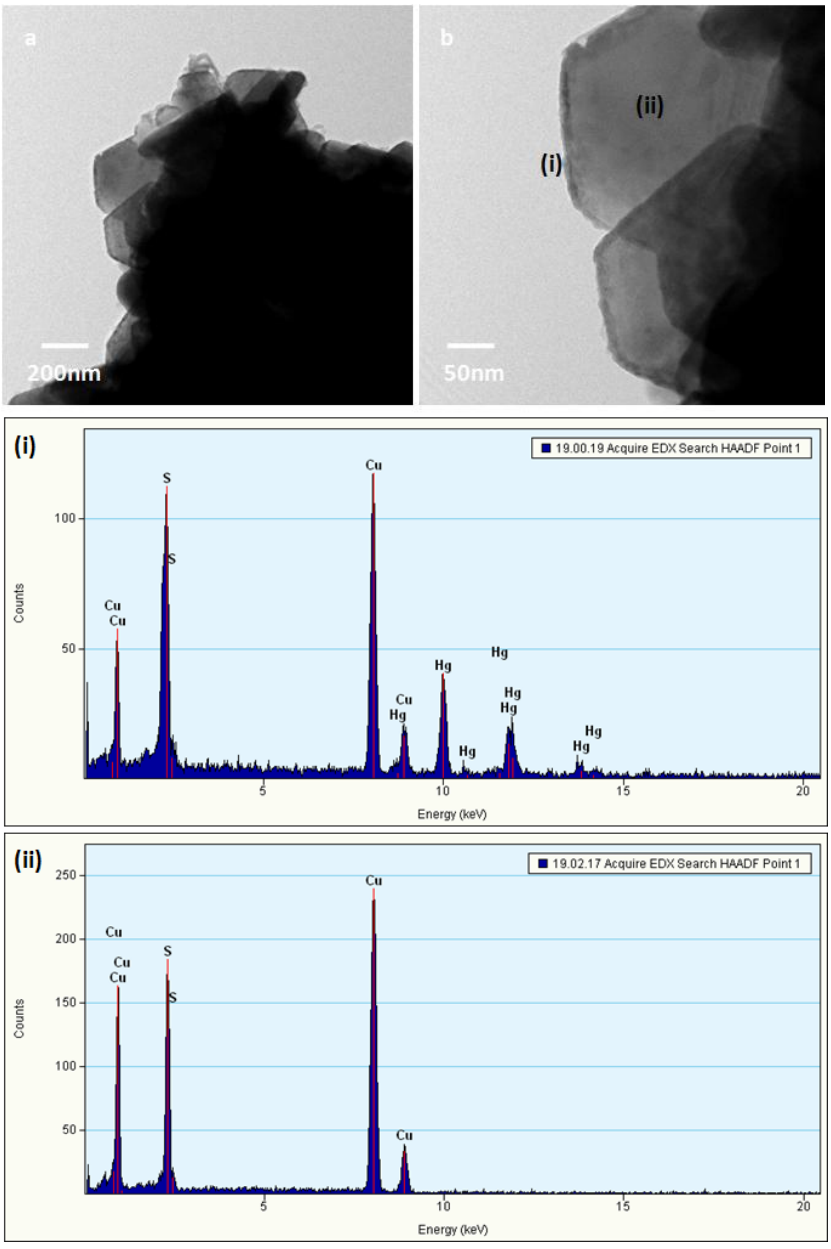

Figure 6.79. Low magnification TEM image (a), high magnification TEM image (b), EDX analysis of darker contrast edge (i) and EDX analysis of brighter contrast region (ii) of reacted CuS in reacted Covellite under reaction condition of 100 ppm Hg(II) solution, pH 9 at temperature of 25°C.

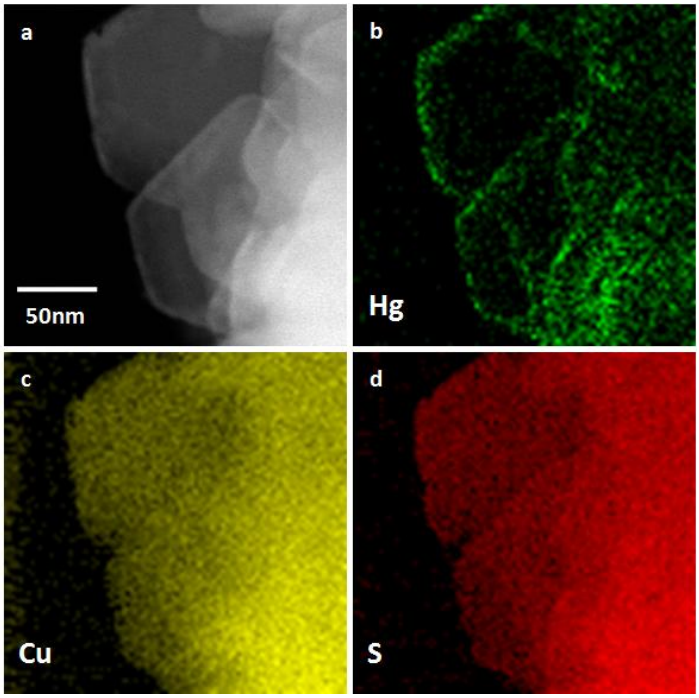

Figure 6.80. EDX mapping of reacted Covellite under reaction condition of 100 ppm Hg(II)solution, pH 9 at temperature of 25°C.

Figure 6.81 depicts the HRTEM image of the darker edge and brighter internal hexagonal plate region. From the well resolved 2D lattice fringes, lattice spacings of 0.24 nm, 0.30 nm and 0.32 nm have been found. However, the lattice spacings identified herein cannot be related well to any lattice plane of HgS, $Hg_3S_2Cl_2$ and even CuS. The mismatch of d-spacing with the reference is believed to be significantly associated to the lattice overlapping between the layered CuS platelet and Hg compounds. Even though the mixing of different lattices in the crystal arrangement has made the analysis become difficult, it is important to note that no growth and destruction of nano-needle crystallite is observed in this sample. This indicates the dark contrast edge region should be composed of HgS where its formation can be evidenced from most of the PXRD pattern collected at pH 9 (**Section 6.6.2**).

In contrast of the selective formation of HgS at the outermost edge relative to the internal region of CuS hexagonal plate, this phenomenon is notably interconnected to

layered structure of CuS shown in **Figure 6.82**. In the atomic arrangement of hexagonal lattice, it was reported that hexagonal metal with a c/a ratio greater than 1.63, surface energy at {101} and {100} surfaces will be 1.5 times greater compared to {001} facets (Matysina, 1999). Similarly, the c/a ratio of CuS is determined to be 4.31 in which an even higher surface energy will be expected at {101} and {100} surfaces (Y. Liu, Qin, Wang, & Cao, 2007). Undoubtedly, higher surface energy at {101} and {100} planes has resulted in a more active surface compared to {001} plane. This has led to an easier intercalation of Hg into the structure of CuS via {101} and {100} plane in relative to {001} plane. Thus, it can be concluded that the sorption of Hg(II) onto CuS should not proceed in such a way by total dissolution of outer CuS region. Instead, the uptake of Hg(II) onto CuS would rather taking place by topotactic exchange reaction of CuS by HgS in which similar observation is in fact observed during the exchange of ZnO by ZnS (X. Huang, et al., 2012).

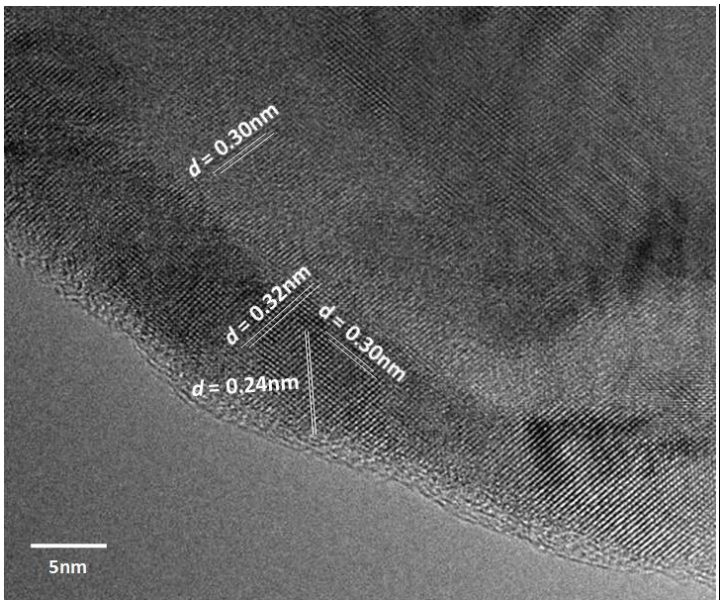

Figure 6.81. HRTEM image of reacted Covellite under reaction condition of 100 ppm Hg(II)solution, pH 9 at temperature of 25°C.

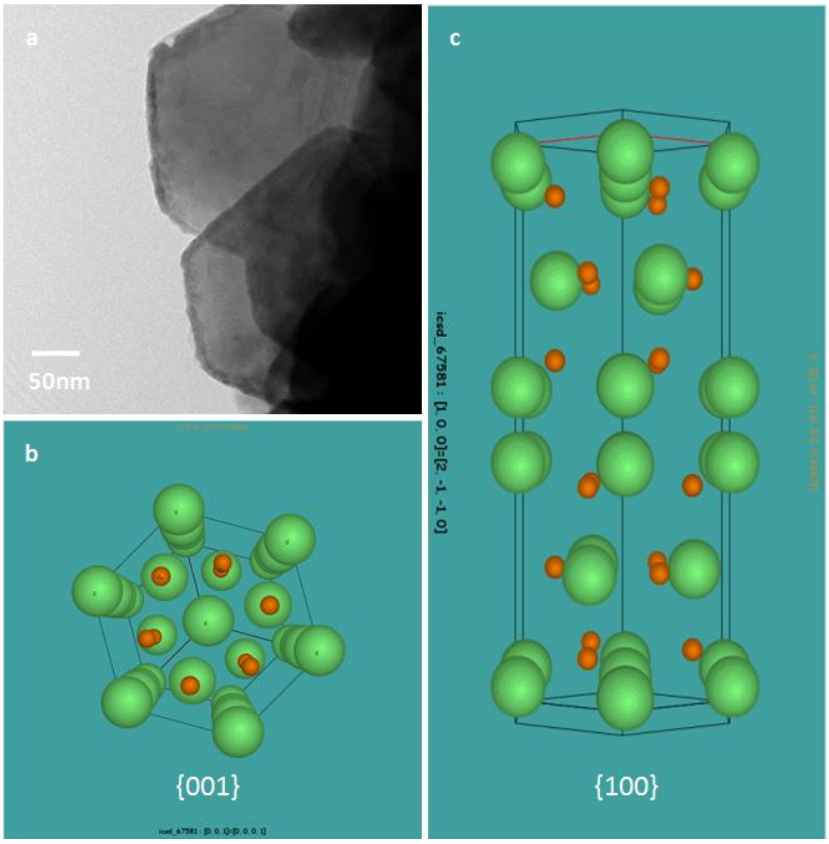

Figure 6.82. High magnification TEM image of reacted Covellite at pH 9 with incident beam from the <001 > direction (a), view of CuS crystal structure from <001 > direction (b) and view of CuS crystal structure from <100> direction (c).

6.10. Summary

From Hg(II) uptake studies, a gradual decrease of the mercury removal with increasing solution pH was observed. The constant decrease of mercury removal with solution pH was confirmed when different concentration of Hg(II) was used in the experiments. On the other hand, the decrease of mercury removal at pH 7 – 9 was also found to be elevated systematically when the experiments were carried out at higher reaction temperature. These observations clearly indicated that the relatively low efficiency of CuS in complexing Hg(II) at pH 7 – 9 in which it can be overcome at high temperature experiments. The mercury uptake trends identified have been discussed using the mercury species present in the solution (mercury speciation diagram). The mercury uptake trends are found to dependent

on the mercury species present in the solution. For example, the relatively high mercury uptake at pH 1 – 6 at 25°C are closely related to $HgCl^+$, HgCl(OH) and $HgCl_2$ species in the solution. Meanwhile, the relatively low mercury uptake at pH 7 – 9 at 25°C is correlated to the sorption of $Hg(OH)_2$ onto CuS in which its sorption can be significantly increased via reaction temperature elevation.

In view of different trends of mercury uptake observed at acidic and alkaline pH, the kinetic studies were further conducted at two different solution pH i.e. pH 1 and 9 under the variation of mercury concentration and solution temperature. From the results, the sorption rate of Hg(II) onto CuS was identified to be faster at pH 1 in contrast to pH 9. In addition, the sorption rate of Hg(II) onto CuS at pH 1 and 9 has significantly increased when the reaction temperature was increased by 10°C. Thus, the inefficient Hg(II) uptake at increasing solution pH can be successfully explained via the different sorption rate of Hg(II) onto CuS at acidic and alkaline pH. The kinetic data was also analyzed using Elovich's kinetic model, Largergren's pseudo first order kinetic model and Ho's pseudo second order kinetic model. In comparison of the three models, it was found that the sorption kinetic data at pH 1 and 9 follows well with Ho's pseudo second order kinetic model with all of the R^2 shown is greater than the nominal value of good fit i.e. 0.9800. This implied that the kinetic order of sorption of Hg(II) onto CuS is two with respect to the number of adsorption site available for the exchange processes. Thus, in order to link the relationship of the kinetic data collected with this model, it is considered that the kinetic order should be two with respect to the overall order for the reaction.

The relatively fast sorption rate of Hg(II) onto CuS at acidic pH can be viewed as the formation of both cubic phase mercury sulfide (Metacinnabar, β-HgS) and monoclinic phase mercuric sulfide chloride or specifically m-$Hg_3S_2Cl_2$ from PXRD analysis. Nonetheless, it is important to note that HgO formation can be also one of the important

pathway that attached Hg(II) onto CuS. Since precipitation of HgO is unreasonable at acidic pH, its formation is believed to be due to the reactions between Hg(II), surface $Cu(OH)_2$ and CuO species which identified from XPS analysis. In addition, the fast rate of sorption of Hg(II) onto CuS at acidic pH can be also accelerated in the presence of H^+. This explained the relative fast sorption rate of Hg(II) onto CuS at acidic pH in contrast to alkaline pH which identified in the kinetic studies.

The relatively slow sorption rate of Hg(II) onto CuS at alkaline pH can be explained by the sole formation of cubic phase mercury sulfide (Metacinnabar, β-HgS) from PXRD analysis. It is important to note that formation of HgO and Hg_2Cl_2 can be also the important pathways that attached Hg(II) onto CuS at pH 9. However, their formation is minor in comparison to the formation of HgS. Furthermore, the slow rate of sorption of Hg(II) onto CuS at alkaline pH can be also due to the competitive adsorption of OH^- onto CuS as well as the lost of CuS surface via the subsequent transformation of CuS to $Cu(OH)_2$ and CuO in the alkaline medium which identified from XPS analysis. This explained the relative slow sorption rate of Hg(II) onto CuS at alkaline pH in contrast to acidic pH which identified in the kinetic studies.

The formation of HgS was also found via the specific S quantification from XPS analysis. The formation of HgS is mainly due to the conversion of active S^- species on CuS surface. From the perspective of morphological changes, a comparatively thicker and darker Hg composing region was found at the edges of the hexagonal plates when looking at the high magnification TEM images. This observation indicates the selective sorption of Hg(II) into the structure of CuS at {101} and {100} plane in relative to {001} plane. Thus, it can be concluded that the sorption of Hg(II) onto CuS should not proceed in a such way by total dissolution of outer CuS region. Instead, the uptake of Hg(II) onto CuS at alkaline pH would rather taking place by topotactic exchange reaction of CuS by HgS.

Nonetheless, a great attention is given to m-$Hg_3S_2Cl_2$ because its PXRD pattern matches well with the PXRD pattern of monoclinic phase $Hg_3S_2Br_2$ in preference to the PXRD pattern of cubic phase $Hg_3S_2Cl_2$. The formation of m-$Hg_3S_2Cl_2$ was also shown to decrease progressively as solution pH increases. The formation of $Hg_3S_2Cl_2$ is also identified by the XPS peak de-convolution studies of reacted mixed phase and pure phase Covellite. Thus, this strongly indicated the formation of monoclinic phase $Hg_3S_2Cl_2$ rather than the conventional cubic phase $Hg_3S_2Cl_2$ which reported in the powder diffraction file (PDF) database. From the perspective of morphological changes, the formation of m-$Hg_3S_2Cl_2$ is associated by the appearance of nanosize ranged needle like architecture namely nano-needle crystallite. This nano-needle crystallite was observed to grow on the edges of initial hexagonal plates from FESEM and TEM analysis. However, it was also found that this nano-needle crystallites was unstable towards the electron beam during the EDX analysis. The destruction of nano-needle crystallites have resulted in stable leftover HgS compound shrunk and led to the higher Hg concentration being detected at the edge region of CuS.

Apart from the Hg(II) uptake studies, a consecutive decrease of copper dissolution and final solution pH has been also detected when initial solution pH is raised. The trend of Cu(II) leaching and final solution pH changes was further confirmed when the experiments were performed at higher reaction temperature. The results significantly suggests that an in-situ re-adsorption of Cu(II) and adsorption of OH^- onto the CuS has taken place at increasing pH in addition to the ion-exchange sorption of Hg(II) onto CuS. The re-adsorption of Cu(II) and OH^- can be viewed as the precipitation of copper sulfate hydroxide, $Cu_4(SO_4)(OH)_6$ and its hydrate $Cu_4(SO_4)(OH)_6(H_2O)$ from PXRD analysis. Whilst, the re-adsorption of Cu(II) and OH^- can be also discussed in term of the formation of $Cu(OH)_2$ and CuO from XPS studies. Furthermore, the precipitation of $Cu_4(SO_4)(OH)_6$ and

$Cu_4(SO_4)(OH)_6(H_2O)$ has actually led to the growth of additional platelet crystallite in which it has been identified from FESEM-EDX analysis.

The loading of Hg(II) onto CuS were also modeled using sorption isotherm models. From the analysis, the fitting of sorption data shows poor R^2 value with Freundlich model. Whilst, the fitting follows well with Langmuir model regardless of solution temperature applied. These results strongly suggested that the experimental data agrees well with the Langmuir isotherm, assuming that all of the sorption sites on CuS are energetically identical in which only one Hg(II) can accommodate one specific sorption site, resulting single monolayer sorption occurs on CuS surface (Langmuir, 1916, 1917, 1918). The maximum loading of Hg(II) onto CuS upon complete saturation, Q_{max} is found to be 434.78 mg Hg(II) / g of sorbent at 25°C.

Presuming that monolayer sorption coverage occurred during the sorption of Hg(II) onto CuS, the value on the Langmuir maximum sorption capacity, Q_{max} has been used in calculating the specific surface area, $S_{specific}$ of CuS at different reaction temperature. From the analysis, the Langmuir monolayer sorption isotherm gives bigger value than the BET multilayer sorption isotherm. This observation is thought of uncommon since surface area calculated from BET multilayer isotherm would always give higher surface area than Langmuir monolayer isotherm. From FESEM analysis, an additional formation of nano-needle crystallite has actually detected to grow on the initial CuS hexagonal plate morphology. Apparently, the growth of these nano-needle crystallites can notably increase the overall surface area of reacted CuS when compared to the unreacted CuS. Thus, the formation of additional morphology in the CuS has explained the discrepancy of surface area calculated using BET and Langmuir approach.

In addition, it was found that the maximum sorption capacity of CuS in removing Hg(II) is notably high when compared to metal oxide, metal sulfide and other sorbent

materials studied in the literature. From the findings, it is observed that high surface area materials like activated carbon, silica and their derivatives do not correlate well with the high sorption capacity in adsorbing Hg(II). On the contrary, it is recognized that only those material that are functionalized with thiourea, sulfur or sulfide will have high affinity towards Hg(II) immobilization even if the surface area is not high in the system. This phenomenon is in good agreement with the hard soft acid base theory proposed by Pearson et. al. (Pearson, 1963) in which the soft acid, Hg(II) tends to interact well with soft base, S in any reaction. Furthermore, the sorption of Hg(II) onto CuS is spontaneous and its favourability increases with reaction temperature elevation in which it can be seen from the isotherm shape factor and Gibb's free energy analysis. Thus, it is apparent that CuS is an effective sorbent material in scavenging Hg(II) with astounding maximum sorption capacity of 434.78 mg/g despite of the low surface area possessed on its hexagonal shape morphology found from FESEM analysis.

CHAPTER 7

CONCLUSION AND FUTURE WORK RECOMMENDATIONS

7.1. Conclusion

In response to the worldwide mercury contamination contributed by both natural and anthropogenic sources, two different domains of aqueous mercury complexation have been carried out using homogeneous complexing agent, Rhodamine B and heterogeneous complexing agent, Covellite (CuS). These studies are foremost important as it provides the understanding and insights of these mercury complexing systems for their potential ability in mitigating aqueous mercury pollution.

The studies on homogeneous mercury complexation with the use of Rhodamine B and iodide suggested two different type of mercury detection technique via UV-Vis spectroscopy can be developed. The first technique is related to the extraction of Rhodamine B-Hg(II)-Iodide complex in organic solvent *i.e.* benzene. This technique gives molar absorptivity, ϵ, 17.68×10^4 l $mole^{-1}cm^{-1}$ and L.O.D = 5 μg / 20 ml = 0.25 ppm of Hg(II). The second technique is associated to the stabilization of Rhodamine B-Hg(II)-Iodide complex in water using protective colloid polymer i.e PVAl. This technique gives a lower absorptivity, ϵ, 16.84×10^3 $lmole^{-1}cm^{-1}$ and L.O.D = 10 μg / 10 ml = 1 ppm of Hg(II). Both of techniques developed have provided a non-destructive approach for trace Hg(II) determination.

For heterogeneous mercury complexation, studies were conducted initially using heavily oxidized Covellite *i.e.* mixed phase Covellite. From Hg(II) uptake assessment, it was identified that mixed phase Covellite exhibit the same Hg(II) uptake behavior as in the case of phase pure Covellite. Firstly, a steady decrease of mercury uptake with increasing

solution pH was found when Hg(II) concentration is elevated. Secondly, the sorption kinetic studies shows that the data tend to fit well with Ho's pseudo second-order kinetic model. Thirdly, the equilibrium data follows well with the Langmuir isotherm in which the monolayer coverage of Hg(II) is found to be ≈416.67 mg Hg(II) / g of sorbent. All these finding confirmed that heavily oxidized CuS *i.e.* mixed phase Covellite possessed similar mercury uptake activity when compared to pure phase Covellite. From PXRD and surface sensitive XPS analysis, the dissolution of oxidized $CuSO_4$ phase has been detected in the reacted mixed phase Covellite. This suggested that the dissolution of $CuSO_4$ layer has re-activated the CuS surface for aqueous Hg(II) uptake. Thus, the oxidation of pure phase CuS to 67% CuS and 33% $CuSO_4$ will not result in any significant performance declination in aqueous Hg(II) uptake.

From the studies of pure phase CuS, both solution and solid phase analysis has provided detail insights on the occurring reactions upon the sorption of Hg(II) onto CuS at acidic and alkaline condition. From the analysis conducted, the main sorption mechanism of Hg(II) onto CuS at acidic pH can be deduced as below:

$$CuS + HgCl_2 \leftrightarrow HgS + CuCl_2 \quad (7.01)$$

$$2HgS + HgCl_2 \leftrightarrow Hg_3S_2Cl_2 \quad (7.02)$$

and overall reaction:

$$CuS + HgS + 2HgCl_2 \leftrightarrow Hg_3S_2Cl_2 + CuCl_2 \quad (7.03)$$

It can be observed that Equation 7.03 has shown the ion-exchange behavior of CuS towards $HgCl_2$. This has led to the soluble Cu^{2+}, HgS and $Hg_3S_2Cl_2$ being detected in the solution

and solid powder respectively. According to HSABT, Hg and S are soft acid and base whereas Cu is borderline acid. The interaction between CuS and $HgCl_2$ would be preferred. A fast step should be occurred between the reaction between CuS and $HgCl_2$. Thus, it is deduced that the second step (Equation 7.02) is the slow step (rate determining step). The overall rate equation that governed the sorption of Hg(II) at acidic medium would then be:

$$\text{Rate} = k_2[HgCl_2][HgS] \quad (7.04)$$

in which the rate equation is a second order kinetic. This is consistent to the pseudo second order rate law that determined earlier. It is important to note that HgO formation can be also one of the important pathway that attached Hg(II) onto CuS at pH 1. Its formation is believed to be due to the reactions between Hg(II), surface $Cu(OH)_2$ and CuO species. In addition, the fast rate of sorption of Hg(II) onto CuS at acidic pH can be also accelerated in the presence of H^+. This has explained the relative fast sorption rate of Hg(II) onto CuS at acidic pH in contrast to alkaline pH which identified in the kinetic studies earlier.

At alkaline pH, the dominant Hg(II) species present is $Hg(OH)_2$. Thus, the elementary steps that made up the main reactions at alkaline pH should be:

$$CuS + Hg(OH)_2 \leftrightarrow CuS\text{-}Hg(OH)_2 \quad (7.05)$$

$$CuS\text{-}Hg(OH)_2 \leftrightarrow HgS + Cu(OH)_2 \quad (7.06)$$

and overall reaction:

$$CuS + Hg(OH)_2 \leftrightarrow HgS + Cu(OH)_2 \quad (7.07)$$

It can be observed that Equation 7.07 have demonstrated the ion-exchange behavior of CuS towards initial Hg(II). This has resulted in the formation of HgS and $Cu(OH)_2$ being detected in the solid powder. According to HSABT, Hg and S are soft acid and base whereas Cu is borderline acid. The interaction between CuS and $Hg(OH)_2$ would be preferred. Nevertheless, the presence of negatively charged OH^- group has hindered the reaction. A correct orientation of CuS-$Hg(OH)_2$ instead of CuS-$O(O_2H)Hg$ must occur for successful reaction. Thus, it is deduced that the interaction between CuS and $Hg(OH)_2$ (Equation 7.05) would be the slow step (rate determining step). The overall rate equation that governed the sorption of Hg(II) at alkaline medium would then be:

$$\text{Rate} = k_2[\text{CuS}][\text{Hg(OH)}_2] \qquad (7.08)$$

in which the rate equation is a second order kinetic. This is consistent to the pseudo second order rate law that determined earlier. It is important to note that HgO and Hg_2Cl_2 formation can be also the pathways that attached mercury onto CuS at pH 9. However, their formation is believed to be minor in comparison to the mechanism above since they are only detected on the CuS surface. Furthermore, the slow rate of sorption of Hg(II) onto CuS at alkaline pH can be also due to the competitive adsorption of OH^- onto CuS as well as the lost of CuS surface via the subsequent transformation of CuS to $Cu(OH)_2$ and CuO in the alkaline medium. This has explained the relative slow sorption rate of Hg(II) onto CuS at alkaline pH in contrast to acidic pH which identified in the kinetic studies earlier.

Beside the Hg(II) uptake studies, a consecutive decrease of copper dissolution and final solution pH has been also detected when initial solution pH is raised. The trend of Cu(II) leaching and final solution pH changes was further confirmed when the experiments were performed at higher reaction temperature. The results significantly suggests that an in-

situ re-adsorption of Cu(II) and adsorption of OH^- onto the CuS has taken place at increasing pH in addition to the ion-exchange sorption of Hg(II) onto CuS. The re-adsorption of Cu(II) and OH^- can be viewed as the precipitation of copper sulfate hydroxide, $Cu_4(SO_4)(OH)_6$ and its hydrate $Cu_4(SO_4)(OH)_6(H_2O)$ from PXRD analysis. Whilst, the re-adsorption of Cu(II) and OH^- can be also discussed in term of the formation of $Cu(OH)_2$ and CuO from XPS studies. Furthermore, the precipitation of $Cu_4(SO_4)(OH)_6$ and $Cu_4(SO_4)(OH)_6(H_2O)$ has actually led to the growth of additional platelet crystallite in which it has been identified from FESEM-EDX analysis.

In a nutshell, it is concluded that the CuS is a powerful sorbent for Hg(II) at a wide range of pH. Even present in its oxidized form, the dissolution of SO_3 and SO_4 layer on CuS surface is possible upon in contact with water. CuS can be classified as a sacrificial mercury immobilizer due to its ion-exchange behavior for Hg(II) which led to leaching of Cu(II) in return. The leaching of Cu(II) into the water system seems to be another environmental treat that harmful to the ecosystems. However, the drawback is that Hg(II) is more toxic than Cu(II). The sorption of Hg(II) onto CuS can also lead to the formation of HgS in which it is the most stable sulfide compound in the environment. HgS is eventually acting as the long term sink for all form of mercury owing to its resistance towards weathering in any condition. Furthermore, it was also confirmed that HgS is working as a secondary adsorbent which further adsorb $HgCl_2$ to form the double salt, $Hg_3S_2Cl_2$. Therefore, it is apparent that the pros are more than the con for the use of CuS in treating the mercury pollution issue. Last but not least, it recommended that CuS can be applied in a controlled manner. This will ensure a more ecosystem friendly CuS as mercury scavenger where the amount of Cu(II) leached into the environment can be reduced to minimal.

7.2. Future Work Recommendations

The studies on both homogeneous and heterogeneous aqueous mercury complexation with Rhodamine B and Covelite respectively have provided us with the understanding on the limitation of both systems when employed in the water stream. Apparently, heterogeneous mercury complexing agent offered a better solution for mercury mitigation owing to its easier separation; superior mercury immobilization ability; as well as its potential source for mercury sink in the environment. Nonetheless, several suggestions and recommendation should be noteworthy for further development of Covellite. The first issue is related to the low surface area properties of Covellite used. Most of the copper sulfides synthesized were of low surface area in contrast to other porous materials like zeolite, carbons, and etc. However, modifications can be made to achieve higher surface area by reducing particle size of the synthesized material at nano-sized range. This can be achieved by surfactant assisted template synthesis in which a more aligned, less agglomerated distribution of particles can be produced. Besides that, the desired material can also be prepared through precipitation method by controlling the synthesis parameters which include reaction temperature, pH, aging, and so on.

The second issue is to the role of supported Covellite system. In the synthesis of Covellite, the large surface area material *i.e.* zeolite, silica, carbon, chitosan and etc can be implemented to decrease the particle agglomeration and thus increase the surface area of the resulting Covellite. Apart from that, the support can also acts as a adsorbent for Hg(II), Cu(II) as well as other contaminant. This can be seen from the case of carbon, silica and chitosan where their adsorbing ability has been proven in the literature. From the economical perspective, the cost in synthesizing support material is notably cheaper than the cost in preparing active Covellite. Therefore, the manufacture cost of supported

Covellite system in large scale can be significantly reduced as the amount of active material required is lowered.

On the other hand, the studies on Covellite and supported Covellite system should be also extended to condensate or particularly mercury in petroleum. It is because mercury in oil and gas has a direct negative impact on petroleum processes. The consequences of mercury in feeds on processing systems include equipment degradation, toxic waste generation, increased risk to the health and safety of workers as well as poisoning of catalysts. Thus, mercury in plant feeds often requires process modifications to avoid the negative consequences and to comply with product specifications. Since the sorption of aqueous Hg(II) onto Covellite can lead to the formation stable HgS and the stable HgS can actually become a secondary adsorbent for Hg. This suggested that Covellite and supported Covellite system can also be used to treat mercury issue in oil and gas industry. Nevertheless, the studies of Covellite and supported Covellite system will still in need of the collaboration from the related oil and gas companies. The design of real-life pilot plant should be conducted in order to assess the efficiency of the prototype system and thus it can be widely employed in the industries.

REFERENCES

Abbaslou, P., & Zaman, T. (2006). A child with elemental mercury poisoning and unusual brain MRI findings. *Clinical Toxicology, 44*(1), 85-88.

ACEPT Group. (2005). X-Ray Emission: Earth, Moon, and Mars. Retrieved 22 Jan 2014, from http://www.asu.edu/courses/phs208/patternsbb/PiN/rdg/pixe/pixe.shtml

Aguado, J., Arsuaga, J. M., & Arencibia, A. (2008). Influence of synthesis conditions on mercury adsorption capacity of propylthiol functionalized SBA-15 obtained by co-condensation. *Microporous and Mesoporous Materials, 109*(1), 513-524.

Aguado, M. A., Cervera-March, S., & Giménez, J. (1995). Continuous photocatalytic treatment of mercury(II) on titania powders. Kinetics and catalyst activity. *Chemical Engineering Science, 50*(10), 1561-1569.

Aharoni, C., & Tompkins, F. C. (1970). Kinetics of adsorption and desorption and the Elovich equation. In D. D. Eley, H. Pines & P. B. Weisz (Eds.), *Advances in catalysis and related subjects* (Vol. 21, pp. 1-49). New York: Academic Press (Elsevier).

Ahmadpour, A., & Do, D. (1996). The preparation of active carbons from coal by chemical and physical activation. *Carbon, 34*(4), 471-479.

Al Rmalli, S. W., Dahmani, A. A., Abuein, M. M., & Gleza, A. A. (2008). Biosorption of mercury from aqueous solutions by powdered leaves of castor tree (Ricinus communis L.). *Journal of Hazardous Materials, 152*(3), 955-959.

Alfassi, Z. B. (1990). *CRC Activation Analysis*: CRC PressINC.

Almeida, I. L. S., & Coelho, N. v. M. M. (2012). Direct Determination of Inorganic Mercury in Ethanol Fuel by Cold Vapor Atomic Absorption Spectrometry. *Energy & Fuels, 26*(9), 6003-6007.

Anoop Krishnan, K., & Anirudhan, T. (2002). Removal of mercury (II) from aqueous solutions and chlor-alkali industry effluent by steam activated and sulphurised activated carbons prepared from bagasse pith: kinetics and equilibrium studies. *Journal of hazardous materials, 92*(2), 161-183.

Aranda, P. R., Colombo, L., Perino, E., De Vito, I. E., & Raba, J. (2013). Solid‐phase preconcentration and determination of mercury (II) using activated carbon in drinking water by X‐ray fluorescence spectrometry. *X‐Ray Spectrometry, 42*(2), 100-104.

Arbeloa, I. L., & Ojeda, P. R. (1981). Molecular forms of Rhodamine B. *Chemical Physics Letters, 79*(2), 347-350.

Arencibia, A., Aguado, J., & Arsuaga, J. M. (2010). Regeneration of thiol-functionalized mesostructured silica adsorbents of mercury. *Applied Surface Science, 256*(17), 5453-5457.

Atkins, P., & De Paula, J. (2010). *Atkins' physical chemistry* (7th ed.): Oxford University Press.

Avino, P., Capannesi, G., Renzi, L., & Rosada, A. (2013). Instrumental neutron activation analysis and statistical approach for determining baseline values of essential and toxic elements in hairs of high school students. *Ecotoxicology and Environmental Safety*.

Baba, Y., Matsumura, N., Shiomori, K., & Kawano, Y. (1998). Selective adsorption of mercury (II) on Chitosan derivatives from hydrochloric acid. *Analytical Sciences, 14*(4), 687-690.

Bach, R. D., & Vardhan, H. B. (1986). A mercury-199 NMR study of the complexation of methylmercury with thia-crown ethers. The absence of a macrocyclic ligand effect. *The Journal of Organic Chemistry, 51*(9), 1609-1610.

Barriada, J. L., Herrero, R., Prada-Rodríguez, D., & Sastre de Vicente, M. E. (2008). Interaction of mercury with chitin: A physicochemical study of metal binding by a natural biopolymer. *Reactive and Functional Polymers, 68*(12), 1609-1618.

Bartolome, J., Whitmore, W. L., & Slotkin, T. A. (1984). Effects of neonatal mercuric chloride administration on growth and biochemical development of neuronal and non-neuronal tissues in the rat: comparison with methylmercury. *Toxicology letters, 22*(1), 101-111.

Baumann, T. F., Reynolds, J. G., & Fox, G. A. (2000). Polymer pendant crown thioethers: synthesis, characterization and Hg^{2+} extraction studies of polymer-supported thiacrowns ([14]aneS_4 and [17]aneS_5). *Reactive and Functional Polymers, 44*(2), 111-120.

Beck, C., Krafchik, B., Traubici, J., & Jacobson, S. (2004). Mercury intoxication: it still exists. *Pediatric dermatology, 21*(3), 254-259.

Beer. (1852). Bestimmung der Absorption des rothen Lichts in farbigen Flüssigkeiten. *Annalen der Physik, 162*(5), 78-88.

Bergdahl, I. A., Schutz, A., & Hansson, G.-A. (1995). Automated determination of inorganic mercury in blood after sulfuric acid treatment using cold vapour atomic absorption spectrometry and an inductively heated gold trap. *Analyst, 120*(4), 1205-1209.

Bhakta, J. N., & Munekage, Y. (2011). Mercury(II) adsorption onto the magnesium oxide impregnated volcanic ash soil derived ceramic from aqueous phase. *International Journal of Environmental Research, 5*(3), 585-594.

Biester, H., Schuhmacher, P., & Müller, G. (2000). Effectiveness of mossy tin filters to remove mercury from aqueous solution by Hg(II) reduction and Hg(0) amalgamation. *Water Research, 34*(7), 2031-2036.

Bijoor, S. (2008). Scanning Electron Microscopy. Retrieved 22 Jan 2014, from http://large.stanford.edu/courses/2007/ap273/bijoor1/

Birk, J. P. (2001). Chapter 17: Additional aspects of aqueous equilibria. *Complex Ion Equilibria* Retrieved 22 Jan 2014, from http://www.public.asu.edu/~jpbirk/CHM-115_BLB/Chpt17/sld037.htm

Biyum, I. A., & Pavlova, N. N. (1963). *Zavodskaya Laboratoriya, 29*, 1407.

Blanchard, G., Maunaye, M., & Martin, G. (1984). Removal of heavy metals from waters by means of natural zeolites. *Water Research, 18*(12), 1501-1507.

Boca Raton, F. (Ed.). (1997). *Neurotoxicity of Methylmercury: Minamata and the Amazon*: CRC Press.

Botta, S. G., Rodríguez, D. J., Leyva, A. G., & Litter, M. I. (2002). Features of the transformation of HgII by heterogeneous photocatalysis over TiO2. *Catalysis Today, 76*(2–4), 247-258.

Bower, J., Savage, K. S., Weinman, B., Barnett, M. O., Hamilton, W. P., & Harper, W. F. (2008). Immobilization of mercury by pyrite (FeS2). *Environmental Pollution, 156*(2), 504-514.

Bratzel Jr, M. P., Dagnall, R. M., & Winefordner, J. D. (1969). A New, simple atom reservoir for atomic fluorescence spectrometry. *Analytica Chimica Acta, 48*(2), 197-203.

Brown, G. E., Henrich, V. E., Casey, W. H., Clark, D. L., Eggleston, C., Felmy, A., et al. (1998). Metal Oxide Surfaces and Their Interactions with Aqueous Solutions and Microbial Organisms. *Chemical Reviews, 99*(1), 77-174.

Brundle, C. R., Evans, C. A., & Wilson, S. (1992). *Encyclopedia of materials characterization: Surfaces, interfaces, thin films*: Butterworth-Heinemann.

Buijs, K., & Maurice, M. J. (1969). Some considerations on apparent deviations from lambert-beer's law. *Analytica Chimica Acta, 47*(3), 469-474.

Bussi, J., Ohanian, M., Vázquez, M., & Dalchiele, E. (2002). Photocatalytic Removal of Hg from Solid Wastes of Chlor-Alkali Plant. *Journal of Environmental Engineering, 128*(8), 733-739.

Cardenas, G., Orlando, P., & Edelio, T. (2001). Synthesis and applications of chitosan mercaptanes as heavy metal retention agent. *International Journal of Biological Macromolecules, 28*(2), 167-174.

Cardona, M., & Ley, L. (1978). *Photoemission in Solids I: General Principles*: Springer-Verlag.

Červený, V., Horváth, M., & Broekaert, J. A. (2012). Determination Of Mercury In Water Samples By Electrochemical Cold Vapor Generation Coupled To Microstrip Microwave Induced Helium Plasma Optical Emission Spectrometry. *Microchemical Journal*.

Charlton, D. S., Harju, J. A., Stepan, D. J., Kühnel, V., Schmit, C. R., Butler, R. D., et al. (Eds.). (1994). *Mercury Pollution: Integration and Synthesis*. Chelsea, M. I.: Lewis Publishers.

Chen, Y.-M., Yu, C.-J., Cheng, T.-L., & Tseng, W.-L. (2008). Colorimetric detection of lysozyme based on electrostatic interaction with human serum albumin-modified gold nanoparticles. *Langmuir, 24*(7), 3654-3660.

Chien, S., & Clayton, W. (1980). Application of Elovich equation to the kinetics of phosphate release and sorption in soils. *Soil Science Society of America Journal, 44*(2), 265-268.

Choi, M., & Jang, J. (2008). Heavy metal ion adsorption onto polypyrrole-impregnated porous carbon. *Journal of colloid and interface science, 325*(1), 287-289.

Choi, S.-C., Chase, T., & Bartha, R. (1994). Enzymatic catalysis of mercury methylation by Desulfovibrio desulfuricans LS. *Applied and Environmental Microbiology, 60*(4), 1342-1346.

Chojnacki, A., Chojnacka, K., Hoffmann, J., & Gorecki, H. (2004). The application of natural zeolites for mercury removal: from laboratory tests to industrial scale. *Minerals Engineering, 17*(7), 933-937.

Christian, G. D. (2003). *Analytical chemistry* (Sixth ed.): Wiley.

Chrysochoou, C., Rutishauser, C., Rauber-Lüthy, C., Neuhaus, T., Boltshauser, E., & Superti-Furga, A. (2003). An 11-month-old boy with psychomotor regression and auto-aggressive behaviour. *European Journal of Pediatrics, 162*(7), 559-561.

Coles, C. A., Rao, S. R., & Yong, R. N. (2000). Lead and cadmium interactions with mackinawite: retention mechanisms and the role of pH. *Environmental Science & Technology, 34*(6), 996-1000.

Crini, G. (2005). Recent developments in polysaccharide-based materials used as adsorbents in wastewater treatment. *Progress in polymer science, 30*(1), 38-70.

Dabrowski, A. (2001). Adsorption-from theory to practice. *Advances in Colloid and Interface Science, 93*(1-3), 135-224.

Dagnall, R., Thompson, K., & West, T. (1967). Studies in atomic-fluorescence spectroscopy—IV: The atomic-fluorescence spectroscopic determination of selenium and tellurium. *Talanta, 14*(5), 557-563.

Dams, R. (1992). Nuclear activation techniques for the determination of trace elements in atmospheric aerosols, particulates and sludge samples. *Pure Appl. Chem, 64*(7), 991-1014.

Danielsson, B., Fredriksson, A., Dahlgren, L., Gårdlund, A., Olsson, L., Dencker, L., et al. (1993). Behavioural effects of prenatal metallic mercury inhalation exposure in rats. *Neurotoxicology and teratology, 15*(6), 391-396.

De, A., & Pal, B. (1979). Extractive spectrophotometric determination of microgram amounts of mercury as a ternary complex with iodide and a triphenylmethane dye. *Microchimica Acta, 72*(3-4), 201-205.

de Bruyn, P. L., & Agar, G. E. (1962). *Froth flotation 50th anniversary volume*: American Institute of Mining, Metallurgical, and Petroleum Engineers.

De Canck, E., Lapeire, L., De Clercq, J., Verpoort, F., & Van Der Voort, P. (2010). New ultrastable mesoporous adsorbent for the removal of mercury ions. *Langmuir, 26*(12), 10076-10083.

Dias, J. M., Alvim-Ferraz, M., Almeida, M. F., Rivera-Utrilla, J., & Sánchez-Polo, M. (2007). Waste materials for activated carbon preparation and its use in aqueous-phase treatment: A review. *Journal of Environmental Management, 85*(4), 833-846.

Domínguez, M. A., Grünhut, M., Pistonesi, M. F., Di Nezio, M. a. S., & Centurión, M. a. E. (2012). Automatic flow-batch system for cold vapor atomic absorption spectroscopy determination of mercury in honey from argentina using online sample treatment. *Journal of Agricultural and Food Chemistry, 60*(19), 4812-4817.

Dou, B., & Chen, H. (2011). Removal of toxic mercury(II) from aquatic solutions by synthesized TiO2 nanoparticles. *Desalination, 269*(1–3), 260-265.

Drake, M. (2012). Brief introduction to the electron microprobe. Retrieved 22 Jan 2014, from http://pirlwww.lpl.arizona.edu/~domanik/UA_Microprobe/Intro.html

Dujardin, M. C., Cazé, C., & Vroman, I. (2000). Ion-exchange resins bearing thiol groups to remove mercury. Part 1: Synthesis and use of polymers prepared from thioester supported resin. *Reactive and Functional Polymers, 43*(1), 123-132.

Ehmann, W. D., & Vance, D. E. (1991). *Radiochemistry and nuclear methods of analysis*. New York: Wiley.

El-Shafey, E. I. (2010). Removal of Zn(II) and Hg(II) from aqueous solution on a carbonaceous sorbent chemically prepared from rice husk. *Journal of hazardous materials, 175*(1–3), 319-327.

Elderfield, R. C. (1950). *Heterocyclic compounds: Polycyclic five- and six-membered compounds containing one O or S atom* (Vol. 2). New York: Wiley.

Eligwe, C. A., Okolue, N. B., Nwambu, C. O., & Nwoko, C. I. A. (1999). Adsorption Thermodynamics and Kinetics of Mercury (II), Cadmium (II) and Lead (II) on Lignite. *Chemical Engineering & Technology, 22*(1), 45-49.

Elliott, J. A. (1917). A New and Delicate Method for the Detection of Mercury. *Journal of the American Medical Association, 68*(23), 1693-1694.

Ertl, G., Knözinger, H., Schüth, F., & Weitkamp, J. (Eds.). (2008). *Handbook of Heterogeneous Catalysis* (2nd ed. Vol. 8). Weiheim: Wiley-VCH.

Evans, H. T., & Konnert, J. A. (1976). Crystal structure refinement of covellite. *American Mineralogist, 61*, 996-1000.

Falter, R., & Schöler, H. F. (1995). Determination of mercury species in natural waters at picogram level with on-line RP C18 preconcentration and HPLC-UV-PCO-CVAAS. *Fresenius' Journal of Analytical Chemistry, 353*(1), 34-38.

Feng, X., Fryxell, G., Wang, L.-Q., Kim, A. Y., Liu, J., & Kemner, K. (1997). Functionalized monolayers on ordered mesoporous supports. *Science, 276*(5314), 923-926.

Fernandez-Nava, Y., Ulmanu, M., Anger, I., Maranon, E., & Castrillon, L. (2011). Use of granular bentonite in the removal of mercury(II), cadmium(II) and lead(II) from aqueous solutions. *Water Air and Soil Pollution, 215*(1-4), 239-249.

Finn, D. W., & Ouellette, M. J. (1992). Compact fluorescent lamps: what you should know. *Progressive Architecture*, 89.

Fogler, H. S. (Ed.). (1999). *Elements of chemical reaction engineering* (3rd ed.): Prentice-Hall International London.

Fredriksson, A., Dencker, L., Archer, T., & Danielsson, B. (1996). Prenatal coexposure to metallic mercury vapour and methylmercury produce interactive behavioural changes in adult rats. *Neurotoxicology and teratology, 18*(2), 129-134.

Freundlich, H. M. F. (1906). Über die adsorption in lösungen. *Zeitschrift für Physikalische Chemie, 57A*, 385 - 470.

Friedli, H. R., Arellano, A. F., Cinnirella, S., & Pirrone, N. (2009). Initial Estimates of Mercury Emissions to the Atmosphere from Global Biomass Burning. *Environmental Science & Technology, 43*(10), 3507-3513.

Fu, F., Chen, R., & Xiong, Y. (2006). Application of a novel strategy—Coordination polymerization precipitation to the treatment of Cu^{2+} containing wastewaters. *Separation and Purification Technology, 52*(2), 388-393.

Fu, F., & Wang, Q. (2011). Removal of heavy metal ions from wastewaters: A review. *Journal of Environmental Management, 92*(3), 407-418.

Fu, F., Zeng, H., Cai, Q., Qiu, R., Yu, J., & Xiong, Y. (2007). Effective removal of coordinated copper from wastewater using a new dithiocarbamate-type supramolecular heavy metal precipitant. *Chemosphere, 69*(11), 1783-1789.

Fullston, D. (1998). *Surface and electrochemical studies in the selective flotation of copper and arsenic minerals. Ph.D. Thesis.* University of South Australia.

Fullston, D., Fornasiero, D., & Ralston, J. (1999). Zeta potential study of the oxidation of copper sulfide minerals. *Colloids and Surfaces A: Physicochemical and Engineering Aspects, 146*(1-3), 113-121.

Gahlmann, A., Kester, K. D., & Mayer, S. G. (2005). Investigating the effect of the zwitterion/lactone equilibrium of Rhodamine B on the cybotactic region of the acetonitrile/$scCO_2$ cosolvent. *The Journal of Physical Chemistry A, 109*(9), 1753-1757.

Gale, T. F. (1981). The embryotoxic response produced by inorganic mercury in different strains of hamsters. *Environmental Research, 24*(1), 152-161.

Gash, A. E., Spain, A. L., Dysleski, L. M., Flaschenriem, C. J., Kalaveshi, A., Dorhout, P. K., et al. (1998). Efficient recovery of elemental mercury from Hg(II)-contaminated aqueous media using a redox-recyclable ion-exchange material. *Environmental Science & Technology, 32*(7), 1007-1012.

Gebremedhin-Haile, T., Olguín, M. T., & Solache-Ríos, M. (2003). Removal of Mercury Ions from Mixed Aqueous Metal Solutions by Natural and Modified Zeolitic Minerals. *Water, Air, and Soil Pollution, 148*(1-4), 179-200.

Gil, S., Costas, M., Pena, F., De La Calle, I., Cabaleiro, N., Lavilla, I., et al. (2010). On-line UV photoreduction in a flow-injection/stopped-flow manifold for determination of

mercury by cold vapour-atomic absorption spectrometry. *Analytical Methods, 2*(11), 1798-1802.

Girgsdies, F. (2009). X-ray Powder Diffraction in Catalysis. Berlin: Nanostructures Group, Inorganic Chemistry Department, Fritz Haber Institute of the Max Planck Society.

Goh, S. W., Buckley, A. N., & Lamb, R. N. (2006). Copper(II) sulfide? *Minerals Engineering, 19*(2), 204-208.

Golkowska, A., & Pszonicki, L. (1973). A study of the composition and properties of the ion-association complex of Rhodamine B with silicomolybdic acid, with a view to its analytical application. *Talanta, 20*(8), 749-754.

Grandjean, P., Murata, K., Budtz-Jørgensen, E., & Weihe, P. (2004). Cardiac autonomic activity in methylmercury neurotoxicity: 14-year follow-up of a Faroese birth cohort. *Journal of Pediatrics, 144*, 169-176.

Greenwood, N. N., & Earnshaw, A. (1984). *Chemistry of the Elements*. Tarrytown, New York: Pergamon Press.

Greenwood, N. N., & Earnshaw, A. (1997). *Chemistry of the Elements* (2nd ed.): Butterworth-Heinemann.

Guerra, D. L., Viana, R. R., & Airoldi, C. (2009). Adsorption of mercury cation on chemically modified clay. *Materials Research Bulletin, 44*(3), 485-491.

Guibal, E. (2004). Interactions of metal ions with chitosan-based sorbents: a review. *Separation and Purification Technology, 38*(1), 43-74.

Gullapalli, S., & Barron, A. (2010). Characterization of Group 12-16 (II-VI) Semiconductor Nanoparticles by UV-visible Spectroscopy. Retrieved 22 Jan 2014, from http://cnx.org/content/m34601/1.1/

Gupta, K., & Kumar, M. R. (1999). Structural changes and release characteristics of crosslinked chitosan beads in response to solution pH. *Journal of Macromolecular Science, Part A, 36*(5-6), 827-841.

Hall, K. R., Eagleton, L. C., Acrivos, A., & Vermeulen, T. (1966). Pore- and solid-diffusion kinetics in fixed-bed adsorption under constant-pattern conditions. *Industrial & Engineering Chemistry Fundamentals, 5*(2), 212-223.

Harada, M. (1995). Minamata disease: Methylmercury Poisoning in Japan Caused by Environmental Pollution. *Critical Reviews in Toxicology, 25*(1), 1-24.

Hasanin, T. H. A., Tsukahara, S., & Fujiwara, T. (2010). Acid-base behavior of Rhodamine B in a reversed micellar medium of cetyltrimethylammonium chloride in 1-hexanol-cyclohexane/water. *Analytical Sciences, 26*(12), 1247-1254.

Hasany, S. M., Saeed, M. M., & Ahmed, M. (1999). Retention of Hg(II) by solid mercury sulfide from acidic solution. *Separation Science and Technology, 34*(3), 487-499.

Hasegawa, Y., Inagake, T., Karasawa, Y., & Fujita, A. (1983). Spectrophotometric determination of gallium (III) after solvent extraction of its chloro-complex with Rhodamine B. *Talanta, 30*(9), 721-723.

Hernandez-Córdoba, M., López-Garcia, I., & Sánchez-Pedreño, C. (1984). Spectrophotometric determination of mercury with thiocyanate and Rhodamine B. *Microchimica Acta, 84*(5), 467-475.

Hirsch, P. B., Howie, A., Nicholson, R. B., Pashley, D. W., & Whelan, M. J. (1965). *Electron Microscopy of Thin Crystals*. Butterworths, London.

Ho, Y. S. (1995). Adsorption of heavy metals from waste streams by peat. *Ph.D. Thesis. University of Birmingham*.

Ho, Y. S., Huang, C. T., & Huang, H. W. (2002). Equilibrium sorption isotherm for metal ions on tree fern. *Process Biochemistry, 37*(12), 1421-1430.

Ho, Y. S., & McKay, G. (1998a). A comparison of chemisorption kinetic models applied to pollutant removal on various sorbents. *Process safety and environmental protection: transactions of the Institution of Chemical Engineers, part B, 76*(4), 332-340.

Ho, Y. S., & McKay, G. (1998b). The kinetics of sorption of basic dyes from aqueous solution by sphagnum moss peat. *The Canadian Journal of Chemical Engineering, 76*(4), 822-827.

Ho, Y. S., & Wang, C. C. (2008). Sorption equilibrium of mercury onto ground-up tree fern. *Journal of Hazardous Materials, 156*(1-3), 398-404.

Ho, Y. S., Wase, D. A. J., & Forster, C. F. (1996). Kinetic studies of competitive heavy metal adsorption by sphagnum moss peat. *Environmental Technology, 17*(1), 71-77.

Horwitz, W., Chichilo, P., Clifford, P., & Reynolds, H. (1965). *Official methods of analysis of the Association of Official Analytical Chemists*: Association of Official Analytical Chemists.

Hosseini-Bandegharaei, A., Hosseini, M. S., Jalalabadi, Y., Sarwghadi, M., Nedaie, M., Taherian, A., et al. (2011). Removal of Hg(II) from aqueous solutions using a novel impregnated resin containing 1-(2-thiazolylazo)-2-naphthol (TAN). *Chemical Engineering Journal, 168*(3), 1163-1173.

Hosseini, M. S., & Naseri, Y. (2003). Determination of thallium(I) by flotation-spectrophotometric method using iodide and Rhodamine B. *Analytical Sciences, 19*(11), 1505-1508.

Hryhorczuk, D., Persky, V., Piorkowski, J., Davis, J., Moomey, C. M., Krantz, A., et al. (2006). Residential mercury spills from gas regulators. *Environmental Health Perspectives, 114*(6), 848.

Huang, C.-C., & Chang, H.-T. (2007). Parameters for selective colorimetric sensing of mercury(ii) in aqueous solutions using mercaptopropionic acid-modified gold nanoparticles. *Chemical Communications, 0*(12), 1215-1217.

Huang, X., Wang, M., Willinger, M.-G., Shao, L., Su, D. S., & Meng, X.-M. (2012). Assembly of three-dimensional hetero-epitaxial ZnO/ZnS core/shell nanorod and single crystalline hollow ZnS nanotube arrays. *ACS Nano, 6*(8), 7333-7339.

Humbert, P. (1986). An XPS and UPS photoemission study of HgO. *Solid State Communications, 60*(1), 21-24.

Hutchison, A. R., & Atwood, D. A. (2003). Mercury pollution and remediation: The chemist's response to a global crisis. *Journal of Chemical Crystallography, 33*(8), 631-645.

Hutton, R. C., & Preston, B. (1980). A simple non-dispersive atomic-fluorescence spectrometer for mercury determination, using cold-vapour generation. *Analyst, 105*(1255), 981-984.

Hyland, M. M., Jean, G. E., & Bancroft, G. M. (1990). XPS and AES studies of Hg(II) sorption and desorption reactions on sulphide minerals. *Geochimica et Cosmochimica Acta, 54*(7), 1957-1967.

Iijima, S. (1991). Helical microtubules of graphitic carbon. *Nature, 354*(6348), 56-58.

Inbaraj, B. S., & Sulochana, N. (2006). Mercury adsorption on a carbon sorbent derived from fruit shell of Terminalia catappa. *Journal of Hazardous Materials, 133*(1-3), 283-290.

International Programme on Chemical Safety (IPCS). (2001). International Chemical Safety Card 1416 - Copper(II) sulfate, pentahydrate Retrieved 11/10/2012, from http://www.inchem.org/documents/icsc/icsc/eics1416.htm

Ireland-Ripert, J., Bermond, A., & Ducauze, C. (1982). Determination of methylmercury in the presence of inorganic mercury by anodic stripping voltammetry. *Analytica Chimica Acta, 143*(0), 249-254.

Irving, H. M. N. H. (1977). *Dithizone. / H. M. N. H. Irving*: The Chemical Society.

Irving, H. M. N. H., & Iwantscheff, G. (1980). The Analytical Applications of Dithizone. *C R C Critical Reviews in Analytical Chemistry, 8*(4), 321-366.

Iwantscheff, G. (1958). *Das Dithizon und seine Anwendung in der Mikro- und Spurenanalyse*: Verlag Chemie.

James, R. O., & Healy, T. W. (1972). Adsorption of hydrolyzable metal ions at the oxide—water interface. III. A thermodynamic model of adsorption. *Journal of colloid and interface science, 40*(1), 65-81.

Jean, G. E., & Bancroft, G. M. (1986). Heavy metal adsorption by sulphide mineral surfaces. *Geochimica et Cosmochimica Acta, 50*(7), 1455-1463.

Jeon, C., & Höll, W. H. (2003). Chemical modification of chitosan and equilibrium study for mercury ion removal. *Water Research, 37*(19), 4770-4780.

Jeong, H. Y., Klaue, B., Blum, J. D., & Hayes, K. F. (2007). Sorption of mercuric ion by synthetic nanocrystalline mackinawite (FeS). *Environmental Science & Technology, 41*(22), 7699-7705.

Jones, C. J., McGugan, P. J., & Lawrence, P. F. (1978). An investigation of the degradation of some dry cell batteries under domestic waste landfill conditions. *Journal of hazardous materials, 2*(3), 259-289.

Jusoh, A., Su Shiung, L., Ali, N. a., & Noor, M. (2007). A simulation study of the removal efficiency of granular activated carbon on cadmium and lead. *Desalination, 206*(1), 9-16.

Kalamegham, R., & Ash, K. O. (1992). A simple ICP-MS procedure for the determination of total mercury in whole blood and urine. *Journal of Clinical Laboratory Analysis, 6*(4), 190-193.

Kang-Yum, E., & Oransky, S. (1992). Chinese patent medicine as a potential source of mercury poisoning. *Veterinary and human toxicology, 34*(3), 235.

Kang, K. C., Kim, S. S., Choi, J. W., & Kwon, S. H. (2008). Sorption of Cu^{2+} and Cd^{2+} onto acid-and base-pretreated granular activated carbon and activated carbon fiber samples. *Journal of Industrial and Engineering Chemistry, 14*(1), 131-135.

Kelly, W. R., Long, S., & Mann, J. (2003). Determination of mercury in SRM crude oils and refined products by isotope dilution cold vapor ICP-MS using closed-system combustion. *Analytical and Bioanalytical Chemistry, 376*(5), 753-758.

Kenduzler, E., Ates, M., Arslan, Z., McHenry, M., & Tchounwou, P. B. (2012). Determination of mercury in fish otoliths by cold vapor generation inductively coupled plasma mass spectrometry (CVG-ICP-MS). *Talanta*.

Khalid, N., Ahmad, S., Kiani, S. N., & Ahmed, J. (1999). Removal of Mercury from Aqueous Solutions by Adsorption to Rice Husks. *Separation Science and Technology, 34*(16), 3139-3153.

Khan, A. T., Atkinson, A., Graham, T. C., Thompson, S. J., Ali, S., & Shireen, K. F. (2004). Effects of inorganic mercury on reproductive performance of mice. *Food and chemical toxicology, 42*(4), 571-577.

Khezami, L., & Capart, R. (2005). Removal of chromium (VI) from aqueous solution by activated carbons: kinetic and equilibrium studies. *Journal of hazardous materials, 123*(1), 223-231.

Kim, C. S., Rytuba, J. J., & Brown, G. E. (2004). EXAFS study of mercury(II) sorption to Fe- and Al-(hydr)oxides: I. Effects of pH. *Journal of Colloid and Interface Science, 271*(1), 1-15.

Kim, Y.-R., Mahajan, R. K., Kim, J. S., & Kim, H. (2009). Highly Sensitive Gold Nanoparticle-Based Colorimetric Sensing of Mercury(II) through Simple Ligand Exchange Reaction in Aqueous Media. *ACS Applied Materials & Interfaces, 2*(1), 292-295.

Kothny, E. L. (1969). Trace determination of mercury, thallium and gold with crystal violet. *Analyst, 94*(1116), 198-203.

Koyun, M., Akman, S., & Güven, A. G. (2004). Mercury intoxication resulting from school barometers in three unrelated adolescents. *European journal of pediatrics, 163*(3), 131-134.

Krajewska, B. (2004). Application of chitin-and chitosan-based materials for enzyme immobilizations: a review. *Enzyme and microbial technology, 35*(2), 126-139.

Kruger, P. C., Bloom, M. S., Arnason, J. G., Palmer, C. D., Fujimoto, V. Y., & Parsons, P. J. (2012). Trace elements in human follicular fluid: development of a sensitive multielement ICP-MS method for use in biomonitoring studies. *Journal of Analytical Atomic Spectrometry, 27*(8), 1245-1253.

Kundu, M., Hasegawa, T., Terabe, K., Yamamoto, K., & Aono, M. (2008). Structural studies of copper sulfide films: Effect of ambient atmosphere. *Science and Technology of Advanced Materials, 9*(3), 035011.

Kunkoro, E., Roussy, J., & Guibal, E. (2005). Mercury recovery by polymer-enhanced ultrafiltration: comparison of chitosan and poly (ethylenimine) used as macrolingand. *Sep. Sci. Technol, 40*, 659-684.

Kurita, K. (2006). Chitin and chitosan: functional biopolymers from marine crustaceans. *Marine Biotechnology, 8*(3), 203-226.

Kurita, K., Sannan, T., & Iwakura, Y. (1979). Studies on chitin. VI. Binding of metal cations. *Journal of Applied Polymer Science, 23*(2), 511-515.

Kurmaev, E. Z., Ek, J. v., Ederer, D. L., Zhou, L., Callcott, T. A., Perera, R. C. C., et al. (1998). Experimental and theoretical investigation of the electronic structure of transition metal sulphides: CuS, FeS_2 and $FeCuS_2$. *Journal of Physics: Condensed Matter, 10*(7), 1687.

Kwon, S., Fan, M., Cooper, A. T., & Yang, H. (2008). Photocatalytic applications of micro-and nano-TiO2 in environmental engineering. *Critical Reviews in Environmental Science and Technology, 38*(3), 197-226.

Laajalehto, K., Kartio, I., & Nowak, P. (1994). XPS study of clean metal sulfide surfaces. *Applied Surface Science, 81*(1), 11-15.

Lagergren, S. (1898). About the theory of so-called adsorption of soluble substances. *Kungliga Svenska Vetenskapsakademiens. Handlingar, 24*(4), 1-39.

Laing, M., & Alsop, P. A. (1970). The structure of primary nickel dithizonate. *Talanta, 17*(3), 242-244.

Lancione, R. L., & Drew, D. M. (1985). Evaluation of ICP atomic fluorescence for the determination of mercury. *Spectrochimica Acta Part B: Atomic Spectroscopy, 40*(1–2), 107-113.

Langmuir, I. (1916). The constitution and fundamental properties of solids and liquids. I. Solids. *Journal of the American Chemical Society, 38*(11), 2221-2295.

Langmuir, I. (1917). The constitution and fundamental properties of solids and liquids. II. Liquids. *Journal of the American Chemical Society, 39*(9), 1848-1906.

Langmuir, I. (1918). The adsorption of gases on plane surfaces of glass, mica and platinum. *Journal of the American Chemical Society, 40*(9), 1361-1403.

Lau, L. D., Rodriguez, R., Henery, S., Manuel, D., & Schwendiman, L. (1998). Photoreduction of Mercuric Salt Solutions at High pH. *Environmental Science & Technology, 32*(5), 670-675.

Lee, J.-S., Ulmann, P. A., Han, M. S., & Mirkin, C. A. (2008). A DNA-gold nanoparticle-based colorimetric competition assay for the detection of cysteine. *Nano letters, 8*(2), 529-533.

Lee, J. D. (1996). *Concise Inorganc Chemistry* (5th ed.). Oxford: Blackwell Science Ltd.

Lefèvre, G., Bessière, J., Ehrhardt, J.-J., & Walcarius, A. (2003). Immobilization of iodide on copper(I) sulfide minerals. *Journal of Environmental Radioactivity, 70*(1-2), 73-83.

Lerch, M., & Bircher, A. J. (2004). Systemically induced allergic exanthem from mercury. *Contact Dermatitis, 50*(6), 349-353.

Ley, L., & Cardona, M. (1979). *Photoemission in Solids II: Case Studies*: Springer-Verlag.

Li, A. M., Chan, M. H., Leung, T., Cheung, R. C., Lam, C. W., & Fok, T. (2000). Mercury intoxication presenting with tics. *Archives of disease in childhood, 83*(2), 174-175.

Li, L., Li, B., Qi, Y., & Jin, Y. (2009). Label-free aptamer-based colorimetric detection of mercury ions in aqueous media using unmodified gold nanoparticles as colorimetric probe. *Analytical and Bioanalytical Chemistry, 393*(8), 2051-2057.

Li, T., Dong, S., & Wang, E. (2009). Label-Free Colorimetric Detection of Aqueous Mercury Ion (Hg^{2+}) Using Hg^{2+}-Modulated G-Quadruplex-Based DNAzymes. *Analytical Chemistry, 81*(6), 2144-2149.

Lide, D. R. (2005). *CRC Handbook of Chemistry and Physics* (86 ed.): CRC Press.

Litman, R., Williams, E. T., & Finston, H. L. (1977). Extraction of mercury by dithizone and stability of the extracted complex. *Analytical Chemistry, 49*(7), 983-987.

Liu, D., Qu, W., Chen, W., Zhang, W., Wang, Z., & Jiang, X. (2010). Highly Sensitive, Colorimetric Detection of Mercury(II) in Aqueous Media by Quaternary Ammonium Group-Capped Gold Nanoparticles at Room Temperature. *Analytical Chemistry, 82*(23), 9606-9610.

Liu, J., Valsaraj, K. T., Devai, I., & DeLaune, R. D. (2008). Immobilization of aqueous Hg(II) by mackinawite (FeS). *Journal of Hazardous Materials, 157*(2-3), 432-440.

Liu, X., Tang, Y., Wang, L., Zhang, J., Song, S., Fan, C., et al. (2007). Optical Detection of Mercury (II) in Aqueous Solutions by Using Conjugated Polymers and Label‐Free Oligonucleotides. *Advanced Materials, 19*(11), 1471-1474.

Liu, Y., Qin, D., Wang, L., & Cao, Y. (2007). A facile solution route to CuS hexagonal nanoplatelets. *Materials Chemistry and Physics, 102*(2–3), 201-206.

Lopez-Garcia, I., Martinez-Aviles, J., & Hernandez-Cordoba, M. (1986). Determination of palladium with thiocyanate and Rhodamine B by a solvent-extraction method. *Talanta, 33*(5), 411-414.

López-Muñoz, M. J., Aguado, J., Arencibia, A., & Pascual, R. (2011). Mercury removal from aqueous solutions of HgCl2 by heterogeneous photocatalysis with TiO2. *Applied Catalysis B: Environmental, 104*(3–4), 220-228.

López-Ramón, V., Moreno-Castilla, C., Rivera-Utrilla, J., & Radovic, L. R. (2002). Ionic strength effects in aqueous phase adsorption of metal ions on activated carbons. *Carbon, 41*(10), 2009-2025.

Lothian, G. F. (1963). Beer's law and its use in analysis. A review. *Analyst, 88*(1050), 678-685.

MacNaughton, M. G., & James, R. O. (1974). Adsorption of aqueous mercury (II) complexes at the oxide/water interface. *Journal of colloid and interface science, 47*(2), 431-440.

Macnulty, B. J., & Woollard, L. D. (1955). The use of Rhodamine B in analytical chemistry: The determination of small quantities of gold. *Analytica Chimica Acta, 13*, 154-158.

Malm, O. (1998). Gold mining as a source of mercury exposure in the Brazilian Amazon. *Environmental Research, 77*(2), 73-78.

Manju, G., Anoop Krishnan, K., Vinod, V., & Anirudhan, T. (2002). An investigation into the sorption of heavy metals from wastewaters by polyacrylamide-grafted iron (III) oxide. *Journal of hazardous materials, 91*(1), 221-238.

Manohar, D. M., Anoop Krishnan, K., & Anirudhan, T. S. (2002). Removal of mercury(II) from aqueous solutions and chlor-alkali industry wastewater using 2-mercaptobenzimidazole-clay. *Water Research, 36*(6), 1609-1619.

Marczenko, Z., & Balcerzak, M. (2000). *Separation, Preconcentration, and Spectrophotometry in Inorganic Analysis*. Amsterdam: Elsevier Science B.V.

Markovs, J., & Clark, K. (2005). *Optimized Mercury Removal in Gas Plants*. Paper presented at the Eighty-Fourth Gas Processors Association Annual Convention.

Márquez, M., Silva, M., & Perez-Bendito, D. (1988). Semi-automatic analysis of mercury in pharmaceuticals by catalytic titration. *Journal of Pharmaceutical and Biomedical Analysis, 6*(3), 307-312.

Martellaro, P. J., Moore, G. A., Peterson, E. S., Abbott, E. H., & Gorenbain, A. E. (2001). Environmental application of mineral sulphides for removal of gas-phase Hg^0 and aqueous Hg^{2+}. *Separation Science and Technology, 36*(5), 1183 - 1196.

Mason, R. P. (2009). Mercury emissions from natural processes and their importance in the global mercury cycle. In R. Mason & N. Pirrone (Eds.), *Mercury Fate and Transport in the Global Atmosphere* (pp. 173-191): Springer US.

Mathew, S., Sukumar, R., Rao, T. P., & Damodaran, A. D. (1992). Third Order Derivative Spectrophotometry Determination of Mercury (II) as the Ternary Complex with Iodide and Pyronine G. *Analytical Letters, 25*(10), 1941-1959.

Matlock, M. M., Henke, K. R., & Atwood, D. A. (2002). Effectiveness of commercial reagents for heavy metal removal from water with new insights for future chelate designs. *Journal of Hazardous Materials, 92*(2), 129-142.

Matlock, M. M., Howerton, B. S., & Atwood, D. A. (2002). Chemical precipitation of heavy metals from acid mine drainage. *Water Research, 36*(19), 4757-4764.

Matlock, M. M., Howerton, B. S., & Atwood, D. A. (2003). Irreversible binding of mercury from contaminated soil. *Advances in Environmental Research, 7*(2), 347-352.

Matusiewicz, H., Horvath, Z., & Barnes, R. M. (1985). Determination of mercury in drinking water by inductively coupled plasma atomic emission spectrometry with electrothermal vaporization. *Applied spectroscopy, 39*(3), 558-560.

Matysina, Z. A. (1999). The relative surface energy of hexagonal close-packed crystals. *Materials Chemistry and Physics, 60*(1), 70-78.

Mellor, J. W. (1923). *A comprehensive treatise on inorganic and theoritical chemistry* (Vol. IV): Longmans, Green and Co.

Mercier, L., & Detellier, C. (1995). Preparation, characterization, and applications as heavy metals sorbents of covalently grafted thiol functionalities on the interlamellar surface of montmorillonite. *Environmental Science & Technology, 29*(5), 1318-1323.

Merrifield, J. D. (2002). *Synthesis and Characterization of Thiol-Grafted Chitosan Beads for Mercury Removal.* The University of Maine.

Meta, V. (2009). X-ray Photoelectron Spectroscopy. *Introduction & Principle* Retrieved 22 Jan 2014, from http://www.vub.ac.be/META/toestellen_xps.php?m=xpand&d=menu7

Miretzky, P., & Cirelli, A. F. (2009). Hg(II) removal from water by chitosan and chitosan derivatives: A review. *Journal of hazardous materials, 167*(1–3), 10-23.

Mishra, S. P., Dubey, S. S., & Tiwari, D. (2004). Inorganic particulates in removal of heavy metal toxic ions: IX. Rapid and efficient removal of Hg(II) by hydrous manganese and tin oxides. *Journal of colloid and interface science, 279*(1), 61-67.

Mishra, S. P., Singh, V. K., & Tiwari, D. (1996). Radiotracer technique in adsorption study: Part XIV. Efficient removal of mercury from aqueous solutions by hydrous zirconium oxide. *Applied Radiation and Isotopes, 47*(1), 15-21.

Mladenova, E., Dakova, I., Tsalev, D., & Karadjova, I. (2012). Mercury determination and speciation analysis in surface waters. *Central European Journal of Chemistry, 10*(4), 1175-1182.

Moeken, H. H. P., & Van-Neste, W. A. H. (1967). Absorptiometric determination of microgram amounts of uranium with Rhodamine B. *Analytica Chimica Acta, 37*, 480-483.

Mohan, D., Gupta, V. K., Srivastava, S. K., & Chander, S. (2000). Kinetics of mercury adsorption from wastewater using activated carbon derived from fertilizer waste. *Colloids and Surfaces A: Physicochemical and Engineering Aspects, 177*(2–3), 169-181.

Moody, J. R., & Paulsen, P. J. (1988). Isotope dilution spark-source mass spectrometric determination of total mercury in botanical and biological samples. *Analyst, 113*(6), 923-927.

Moore, G. A., Martellaro, P. J., & Peterson, E. S. (2000). Mercury-sorption characteristics of nanoscale metal sulfides. In S. Abdel hamid & J. Mietek (Eds.), *Studies in Surface Science and Catalysis* (Vol. 129, pp. 765-772): Elsevier.

Moreno-Castilla, C., & Rivera-Utrilla, J. (2001). Carbon materials as adsorbents for the removal of pollutants from the aqueous phase. *MRS Bulletin, 26*(11), 890-894.

Moreno-Villoslada, I., Jofre, M., Miranda, V., Gonzalez, R., Sotelo, T., Hess, S., et al. (2006). pH dependence of the interaction between Rhodamine B and the water-soluble poly(sodium 4-styrenesulfonate). *Journal of Physical Chemistry B, 110*(24), 11809-11812.

Morgan, D., Chanda, S., Price, H., Fernando, R., Liu, J., Brambila, E., et al. (2002). Disposition of inhaled mercury vapor in pregnant rats: maternal toxicity and effects on developmental outcome. *Toxicological Sciences, 66*(2), 261-273.

Morita, M., Yoshinaga, J., & Edmonds, J. (1998). The determination of mercury species in environmental and biological samples (Technical report). *Pure and Applied Chemistry, 70*(8), 1585-1615.

Moromisato, D. Y., Anas, N. G., & Goodman, G. (1994). Mercury inhalation poisoning and acute lung injury in a child. Use of high-frequency oscillatory ventilation. *CHEST Journal, 105*(2), 613-615.

Moulder, J. F., Stickle, W. F., Sobol, P. E., & Bomben, K. D. (1992). *Handbook of x-ray photoelectron spectroscopy*. Eden Prairie, Minnesota: Physical Electronics Division, Perkin-Elmer Corporation

Mufazzal Saeed, M., Moosa Hasany, S., & Ahmed, M. (1999). Adsorption and thermodynamic characteristics of Hg(II)-SCN complex onto polyurethane foam. *Talanta, 50*(3), 625-634.

Murphy, E. A., & Aucott, M. (1999). A Methodology to Assess the Amounts of Pesticidal Mercury Used Historically in New Jersey. *Journal of Soil Contamination, 8*(1), 131 - 148.

Muzzarelli, R. (Ed.). (1973). *Natural chelating polymers: alginic acids, chitin and chitosan*: Oxford: Pergamon.

Nabais, J. V., Carrott, P. J. M., Carrott, M. M. L. R., Belchior, M., Boavida, D., Diall, T., et al. (2006). Mercury removal from aqueous solution and flue gas by adsorption on activated carbon fibres. *Applied Surface Science, 252*(17), 6046-6052.

Nam, J., Won, N., Jin, H., Chung, H., & Kim, S. (2009). pH-induced aggregation of gold nanoparticles for photothermal cancer therapy. *Journal of the American Chemical Society, 131*(38), 13639-13645.

Namasivayam, C., & Senthilkumar, S. (1997). Recycling of industrial solid waste for the removal of mercury (II) by adsorption process. *Chemosphere, 34*(2), 357-375.

National Research Council. (2000). *Toxicological effects of methylmercury*: National Academies Press.

Nefedov, V. I., Sergushin, N. P., Band, I. M., & Trzhaskovskaya, M. B. (1973). Relative intensities in x-ray photoelectron spectra. *Journal of Electron Spectroscopy and Related Phenomena, 2*(4), 383-403.

Ngah, W., & Fatinathan, S. (2008). Adsorption of Cu (II) ions in aqueous solution using chitosan beads, chitosan–GLA beads and chitosan–alginate beads. *Chemical Engineering Journal, 143*(1), 62-72.

Nippon Instrument Corporation. (2005). Reducing Vaporization Mercury Analyzer Mercury/RA-3000 Measurement Manual. *Instruction Manual: Mercury/RA-3000 system*.

Nooney, R. I., Kalyanaraman, M., Kennedy, G., & Maginn, E. J. (2001). Heavy Metal Remediation Using Functionalized Mesoporous Silicas with Controlled Macrostructure. *Langmuir, 17*(2), 528-533.

Oh, Y., Bag, S., Malliakas, C. D., & Kanatzidis, M. G. (2011). Selective surfaces: High-surface-area zinc tin sulfide chalcogels. *Chemistry of Materials, 23*(9), 2447-2456.

Okoronkwo, N. E., Igwe, J. C., & Okoronkwo, I. J. (2007). Environmental impacts of mercury and its detoxification from aqueous solutions. *African Journal of Biotechnology, 6*(4), 335-340.

Olkhovyk, O., Antochshuk, V., & Jaroniec, M. (2004). Benzoylthiourea-modified MCM-48 mesoporous silica for mercury(II) adsorption from aqueous solutions. *Colloids and Surfaces A: Physicochemical and Engineering Aspects, 236*(1-3), 69-72.

Ombaba, J. M. (1996). Total Mercury Determination in Biological and Environmental Standard Samples by Gold Amalgamation Followed by Cold Vapor Atomic Absorption Spectrometry. *Microchemical Journal, 53*(2), 195-200.

Otto, M., Ahlemeyer, C., Tasche, H., & von Muhlendahl, K. E. (1994). Mercury exposure. [10.1038/367110b0]. *Nature, 367*(6459), 110-110.

Pacyna, E. G., Pacyna, J. M., Steenhuisen, F., & Wilson, S. (2006). Global anthropogenic mercury emission inventory for 2000. *Atmospheric Environment, 40*(22), 4048-4063.

Pan, S., Zhang, Y., Shen, H., & Hu, M. (2012). An intensive study on the magnetic effect of mercapto-functionalized nano-magnetic Fe3O4 polymers and their adsorption

mechanism for the removal of Hg(II) from aqueous solution. *Chemical Engineering Journal, 210*(0), 564-574.

Paradkar, R. P., & Williams, R. R. (1994). Micellar Colorimetric Determination of Dithizone Metal Chelates. *Analytical Chemistry, 66*(17), 2752-2756.

Parham, H., Zargar, B., & Shiralipour, R. (2012). Fast and efficient removal of mercury from water samples using magnetic iron oxide nanoparticles modified with 2-mercaptobenzothiazole. *Journal of hazardous materials, 205–206*(0), 94-100.

Park, S. W., & Huang, C. P. (1989). Chemical substitution reaction between Cu(II) and Hg(II) and hydrous CdS(s). *Water Research, 23*(12), 1527-1534.

Pattrick, R. A. D., Mosselmans, J. F. W., Charnock, J. M., England, K. E. R., Helz, G. R., Garner, C. D., et al. (1997). The structure of amorphous copper sulfide precipitates: An X-ray absorption study. *Geochimica et Cosmochimica Acta, 61*(10), 2023-2036.

Pearson, R. G. (1963). Hard and soft acids and bases. *Journal of the American Chemical Society, 85*(22), 3533-3539.

Pérez-Quintanilla, D., Del Hierro, I., Fajardo, M., & Sierra, I. (2006). Preparation of 2-mercaptobenzothiazole-derivatized mesoporous silica and removal of Hg (II) from aqueous solution. *Journal of Environmental Monitoring, 8*(1), 214-222.

Pervukhina, N. V., Vasil'ev, V. I., Magarill, S. A., Borisov, S. V., & Naumov, D. Y. (2006). Crystal chemistry of mercury sulfohalides of composition Hg(3)S(2)Hal(2) (Hal : Cl, Br). I. Crystal structures of two polymorphic modifications of Hg3S2Cl2-xBrx (x approximate to 0.5). *Canadian Mineralogist, 44*, 1239-1246.

Phillips, H. O., & Kraus, K. A. (1963). Adsorption on inorganic materials. V. Reaction of cadmium sulfide with copper(II), mercury(II) and silver(I). *Journal of the American Chemical Society, 85*(4), 486-487.

Phillips, H. O., & Kraus, K. A. (1965). Adsorption on inorganic materials. VI. Reaction of insoluble sulfides with metal ions in aqueous media. *Journal of Chromatography A, 17*, 549-557.

Pinilla Gil, E., & Ostapczuk, P. (1994). Potentiometric stripping determination of mercury(II), selenium(IV), copper(II) and lead(II) at a gold film electrode in water samples. *Analytica Chimica Acta, 293*(1–2), 55-65.

Pirrone, N., Cinnirella, S., Feng, X., Finkelman, R. B., Friedli, H. R., Leaner, J., et al. (2010). Global mercury emissions to the atmosphere from anthropogenic and natural sources. *Atmospheric Chemistry and Physics, 10*, 5951 - 5964.

Pirrone, N., Munthe, J., Barregård, L., Ehrlich, H., Petersen, G., Fernandez, R., et al. (2001). Ambient Air Pollution by Mercury (Hg)-Position Paper. *Office for Official Publications of the European Communities*.

Plazinski, W., Rudzinski, W., & Plazinska, A. (2009). Theoretical models of sorption kinetics including a surface reaction mechanism: A review. *Advances in Colloid and Interface Science, 152*(1–2), 2-13.

Polavarapu, L., & Xu, Q.-H. (2008). Water-soluble conjugated polymer-induced self-assembly of gold nanoparticles and its application to SERS. *Langmuir, 24*(19), 10608-10611.

Poots, V. J. P., McKay, G., & Healy, J. J. (1978). Removal of basic dye from effluent using wood as an adsorbent. *Journal of the Water Pollution Control Federation, 50*, 926 - 935.

Procopio, J. R., da Silva, M. P., del Carmen Asensio, M., Sevilla, M. T., & Hernandez, L. (1992). HPLC analysis of thimerosal and its degradation products in ophthalmic solutions with electrochemical detection. *Talanta, 39*(12), 1619-1623.

Pröfrock, D., & Prange, A. (2012). Inductively Coupled Plasma-Mass Spectrometry (ICP-MS) for Quantitative Analysis in Environmental and Life Sciences: A Review of Challenges, Solutions, and Trends. *Applied spectroscopy, 66*(8), 843-868.

Puanngam, M., Dasgupta, P. K., & Unob, F. (2012). Automated on-line preconcentration of trace aqueous mercury with gold trap focusing for cold vapor atomic absorption spectrometry. *Talanta*.

Rabenstein, D. L. (1978). The aqueous solution chemistry of methylmercury and its complexes. *Accounts of Chemical Research, 11*(3), 100-107.

Ramakrishna, T. V., Aravamudan, G., & Vijayakumar, M. (1976). Spectrophotometric determination of mercury(II) as the ternary complex with Rhodamine 6G and iodide. *Analytica Chimica Acta, 84*(2), 369-375.

Ramette, R. W., & Sandell, E. B. (1956). Rhodamine B equilibria. *Journal of the American Chemical Society, 78*(19), 4872-4878.

Reed, B. E., Vaughan, R., & Jiang, L. (2000). As(III), As(V), Hg, and Pb Removal by Fe-Oxide Impregnated Activated Carbon. *Journal of Environmental Engineering-asce, 126*(9).

Rhea, D. T., Farag, A. M., Harper, D. D., McConnell, E., & Brumbaugh, W. G. (2013). Mercury and Selenium Concentrations in Biofilm, Macroinvertebrates, and Fish Collected in the Yankee Fork of the Salmon River, Idaho, USA, and Their Potential Effects on Fish Health. *Archives of environmental contamination and toxicology, 64*(1), 130-139.

Rietveld, H. M. (1967). Line profiles of neutron powder-diffraction peaks for structure refinement. *Acta Crystallographica, 22*(1), 151-152.

Rietveld, H. M. (1969). A profile refinement method for nuclear and magnetic structures. *Journal of Applied Crystallography, 2*(2), 65-71.

Rievaj, M., Mesároš, Š., & Bustin, D. (1993). Determination of Mercury and Copper Traces in Ultrapure Spectral Carbon by DPASV on a Gold-Fibre Microelectrode. *Collection of Czechoslovak chemical communications, 58*(12), 2918-2923.

Rinaldi, A., Abdullah, N., Ali, M., Furche, A., Hamid, S. B. A., Su, D. S., et al. (2009). Controlling the yield and structure of carbon nanofibers grown on a nickel/activated carbon catalyst. *Carbon, 47*(13), 3023-3033.

Rinaudo, M. (2006). *Characterization and properties of some polysaccharides used as biomaterials.* Paper presented at the Macromolecular Symposia.

Roginsky, S., & Zeldovich, Y. (1934). *Acta Physicochim., 1*, 554.

Rudzinski, W., & Plazinski, W. (2009). On the applicability of the pseudo-second order equation to represent the kinetics of adsorption at solid/solution interfaces: a theoretical analysis based on the statistical rate theory. *Adsorption, 15*(2), 181-192.

Saha, K., Agasti, S. S., Kim, C., Li, X., & Rotello, V. M. (2012). Gold nanoparticles in chemical and biological sensing. *Chemical Reviews, 112*(5), 2739-2779.

Saint'Pierre, T. D., Chavez Rocha, R. C., & Duyck, C. B. (2012). Determination of Hg in water associate to crude oil production by electrothermal vaporization inductively coupled plasma mass spectrometry. *Microchemical Journal*.

Sanchez-Polo, M., & Rivera-Utrilla, J. (2002). Adsorbent-adsorbate interactions in the adsorption of Cd (II) and Hg (II) on ozonized activated carbons. *Environmental Science & Technology, 36*(17), 3850-3854.

Sanchez-Rodas, D., Corns, W., Chen, B., & Stockwell, P. (2010). Atomic Fluorescence Spectrometry: a suitable detection technique in speciation studies for arsenic, selenium, antimony and mercury. *Journal of Analytical Atomic Spectrometry, 25*(7), 933-946.

Schecher, W. D., & McAvoy, D. C. (1992). MINEQL+: A software environment for chemical equilibrium modeling. *Computers, Environment and Urban Systems, 16*(1), 65-76.

Schwuger, M. J., Subklew, G., & Woller, N. (2001). New alternatives for waste water remediation with complexing surfactants. *Colloids and Surfaces A: Physicochemical and Engineering Aspects, 186*(3), 229-242.

Scofield, J. H. (1976). Hartree-Slater subshell photoionization cross-sections at 1254 and 1487 eV. *Journal of Electron Spectroscopy and Related Phenomena, 8*(2), 129-137.

Seals, R. D., Alexander, R., Taylor, L. T., & Dillard, J. G. (1973). Core electron binding energy study of group IIb-VIIa compounds. *Inorganic Chemistry, 12*(10), 2485-2487.

Shafaei, A., Ashtiani, F. Z., & Kaghazchi, T. (2007). Equilibrium studies of the sorption of Hg(II) ions onto chitosan. *Chemical Engineering Journal, 133*(1-3), 311-316.

Shafawi, A., Ebdon, L., Foulkes, M., Stockwell, P., & Corns, W. (2000). Preliminary evaluation of adsorbent-based mercury removal systems for gas condensate. *Analytica Chimica Acta, 415*(1-2), 21-32.

Shah, A., Kazi, T., Baig, J., Afridi, H., Kandhro, G., Arain, M., et al. (2010). Total mercury determination in different tissues of broiler chicken by using cloud point extraction and cold vapor atomic absorption spectrometry. *Food and chemical toxicology, 48*(1), 65-69.

Shannon, R. (1976). Revised effective ionic radii and systematic studies of interatomic distances in halides and chalcogenides. *Acta Crystallographica Section A, 32*(5), 751-767.

Sheela, T., Nayaka, Y. A., Viswanatha, R., Basavanna, S., & Venkatesha, T. G. (2012). Kinetics and thermodynamics studies on the adsorption of Zn(II), Cd(II) and Hg(II) from aqueous solution using zinc oxide nanoparticles. *Powder Technology, 217*(0), 163-170.

Shiue, Y.-S., Hung, S.-K., Chen, I.-H., & Chang, C.-S. (2011). TEM Phase Plate Loading System: Google Patents.

Siegbahn, K., Nordling, C., Fahlman, A., Nordberg, R., Hamrin, K., Hedman, J., et al. (1967). *ESCA (Atomic, Molecular and Solid State Structure Studied by Means of Electron Spectroscopy)* (Vol. 20).

Singh, H. B., Kumar, B., Sharma, R. L., & Katyal, M. (1989). Direct spectrophotometric determination of trace amounts of mercury(II) in aqueous media as its dithizonate complex in the presence of a neutral surfactant. *Analyst, 114*(7), 853-855.

Smith, D. J. (Ed.). (2005). *Handbook of Microscopy for Nanotechnology*: Springer-Verlag.

Solis, M. T., Yuen, E., Cortez, P. S., & Goebel, P. J. (2000). Family poisoned by mercury vapor inhalation. *The American Journal of Emergency Medicine, 18*(5), 599-602.

Solubility product constants. (2003). Retrieved 6 Nov 2012, from http://www.ktf-split.hr/periodni/en/abc/kpt.html

Sommer, L. (1989). *Analytical absorption spectrophotometry in the visible and ultraviolet: the principles*: Elsevier.

Song, X. L., Zhang, Y., Yan, C. Y., Jiang, W. J., & Xie, H. J. (2012). *Adsorption of mercury ion on activated carbons from rice husk.* Paper presented at the Conference on Advanced Materials and Engineering Applications, AMEA 2012, Hong Kong.

Sørensen, N., Murata, K., Budtz-Jørgensen, E., Weihe, P., & Grandjean, P. (1999). Prenatal methylmercury exposure as a cardiovascular risk factor at seven years of age. *Epidemiology*, 370-375.

Sorlier, P., Denuzière, A., Viton, C., & Domard, A. (2001). Relation between the degree of acetylation and the electrostatic properties of chitin and chitosan. *Biomacromolecules, 2*(3), 765-772.

Sparks, D. L. (1986). Kinetics of reactions in pure and in mixed systems. *Soil physical chemistry*, 83-145.

Sreeprasad, T. S., Maliyekkal, S. M., Lisha, K. P., & Pradeep, T. (2011). Reduced graphene oxide–metal/metal oxide composites: Facile synthesis and application in water purification. *Journal of hazardous materials, 186*(1), 921-931.

Srivastava, S., Frankamp, B. L., & Rotello, V. M. (2005). Controlled plasmon resonance of gold nanoparticles self-assembled with PAMAM dendrimers. *Chemistry of Materials, 17*(3), 487-490.

Stanisz, E., Werner, J., & Matusiewicz, H. (2013). Mercury species determination by task specific ionic liquid-based ultrasound-assisted dispersive liquid-liquid microextraction combined with cold vapour generation atomic absorption spectrometry. *Microchemical Journal*.

Stock, A. (1931). The determination of very small amounts of mercury and its importance. *Naturwissenschaften, 19*(23-25), 499-502.

Stroh, A., Vollkopf, U., & Denoyer, E. R. (1992). Analysis of samples containing large amounts of dissolved solids using microsampling flow injection inductively coupled plasma mass spectrometry. *Journal of Analytical Atomic Spectrometry, 7*(8), 1201-1205.

Study Notes: AAS Detector. Retrieved 22 Jan 2014, from http://toolboxes.flexiblelearning.net.au/demosites/series5/508/Laboratory/StudyNotes/snAASDetector.htm

Sunderland, E. M., & Chmura, G. L. (2000). An inventory of historical mercury emissions in Maritime Canada: implications for present and future contamination. *The Science of The Total Environment, 256*(1), 39-57.

Swaddle, T. W. (1997). *Inorganic Chemistry: An Industrial and Environmental Persepective*. SanDiego, CA: Academic Press.

Tabakci, M., & Yilmaz, M. (2008). Synthesis of a chitosan-linked calix [4] arene chelating polymer and its sorption ability toward heavy metals and dichromate anions. *Bioresource technology, 99*(14), 6642-6645.

Tanabe, K., Chiba, K., Haraguchi, H., & Fuwa, K. (1981). Determination of mercury at the ultratrace level by atmospheric pressure helium microwave-induced plasma emission spectrometry. *Analytical Chemistry, 53*(9), 1450-1453.

Tao, H., & Miyazaki, A. (1991). Determination of Germanium, Arsenic, Antimony, Tin and at Trace Levels by Continuous Hydride Generation-Helium Microwave-Induced Plasma Atomic Emission Spectrometry. *Analytical Sciences, 7*, 55-59.

Tassel, F., Rubio, J., Misra, M., & Jena, B. C. (1997). Removal of mercury from gold cyanide solution by dissolved air flotation. *Minerals Engineering, 10*(8), 803-811.

Telmer, K. H., & Veiga, M. M. (2009). World emissions of mercury from artisanal and small scale gold mining. In R. Mason & N. Pirrone (Eds.), *Mercury Fate and Transport in the Global Atmosphere* (pp. 131-172): Springer US.

Tiwari, R. K., Ghosh, S. K., Rupainwar, D. C., & Sharma, Y. C. (1993). Managing aqueous solutions rich in Mn(II): An inexpensive technique. *Colloids and Surfaces A: Physicochemical and Engineering Aspects, 70*(2), 131-137.

Tong, S. S. C., Gutenmann, W. H., & Lisk, D. J. (1969). Determination of mercury in apples by spark source mass spectrometry. *Analytical Chemistry, 41*(13), 1872-1874.

Torres, A. D., Rai, A. N., & Hardiek, M. L. (2000). Mercury intoxication and arterial hypertension: report of two patients and review of the literature. *Pediatrics, 105*(3), e34-e34.

Tsubaki, T., & Takahashi, H. (1986). *Recent Advances in Minamata Disease Studies : Methylmercury Poisoning in Minamata and Niigata, Japan*. Tokyo: Kodansha.

Tsubouchi, M. (1970). Spectrophotometric determination of trace amounts of mercury(II) by extraction with Bindschedler's green. *Analytical Chemistry, 42*(9), 1087-1088.

Tunnessen, W. W., McMahon, K. J., & Baser, M. (1987). Acrodynia: exposure to mercury from fluorescent light bulbs. *Pediatrics, 79*(5), 786-789.

U.S. Centers for Disease Control (ATSDR). (1999a). Public Health Statement for Mercury. from http://www.atsdr.cdc.gov/phs/phs.asp?id=112&tid=24

U.S. Centers for Disease Control (ATSDR). (1999b). Toxicological Profile for Mercury. from http://www.atsdr.cdc.gov/toxprofiles/tp.asp?id=115&tid=24

U.S. EIA. (2009). International Energy Outlook from www.eia.doe.gov/oiaf/archive/ieo09/index.html

U.S. EPA. (1997a). Mercury Study Report to Congress, Volume III: Fate and Transport of Mercury in the Environment.

U.S. EPA. (1997b). Mercury Study Report to Congress, Volume V: Health Effects of Mercury and Mercury Compounds.

U.S. EPA. (2004). Fish Advisories.

U.S. FDA. (2006). Thimerosal in Vaccines: Frequently Asked Questions., from http://www.fda.gov/cber/vaccine/thimfaq.htm

Ueno, K., Shiraishi, K., Tōgō, T., Yano, T., Yoshida, I., & Kobaybashi, H. (1979). Dual-wavelength spectrophotometric determination of traces of mercury(II) with solubilized dithizone: An approach to simplified analytical procedures for environmental pollutants. *Analytica Chimica Acta, 105*(0), 289-295.

UNEP. (2002). Global Mercury Assessment.

UNEP. (2009). The twenty-fifth session of the United Nations Environment Programme (UNEP) Governing Council/Global Ministerial Environment Forum

UNEP. (2011). Decisions of the twenty-sixth session of the Governing Council/Global Ministerial Environment Forum.

UNEP Chemicals. (2002). Global Mercury Assessment.

University of London. (2005). Surface Sensitivity & Surface Specificity. Retrieved 22 Jan 2014, from http://www.chem.qmul.ac.uk/surfaces/scc/scat5_1.htm

van Dijk, J., Hartgers, B., Jonkers, J., & van der Mullen, J. (2000). A collisional radiative model for mercury in high-current discharges. *Journal of Physics D: Applied Physics, 33*(21), 2798.

Van Leeuwen, P. W., & Leeuwen, P. W. (2004). *Homogeneous catalysis: understanding the art*: Springer.

Varma, A., Deshpande, S., & Kennedy, J. (2004). Metal complexation by chitosan and its derivatives: a review. *Carbohydrate Polymers, 55*(1), 77-93.

Visvanathan, C. (2003). *Treatment and Disposal of Mercury Contaminated Waste from Oil and Gas Exploration Facilities*. Paper presented at the International Environmental Disaster and Emergency Response Conference.

Wagler, H., & Koch, H. (1984). Contributions to the question of the existence of a tautomerism in solutions of dithizone in organic solvents - I: The correlation between the solvent-dependent differences in the response of systems palladium / copper-dithizone and / dithizone and the solvent-dependent spectra of the distinction dithizone. *Talanta, 31*(12), 1101-1108.

Wajima, T., & Sugawara, K. (2011). Adsorption behaviors of mercury from aqueous solution using sulfur-impregnated adsorbent developed from coal. *Fuel Processing Technology, 92*(7), 1322-1327.

Wang, C.-I., Huang, C.-C., Lin, Y.-W., Chen, W.-T., & Chang, H.-T. (2012). Catalytic gold nanoparticles for fluorescent detection of mercury(II) and lead(II) ions. *Analytica Chimica Acta, 745*(0), 124-130.

Wang, M., Zhang, Q., Hao, W., & Sun, Z. X. (2011). Surface stoichiometry of zinc sulfide and its effect on the adsorption behaviors of xanthate. *Chemistry Central Journal, 5*(1), 1-10.

Wang, Q., Kim, D., Dionysiou, D. D., Sorial, G. A., & Timberlake, D. (2004). Sources and remediation for mercury contamination in aquatic systems--a literature review. *Environmental Pollution, 131*(2), 323-336.

Watson, C. M., Dwyer, D. J., Andle, J. C., Bruce, A. E., & Bruce, M. R. M. (1999). Stripping Analyses of Mercury Using Gold Electrodes: Irreversible Adsorption of Mercury. *Analytical Chemistry, 71*(15), 3181-3186.

Webi, T. W., & Chakravort, R. K. (1974). Pore and solid diffusion models for fixed-bed adsorbers. *AIChE Journal, 20*(2), 228-238.

Wen, X., Wu, P., Chen, L., & Hou, X. (2009). Determination of cadmium in rice and water by tungsten coil electrothermal vaporization-atomic fluorescence spectrometry and tungsten coil electrothermal atomic absorption spectrometry after cloud point extraction. *Analytica Chimica Acta, 650*(1), 33-38.

WHO/IPCS. (1990). *Methylmercury, Environmental Health Criteria No. 101*. Geneva, Switzerland: World Health Organization.

Wikipedia. (2013). Full width at half maximum. Retrieved 22 Jan 2014

Wikipedia. (2014). Electromagnetic radiation. Retrieved 22 Jan 2014, from http://en.wikipedia.org/wiki/Electromagnetic_radiation

Winefordner, J. D., & Staab, R. A. (1964). Study of Experimental Parameters in Atomic Fluorescence Flame Spectrometry. *Analytical Chemistry, 36*(7), 1367-1369.

Wittke, J. (2008). Types of signals. Retrieved 22 Jan 2014, from http://www4.nau.edu/microanalysis/Microprobe-SEM/Signals.html

Wolthers, M., Charlet, L., van Der Linde, P. R., Rickard, D., & van Der Weijden, C. H. (2005). Surface chemistry of disordered mackinawite (FeS). *Geochimica et Cosmochimica Acta, 69*(14), 3469-3481.

Wu, C.-C., & Yang, M.-H. (1976). The retention behavior of radionuclides on copper(II) sulfide. *Analytica Chimica Acta, 84*(2), 335-345.

Wu, Q., Apte, S. C., Batley, G. E., & Bowles, K. C. (1997). Determination of the mercury complexation capacity of natural waters by anodic stripping voltammetry. *Analytica Chimica Acta, 350*(1–2), 129-134.

Yan, T. (1992). United States Patent No. 5080799.

Yap, P. L. (2012). Synthesis and Characterization of Unsupported Copper Sulfide for Mercury Trapping in Aqueous System. *M.Sc. Thesis. University of Malaya*.

Yap, P. L., Auyoong, Y. L., Kutty, M. G., Timpe, O., Behrens, M., & Abd Hamid, S. B. (2012). Facile Remediation Method of Copper Sulfide by Nitrogen Pre-Treatment. *Advanced Materials Research, 361-363*, 1445-1450.

Yardim, M. F., Budinova, T., Ekinci, E., Petrov, N., Razvigorova, M., & Minkova, V. (2003). Removal of mercury(II) from aqueous solution by activated carbon obtained from furfural. *Chemosphere, 52*(5), 835-841.

Yin, M., Li, Z., Liu, Z., Yang, X., & Ren, J. (2011). Magnetic Self-Assembled Zeolite Clusters for Sensitive Detection and Rapid Removal of Mercury(II). *ACS Applied Materials & Interfaces, 4*(1), 431-437.

Yoshino, M., Tanaka, H., & Okamoto, K. (1995). Speciation of organomercury by HPLC using chromium(II) reduction/atomic fluorescence spectrometry. *Bunseki kagaku, 44*(9), 691-695.

You, J., Hu, H., Zhou, J., Zhang, L., Zhang, Y., & Kondo, T. (2013). Novel Cellulose Polyampholyte–Gold Nanoparticle-Based Colorimetric Competition Assay for the Detection of Cysteine and Mercury(II). *Langmuir, 29*(16), 5085-5092.

Young, R. A. (1993). *The Rietveld Method*: International Union of Crystallography.

Yuan, C.-G., Wang, J., & Jin, Y. (2012). Ultrasensitive determination of mercury in human saliva by atomic fluorescence spectrometry based on solidified floating organic drop microextraction. *Microchimica Acta, 177*(1-2), 153-158.

Yui, T., Imada, K., Okuyama, K., Obata, Y., Suzuki, K., & Ogawa, K. (1994). Molecular and crystal structure of the anhydrous form of chitosan. *Macromolecules, 27*(26), 7601-7605.

Yun, Z., He, B., Wang, Z., Wang, T., & Jiang, G. (2012). Evaluation of different extraction procedures for determination of organic mercury species in petroleum by high performance liquid chromatography coupled with cold vapor atomic fluorescence spectrometry. *Talanta*.

Zen, J.-M., & Chung, M.-J. (1995). Square-wave voltammetric stripping analysis of mercury(II) at a poly(4-vinylpyridine)/gold film electrode. *Analytical Chemistry, 67*(19), 3571-3577.

Zhang, F.-S., Nriagu, J. O., & Itoh, H. (2005). Mercury removal from water using activated carbons derived from organic sewage sludge. *Water Research, 39*(2), 389-395.

Zhang, X.-Y., Wang, Q.-C., Zhang, S.-Q., Sun, X.-J., & Zhang, Z.-S. (2009). Stabilization/solidification (S/S) of mercury-contaminated hazardous wastes using thiol-functionalized zeolite and Portland cement. *Journal of hazardous materials, 168*(2–3), 1575-1580.

Zhou, L., Liu, S., & Huang, Q. (2007). Adsorption of mercury and uranyl onto poly (ethyleneimine) grafted chitosan microspheres. *Mod. Chem. Ind, 27*, 175-177.

Zhou, L., Wang, Y., Liu, Z., & Huang, Q. (2009). Characteristics of equilibrium, kinetics studies for adsorption of Hg (II), Cu (II), and Ni (II) ions by thiourea-modified magnetic chitosan microspheres. *Journal of hazardous materials, 161*(2), 995-1002.

Zhu, J., Deng, B., Yang, J., & Gang, D. (2009). Modifying activated carbon with hybrid ligands for enhancing aqueous mercury removal. *Carbon, 47*(8), 2014-2025.

Zhu, Y., Xu, L., Ma, W., Xu, Z., Kuang, H., Wang, L., et al. (2012). A one-step homogeneous plasmonic circular dichroism detection of aqueous mercury ions using nucleic acid functionalized gold nanorods. *Chemical Communications, 48*(97), 11889-11891.

Zhu, Z., Liu, Z., Zheng, H., & Hu, S. (2010). Non-chromatographic determination of inorganic and total mercury by atomic absorption spectrometry based on a dielectric barrier discharge atomizer. *Journal of Analytical Atomic Spectrometry, 25*(5), 697-703.

APPENDICES

Appendix A

Fitted parameters in Rietveld refinement of unreacted mixed phase Covellite:

Global R-Values

R_{exp} : 11.64 R_{wp} : 13.77 R_p : 10.45 GOF : 1.18

$R_{exp`}$: 21.50 $R_{wp`}$: 25.43 $R_{p`}$: 23.92 DW : 1.10

R-Values

R_{exp} : 11.64 R_{wp} : 13.77 R_p : 10.45 GOF : 1.18

$R_{exp`}$: 21.50 $R_{wp`}$: 25.43 $R_{p`}$: 23.92 DW : 1.10

Quantitative Analysis - Rietveld

Phase 1 : CuS_ICSD-36155		67.27(39) %
Phase 2 : $CuSO_4$_$5H_2O$_ICSD-4305		32.73(39) %

Background

Chebychev polynomial, Coefficient	0	55.60(20)
	1	-69.45(33)
	2	39.21(25)
	3	-16.56(18)
	4	5.20(15)

Instrument

Primary radius (mm)	217.5
Secondary radius (mm)	217.5

Corrections

Zero error	0.01820(96)
LP Factor	27.3

Miscellaneous

X Calculation Step	0.02
Start X	7

Structure 1

Phase name	CuS_ICSD-36155
R-Bragg	4.111
Spacegroup	P63/mmc
Scale	0.00019074(80)
Cell Mass	573.674
Cell Volume ($Å^3$)	203.686(12)
Wt% - Rietveld	67.27(39)
Crystallite Size	
Cry size Lorentzian (nm)	115.4(48)
k: 1 LVol-IB (nm)	73.5(31)
k: 0.89 LVol-FWHM (nm)	102.7(43)
Strain	
Strain L	0.2474(90)
e0	0.0618(23)
Crystal Linear Absorption Coeff. (1/cm)	307.968(18)
Crystal Density (g/cm^3)	4.67686(27)
Preferred Orientation Spherical Harmonics	
Order	6
y00	1
y20	-0.0403(99)
y40	0.175(10)

y60	-0.0032(12)
y66p	-0.0319(75)
Lattice parameters	
a (Å)	3.792272(91)
c (Å)	16.35426(53)

Site	Np	x	y	z	Atom	Occ	Beq
Cu1	4	0.33333	0.66667	0.10700	Cu+2	1	1
Cu2	2	0.33333	0.66667	0.75000	Cu+2	1	1
S1	4	0.00000	0.00000	0.06250	S	1	1
S2	2	0.33333	0.66667	0.25000	S	1	1

Structure 2

Phase name	$CuSO_4\_5H_2O\_ICSD-4305$
R-Bragg	7.522
Spacegroup	P-1
Scale	0.0000622(11)
Cell Mass	479.213
Cell Volume ($Å^3$)	363.728(40)
Wt% - Rietveld	32.73(39)
Crystallite Size	
Cry size Lorentzian (nm)	213(32)
Cry size Gaussian (nm)	98.6(64)
k: 1 LVol-IB (nm)	62.6(42)
k: 0.89 LVol-FWHM (nm)	68.9(42)
Crystal Linear Absorption Coeff. (1/cm)	72.5992(80)
Crystal Density (g/cm^3)	2.18777(24)
Lattice parameters	
a (Å)	6.11973(37)
b (Å)	10.72272(67)

c (Å)	5.96436(36)
alpha (°)	82.3783(42)
beta (°)	107.2950(44)
gamma (°)	102.5943(44)

Site	Np	x	y	z	Atom	Occ	Beq
Cu1	1	0.00000	0.00000	0.00000	Cu+2	1	1
Cu2	1	0.50000	0.50000	0.00000	Cu+2	1	1
S1	2	0.01330	0.28710	0.62530	S	1	1
O1	2	0.90720	0.15200	0.67340	O-2	1	1
O2	2	0.24420	0.31720	0.79600	O-2	1	1
O3	2	0.86010	0.37240	0.63630	O-2	1	1
O4	2	0.04440	0.30220	0.38490	O-2	1	1
O5	2	0.81760	0.07370	0.15190	O-2	1	1
O6	2	0.28870	0.11770	0.14900	O-2	1	1
O7	2	0.46540	0.40630	0.29750	O-2	1	1
O8	2	0.75600	0.41610	0.01910	O-2	1	1
O9	2	0.43500	0.12630	0.62890	O-2	1	1

Appendix B

Nitrogen adsorption and desorption isotherms of unreacted pure phase Covellite:

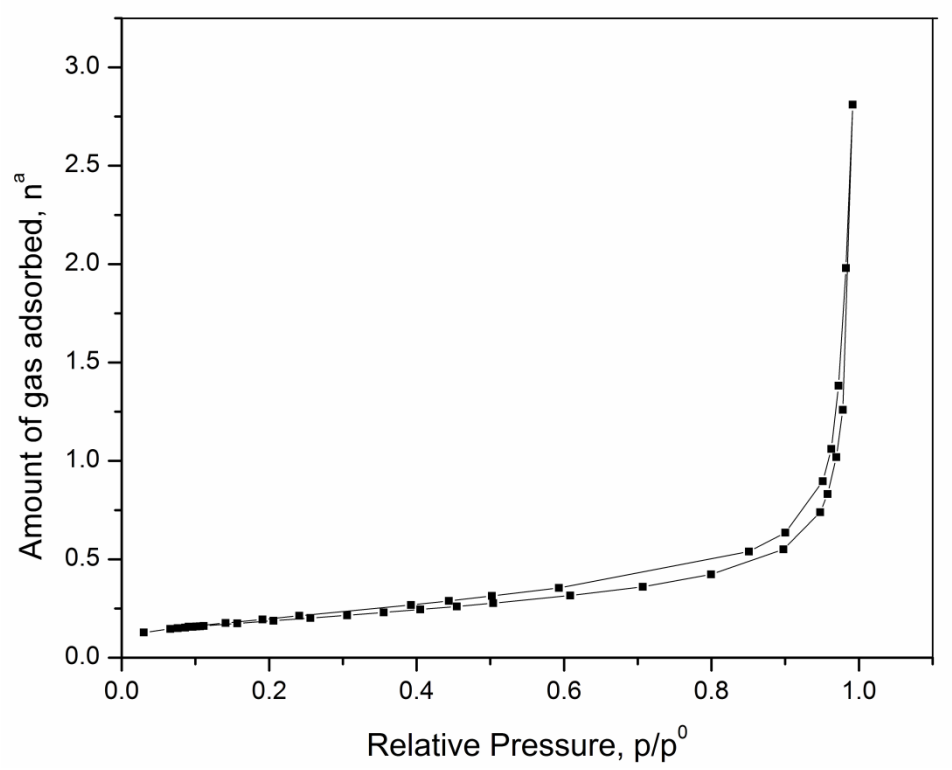

Multipoint BET measurement of unreacted pure phase Covellite:

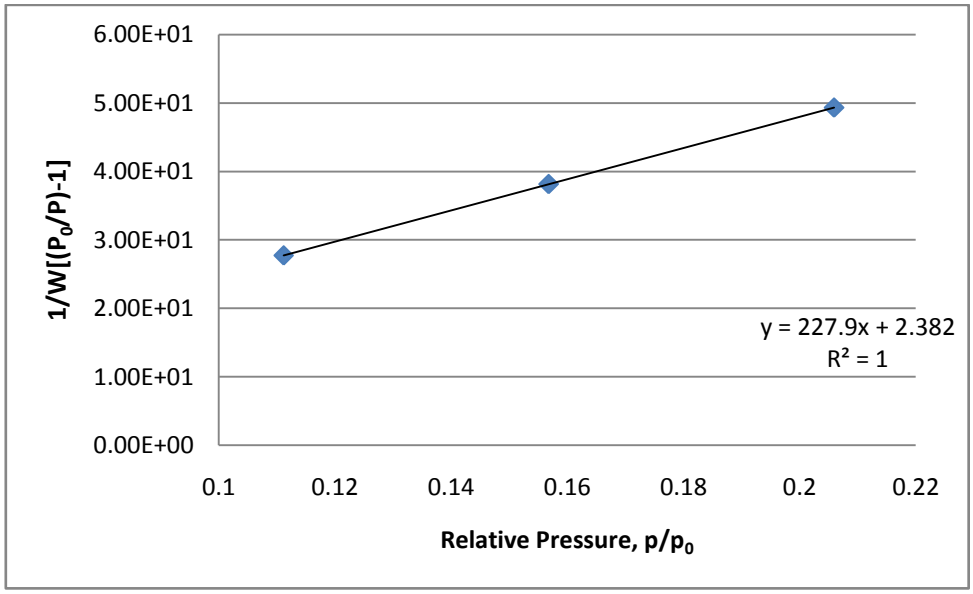

Appendix C

Fitted parameters in Rietveld refinement of reacted pure phase Covellite under reaction condition of 600 ppm Hg(II), pH 2 and temperature of 25°C:

Global R-Values

R_{exp} : 9.85 R_{wp} : 12.19 R_p : 9.47 GOF : 1.24

$R_{exp`}$: 23.50 $R_{wp`}$: 29.08 $R_{p`}$: 28.69 DW : 0.97

R-Values

R_{exp} : 9.85 R_{wp} : 12.19 R_p : 9.47 GOF : 1.24

$R_{exp`}$: 23.50 $R_{wp`}$: 29.08 $R_{p`}$: 28.69 DW : 0.97

Quantitative Analysis - Rietveld

Phase 1 : CuS_ICSD-36155	72.4(16) %
Phase 2 : modified_from_$Hg_3S_2Br_2$_ICSD-82786	27.6(16) %

Background

Chebychev polynomial, Coefficient	0	84.16(27)
	1	-92.30(32)
	2	42.22(34)
	3	-12.13(27)
	4	0.01(23)

Instrument

Primary radius (mm)	217.5
Secondary radius (mm)	217.5

Corrections

Zero error	-0.0073(18)
LP Factor	27.3

Miscellaneous

X Calculation Step	0.02
Start X	7

Structure 1

Phase name	CuS_ICSD-36155
R-Bragg	3.449
Spacegroup	P63/mmc
Scale	0.00010866(75)
Cell Mass	573.674
Cell Volume ($Å^3$)	203.338(21)
Wt% - Rietveld	72.4(16)
Crystallite Size	
Cry size Lorentzian (nm)	127.1(97)
Strain	
Strain L	0.195(15)
Crystal Linear Absorption Coeff. (1/cm)	308.495(32)
Crystal Density (g/cm^3)	4.68485(49)
Preferred Orientation Spherical Harmonics	
Order	6
y00	1
y20	-0.038(16)
y40	0.155(16)
y60	-0.0121(19)
y66p	-0.014(13)
Lattice parameters	
a (Å)	3.79014(17)
c (Å)	16.34476(89)

Site	Np	x	y	z	Atom	Occ	Beq
Cu1	4	0.33333	0.66667	0.10700	Cu+2	1	1
Cu2	2	0.33333	0.66667	0.75000	Cu+2	1	1
S1	4	0.00000	0.00000	0.06250	S	1	1
S2	2	0.33333	0.66667	0.25000	S	1	1

Structure 2

Phase name	modified_from_$Hg_3S_2Br_2$_ICSD-82786
R-Bragg	5.312
Spacegroup	C12/m1
Scale	0.000000630(50)
Cell Mass	5340(100)
Cell Volume ($Å^3$)	1437.25(48)
Wt% - Rietveld	27.6(16)
Crystallite Size	
Cry size Lorentzian (nm)	32.5(15)
Cry size Gaussian (nm)	91(21)
Crystal Linear Absorption Coeff. (1/cm)	1120(25)
Crystal Density (g/cm^3)	6.17(12)
Lattice parameters	
a (Å)	17.5844(23)
b (Å)	8.9823(10)
c (Å)	10.1043(22)
beta (°)	115.769(22)

Site	Np	x	y	z	Atom	Occ	Beq
Hg1	4	0.0878(19)	0.00000	0.7163(39)	Hg+2	0.349(55)	1
					Cu+2	0.651(55)	1
Hg2	4	0.2123(14)	0.00000	0.2858(26)	Hg+2	0.847(73)	1

					Cu+2	0.153(73)	1
Hg3	8	0.13217(74)	0.2625(13)	0.0016(23)	Hg+2	1.000(61)	1
					Cu+2	0.000(61)	1
Hg4	8	0.06316(93)	0.2661(14)	0.2981(11)	Hg+2	0.897(57)	1
					Cu+2	0.103(57)	1
Br1	2	0.00000	0.00000	0.00000	Cl-1	1	1
Br2	2	0.00000	0.50000	0.00000	Cl-1	1	1
Br3	4	0.11540	0.50000	0.49980	Cl-1	1	1
Br4	4	0.12280	0.00000	0.49100	Cl-1	1	1
Br5	4	0.25040	0.50000	0.99650	Cl-1	1	1
S1	8	0.19810	0.25640	0.26240	S	1	1
S2	8	0.06860	0.25670	0.74660	S	1	1

Appendix D:

CuS and m-$Hg_3S_2Cl_2$ peak area evaluation in PXRD patterns of Figure 6.33 – Figure 6.38:

1) Reaction condition: 50 ppm and 25°C – Data evaluated according to Figure 6.33 & depicted in Figure 6.43 (a).

pH	Peak maximum position, 2θ (°)	Crystal Phase	FWHM, 2θ (°)	Peak Height (cps)	Peak Area (a.u.)	Peak Area Quantification Ratio
1	31.78	CuS	0.2010	874.00	334.20	0.0956
	34.59	m-$Hg_3S_2Cl_2$	0.2680	17.40	31.94	
2	31.78	CuS	0.1920	719.00	292.30	0.1050
	34.55	m-$Hg_3S_2Cl_2$	*N.A.	10.40	30.68	
3	31.80	CuS	0.1970	874.00	337.20	0.0923
	34.42	m-$Hg_3S_2Cl_2$	*N.A.	13.60	31.13	
4	31.78	CuS	0.1990	879.00	329.10	0.0923
	34.47	m-$Hg_3S_2Cl_2$	0.1690	12.20	30.39	
5	31.79	CuS	0.1940	987.00	362.30	0.0883
	34.50	m-$Hg_3S_2Cl_2$	*N.A.	14.90	31.98	
6	31.80	CuS	0.1980	796.00	318.10	0.1021
	34.57	m-$Hg_3S_2Cl_2$	0.2560	12.10	32.47	
7	31.79	CuS	0.1960	901.00	354.80	0.0899
	34.55	m-$Hg_3S_2Cl_2$	0.2930	17.20	31.90	
8	31.80	CuS	0.1990	942.00	355.00	0.1001
	34.44	m-$Hg_3S_2Cl_2$	0.1330	17.00	35.52	
9	31.80	CuS	0.2050	981.00	368.80	0.0880
	34.90	m-$Hg_3S_2Cl_2$	0.2700	17.60	32.44	

*N.A. denotes peak is not available.

2) Reaction condition: 150 ppm and 25°C – Data evaluated according to Figure 6.34 & depicted in Figure 6.43 (b).

pH	Peak maximum position, 2θ (°)	Crystal Phase	FWHM, 2θ (°)	Peak Height (cps)	Peak Area (a.u.)	Peak Area Quantification Ratio
1	31.80	CuS	0.1850	1013.00	365.30	0.2902
	34.69	m-$Hg_3S_2Cl_2$	0.1920	233.00	106.00	
2	31.80	CuS	0.1780	778.00	307.10	0.2683
	34.69	m-$Hg_3S_2Cl_2$	0.1920	151.00	82.38	
3	31.80	CuS	0.1870	1002.00	359.00	0.2483
	34.71	m-$Hg_3S_2Cl_2$	0.2140	165.00	89.13	
4	31.80	CuS	0.1880	1059.00	375.80	0.2168
	34.70	m-$Hg_3S_2Cl_2$	0.2070	159.00	81.47	
5	31.81	CuS	0.1850	908.00	336.80	0.2087
	34.68	m-$Hg_3S_2Cl_2$	0.1950	125.00	70.28	
6	31.80	CuS	0.1830	789.00	310.40	0.1932
	34.66	m-$Hg_3S_2Cl_2$	0.2120	81.00	59.97	
7	31.80	CuS	0.1910	872.00	338.40	0.1771
	34.74	m-$Hg_3S_2Cl_2$	0.2370	67.80	59.93	
8	31.80	CuS	0.1900	909.00	352.10	0.1560
	34.70	m-$Hg_3S_2Cl_2$	0.1530	58.30	54.94	
9	31.80	CuS	0.2010	782.00	316.80	0.1601
	34.70	m-$Hg_3S_2Cl_2$	0.1990	38.80	50.72	

3) Reaction condition: 250 ppm and 25°C – Data evaluated according to Figure 6.35 & depicted in Figure 6.43 (c) and Figure 6.44 (a).

pH	Peak maximum position, 2θ (°)	Crystal Phase	FWHM, 2θ (°)	Peak Height (cps)	Peak Area (a.u.)	Peak Area Quantification Ratio
1	31.79	CuS	0.2300	1393.00	588.90	0.4517
	34.65	m-$Hg_3S_2Cl_2$	0.3020	414.00	266.00	
2	31.79	CuS	0.2300	864.00	362.90	0.4326
	34.67	m-$Hg_3S_2Cl_2$	0.2740	253.00	157.00	
3	31.76	CuS	0.2290	941.00	397.70	0.4340
	34.61	m-$Hg_3S_2Cl_2$	0.2730	289.00	172.60	
4	31.78	CuS	0.2320	907.00	386.10	0.4325
	34.68	m-$Hg_3S_2Cl_2$	0.3020	275.00	167.00	
5	31.78	CuS	0.2370	1080.00	447.20	0.4226
	34.67	m-$Hg_3S_2Cl_2$	0.2650	333.00	189.00	
6	31.76	CuS	0.2310	1105.00	456.80	0.3892
	34.69	m-$Hg_3S_2Cl_2$	0.2550	312.00	177.80	
7	31.79	CuS	0.2330	1237.00	512.20	0.1993
	34.72	m-$Hg_3S_2Cl_2$	0.2850	66.90	102.10	
8	31.79	CuS	0.2250	2578.00	953.20	0.1140
	34.39	m-$Hg_3S_2Cl_2$	0.5370	18.20	108.70	
9	31.79	CuS	0.2230	2633.00	956.80	0.1090
	35.05	m-$Hg_3S_2Cl_2$	0.4990	23.90	104.30	

4) Reaction condition: 600 ppm and 25°C – Data evaluated according to Figure 6.36 & depicted in Figure 6.43 (d).

pH	Peak maximum position, 2θ (°)	Crystal Phase	FWHM, 2θ (°)	Peak Height (cps)	Peak Area (a.u.)	Peak Area Quantification Ratio
1	31.83	CuS	0.1910	596.00	211.20	0.8234
	34.67	m-$Hg_3S_2Cl_2$	0.2170	405.00	173.90	
2	31.80	CuS	0.1920	629.00	219.20	0.7897
	34.64	m-$Hg_3S_2Cl_2$	0.2240	361.00	173.10	
3	31.79	CuS	0.1880	642.00	218.70	0.7892
	34.66	m-$Hg_3S_2Cl_2$	0.2200	376.00	172.60	
4	31.81	CuS	0.1990	583.00	218.10	0.8519
	34.67	m-$Hg_3S_2Cl_2$	0.2210	429.00	185.80	
5	31.80	CuS	0.1990	552.00	199.40	0.8761
	34.69	m-$Hg_3S_2Cl_2$	0.2270	415.00	174.70	
6	31.81	CuS	0.1740	554.00	190.10	0.9074
	34.71	m-$Hg_3S_2Cl_2$	0.2250	378.00	172.50	
7	31.80	CuS	0.1750	423.00	163.20	0.9510
	34.71	m-$Hg_3S_2Cl_2$	0.2280	294.00	155.20	
8	31.79	CuS	0.2110	353.00	163.50	0.7761
	34.73	m-$Hg_3S_2Cl_2$	0.2280	208.00	126.90	
9	31.80	CuS	0.1690	910.00	289.50	0.1920
	34.49	m-$Hg_3S_2Cl_2$	0.1160	14.40	55.59	

5) Reaction condition: 250 ppm and 35°C – Data evaluated according to Figure 6.37 & depicted in Figure 6.44 (b).

pH	Peak maximum position, 2θ (°)	Crystal Phase	FWHM, 2θ (°)	Peak Height (cps)	Peak Area (a.u.)	Peak Area Quantification Ratio
1	31.80	CuS	0.1700	537.00	168.80	0.7056
	34.65	m-$Hg_3S_2Cl_2$	0.2060	272.00	119.10	
2	31.79	CuS	0.1690	645.00	192.10	0.6773
	34.65	m-$Hg_3S_2Cl_2$	0.2170	310.00	130.10	
3	31.80	CuS	0.1650	531.00	165.80	0.6653
	34.66	m-$Hg_3S_2Cl_2$	0.2170	234.00	110.30	
4	31.79	CuS	0.1630	585.00	180.60	0.6523
	34.69	m-$Hg_3S_2Cl_2$	0.2420	261.00	117.80	
5	31.79	CuS	0.1630	611.00	184.50	0.6249
	34.68	m-$Hg_3S_2Cl_2$	0.1970	266.00	115.30	
6	31.80	CuS	0.1550	663.00	191.50	0.5864
	34.67	m-$Hg_3S_2Cl_2$	0.2290	233.00	112.30	
7	31.80	CuS	0.1560	441.00	143.70	0.5681
	34.69	m-$Hg_3S_2Cl_2$	0.2280	136.00	81.64	
8	31.80	CuS	0.1710	525.00	175.60	0.3894
	34.75	m-$Hg_3S_2Cl_2$	0.2150	88.50	68.38	
9	31.78	CuS	0.1820	641.00	201.70	0.2393
	34.80	m-$Hg_3S_2Cl_2$	0.1120	40.50	48.26	

6) Reaction condition: 250 ppm and 45°C – Data evaluated according to Figure 6.38 & depicted in Figure 6.44 (c).

pH	Peak maximum position, 2θ (°)	Crystal Phase	FWHM, 2θ (°)	Peak Height (cps)	Peak Area (a.u.)	Peak Area Quantification Ratio
1	31.81	CuS	0.1730	576.00	177.30	0.7214
	34.66	m-$Hg_3S_2Cl_2$	0.2130	262.00	127.90	
2	31.81	CuS	0.1720	346.00	121.00	0.6988
	34.66	m-$Hg_3S_2Cl_2$	0.2140	151.00	84.55	
3	31.80	CuS	0.1610	568.00	171.20	0.5684
	34.62	m-$Hg_3S_2Cl_2$	0.2570	151.00	97.31	
4	31.79	CuS	0.1810	466.00	154.70	0.5670
	34.70	m-$Hg_3S_2Cl_2$	0.2430	138.00	87.72	
5	31.80	CuS	0.1670	539.00	166.50	0.5847
	34.68	m-$Hg_3S_2Cl_2$	0.2360	160.00	97.35	
6	31.81	CuS	0.1850	539.00	173.60	0.5708
	34.66	m-$Hg_3S_2Cl_2$	0.2470	162.00	99.09	
7	31.80	CuS	0.1760	517.00	170.20	0.5639
	34.70	m-$Hg_3S_2Cl_2$	0.2500	145.00	95.97	
8	31.80	CuS	0.1720	469.00	155.60	0.4136
	34.75	m-$Hg_3S_2Cl_2$	0.1060	81.30	64.36	
9	31.80	CuS	0.1880	486.00	166.70	0.3349
	34.79	m-$Hg_3S_2Cl_2$	0.0908	27.10	55.83	

Appendix E:

PXRD patterns of unreacted and reacted CuS:

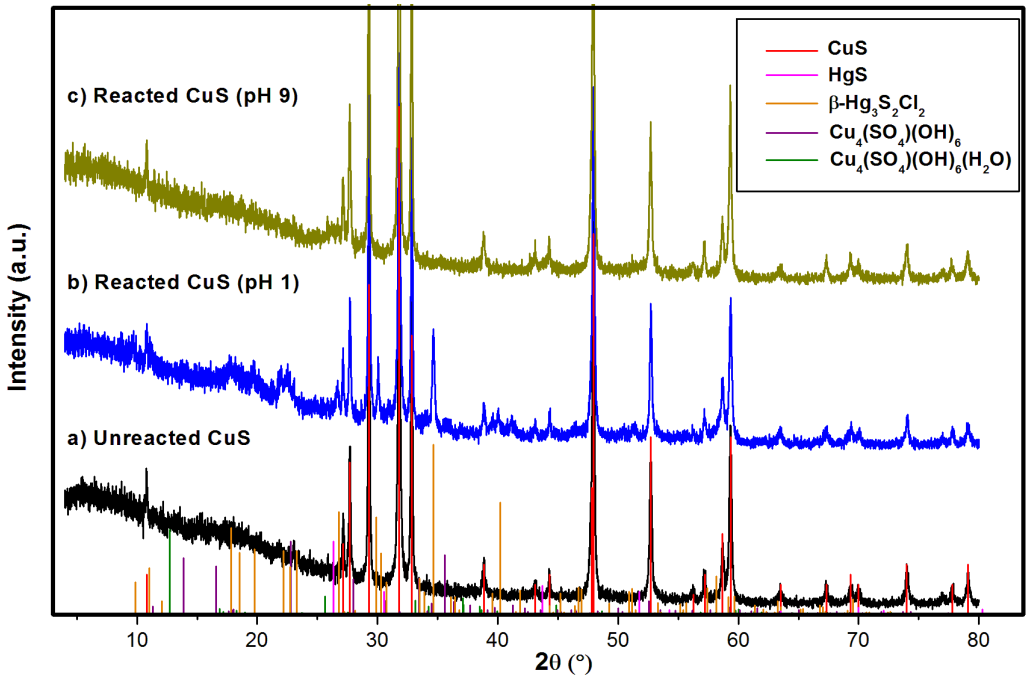

PXRD pattern of unreacted and reacted Covellite under reaction condition of 100 ppm Hg(II) at 25°C, pH of 1 and 9.

Appendix F:

FESEM image of unreacted and reacted CuS:

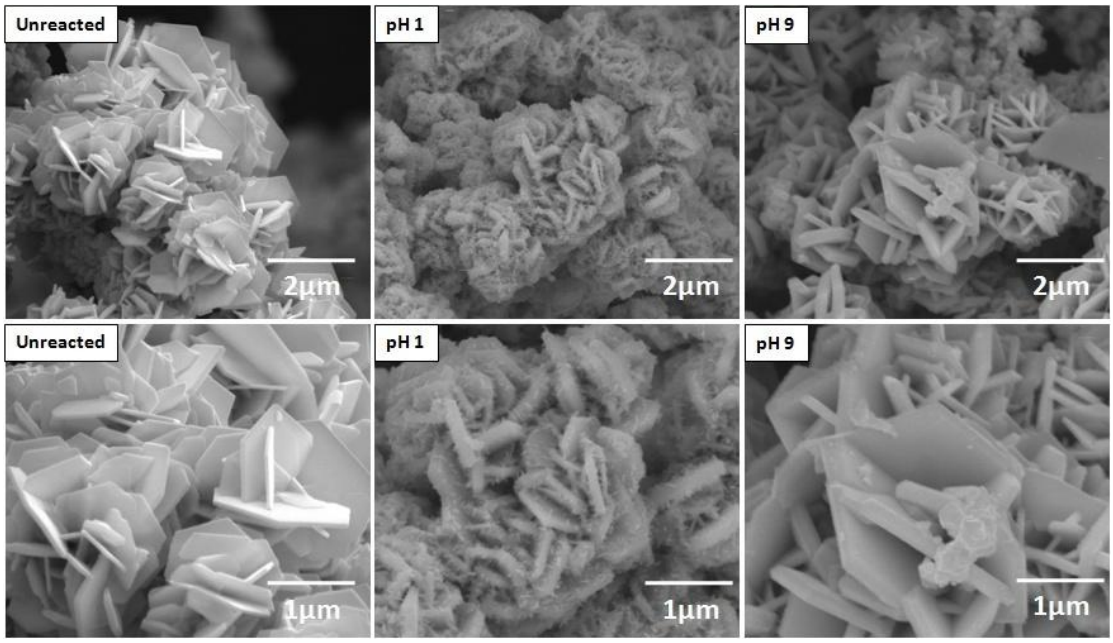

FESEM images of unreacted and reacted Covellite under reaction condition of 100 ppm Hg(II) at 25°C, pH of 1 and 9.